

BRIGHT $Z \sim 3$ LYMAN BREAK GALAXIES IN DEEP WIDE FIELD SURVEYS

by

Fuyan Bian

A Dissertation Submitted to the Faculty of the
DEPARTMENT OF ASTRONOMY
In Partial Fulfillment of the Requirements
For the Degree of
DOCTOR OF PHILOSOPHY
In the Graduate College
THE UNIVERSITY OF ARIZONA

2013

THE UNIVERSITY OF ARIZONA
GRADUATE COLLEGE

As members of the Dissertation Committee, we certify that we have read the dissertation prepared by Fuyan Bian entitled “Bright $Z \sim 3$ Lyman Break Galaxies in Deep Wide Field Surveys” and recommend that it be accepted as fulfilling the dissertation requirement for the Degree of Doctor of Philosophy.

_____ Date: 26 November 2012
Dr. Xiaohui Fan

_____ Date: 26 November 2012
Dr. Romeel Davé

_____ Date: 26 November 2012
Dr. Arjun Dey

_____ Date: 26 November 2012
Dr. Richard Green

_____ Date: 26 November 2012
Dr. Ann Zabludoff

Final approval and acceptance of this dissertation is contingent upon the candidate’s submission of the final copies of the dissertation to the Graduate College.

I hereby certify that I have read this dissertation prepared under my direction and recommend that it be accepted as fulfilling the dissertation requirement.

_____ Date: 26 November 2012
Dissertation Director: Dr. Xiaohui Fan

STATEMENT BY AUTHOR

This dissertation has been submitted in partial fulfillment of requirements for an advanced degree at The University of Arizona and is deposited in the University Library to be made available to borrowers under rules of the Library.

Brief quotations from this dissertation are allowable without special permission, provided that accurate acknowledgment of source is made. Requests for permission for extended quotation from or reproduction of this manuscript in whole or in part may be granted by the head of the major department or the Dean of the Graduate College when in his or her judgment the proposed use of the material is in the interests of scholarship. In all other instances, however, permission must be obtained from the author.

SIGNED: Fuyan Bian

ACKNOWLEDGMENTS

First and foremost, I would like to thank my advisor, Xiaohui Fan. His advice and encouragement play crucial roles in my research. He always inspires me to develop independent thinking and research skills, and to collaborate with others in different fields. Without his support, I could not have done my doctoral work. I would also like to thank my prelim and thesis committee members: Romeel Dave, Arjun Dey, Daniel Eisenstein, Richard Green, Ann Abludoff, who gave me extensive suggestions and comments on my researches and asked me inspired questions to improve my thesis work.

I want to thank my officemates Alan Cooney, Andras Gaspar, Jennifer Donley, Dennis Just, David Lesser, Jeremiah Murphy, Jan-Torge Schindler, Justin Spilker, Brandon Swift, Brian Svoboda, Xiaoying, Xu. I had a wonderful time with them. I also want to thank graduate students: Lei Bai, Amanda Ford, Cui Jun, Jenna Kloosterman, Derek Kopon, Kyle Penner, Wiphu Rujopakarn, Yong Shi, Suresh Sivanandam, Gregory Walth, Kenneth Wong, Ya-Lin Wu, Lei Xu, Chang You. I enjoy the time with them to discuss the science, talk about the life in Tucson, have parties and go to hiking.

My special thanks to our current and previous research group members: Zheng Cai, Brenda Frye, Linhua Jiang, Ian McGreer, Dan Stark, Ran Wang. I enjoy the extensive discussions on the high-redshift galaxies and quasars in the group meeting, which really opened my eyes and inspired me coming up a lot of new scientific ideas. They also helped me to solve a lot of technical problems and from them I learned how to carry out observing and how to do research effectively.

I would like to thank the Steward and NOAO TAC. They are very supportive and generous on the telescope application from graduate students. Without their support of the telescope time on my researches, I could not have my thesis work done. I also would like to thank the LBTO, NOAO, MMT staff for their great supports on the observing preparation and observations. Without their helps, I could not take the beautiful data for this thesis.

Finally, I would like to thank my wife Yan Zhang and my daughter Sihan Emma Bian.

DEDICATION

I dedicate this thesis to my wife, Yan Zhang

TABLE OF CONTENTS

| | |
|--------------------------------------------------------------------|----|
| LIST OF FIGURES | 10 |
| LIST OF TABLES | 17 |
| ABSTRACT | 18 |
| CHAPTER 1 INTRODUCTION | 20 |
| 1.1 High-redshift Galaxy Surveys | 20 |
| 1.2 Ultra-violet Luminosity Function | 21 |
| 1.3 Clustering of High-redshift Star-forming Galaxies | 22 |
| 1.4 Physical Properties of High-redshift Galaxies | 22 |
| 1.5 Far-infrared Properties of UV-selected Galaxies | 23 |
| 1.6 Galaxy SFR-stellar Mass Main Sequence | 24 |
| 1.7 Deep and Wide Field Surveys | 25 |
| CHAPTER 2 LBT/LUCIFER OBSERVATIONS OF THE $Z \sim 2$ LENSED GALAXY | |
| J0900+2234 | 28 |
| 2.1 Introduction | 29 |
| 2.2 Observations and Data Reduction | 31 |
| 2.2.1 LUCIFER | 31 |
| 2.2.2 LUCIFER Imaging & Spectroscopy | 32 |
| 2.2.3 Data Reduction | 32 |
| 2.2.3.1 Imaging Reduction | 32 |
| 2.2.3.2 Spectroscopy Reduction | 34 |
| 2.3 Measurements | 39 |
| 2.3.1 NIR Photometry: Discovery of a New Lensed Galaxy | 39 |
| 2.3.2 Emission Line Measurements | 40 |
| 2.4 Lensed Model | 42 |
| 2.5 Physical Properties | 43 |
| 2.5.1 Emission-Line Diagnostics | 43 |
| 2.5.2 Reddening and Extinction | 45 |
| 2.5.3 Star Formation Rate | 48 |
| 2.5.4 Oxygen Abundance | 49 |
| 2.5.5 Electron Density | 52 |
| 2.5.6 Virial Mass and Gas Mass | 52 |
| 2.5.7 Measurement Uncertainty | 54 |
| 2.6 Conclusions | 56 |

TABLE OF CONTENTS — *Continued*

| | |
|-----------------------------------------------------------------------------------------------------------------------------------------------------------------------------|-----|
| CHAPTER 3 THE LBT BOÖTES FIELD SURVEY: I. THE REST-FRAME ULTRAVIOLET AND NEAR-INFRARED LUMINOSITY FUNCTIONS AND CLUSTERING OF BRIGHT LYMAN BREAK GALAXIES AT $Z \sim$ | |
| 3 | 58 |
| 3.1 Introduction | 59 |
| 3.2 Observations | 62 |
| 3.3 Data Reduction | 66 |
| 3.3.1 Bias and Flat Correction | 66 |
| 3.3.2 Image Quality Measurement | 68 |
| 3.3.3 Astrometric Calibration | 69 |
| 3.3.4 Image Co-addition | 69 |
| 3.3.5 Photometric Calibration | 70 |
| 3.3.6 Survey Depth | 73 |
| 3.4 LBG Sample Selection | 73 |
| 3.4.1 Photometry | 73 |
| 3.4.2 Sample Selection Criteria | 75 |
| 3.4.3 Selection Function | 76 |
| 3.4.4 A Photometrically-Selected Sample of $z \sim 3$ LBGs | 79 |
| 3.5 UV Luminosity Function | 80 |
| 3.5.1 Results | 80 |
| 3.5.2 UV Luminosity Density | 83 |
| 3.5.3 Systematic uncertainties of LF measurement | 85 |
| 3.5.4 Discussion | 90 |
| 3.6 Near-IR Luminosity Function | 90 |
| 3.6.1 The Rest-frame UV/Near-IR Color Relation of LBGs | 91 |
| 3.6.2 Results | 92 |
| 3.6.3 Discussion | 94 |
| 3.6.4 Stellar mass function | 96 |
| 3.7 The Evolution of UV LF and SMF | 99 |
| 3.8 Clustering Properties of LBGs | 104 |
| 3.8.1 Result | 104 |
| 3.8.2 Discussion | 109 |
| 3.9 SUMMARY | 113 |
| CHAPTER 4 AN ULTRAVIOLET ULTRA-LUMINOUS LYMAN BREAK GALAXY AT $Z = 2.78$ IN NDWFS BOÖTES FIELD | |
| 4.1 Introduction | 117 |
| 4.2 Observations | 118 |
| 4.3 Results | 120 |
| 4.3.1 Lensed or Unlensed? | 120 |

| | |
|------------------------------------------------------------------------------------------------------------------|----------------------------------------------------------------------------------------|
| TABLE OF CONTENTS — <i>Continued</i> | |
| 4.3.2 | Morphology 122 |
| 4.3.3 | Spectroscopy 124 |
| 4.3.4 | Physical Properties 132 |
| 4.4 | Discussion 134 |
| CHAPTER 5 THE LBT BOÖTES FIELD SURVEY: II. A POPULATION OF UV ULTRA-LUMINOUS LBGs AT $Z \sim 3$ 137 | |
| 5.1 | Introduction 137 |
| 5.2 | Observations 139 |
| 5.2.1 | Imaging Observations and Target Selection 139 |
| 5.2.2 | MMT Spectroscopic observations and Data Reduction . . . 141 |
| 5.3 | Results 143 |
| 5.3.1 | Spectral Identification 143 |
| 5.3.2 | Notes on Individual LBGs 149 |
| 5.3.3 | The Bright End UV Luminosity Function 150 |
| 5.3.4 | Rest-frame UV Spectrum of Ultra-luminous LBGs 153 |
| 5.3.4.1 | Systemic Redshift 156 |
| 5.3.4.2 | Galactic-scale Outflows 157 |
| 5.3.4.3 | Initial Mass Function 158 |
| 5.3.5 | IRAC Colors 159 |
| 5.3.6 | Physical Properties 162 |
| 5.4 | Discussion 169 |
| 5.4.1 | Evolutionary Stage of ULBGs 169 |
| 5.4.1.1 | Post-starburst Scenario 170 |
| 5.4.1.2 | Pre-starburst Scenario 171 |
| 5.4.2 | Outflows Velocity in LBGs 172 |
| 5.4.3 | Initial Mass Function 173 |
| 5.5 | Summary and Conclusions 174 |
| CHAPTER 6 CONCLUSION AND FUTURE STUDIES 177 | |
| 6.1 | Conclusion 177 |
| 6.2 | Further Studies 179 |
| 6.2.1 | The Nature of the ULBGs 180 |
| 6.2.2 | Galaxy Evolution in the Early Universe with the Deep and Wide Surveys 180 |
| APPENDIX A INTEGRAL CONSTRAINT 182 | |
| APPENDIX B HALO OCCUPATION DISTRIBUTION 184 | |

| | |
|------------------------------------------------------------|-----|
| TABLE OF CONTENTS — <i>Continued</i> | |
| APPENDIX C ULTRA-LUMINOUS LBGS IN SDSS STRIPE 82 FIELD . . | 186 |
| REFERENCES | 189 |

LIST OF FIGURES

| | | |
|------------|----------------------------------------------------------------------------------------------------------------------------------------------------------------------------------------------------------------------------------------------------------------------------------------------------------------------------------------------------------------------------------------------------------------------------------------------------------------------------------------------------------------------------------------------------------------------------------------------------------------------------------------|----|
| FIGURE 1.1 | SURVEY MAGNITUDE LIMIT AND SURVEY AREA OF THE SPECTROSCOPIC FOLLOW-UP SURVEYS OF HIGH-REDSHIFT GALAXIES. OUR NDWFS BOÖTES FIELD SURVEY AND SDSS STRIPE82 SURVEY OF LUMINOUS $z \sim 3$ LBGs LOCATE AT A UNIQUE AREA. . . | 26 |
| FIGURE 2.1 | J , H , AND Ks BAND IMAGES OF J0900+2234 FROM LUCIFER, NORTH IS UP, AND EAST IS LEFT. EACH IMAGE SHOWN HAS $40'' \times 40''$ THE PREVIOUSLY DISCOVERED A, B, C, AND D COMPONENTS ARE LABELED IN THE J -BAND IMAGE. THE A, B, AND D COMPONENTS ARE IMAGES OF THE STAR-FORMING GALAXY AT $z \sim 2$. OUR FOLLOW-UP SPECTROSCOPY SHOWS THAT C IS NOT AN IMAGE OF THE SAME GALAXY. THE NEWLY DISCOVERED A1 ARC FROM ANOTHER LENSED GALAXY IS ALSO LABELED IN THE IMAGE. | 33 |
| FIGURE 2.2 | ONE-DIMENSIONAL $H+K$ BAND SPECTRA FOR THE TWO COMPONENTS OF J0900+2234. THE DASHED LINE IS 1σ ERROR OF THE SPECTRUM, AND THE DASH DOT LINE REPRESENT THE ZERO FLUX. | 36 |
| FIGURE 2.2 | CONTINUED FIGURE 2.2 | 37 |
| FIGURE 2.3 | THE Ks -BAND IMAGE AND THE RESIDUAL IMAGE WITH ALL MODEL COMPONENTS FIT BY GALFIT SUBTRACTED. | 38 |
| FIGURE 2.4 | THE H II REGION DIAGNOSTIC DIAGRAM OF $\log(N \text{ II } \lambda 6584 / H\alpha)$ AND $\log(O \text{ III } \lambda 5007 / H\beta)$. THE OPEN RECTANGLES SHOW THE LOCATION OF THE A (LEFT) AND B (RIGHT) COMPONENTS. THE OPEN DIAMONDS REPRESENT $z \sim 1 - 1.5$ DEEP2 OBJECTS (LIU ET AL., 2008) AND THE OPEN TRIANGLES REPRESENT $z \sim 2$ LENSED STAR-FORMING GALAXIES (HAINLINE ET AL., 2009) THE GREY POINTS REPRESENT SDSS STAR-FORMING GALAXIES AND AGNs. THE DOTTED LINE AND DASHED LINE ARE EMPIRICAL (KAUFFMANN ET AL., 2003) AND THEORETICAL (KEWLEY ET AL., 2001) SEPARATION OF STAR-FORMING GALAXIES AND AGNs. | 44 |
| FIGURE 2.5 | g , r , i , J , H AND Ks -BAND AB MAGNITUDES OF THE KNOT A (THE UPPER PANEL) AND THE KNOT B (THE BOTTOM PANEL) AND THEIR BEST-FIT MODEL SPECTRA. THE BEST FIT AGE IS 180 MYRS FOR BOTH KNOTS AND THE LENSED CORRECTED STELLAR MASS IS $1.9 \times 10^{10} M_{\odot}$ | 46 |

LIST OF FIGURES — *Continued*

- FIGURE 2.6 THE STELLAR MASS AND METALLICITY RELATION FOR THE SDSS GALAXIES (GREY POINTS) AND THE GALAXIES AT $z \sim 2$ (FILLED TRIANGLE ERB ET AL., 2006A). THE OPEN RECTANGLE REPRESENTS THE LENSED GALAXY J0900+2234, WHICH IS SIGNIFICANTLY LOWER THAN THE RELATION IN THE GALAXIES AT $z \sim 2$. . . 51
- FIGURE 3.1 U_{spec} COVERAGE MAP FOR THE BOÖTES FIELD. THE BLACK REGION IS COVERED BY THE NDWFS B_w , R , AND I BANDS. THERE ARE TOTAL 81 FIELDS DESIGNED TO COVER THE WHOLE RECTANGLE REGION. 63 OF THEM, WHICH HAS A LARGE OVERLAP REGION WITH THE NDWFS BROAD BAND COVERAGE, WERE OBSERVED. . . 63
- FIGURE 3.2 RELATIVE TRANSMISSION CURVES OF THE LBC U_{spec} -BAND (PURPLE CURVE) AND Y -BAND (RED CURVE). THE U_{spec} -BAND AND Y -BAND FILTER CURVES HAVE BEEN CORRECTED BY BOTH THE CCD Q.E. CURVE AND THE ATMOSPHERE TRANSMISSION. THIS PLOT ALSO SHOWS THE TRANSMISSION CURVES OF B_w (BLUE CURVE), R AND I BANDS IN THE NDWFS BOÖTES FIELD. THE CURVES ARE NORMALIZED BY THE PEAK TRANSMITTANCE. 64
- FIGURE 3.3 IMAGE QUALITY OF THE U_{spec} BAND IMAGES. THE HISTOGRAM SHOWS THE DISTRIBUTION OF THE FWHMS OF EACH CHIP OF THE LBC. THE MEDIAN OF FWHM IS 1.33/1.25 BEFORE/AFTER REMOVING THE BAD IMAGE QUALITY IMAGES (FWHM $> 1.8''$) . . 66
- FIGURE 3.4 ACCURACY OF THE ASTROMETRY. THE DISTRIBUTION OF THE DIFFERENCE OF $\text{R.A.} \times \cos(\text{DECL.})$ AND DECL. BETWEEN LBC U_{spec} -BAND IMAGES AND SDSS IMAGES. THE FWHMS OF BOTH R.A. AND DECL. ARE ABOUT $0.2''$, WHICH CORRESPONDS TO A 1σ UNCERTAINTY OF $0.08''$ IN ASTROMETRY. 67
- FIGURE 3.5 DISTRIBUTION OF MAGNITUDE WITH 5σ DETECTION FOR U_{spec} BAND. THE MEDIAN DEPTH IS 25.2 MAG. 72
- FIGURE 3.6 LEFT PANEL SHOWS THE U_{spec} (PURPLE CURVE), B_w (BLUE CURVE), AND R (RED CURVE) BROAD BAND FILTERS RELATIVE TRANSMISSION CURVE AND THE SPECTRUM OF A MODEL OF 300 MYR OLD STAR-FORMING GALAXY WITH A CONSTANT SFR AT $z \sim 3$ (BLACK CURVE). RIGHT PANEL SHOWS THE COLOR EVOLUTION OF THE MODEL GALAXY AS A FUNCTION OF REDDENING AND REDSHIFTS IN THE $B_w - R$ VERSUS $U_{\text{spec}} - B_w$ DIAGRAM. THE LEFT-MOST POINTS ARE FOR REDSHIFT $z \sim 2.5$. THE POINT STEP CORRESPONDS TO INTERVALS OF $\delta z = 0.1$. THE REGION CIRCLED BY THE SOLID LINE INDICATED THE SELECTION CRITERIA. THE DOTS ARE THE SOURCES THAT ARE WELL DETECTED ($\text{mag_err} < 0.05$) IN ALL THREE BANDS, WHICH SHOWS A TIGHT STELLAR LOCUS. . . . 74

LIST OF FIGURES — *Continued*

| | | |
|-------------|-------------------------------------------------------------------------------------------------------------------------------------------------------------------------------------------------------------------------------------------------------------------------------------------------------------------------------------------------------------------------------------------------------------------------------------------------------------------------------------------------------------------------------------------------------------------------------------------------------------------------------------------------------------------------------------------------------|----|
| FIGURE 3.7 | SELECTION COMPLETENESS AS A FUNCTION OF REDSHIFT IN DIFFERENT R -BAND MAGNITUDE BINS. | 77 |
| FIGURE 3.8 | $B_W - R$ VERSUS $U_{\text{spec}} - B_W$ COLOR-COLOR DIAGRAM. THE PHOTOMETRICALLY-SELECTED LBGs AT $z \sim 3$ ARE SELECTED IN THE REGION BOUNDED BY THE SOLID LINE. TOTAL 14,485 PHOTOMETRICALLY- SELECTED LBGs ARE SELECTED AS U-DROPOUTS. THE CROSSES REPRESENT THE SELECTED LBG. THE REASON FOR THE SHARP EDGE AT $B_W - R = 1.9$ AND $U_{\text{spec}} - B_W = 1.0$ IS THAT WE DO NOT PLOT THE U_{spec} BAND UNDETECTED SOURCES WITHOUT FALLING IN THE SELECTION CRITERION REGION. | 78 |
| FIGURE 3.9 | SURFACE DENSITY OF $z \sim 3$ LBGs AS FUNCTION OF R - BAND MAGNITUDE IN THIS WORK (RED TRIANGLES) AND IN STEI- DEL ET AL. (1999) (BLUE DIAMONDS). | 79 |
| FIGURE 3.10 | REST-FRAME UV (1700Å) luminosity function of the $z \sim 3$ LBGs in Boötes field (red triangles) and the best-fit Schechter func- tion (red solid lines). For comparison, the LF of the $z \sim 3$ LBGs in Reddy & Steidel (2009) and best-fit Schechter function are also plotted (blue diamonds and the dashed line) which explores the faint end of the LBGs. The bright end of the LF in this work shows excess compared with the Schechter function. The excess can be ex- plained by the $z \sim$ quasar LF (black solid line) (Hunt et al., 2004). The red squares represent the residue value that quasar LF is sub- tracted from the LBG LF measurements. | 81 |
| FIGURE 3.11 | MODEL SPECTRA OF $z \sim 3$ LBGs AND LOW REDSHIFT INTERLOPERS: $z = 1.1$ STAR-FORMING GALAXY AND AN A TYPE STAR. ALL THE SPECTRA ARE SCALED TO THE $R = 22.5$. THE TWO UPWARD ARROWS REPRESENT THE 5σ FLUX LIMITS OF THE [3.6] AND [4.5] BAND IN BOÖTES FIELD. | 87 |
| FIGURE 3.12 | RELATION BETWEEN R MAGNITUDE AND $R - [4.5]$ COLOR. THE BLACK SOLID LINE SHOWS THE TYPICAL MAGNITUDE LIMITS OF THE [4.5] BAND, AND THE BLUE SOLID LINE REPRESENTS THE BEST-FITTED LINEAR REGRESSION LINE WITH SURVIVAL ANALYSIS METHOD. THE ERROR BAR REPRESENTS TYPICAL ERRORS FOR R - BAND MAGNITUDE AND $R - [4.5]$ COLOR. | 92 |
| FIGURE 3.13 | $z \sim 3$ LBG LF OF [4.5] BAND (REST-FRAME J -BAND) THE SOLID LINE REPRESENTS THE BEST-FIT SCHECHTER FUNCTION FOR THE [4.5] BAND (REST-FRAME $1.1\mu\text{M}$) LF, AND THE DASHED LINE REPRESENTS THE J -BAND LF FOR THE GALAXY IN THE LOCAL UNIVERSE. THE DOTTED LINE IS THE PREDICTED J -BAND LF AT $z \sim 0.1$ IF WE ASSUME A PURELY PASSIVE EVOLUTION IN THESE GALAXIES FROM $z \sim 3$ | 93 |

LIST OF FIGURES — *Continued*

- FIGURE 3.14 STELLAR MASS FUNCTIONS OF $z \sim 3$ LBGs FROM THIS WORK (BLACK SOLID LINE), AND K-SELECTED GALAXIES (KAJISAWA ET AL., 2009; MARCHESINI ET AL., 2009, K09, RED CURVE, M09, BLUE CURVE). THE GREEN CURVE REPRESENTS THE $z \sim 3$ STELLAR MASS FUNCTION DERIVED FROM COSMOLOGICAL SIMULATIONS WITH MOMENTUM-CONSERVED WIND FEEDBACK MODEL (DAVÉ ET AL., 2011, D11). 96
- FIGURE 3.15 EVOLUTION OF BEST-FIT PARAMETERS OF SCHECHTER FUNCTIONS OF UV LF (LEFT PANEL) AND SMF (RIGHT PANEL) WITH REDSHIFTS. LEFT PANEL: FOR CHARACTERISTIC ABSOLUTE MAGNITUDE, WE USE THE DUST-CORRECTED VALUE ($M_{UV,COR}^*$). THE BLACK TRIANGLE IS FROM THIS WORK, AND THE RED DIAMONDS ARE FROM BOUWENS ET AL. (2007, 2011B). RIGHT PANEL: THE BLACK TRIANGLE IS FROM THIS WORK, AND THE RED DIAMONDS ARE FROM LEE ET AL. (2011). THE PREDICTION OF TWO DIFFERENT GALAXY EVOLUTION MODELS ARE PLOTTED IN BOTH PANELS. THE GREEN CURVES REPRESENT THE HIERARCHICAL STAR FORMATION MODEL WITH DIFFERENT ASSUMPTIONS ON EVOLUTION OF THE HALO MASS TO DUST CORRECTED UV LUMINOSITY OR STELLAR MASS RATIO. THE GREEN DASHED, SOLID AND DOTTED CURVES REPRESENT MODELS WITH THE RATIO CONSTANT WITH COSMIC TIME, $\propto (1+z)^{-1}$, AND $\propto (1+z)^{-1.5}$, RESPECTIVELY. THE BLACK SOLID CURVES REPRESENT THE SMOOTHLY RISING STAR FORMATION MODEL. THE DASHED, SOLID AND DOTTED BLACK CURVES REPRESENT MODELS WITH sSFR OF 1.5 Gyr^{-1} , 2.0 Gyr^{-1} , AND 2.5 Gyr^{-1} , RESPECTIVELY. 100
- FIGURE 3.16 ANGULAR CORRELATION FUNCTIONS FOR TWO SUBSAMPLES AT $23.5 < R < 24.0$ (RED ASTERISKS) AND AT $24.0 < R < 24.5$ (BLUE DIAMONDS). THE RED AND BLUE SOLID LINES PRESENT THE BEST-FIT POWER LAW OF THE BRIGHT AND FAINT SUBSAMPLES, RESPECTIVELY. THE RED AND BLUE DASHED CURVES ARE THE BEST-FIT HOD MODELS OF THE BRIGHT AND FAINT, RESPECTIVELY. 105

LIST OF FIGURES — *Continued*

- FIGURE 3.17 SCALED STAR FORMATION RATE (SFR) VERSUS HOSTING HALO MASS. THE DASHED LINE REPRESENTS THE RELATION IN EQ. 3.22 DERIVED FROM THE COLD FLOW MODEL (DEKEL ET AL., 2009), AND THE SOLID LINES REPRESENT THAT THE STAR FORMATION EFFICIENCIES ARE 20%, 10% AND 5% OF THE TOTAL COLD FLOW ACCRETION MASS. THE LBGs AT $z \sim 3$ (GREEN OPEN SQUARES (THIS WORK)), $z \sim 4$ (ORANGE ASTERISKS (LEE ET AL., 2006) AND DIAMONDS ((OUCHI ET AL., 2005))), AND $z \sim 5$ (BLUE ASTERISKS (LEE ET AL., 2006)) FOLLOW THE 10% COSMIC STAR FORMATION EFFICIENCY LINE VERY WELL, WHILE THE SMGS (RED TRIANGLE) AT $z \sim 2$ IS ABOUT 0.85 DEX HIGHER. THE FILLED CIRCLES ARE THE PREDICTIONS OF THE COSMIC STAR FORMATION EFFICIENCY FROM THE COSMOLOGICAL SIMULATIONS WITH MOMENTUM-DRIVEN GAS OUTFLOWS RECIPE (OPPENHEIMER & DAVÉ, 2008). THE POINTS ARE COLOR CODED BY REDSHIFT (GREEN $z=3$, ORANGE $z=4$, AND BLUE $z=5$). 110
- FIGURE 4.1 THE U -, B_W -, R -, I -, z -, AND Y -BAND IMAGES OF J1432+3358. A CONTOUR PLOT IS ALSO SHOWN IN B_W - AND R -BAND IMAGES. THE YELLOW FILLED CIRCLES REPRESENT THE SIZE OF POINT SPREAD FUNCTIONS (PSF) IN EACH IMAGE. THE TYPICAL IMAGE QUALITIES FOR U -, B_W -, R -, I -, z -, AND Y -BAND IMAGES ARE $1''.0$, $1''.3$, $1''.2$, $1''.2$, $0''.5$ AND $0''.6$, RESPECTIVELY. THE SLIT POSITION AND ORIENTATION ARE ALSO SHOWN IN R -BAND IMAGE. 123
- FIGURE 4.2 THE 2D SPECTRUM (TOP PANEL) AND THE 1D SPECTRUM (TOP PANEL) OF THE $\text{Ly}\alpha$ EMISSION LINE. THERE ARE 3 SIGNIFICANT COMPONENTS RESOLVED IN 2D SPECTRUM IMAGE. THE COMPONENTS OF 'A' AND 'B' CORRESPOND TO THE REDSHIFTED STRONGER PEAK AND THE BLUESHIFTED WEAKER PEAK, RESPECTIVELY. THE COMPONENT OF 'C' CORRESPONDS TO THE $\text{Ly}\alpha$ EMISSION FROM THE FAINTER COMPONENT WHICH WAS RESOLVED IN z -BAND IMAGE. THE CENTRAL WAVELENGTH DIFFERENCE BETWEEN COMPONENTS 'A' AND 'C' IS ABOUT 3.6 \AA 125

LIST OF FIGURES — *Continued*

| | | |
|------------|---------------------------------------------------------------------------------------------------------------------------------------------------------------------------------------------------------------------------------------------------------------------------------------------------------------------------------------------------------------------------------------------------------------------------------------------------------------------------------------------|-----|
| FIGURE 4.3 | THE REST-FRAME UV SPECTRUM OF J1432+3358 IN THE WAVELENGTH RANGE 1100-1700 Å (THE THIN BLACK SOLID CURVE). FOR COMPARISON, THE COMPOSITE SPECTRUM OF A SAMPLE OF $z \sim 3$ LBGs IS ALSO SHOWN WITH A RED THICK SOLID CURVE (SHAPLEY ET AL., 2003). THE TOP X-AXIS REPRESENTS THE OBSERVED-FRAME WAVELENGTH. BOTH SPECTRA ARE SCALED BY THE PEAK VALUE OF THE $\text{Ly}\alpha$ EMISSION LINE, AND THE COMPOSITE SPECTRUM IS SHIFTED BY +0.1 IN FLUX DENSITY DIRECTION FOR CLARITY. | 126 |
| FIGURE 4.4 | THE SPECTRA AROUND THE ABSORPTION LINES (THE BACK CURVES IN HISTOGRAM MODE) AND BEST-FIT GAUSSIAN MODELS (THE RED CURVES). THE FLUX IS SCALED BY THE CONTINUUM FLUX. | 127 |
| FIGURE 4.5 | THE BEST-FIT STELLAR SYNTHESIS MODEL (SOLID CURVE) AND PHOTOMETRIC DATA POINTS FROM U -BAND TO IRAC4-BAND (RED SQUARES). | 132 |
| FIGURE 5.1 | THE MMT BCS SPECTRA OF CONFIRMED ULBGs. | 144 |
| FIGURE 5.1 | CONTINUED FIGURE. | 145 |
| FIGURE 5.1 | CONTINUED FIGURE. | 146 |
| FIGURE 5.1 | CONTINUED FIGURE. | 147 |
| FIGURE 5.2 | REST-FRAME UV LF OF ULBGs. THE RED DATA POINTS AND CURVE ARE THE LF MEASUREMENTS AND BEST-FITTED SCHECHTER FUNCTION FROM BIAN ET AL. (2012), AND THE BLUE DATA POINTS AND CURVE ARE THE LF MEASUREMENTS AND BEST-FITTED SHECHTER FUNCTION FROM REDDY & STEIDEL (2009). THE GREEN DATA POINT IS THE LF MEASUREMENT OF THE ULBG SAMPLE, WHICH PROBES THE LUMINOSITY REGIME THAT HAS NEVER BEEN STUDIED BEFORE. | 151 |
| FIGURE 5.3 | REST-FRAME UV COMPOSITE SPECTRUM OF ULBGs (BLUE CURVE). FOR COMPARISON, THE COMPOSITE SPECTRUM OF TYPICAL LBGs IS ALSO PLOTTED (RED CURVE) | 154 |
| FIGURE 5.4 | ZOOM-IN SPECTRA OF C I STELLAR PHOTOSPHERIC ABSORPTION LINE, $\text{Ly}\alpha$ EMISSION LINE, LOW IONIZED ISM ABSORPTION LINES, AND HIGH IONIZED ISM ABSORPTION LINES. | 155 |
| FIGURE 5.5 | THE P-CYGNI PROFILE OF THE C IV AND MODEL SPECTRA WITH DIFFERENT IMF. | 158 |

LIST OF FIGURES — *Continued*

| | | |
|------------|---------------------------------------------------------------------------------------------------------------------------------------------------------------------------------------------------------------------------------------------------------------------------------------------------------------------------------------------------------|-----|
| FIGURE 5.6 | DISTRIBUTION OF LBGs AND QSOs IN THE $[3.6] - [4.5]$ VERSUS $[5.8] - [8.0]$ COLOR-COLOR DIAGRAM. THE REGION ENCLOSED BY THE BLACK SOLID LINE IS THE AGN/QSOs SELECTION REGION. THE BLUE TRIANGLE REPRESENTS THE AVERAGE COLOR OF THE LBG SAMPLE AND THE PINK DIAMOND REPRESENTS THE AVERAGE COLOR OF THE QSO SAMPLE. | 160 |
| FIGURE 5.7 | BROAD BAND PHOTOMETRY SED FITTING RESULTS. | 163 |
| FIGURE 5.7 | CONTINUED FIGURE. | 164 |
| FIGURE 5.7 | CONTINUED FIGURE. | 165 |
| FIGURE 5.7 | CONTINUED FIGURE. | 166 |
| FIGURE 5.8 | DISTRIBUTION OF STELLAR MASS, SFR, $E(B - V)$ AND AGE OF ULBGs (BLACK), $z \sim 3$ LBGs (RED) AND $z \sim 2$ UV-SELECTED GALAXIES (BLUE). | 167 |
| FIGURE 5.9 | SFR AND STELLAR MASS RELATION OF ULBs. THE SFR AND STELLAR MASS ARE DERIVED FROM THE BROAD BAND SED FITTING. THE SOLID LINES REPRESENT THE RELATION OF MAIN SEQUENCE (DADDI ET AL., 2007), AND THE SFRs ARE FOUR TIMES ($4 \times MS$) AND TEN TIMES ($10 \times MS$) HIGHER THAN THOSE IN MAIN SEQUENCE GALAXIES FOR A GIVEN STELLAR MASS. | 168 |
| FIGURE C.1 | THE MMT BCS SPECTRA OF CONFIRMED ULBGs IN SDSS DEEP STRIPE FIELD. | 187 |
| FIGURE C.1 | CONTINUED FIGURE | 188 |

LIST OF TABLES

| | | |
|-----------|-------------------------------------------------------------------------------------------|-----|
| TABLE 2.1 | LUCIFER OBSERVATION LOG OF J0900+2234. | 31 |
| TABLE 2.2 | THE BEST-FIT PROFILE PARAMETERS FOR THE LENS GALAX- IES AND LENSED COMPONENTS. | 35 |
| TABLE 2.3 | PHOTOMETRY OF THE LUCIFER IMAGES FROM GALFIT. . | 39 |
| TABLE 2.4 | RESULTS OF EMISSION LINE MEASUREMENTS. | 41 |
| TABLE 2.5 | SUMMARY OF THE PHYSICAL PROPERTIES OF J0900+2234. . | 55 |
| TABLE 3.1 | SUMMARY OF THE U_{spec} , B_{W} AND R -BAND 5σ DEPTH | 71 |
| TABLE 3.2 | SCHECHTER PARAMETERS OF UV LFs AND LUMINOSITY DENSITIES | 84 |
| TABLE 3.3 | ACF AND THE COMOVING CORRELATION LENGTHS FOR $z \sim 3$ LBGs | 108 |
| TABLE 4.1 | MAGNITUDE AND MORPHOLOGICAL PROPERTIES OF J1432+3358.121 | |
| TABLE 4.2 | LY α EMISSION AND STRONG INTERSTELLAR ABSORPTION LINES. | 128 |
| TABLE 5.1 | OBSERVING LOG. | 142 |
| TABLE 5.2 | LY α EMISSION AND STRONG INTERSTELLAR ABSORPTION LINES. | 176 |
| TABLE 5.3 | PHYSICAL PROPERTIES OF ULBGs AND TYPICAL LBGs. . . | 176 |

ABSTRACT

In my thesis I investigate the luminous $z \sim 3$ Lyman break galaxies in deep wide field surveys.

In the first part of the thesis, I use the LBT/LUCIFER to observe a lensed high-redshift star-forming galaxy (J0900+2234) at $z = 2.03$. With the high S/N near-IR spectroscopic observations, I reveal the detailed physical properties of this high-redshift galaxy, including SFR, metallicity, dust extinction, dynamical mass, and electron number density.

In the second part of the thesis, I select a large sample of LBGs at $z \sim 3$ from our new LBT Boötes field survey, and study the bright end luminosity function (LF), stellar mass function (SMF) and clustering properties of bright LBGs ($1L^* < L < 2.5L^*$). Together with other LF and SMF measurements, the evolution of LF and SMF can be well described by continuously rising star formation history model. Using the clustering measurements in this work and other works, a tight relation between the average host galaxy halo mass and the galaxy star formation rate is found, which can be interpreted as arising from cold flow accretion. The relation also suggests that the cosmic star formation efficiency is about 5%-20% of the total cold flow mass. This cosmic star formation efficiency does not evolve with redshift (from $z \sim 5$ to $z \sim 3$), hosting dark matter halo mass ($10^{11} - 10^{13} M_\odot$), or galaxy luminosity (from $0.3L^*$ to $3L^*$).

In the third and fourth parts, with the spectroscopic follow-up observations of the bright LBGs, I establish a sample of spectroscopically-confirmed ultra-luminous LBGs (ULBGs) in NOAO Boötes field. With this new ULBG sample, the rest-frame UV LF of LBG at $M_{1700\text{\AA}}^\circ = -23.0$ was measured for the first time. I find that the ULBGs have larger outflow velocity, broader $\text{Ly}\alpha$ emission and ISM

absorption line profiles, and more prominent C IV P-Cygni profile. This profile may imply a top-heavy IMF in these ULBGs. The ULBGs have larger stellar mass and SFR, but smaller dust extinction than the typical L^* LBGs at $z \sim 2 - 3$. We proposed two evolutionary scenarios, pre-burst and post-burst. The properties of the ULBGs, especially the morphologies, prefer the pre-starburst scenario. Further high spatial resolution HST imaging and IFU spectroscopic observations will allow us to distinguish these two scenarios.

CHAPTER 1

INTRODUCTION

In my thesis, I study bright Lyman Break Galaxies (LBGs) in deep wide field surveys, NOAO Deep Wide Field Survey (NDWFS) Boötes field and Sloan Digital Sky Survey (SDSS) Stripe 82 field. These bright LBGs have not been well studied due to the small survey area in the previous deep field surveys.

1.1 High-redshift Galaxy Surveys

Over the last decade, various high-redshift galaxy selection methods have been developed and established a large sample of high-redshift galaxies to probe the star formation and mass build-up process in the early Universe. The following optical and near-infrared (near-IR) methods are commonly employed to select high-redshift galaxies: (1) the dropout method (the Lyman break technique) using the fact that little flux is emitted bluewards of the Lyman limit (912\AA , e.g., Steidel et al., 1996a,b). This method could be used to select a wide redshift range of high-redshift galaxies ($1 < z < 11$); (2) the BzK selection method, using the fact that the Balmer break falls between the optical z -band filter and the near-IR K -band filter to pick up active and passive galaxies at $1.4 < z < 2.5$ (Daddi et al., 2004); (3) the distant red galaxy selection, using the $J_s - K_s > 2.3$ color cut to select galaxies at $z \sim 2.6$, whose Balmer break falls between the J - and K -bands (Franx et al., 2003). (4) $\text{Ly}\alpha$ emitters and $\text{Ly}\alpha$ blobs selection, using the narrow band filter to cover the strong $\text{Ly}\alpha$ emission line (e.g., Hu & McMahon, 1996; Cowie & Hu, 1998; Francis et al., 1996), and an alternative method was developed to use broad-band filter to select $\text{Ly}\alpha$ blobs (Prescott et al., 2012). The selection methods mentioned above require the selected galaxies detected in the

rest-frame optical and near-IR wavelength, thus they are low dust content with moderate star formation rates (SFRs) ($1 - 100 M_{\odot} \text{ yr}^{-1}$). Complementary methods of selecting high-redshift star-forming galaxies have been developed. These methods relies on either deep blank field millimeter/sub-millimeter surveys or large mid-infrared to UV luminosity ratios to select dusty galaxies with extremely high SFRs ($> 500 M_{\odot} \text{ yr}^{-1}$), submillimeter galaxies (SMGs, e.g., Smail et al., 1997) and dust obscured galaxies (DOGs, e.g., Dey et al., 2008; Fiore et al., 2008).

1.2 Ultra-violet Luminosity Function

The spectroscopic follow-up observations of these high-redshift galaxies were carried out, and it has been found that these photometrical-selection methods are quite efficient to search for high-redshift galaxies (e.g., Steidel et al., 2003, 2004; Daddi et al., 2004; Chapman et al., 2005; Stark et al., 2010). Using the large samples of high redshift galaxies, the rest-frame ultraviolet (UV) luminosity functions of high-redshift galaxies from $z \sim 2$ out to $z \sim 8$ have been measured, (e.g., Ly et al., 2009; Reddy & Steidel, 2009; Steidel et al., 1999; Sawicki & Thompson, 2006a; Bouwens et al., 2007, 2008; Yan et al., 2011b). The rest-frame UV lights trace the massive star formation, thus the rest-frame UV LF can be used as a fundamental tracer of galaxy formation and evolution, and it is also applied to compute the intrinsic UV luminosity density after correcting dust extinctions and to constrain the history of star formation (e.g., Madau et al., 1996). Studies have shown that the SFR density peaked at $1 < z < 3$, which is an order of magnitude higher than that in the local Universe.

1.3 Clustering of High-redshift Star-forming Galaxies

Clustering of high-redshift galaxies has been well studied in the redshift interval, $2.0 < z < 5.0$ (Giavalisco & Dickinson, 2001; Adelberger et al., 2005b; Ouchi et al., 2005; Lee et al., 2006). These studies, together with the halo occupation distribution, connected the galaxy distribution to their hosting dark matter halo properties. Giavalisco & Dickinson (2001) investigated the relation between the clustering strength of $z \sim 3$ LBGs and their UV luminosity. They found evidence of clustering segregation, i.e., brighter galaxies are more strongly clustered. This result is also supported by the studies on the clustering of LBGs at other redshift ranges (e.g., Lee et al., 2006). Using the UV-selected galaxy at different redshift ranges ($1.4 < z < 3.5$), Adelberger et al. (2005b) found that the mass of the dark matter halos hosting galaxies with similar brightness decreases with redshift, and concluded that the LBGs would evolve into elliptical galaxies in the local. At small scales ($\theta < 1''$), the correlation function of LBGs shows excess powers compared to single power-law distribution of the correlation function, which suggests that multiple galaxies are in the same massive dark matter halo in the context of halo occupation distribution (HOD, Ouchi et al., 2005; Lee et al., 2006, 2009). Combined with the UV LF, clustering results also can be used to infer the nature of star formation in the LBGs and its dependence on their host halo mass (Lee et al., 2009).

1.4 Physical Properties of High-redshift Galaxies

The high signal-to-noise ratio (S/N) optical and near-IR spectroscopic follow-up observations of lensed galaxies and composite spectrum of normal high-redshift galaxies have revealed the detailed physical properties in these galaxies, including SFR, dust extinction, metallicity, initial mass function, and outflow velocity.

(Pettini et al., 2000, 2002; Shapley et al., 2003; Erb et al., 2006b; Hainline et al., 2009; Quider et al., 2009, 2010; Jones et al., 2012). Another method to probe the properties of the high-redshift galaxies is to fit the broad band photometric results with the stellar synthesis model (e.g., Bruzual & Charlot, 2003). This method could put constraints on SFRs, dust extinctions, stellar masses and ages of high-redshift galaxies (Papovich et al., 2001; Shapley et al., 2001, 2005). Using the stellar mass from the SED fitting and the metallicity from the nebular line measurements in near-IR spectra, the mass-metallicity relation in the galaxies at $1 < z < 3.5$ has been studied (Erb et al., 2006a; Maiolino et al., 2008; Wuyts et al., 2012), and a more general relation between stellar mass, metallicity, and SFR has been proposed (Mannucci et al., 2010), and they found that high-redshift galaxies up to $z \sim 2.5$ hold the same mass-metallicity-SFR relation derived from the local SDSS galaxies.

1.5 Far-infrared Properties of UV-selected Galaxies

The Far-infrared(FIR)/submillimeter observations are also conducted on the UV/optical selected galaxies. Chapman et al. (2000) and Chapman & Casey (2009) carried out JCMT/SCUBA $850\mu\text{m}$ surveys observing spectroscopically-confirmed LBGs to study the connection between the rest-frame UV and FIR properties. They found that the LBGs do not constitute a large fraction of the bright SMG population ($S_{850\mu\text{m}} > 5 \text{ mJy}$), but could contribute significantly to the population of submm selected galaxies in the 1-2 mJy regime. Reddy et al. (2010) and Reddy et al. (2011) used the *Spitzer* MIPS $24 \mu\text{m}$ and stacked *Herschel Space Observatory* 100 and $160\mu\text{m}$ imaging to investigate the infrared luminosity (L_{IR}) in the L^* UV-selected galaxies. They found that the correlation between UV slope (β) and the ratio between the IR luminosity and UV luminosity ($L_{\text{IR}}/L_{\text{UV}}$) in L^* UV-selected

galaxies at $z \sim 2$ is similar to that in local starburst galaxies (Meurer et al., 1999). They also found that the young UV-selected galaxies at $z \sim 2$ follow the relation observed in the SMC (Baker et al., 2001; Siana et al., 2009; Reddy et al., 2010) and the high-redshift ultra-luminous infrared galaxies (ULIRGs) with $L_{\text{bol}} \gtrsim 10^{12} L_{\odot}$ have larger $L_{\text{IR}}/L_{\text{UV}}$ relative to normal $z \sim 2$ UV-selected galaxies. The CO line observations in normal high- z galaxies have shown that the gas fraction in high-redshift galaxies is an order of magnitude higher than that in local star-forming galaxies (Daddi et al., 2010b; Tacconi et al., 2010; Riechers et al., 2010).

1.6 Galaxy SFR-stellar Mass Main Sequence

There are two star formation models to build up galaxies: (1) steady growth model in disk galaxies, which results in galaxies located on the SFR-stellar mass main sequence; and (2) starburst model triggered by major mergers, which results in galaxies with higher SFRs for a given stellar mass and located above the SFR-stellar mass main sequence.

A tight correlation between the SFR and stellar mass has been found, and this relation is defined as the SFR-stellar mass main sequence. The galaxy main sequence has been found in both nearby star-forming galaxies and high-redshift galaxies (e.g., Brinchmann et al., 2004; Elbaz et al., 2007; Daddi et al., 2007; Wuyts et al., 2011). These studies suggested that the scattering of the main sequence does not evolve with cosmic time, but the zeropoint of the relation changes significantly from $z \sim 0.1$ to $z \sim 1.0 - 2.0$ (Noeske et al., 2007), i.e., the ratio of SFR to stellar mass, also known as specific SFR (sSFR), for a given stellar mass increases with redshift from $z \sim 0.1$ to $z \sim 1.0 - 2.0$. It has been found that the sSFR does not change significantly at $z > 2.0$ (e.g., Stark et al., 2009; González et al., 2010). However, cosmological simulations have difficulties to reproduce this evolution

of sSFR, in which the sSFR keeps rising beyond the redshift of $z \sim 2$ (e.g., Davé et al., 2011). Stark et al. (2012) argued that stellar mass in high-redshift galaxies has been overestimated due to the contamination of the strong rest-frame optical nebular emission lines. After correcting this effect, they found that the sSFR increases with redshift even beyond $z \sim 2$. The sSFR does not only evolve with cosmic time, but it also depends on the stellar mass. Studies have shown that the sSFR increases as stellar mass decreases (e.g., Rodighiero et al., 2011), however, Reddy et al. (2012) found that the sSFR does not depend on stellar mass significantly. Although it is still an open question how the SFR-stellar mass relation changes with redshift and stellar mass, it is well accepted that the majority of the galaxies located on the main sequence are in a steady, continuous growth phase, and the SFR in the galaxies off the main sequence is triggered by major mergers, though some of the galaxies in the early stage of major merger may lie close to the main sequence (e.g., Kartaltepe et al., 2011). Rodighiero et al. (2011) investigated the relative contribution of these two star formation modes to the global SFR density at $z \sim 2$ using the distribution of the BzK galaxies in the SFR-stellar mass diagram. They found that the off main sequence starbursts only contribute 10% of the total cosmic star formation density at $z \sim 2$.

1.7 Deep and Wide Field Surveys

The multi-wavelength observations and studies of high-redshift galaxies have established a comprehensive picture of L^* high-redshift galaxies. However, the luminosity regime of $L > L^*$ has not been well explored. Most of optical/NIR spectroscopic surveys of high-redshift galaxies are deep field surveys with survey area less than 1 deg^2 (Figure 1.1). So far, the largest $z \sim 2 - 3$ LBGs survey with spectroscopic redshifts only covers a total area of around one deg^2 with > 2000

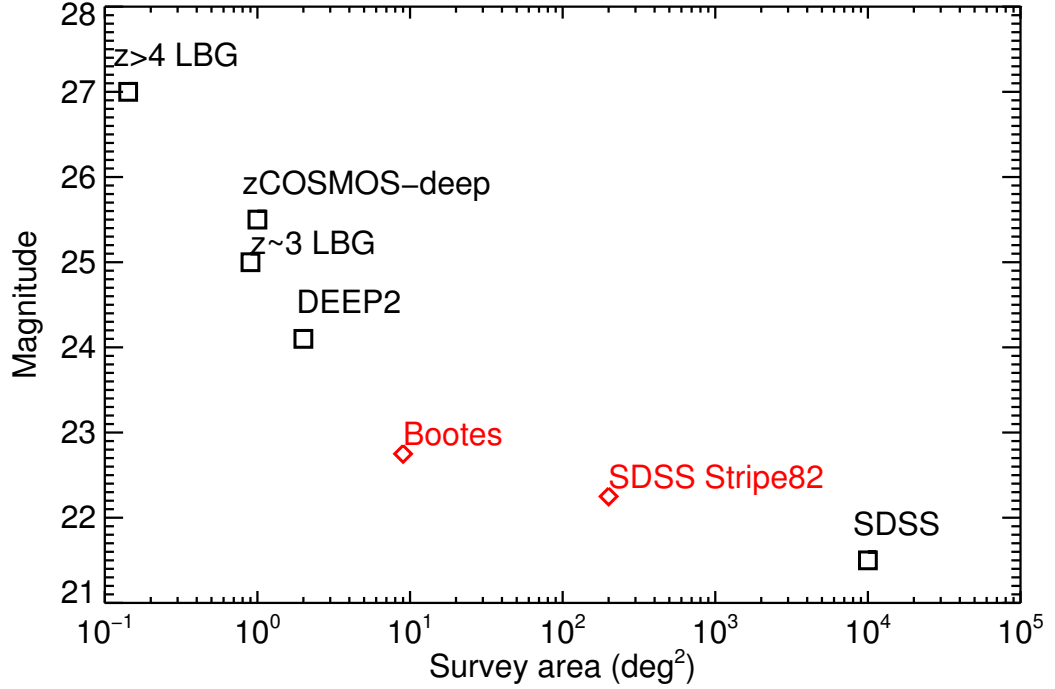


Figure 1.1: Survey magnitude limit and survey area of the spectroscopic follow-up surveys of high-redshift galaxies. Our NDWFS Boötes field survey and SDSS stripe82 survey of luminous $z \sim 3$ LBGs locate at a unique area.

spectroscopic redshifts (e.g., Steidel et al., 2003; Reddy & Steidel, 2009).

Due to the small survey volume and the rapid decline of galaxy luminosity function at the bright end, these surveys are not suited to reveal the most luminous and most massive systems. A sample of bright LBGs was discovered in the Sloan Digital Sky Survey (SDSS), however, the HST follow-up observations showed that these galaxies are unresolved point sources, suggesting that these objects are quasars rather than galaxies (Bentz et al., 2008). To date, only one unlensed LBG at $z \sim 3$ with R -band magnitude brighter than 22.5 has been found (Cooke et al., 2008). The nature and properties of this type of galaxy are still unknown, so it is important to build up a sample of these UV ultra-luminous

galaxies and perform detailed follow-up observations on them.

This thesis is organized as follows: in chapter 2, the detailed physical properties in the lensed star-forming galaxy, J0900+2234, are studied; in chapter 3, the luminosity function and clustering of a large sample of $z \sim 3$ LBGs selected in the LBT Boötes field survey are studied, and various galaxy formation and evolution models are tested with the evolution of luminosity function and clustering of LBGs with cosmic time; in chapter 4, the nature and physical properties of the ultra-luminous LBGs (ULBGs) ($R = 22.3$), J1432+3358, are studied; and in chapter 5, we will study a sample of ULBGs discovered in the NOAO Boötes fields.

CHAPTER 2

LBT/LUCIFER OBSERVATIONS OF THE $Z \sim 2$ LENSED GALAXY
J0900+2234

We present rest-frame optical images and spectra of the gravitationally lensed, star-forming galaxy J0900+2234 ($z = 2.03$). The observations were performed with the newly commissioned LUCIFER1 near-infrared (NIR) instrument mounted on the Large Binocular Telescope (LBT). We fitted lens models to the rest-frame optical images and found the galaxy has an intrinsic effective radius of 7.4 ± 0.8 kpc with a lens magnification factor of about 5 for the A and B components. We also discovered a new arc belonging to another lensed high- z source galaxy, which makes this lens system a potential double Einstein ring system. Using the high S/N rest-frame optical spectra covering $H+K$ band, we detected $H\beta$, [O III], $H\alpha$, [N II], and [S II] emission lines. Detailed physical properties of this high- z galaxy were derived. The extinction towards the ionized H II regions ($E_g(B - V)$) was computed from the flux ratio of $H\alpha$ and $H\beta$ and appears to be much higher than that towards stellar continuum ($E_s(B - V)$), derived from the optical and NIR broad band photometry fitting. The metallicity was estimated using N2 and O3N2 indices. It is in the range of $\frac{1}{5} - \frac{1}{3}$ solar abundance, which is much lower than the typical $z \sim 2$ star-forming galaxies. From the flux ratio of [S II] $\lambda 6717$ and [S II] $\lambda 6732$, we found that the electron number density of the H II regions in the high- z galaxy were $\simeq 1000 \text{ cm}^{-3}$, consistent with other $z \sim 2$ galaxies but much higher than that in local H II regions. The star-formation rate was estimated via the $H\alpha$ luminosity, after correction for the lens magnification, to be about $365 \pm 69 M_\odot \text{ yr}^{-1}$. Combining the FWHM of $H\alpha$ emission lines and the half-light radius, we found the dynamical mass of the lensed galaxy is $(5.8 \pm 0.9) \times 10^{10} M_\odot$.

The gas mass is $(5.1 \pm 1.1) \times 10^{10} M_{\odot}$ from the $H\alpha$ flux surface density by using global Kennicutt-Schmidt Law, indicating a very high gas fraction of 0.79 ± 0.19 in J0900+2234.

2.1 Introduction

The redshifts between $1 < z < 3$ mark the time of peak cosmic star formation (Madau et al., 1996) and quasar activity (Fan et al., 2001). The current-day Hubble sequence was being built up, and a large fraction of present-day stars were formed (Dickinson et al., 2003). Observations of galaxies in this redshift range provide a direct picture of the formation and evolution of galaxies and the assembly of their central supermassive black holes.

By obtaining rest-frame optical spectra, we can perform detailed studies of the star formation history, as well as properties of the ISM and stellar populations in galaxies. However, well-known diagnostic optical emission lines are shifted into the near infrared (NIR) for $z = 1 - 3$. Since high- z galaxies (e.g., Lyman Break Galaxies or LBGs) are faint, it is difficult to obtain high signal to noise ratio (S/N) NIR spectra with current facilities, especially for weak emission and absorption lines. Therefore, many previous NIR spectroscopic studies have been focused on the strong [O III] or $H\alpha$ emission lines (e.g., Pettini et al., 2001; Erb et al., 2003, 2006b,a,c), from which only limited inferences can be drawn.

One method of addressing this problem is to observe high- z star-forming galaxies which have been gravitationally lensed by foreground massive galaxies or clusters. Lensing can boost the observed flux of high redshift galaxies by several tens or more, so that high S/N spectroscopy in the NIR becomes feasible. One of the first lensed galaxies to be studied in this way was the serendipitously discovered MS1513-cB58 at $z = 2.73$ (Yee et al., 1996; Bechtold et al., 1997;

Teplitz et al., 2000). Subsequently, several groups began systematic searches for strongly lensed high redshift galaxies towards clusters of galaxies (Sand et al., 2005; Richard et al., 2008) and red galaxies in the Sloan Digital Sky Survey (SDSS, York et al., 2000) images (e.g., Belokurov et al., 2009; Kubo et al., 2009). These searches are finding lensed star-forming galaxies at redshifts $z > 2$ (e.g., Allam et al., 2007; Lin et al., 2009; Diehl et al., 2009; Koester et al., 2010) which can then be followed-up in the NIR, or rest-frame optical and UV (e.g., Smail et al., 2007; Hainline et al., 2009; Finkelstein et al., 2009; Quider et al., 2009, 2010; Pettini et al., 2010).

The object of this paper is the lensed system J0900+2234 ($z=2.03$; Diehl et al., 2009) which was discovered in SDSS images, and then confirmed with follow-up deep optical g, r, i imaging and spectroscopy. The lens galaxy is at $z = 0.49$ based on SDSS spectroscopy. In this paper, we report J, H, K_s imaging and $H+K$ spectroscopy of J0900+2234 with the newly commissioned LUCIFER instrument (Ageorges et al., 2010) at the Large Binocular Telescope (LBT; Hill et al., 2008). We detected the nebular emission lines $H\beta$, $[O\ III]\lambda\lambda 4959, 5007$, $H\alpha$, $[N\ II]\lambda 6583$, and $[S\ II]\lambda\lambda 6717, 6732$ with simultaneous $H+K$ band spectral coverage from 1.40–2.20 μm . The wide simultaneous wavelength range coverage not only improves observing efficiency, but also helps to reduce the measurement uncertainties of the line ratios (e.g., $H\alpha/H\beta$) resulting from the flux calibration and slit losses variation between different exposures.

This paper is organized as follows: In § 2.2, we describe the observations and reduction of the LUCIFER data. In § 2.3, we describe the photometry, reconstruction of the source with lens modeling and line flux measurements. In § 2.4, we construct a simple lensing model using the J0900+2234 NIR imaging. In § 2.5, we report the detailed physical properties of J0900+2234 and discuss the

Table 2.1: LUCIFER Observation Log of J0900+2234.

| Date(UT) | mode | Camera | Filter | Slit PA (degree) | Exp. Time(s) |
|--------------|--------------|--------|--------|------------------|-----------------|
| Jan. 06 2010 | imaging | N3.15 | J | - | 10×60 |
| | | | H | - | 10×60 |
| | | | Ks | - | 10×60 |
| Feb. 13 2010 | spectroscopy | N1.8 | $H+K$ | 86.57 | 24×300 |

systematic uncertainties of the physical property measurements. In § 2.6, our main results are summarized. Throughout this paper, we use a cosmology with $H_0 = 70 \text{ km s}^{-1} \text{ Mpc}^{-1}$, $\Omega_M = 0.3$, and $\Omega_\Lambda = 0.7$. The magnitudes are all AB magnitudes.

2.2 Observations and Data Reduction

2.2.1 LUCIFER

LUCIFER1 was built by a collaboration of five German institutes. It is the first of a pair of NIR imagers/spectrographs for the LBT. It is mounted on the bent Gregorian focus of the left primary mirror. The wavelength coverage is from 0.85 to $2.4 \mu\text{m}$ ($zJHK$ bands) in imaging, long-slit and multiobject spectroscopy modes. The detector is a Rockwell HAWAII-2 Hd-CdTe $2048 \times 2048 \text{ pixel}^2$ array with a pixel size of $18.5 \mu\text{m}$. The quantum efficiency (QE) is about 75% in the H and K bands. In the currently available seeing limited mode, the pixel scales are $0.25''$ and $0.12''$ for N1.8 & N3.75 cameras, respectively. The commissioning finished in early December 2009 and has been immediately followed by 12 nights of scientific demonstration observing. The instrument has been in regular science operation since mid-December 2009.

2.2.2 LUCIFER Imaging & Spectroscopy

J0900+2234 was observed with LUCIFER1 on the LBT on 6 January 2010 in imaging mode and on 13 February 2010 in long slit spectroscopy mode (Table 5.1). In the imaging mode, the N3.75 camera was used; the $18.5\ \mu\text{m}$ pixels correspond to $0.12''$ on the sky, for a $4.0' \times 4.0'$ field-of-view. The seeing was $0.7''$ with thin clouds. For each filter (J , H , and K_s), we obtained ten randomly dithered exposures of 60s each. For the spectroscopic observations, the seeing was $0.5\text{-}0.6''$ and the conditions were photometric. The spectra were taken with N1.8 camera, yielding a plate scale of $0.25''$ per pixel. An order separation filter and the 200 l/mm $H+K$ grating were used to cover the wavelength range from 1.40 to $2.20\ \mu\text{m}$ simultaneously. A $1.0''$ by $3.9'$ slit was used, resulting in spectral resolution of $16\ \text{\AA}$. The total exposure time was 24×300 seconds with the telescope nodded $\sim 7''$ along the slit between each exposure. The instrument was rotated to $\text{PA}=86.57^\circ$ in order to place the two brightest lensed components in the slit. Dark exposures and internal quartz lamp flats were obtained in the afternoon, and an Ar lamp was observed for wavelength calibration during the night.

2.2.3 Data Reduction

2.2.3.1 Imaging Reduction

The imaging data were reduced using standard IDL routines. The dark frames were median combined to create a master dark frame. A super-sky flat was constructed from combining the science frames after dark subtraction. The science images were dark subtracted, and then divided by the super-sky flat to correct for the detector response. The science images were registered to the SDSS-DR6 catalog using SCAMP (Bertin, 2006) for astrometric calibration; the residuals are less than $0.1''$ RMS. Finally, the sky background was subtracted from the science frames which were then co-added using SWarp (Bertin et al., 2002). Photometric

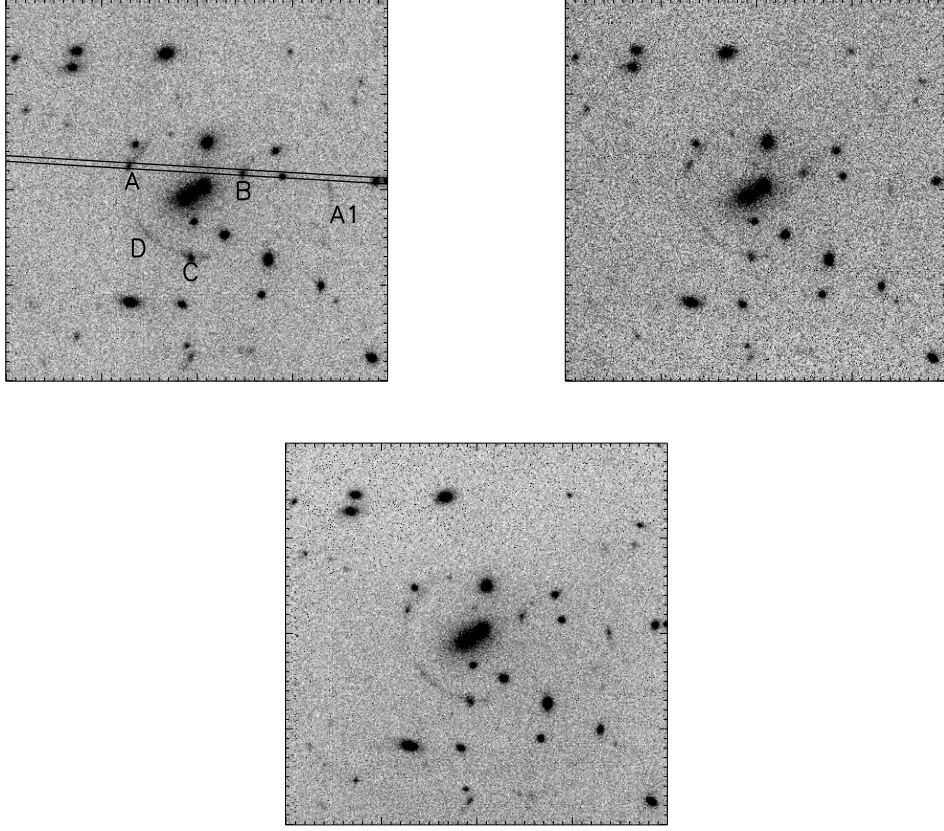


Figure 2.1: J , H , and Ks band images of J0900+2234 from LUCIFER, North is up, and east is left. Each image shown has $40'' \times 40''$. The previously discovered A, B, C, and D components are labeled in the J -band image. The A, B, and D components are images of the star-forming galaxy at $z \sim 2$. Our follow-up spectroscopy shows that C is not an image of the same galaxy. The newly discovered A1 arc from another lensed galaxy is also labeled in the image.

zeropoints were determined from 2MASS stars in the field-of-view.

The fully reduced J , H , Ks -band images are shown in Fig. 2.1. In addition to the lensed galaxy (components A, B, C, and D in Fig. 2.1) found by Diehl et al. (2009), we discovered another component, A1. The color of A1 suggests that it

is also a high-redshift galaxy image lensed by the foreground red galaxy, but not the same galaxy appearing in images as A, B, C or D (see details in section 2.3.1).

2.2.3.2 Spectroscopy Reduction

To reduce the LUCIFER spectra, we modified an IDL long-slit reduction package written by G. D. Becker for NIRSPEC (Becker et al., 2009). In this package, the following sky background subtraction procedure is used. First, four types of calibration files were created: a median-combined normalized internal flat field to correct the pixel-to-pixel variations in QE, a median-combined dark image, and two transformation maps created by tracing bright standard stars and bright sky lines. These two transformation maps were used to transform the NIR detector (x, y) coordinates to the slit position and wavelength coordinates. Then, the dark image was subtracted from the science frames which were then divided by the flat field. The background in each science frame was subtracted using a fit to the science frames obtained before and after it in two dimensions, based on the transformation maps. A second-order polynomial function and a b -spline function were used to fit the sky background residual along the slit direction and the dispersion direction, respectively. After the sky background subtraction, the x and y direction distortion of the science frames were corrected based on the transformation maps created in the first step. The one-dimensional spectra were extracted from individual two-dimensional spectrum frames and combined together to give the averaged spectrum shown in Fig. 5.1. The wavelength calibration was derived from observations of Ar lamps and applied to the averaged spectrum. The spectrum was corrected for telluric features with the spectrum of an AIV star observed at the same average air mass as the science exposures. Finally, we derived the flux calibration by normalizing the spectrum to the H -band magnitude.

Table 2.2: The best-fit profile parameters for the lens galaxies and lensed components.

| Component | Model | Effective Radius ($R_e('')$) | Axis ratios (b/a) | Position angle ($\theta(^{\circ})$) |
|-----------|------------------|--------------------------------|-----------------------|---------------------------------------|
| G1 | de Vaucouleurs | 4.19 ± 0.08 | 0.70 ± 0.01 | -60.63 ± 1.00 |
| G2 | de Vaucouleurs | 1.52 ± 0.03 | 0.73 ± 0.01 | 7.16 ± 1.47 |
| A | exponential disk | 0.45 ± 0.04 | 0.36 ± 0.03 | -17.84 ± 3.22 |
| B | exponential disk | 0.55 ± 0.04 | 0.58 ± 0.04 | -15.70 ± 4.93 |
| V | exponential disk | 0.45 ± 0.02 | 0.71 ± 0.03 | 48.90 ± 5.48 |
| D | exponential disk | 2.39 ± 0.27 | 0.11 ± 0.01 | 46.52 ± 0.95 |
| A1 | exponential disk | 0.63 ± 0.05 | 0.34 ± 0.02 | 12.40 ± 2.38 |

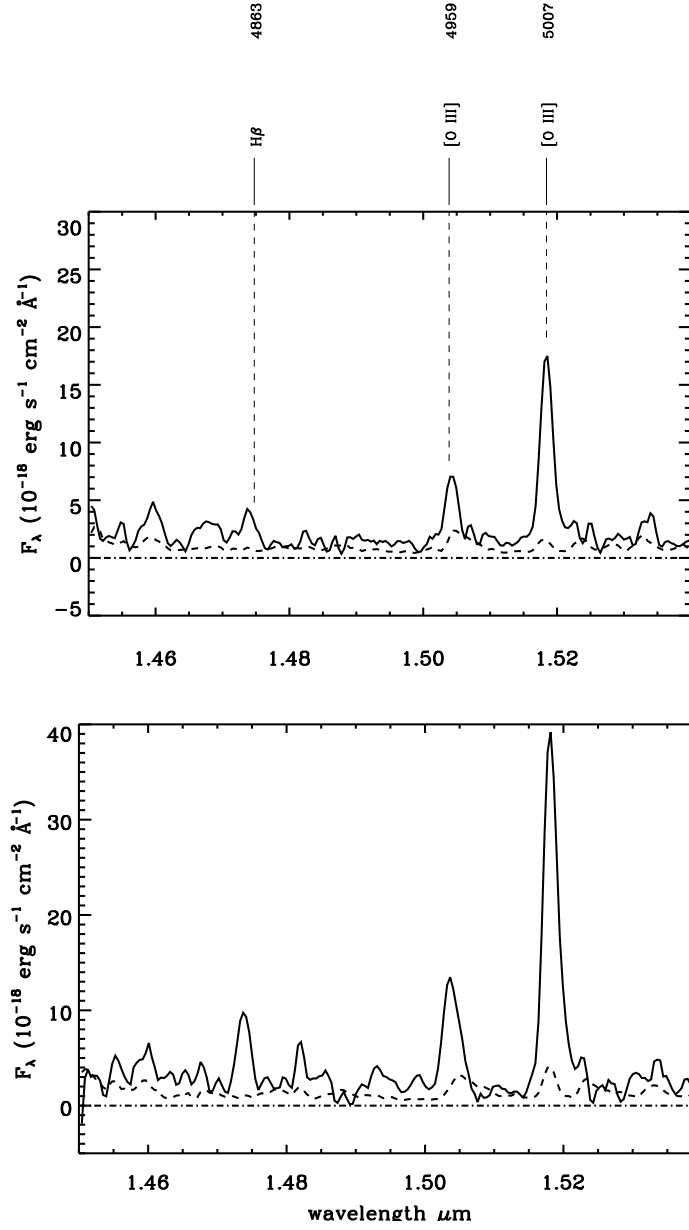


Figure 2.2: One-dimensional $H+K$ band spectra for the two components of J0900+2234. The dashed line is 1σ error of the spectrum, and the dash dot line represent the zero flux.

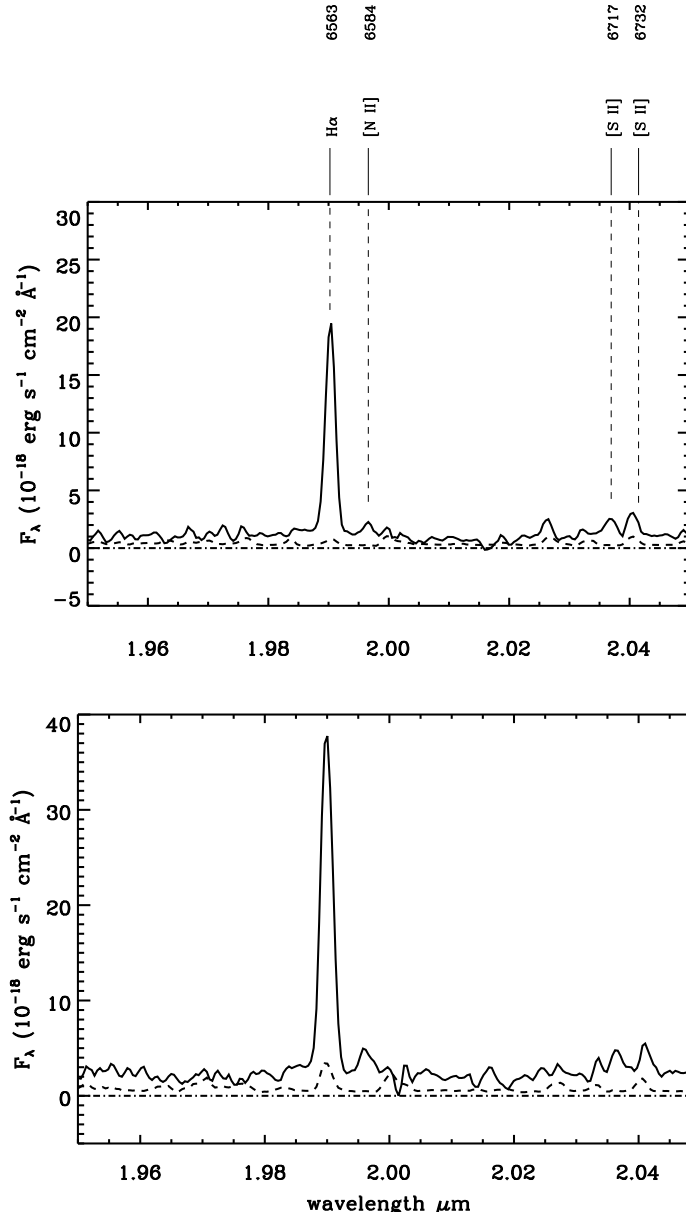


Figure 2.2: Continued Figure 2.2

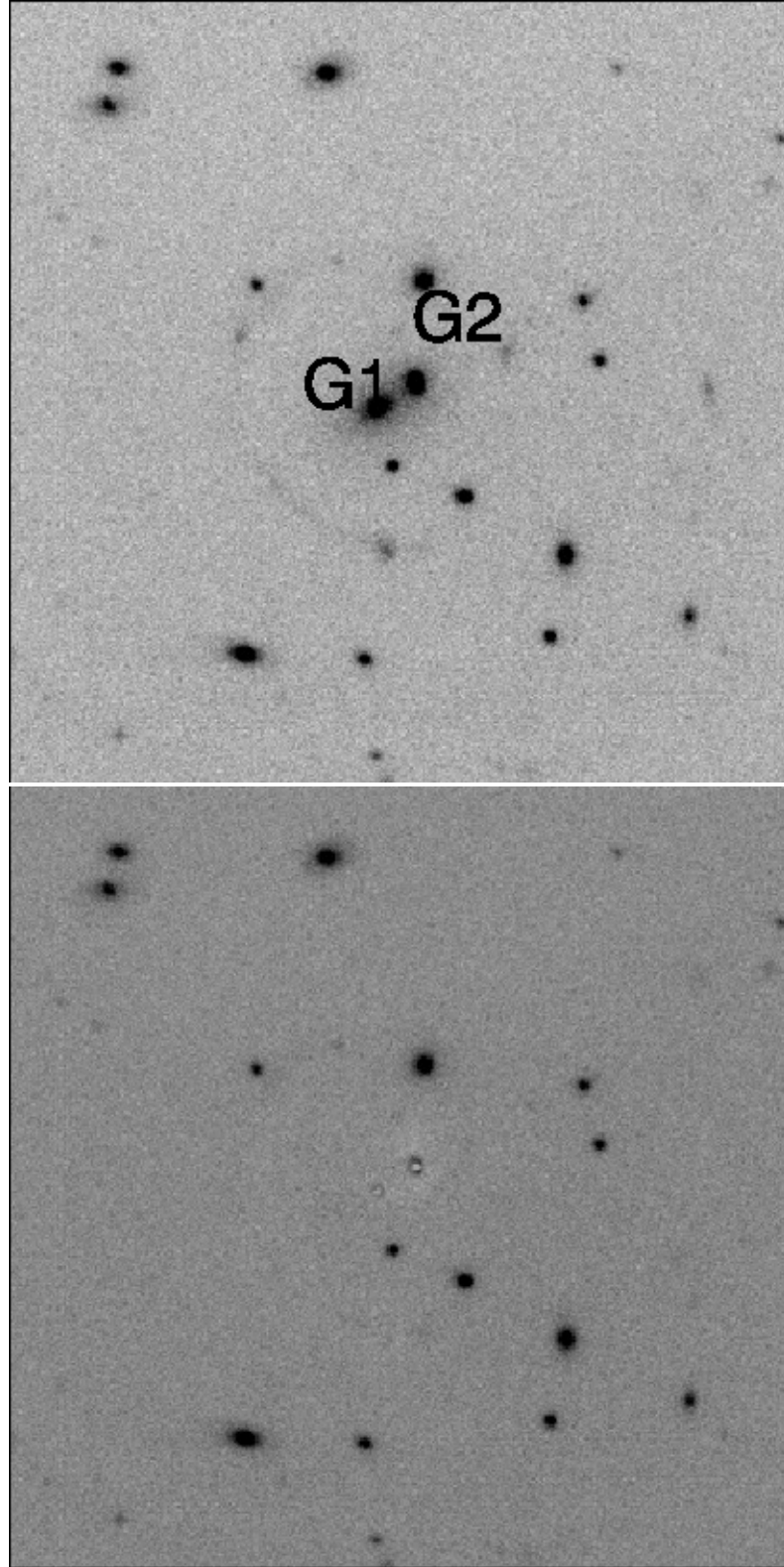


Figure 2.3: The K_s -band image and the residual image with all model components fit by GALFIT subtracted.

Table 2.3: Photometry of the LUCIFER images from GALFIT.

| Component | J_{AB} | H_{AB} | Ks_{AB} |
|-----------|------------------|------------------|------------------|
| G1 | 17.34 ± 0.01 | 16.98 ± 0.01 | 16.68 ± 0.03 |
| G2 | 18.43 ± 0.01 | 18.06 ± 0.01 | 17.69 ± 0.02 |
| A | 20.99 ± 0.03 | 20.87 ± 0.04 | 20.87 ± 0.06 |
| B | 20.63 ± 0.02 | 20.33 ± 0.04 | 20.30 ± 0.04 |
| C | 20.45 ± 0.03 | 20.44 ± 0.04 | 19.97 ± 0.03 |
| D | 20.79 ± 0.07 | 21.08 ± 0.18 | 20.23 ± 0.09 |
| A1 | 21.81 ± 0.09 | 21.26 ± 0.11 | 20.47 ± 0.04 |

2.3 Measurements

2.3.1 NIR Photometry: Discovery of a New Lensed Galaxy

The GALFIT program (Peng et al., 2002, 2010a) was used to model the central lensing galaxies and lensed components. We fit each of the two central massive galaxies with de Vaucouleurs models, and fit the three lensed knots and two arcs with exponential disk models. The initial input parameters – namely, position, total magnitude, axis ratio, and position angle for each component – were determined using SExtractor (Bertin & Arnouts, 1996). We used the Ks band co-added image to fit the profile parameters (Fig. 2.3 and Table 2.2), and fixed these parameters when fitting the J and H -band images to obtain the magnitude of each component (Table 2.3). The values of best-fit reduced χ^2 for J , H , and Ks bands are 1.064, 1.094, and 1.088, respectively.

The NIR colors of the A and B components are similar, with $J - H \sim 0.1$ and $H - Ks \sim 0.0$, while the colors of the C and D components appear to be different from those of the A and B components. For D component, the reason

for this discrepancy may be that the exponential disk profile is not a good fit to the observed arc structure. For the C component, the follow-up spectroscopy was performed with MMT/Blue Channel spectrograph, which shows that the C component is not part of this lens system.

Current data are not yet deep enough to uncover other components of the weak A1 component. If confirmed by spectroscopy and deeper imaging, this newly discovered arc would make J0900+2234 a rare example of a double Einstein ring system lensed by galaxy.

2.3.2 Emission Line Measurements

We used the IDL MPFIT¹ package to fit the emission lines. The results are listed in Table 5.2. The $H\beta$, $[O\ III]\lambda 4959$ and $[O\ III]\lambda 5007$ were fit as Gaussian functions individually. The positions of $H\alpha$ and $[N\ II]\lambda 6583$ as well as $[S\ II]\lambda\lambda 6717, 6732$ are close to each other, so they were fit by two Gaussian functions together to deblend these two lines. The observed line wavelength, line flux, and full width at half maximum (FWHM) were derived from the Gaussian fitting (Table 5.2). Monte Carlo (MC) simulation was used to estimate the uncertainties of line flux and FWHM. One thousand artificial spectra were generated by perturbing the flux of each data point from the true spectrum by a random amount proportional to the 1σ flux error. We then measured the line flux of each fake spectrum with leaving all the parameters free for both the single lines and deblended line pairs. The standard deviations of the distributions of the line flux and the FWHM were adopted as the uncertainty of measurements of the line flux and the FWHM (Table 4). The emission line redshifts of A and B knots are 2.0321 ± 0.0009 and 2.0318 ± 0.0005 , respectively, and are consistent with each other within $\Delta z/(1+z) = 0.0001$. These results also agree with the mean redshift from the optical spectra, $z =$

¹<http://cow.physics.wisc.edu/craigm/idl/idl.html>

Table 2.4: Results of emission line measurements.

| Components | Lines | wavelength | flux | FWHM |
|------------|---------------------------|------------|--------------------------------------|----------------|
| | | Å | 10^{-17} ergs s $^{-1}$ cm $^{-2}$ | Å |
| A | H β λ 4863 | 14738.9 | 4.85 ± 1.78 | 18.2 ± 8.2 |
| B | H β λ 4863 | 14738.1 | 15.08 ± 1.36 | 18.7 ± 1.4 |
| A | [O III] λ 4959 | 15043.0 | 14.15 ± 2.99 | 22.5 ± 8.1 |
| B | [O III] λ 4959 | 15037.4 | 29.98 ± 3.93 | 23.1 ± 2.6 |
| A | [O III] λ 5007 | 15184.6 | 37.24 ± 1.78 | 22.4 ± 1.1 |
| B | [O III] λ 5007 | 15182.7 | 93.81 ± 4.07 | 26.4 ± 1.1 |
| A | H α λ 6563 | 19902.8 | 37.01 ± 0.79 | 19.0 ± 0.4 |
| B | H α λ 6563 | 19899.5 | 84.68 ± 3.21 | 21.8 ± 0.6 |
| A | [N II] λ 6584 | 19965.1 | 1.56 ± 0.35 | 14.6 ± 4.3 |
| B | [N II] λ 6584 | 19961.9 | 5.66 ± 0.88 | 22.3 ± 3.8 |
| A | [S II] λ 6717 | 20367.5 | 3.56 ± 0.50 | 22.0 ± 3.9 |
| B | [S II] λ 6717 | 20365.1 | 5.11 ± 1.01 | 19.9 ± 5.6 |
| A | [S II] λ 6732 | 20405.6 | 4.06 ± 0.98 | 17.3 ± 5.3 |
| B | [S II] λ 6732 | 20410.4 | 6.06 ± 1.87 | 20.6 ± 8.6 |

2.0325 ± 0.0003 (Diehl et al., 2009).

2.4 Lensed Model

The lens modeling is performed using LENSFIT (Peng et al., 2006). Briefly, LENSFIT is patterned after, and works like GALFIT (Peng et al., 2002, 2010a). LENSFIT is designed to specifically deal with situations where the image geometry is crowded: it allows one to decompose foreground and background galaxy light profiles, and determine the lens deflection model, simultaneously. The number of light profile and singular isothermal ellipsoid (SIE) deflection models is unrestricted, and the optimization process is done using the Levenberg-Marquardt algorithm in Numerical Recipes (Press et al., 1992).

In J0900+2234, the deflection model is potentially quite complicated because the system is embedded in a compact cluster environment. There are at least two primary deflectors, and potentially 5 in all, just within the Einstein ring of the system which has a radius of roughly 7.7 arcseconds. Due to the low signal-to-noise of the source detection, it is difficult to determine an accurate lens model. However, it is clear from visual inspection that a single SIE deflector probably would not suffice because the geometric center of the lensed arcs falls in the gap between the two primary deflectors. Therefore, the simplest lens deflection model we adopt is that of two SIEs held to the position of the light profile of the two primary lensing galaxies. We also hold the SIE axis ratios fixed to the light profile models of the lenses, but allow the Einstein ring radii and position angle parameters to be free in the fit. We simultaneously optimize the light profiles of all the foreground sources and the background galaxy light profiles, in all 14 objects in *J*-band image.

With the limitation of our lens model and the data S/N in mind, we infer that

the size of the background source is 0.8-1.0 arcsecond which corresponds to the physical size of 6.6-8.2 kpc, in deprojected angular size, and it has a luminosity of 21.7 to 21.8 mag (AB) in J band, given a magnification of the A and B components together is 4.6-5.0. For the further analysis, we use the effective radius of 7.4 kpc and the A and B component magnification of 4.8. The Sersic index is quite high, from $n=3.5$ to $n=4$. The major uncertainty of the lens fitting is caused by the influence of the bright foreground source C, which is right on the Einstein ring and the source elsewhere has quite low S/N.

2.5 Physical Properties

With LUCIFER we obtained $H+K$ (1.40-2.20 μm) spectra of the A and B components of the lensed galaxy J0900+2234 (Fig. 5.1). The $H\beta$, $[\text{O III}]\lambda\lambda 4959, 5007$, $H\alpha$, $[\text{N II}]\lambda 6583$, and $[\text{S II}]\lambda\lambda 6717, 6732$ lines were detected. In this section, we discuss the physical properties which can be derived from these observations.

2.5.1 Emission-Line Diagnostics

First, it is important to examine the observed values of well-known empirical line ratio diagnostics to determine whether the emission is from an H II region, active galaxy, or shocked gas. The line ratios of the A and B components on the diagram of Baldwin et al. (1981) (BPT diagram) are shown in Fig. 2.4. The weak N II emission rules out the possibility that the emission is from the activity of a central active galactic nucleus (AGN). The location of the A and B components on the BPT diagram are similar to other high- z star forming galaxies (e.g., Liu et al., 2008; Hainline et al., 2009). They have relatively higher $[\text{O III}]\lambda 5007/H\beta$ values and lower $[\text{N II}]\lambda 6584/H\alpha$ values compared to the local star-forming galaxies from SDSS (Fig. 2.4). This offset could be the result of relatively intensive star formation activity and high electron density in these high redshift galaxies, com-

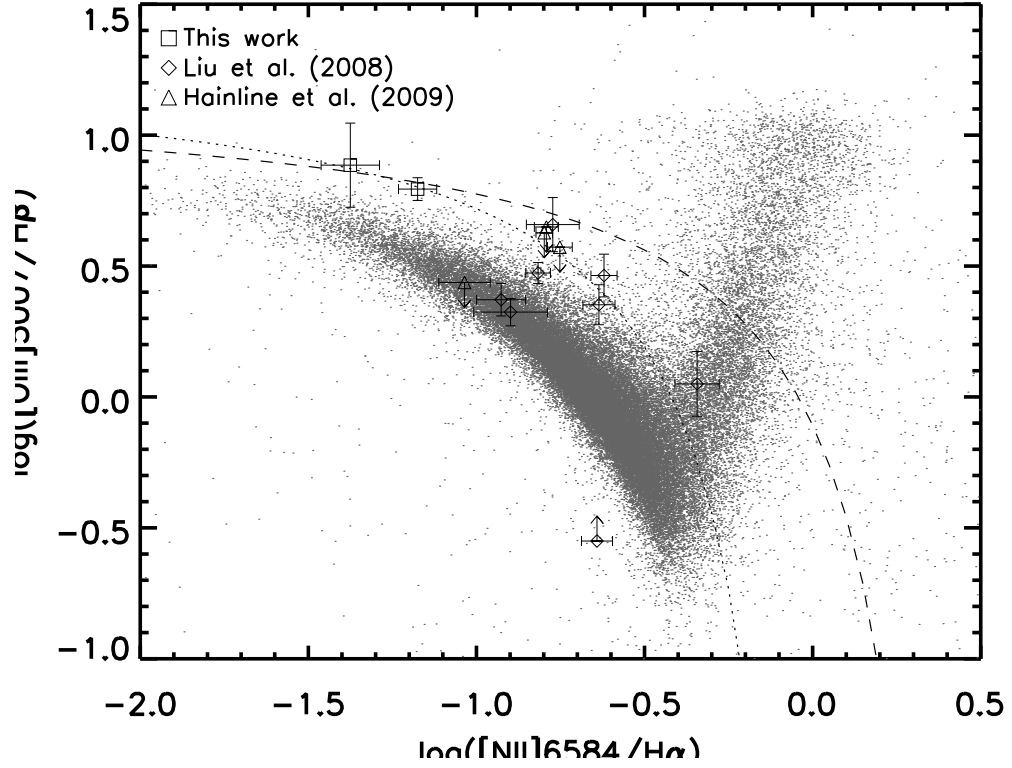


Figure 2.4: The H II region diagnostic diagram of $\log([N \text{ II}]\lambda 6584/H\alpha)$ and $\log([O \text{ III}]\lambda 5007/H\beta)$. The open rectangles show the location of the A (left) and B (right) components. The open diamonds represent $z \sim 1 - 1.5$ DEEP2 objects (Liu et al., 2008) and the open triangles represent $z \sim 2$ lensed star-forming galaxies (Hainline et al., 2009). The grey points represent SDSS star-forming galaxies and AGNs. The dotted line and dashed line are empirical (Kauffmann et al., 2003) and theoretical (Kewley et al., 2001) separation of star-forming galaxies and AGNs.

pared to the local sample. Overall, we conclude that the line emission is from gas that is photo-ionized by a hot stellar continuum, that is, the emission is from star-formation regions.

2.5.2 Reddening and Extinction

We estimated the extinction of the lensed galaxy by two methods: (1) a fit to the stellar continuum as measured by broad band photometry, and (2) Balmer decrement. These two methods represent dust extinction to the stellar continuum $E_s(B-V)$ and the dust extinction to the nebular gas in the H II region ($E_g(B-V)$), respectively. One expects these two estimates to differ, and indeed some previous studies have observed that there is more extinction towards the ionized gas than the stellar continuum in local star-forming galaxies (Calzetti et al., 2000) and high redshift galaxies (e.g., Förster Schreiber et al., 2009). In contrast, Erb et al. (2006b) did not find any extinction difference between ionized gas and the stellar continuum in star-forming galaxies at redshift of ~ 2 . For lensed galaxies, the reddening derived from individual images often differs because of reddening by different amounts of foreground dust, since the images traverse different sight-lines through the lensing galaxies.

With optical photometry alone, one can measure only the UV continuum shape in high redshift galaxies, making it difficult to distinguish between reddening by dust and age of the stellar population. By adding the NIR photometry, we can measure the Balmer break (3600-3700 Å) which is sensitive to the age of the stellar population, and the 4000 Å break strength only weakly depends on metallicity. By combining our NIR photometry with the optical, we can fit stellar population models and simultaneously determine the age of the galaxy and average extinction.

Here we used the J , H , and K_s -band (rest-frame optical bands) magnitudes

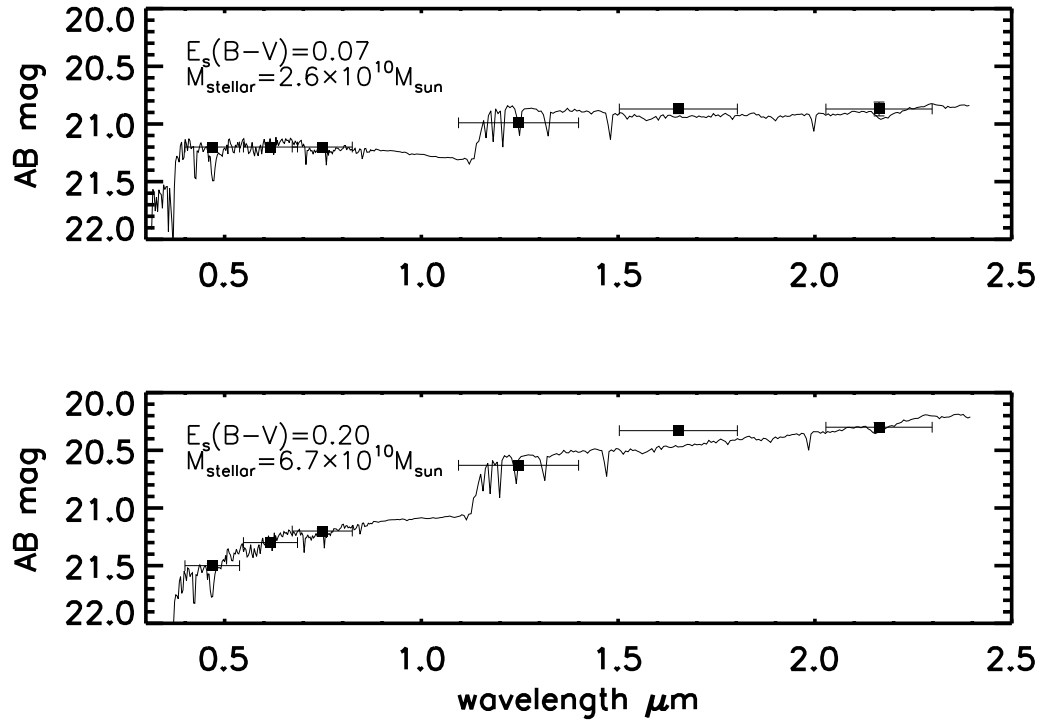


Figure 2.5: g , r , i , J , H and Ks -band AB magnitudes of the knot A (the upper panel) and the knot B (the bottom panel) and their best-fit model spectra. The best fit age is 180 Myrs for both knots and the lensed corrected stellar mass is $1.9 \times 10^{10} M_{\odot}$.

combining with the g , r , and i -band (rest-frame UV bands) magnitudes ($3''$ from Diehl et al. (2009)) to estimate the $E_s(B - V)$ and the age of the galaxy. The Bruzual & Charlot (2003, BC03) standard simple stellar population (SSP) model was used to build the spectral templates of star-forming galaxies. We adopted constant star formation rate (SFR) with the Chabrier initial mass function (IMF, Chabrier, 2003), and solar metallicity, to generate a series of spectra with different ages and reddening. Fig. 2.5 shows the best-fit spectra with the photometry data of A and B components. From the fitting, we found that the ages of the components A and B were consistent with each other, and equal to 180 Myr, with the values of $E_s(B - V)$ equal to 0.07 and 0.20 for the components A and B, respectively. Based on the metallicity found in section 2.5.4, we also generated the spectra with 0.25 solar metallicity to fit the broad band photometry data, and found similar results.

With this fit to the stellar population we derive the intrinsic stellar mass of the source galaxy is $1.9 \times 10^{10} M_\odot$ after correcting for lensing magnification, which is smaller than the mean stellar mass of $3.6 \times 10^{10} M_\odot$ found in a $z \sim 2$ UV-selected galaxy sample (Erb et al., 2006a). Using Ks band magnitude to approach the rest-frame R band magnitude, we found the M/L_R in J0900+2234 is 0.13. Shapley et al. (2005) found that the mean of M/L_R is 0.29 with a large scatter from 0.02 to 1.4 (where the values have been divided by 1.8 to convert the Salpeter IMF to Chabrier IMF) in $z \sim 2$ UV-selected star-forming galaxies. Considering the high scatter, M/L_R in J0900+2234 agrees with other $z \sim 2$ star-forming galaxies. The intrinsic UV ($\sim 1700 \text{ \AA}$) brightness of the J0900+2234 is 22.1 magnitude, so that the absolute magnitude is $M(1700)_{AB} = -22.7$, compared to $L^* = -20.20$ – -20.97 at $z \sim 2$ (e.g. Oesch et al., 2010; Reddy et al., 2008; Reddy & Steidel, 2009). Thus, J0900+2234 has $L/L^* \approx 5 - 10$, and is an intrinsically luminous galaxy. Galaxies with these high luminosity is very rare, and their number density is about a few

$10^{-6} \text{ Mpc}^{-3} \text{ mag}^{-1}$ base on the luminosity function from Reddy et al. (2008) and Reddy & Steidel (2009). The high intrinsic UV luminosity indicates a high SFR (see details in Section 2.5.3) in this galaxy.

We estimated $E_g(B - V)$ of J0900+2234 using the flux ratio of $\text{H}\alpha$ and $\text{H}\beta$ lines. Under Case B H I recombination at a temperature $T=10,000 \text{ K}$ and electron density $n \leq 100 \text{ cm}^{-3}$ (Zaritsky et al., 1994), the intrinsic value of $\text{H}\alpha/\text{H}\beta$ is 2.86 (Osterbrock & Ferland, 2006). Using the extinction law proposed by Calzetti et al. (2000), we found the values of $E_g(B - V)$ were 0.84 ± 0.31 and 0.59 ± 0.08 for the A and B components. For both A and B components, the values of $E_g(B - V)$ are significantly larger than those of $E_s(B - V)$, in agreement with the results of Calzetti et al. (2000) and Förster Schreiber et al. (2009). The stars and line-emitting gas are not co-spatial, and the line-emitting regions are dustier than the galaxy as a whole. Note that the low S/N of the $\text{H}\beta$ line in knot a makes the uncertainty of the $E_g(B - V)$ for component A large. Therefore, we use the value of $E_g(B - V) = 0.59 \pm 0.08$ of knot B for further analysis.

2.5.3 Star Formation Rate

We estimated the star-formation rate (SFR) in J0900+2234 using the luminosity of $\text{H}\alpha$ ($L_{\text{H}\alpha}$, Kennicutt, 1998a). The relation between the SFR and $L_{\text{H}\alpha}$ is

$$\text{SFR}(M_{\odot}\text{yr}^{-1}) = 7.9 \times 10^{-42} \frac{L_{\text{H}\alpha}}{\text{ergs s}^{-1}} \quad (2.1)$$

The $\text{H}\alpha$ fluxes of the A and B components are $37.01 \pm 0.79 \times 10^{-17} \text{ ergs s}^{-1} \text{ cm}^{-2}$ and $84.64 \pm 3.21 \times 10^{-17} \text{ ergs s}^{-1} \text{ cm}^{-2}$. We used $E_g(B - V) = 0.59 \pm 0.08$ to correct the fluxes for extinction and found the extinction-corrected fluxes are $(225.5 \pm 55.5) \times 10^{-17} \text{ ergs s}^{-1} \text{ cm}^{-2}$ and $(516.0 \pm 128.0) \times 10^{-17} \text{ ergs s}^{-1} \text{ cm}^{-2}$. The extinction-corrected luminosities are therefore $(15.4 \pm 3.8) \times 10^{43} \text{ ergs s}^{-1}$ and $(6.75 \pm 1.66) \times 10^{43} \text{ ergs s}^{-1}$. The lensed SFRs of components A and B are

$533 \pm 131 M_{\odot} \text{ yr}^{-1}$ and $1220 \pm 303 M_{\odot} \text{ yr}^{-1}$. We added the components A and B SFRs together, corrected for the magnification, and found that the intrinsic SFR of the lensed galaxy was $365 \pm 69 M_{\odot} \text{ yr}^{-1}$. Note that if we use the Chabrier IMF, the SFR derived from the $L_{H\alpha}$ will be $203 \pm 38 M_{\odot} \text{ yr}^{-1}$. We also estimate the SFR from the UV luminosity (Kennicutt, 1998a) which is derived from the average of g and r band flux. We found that the SFR is $276 M_{\odot} \text{ yr}$ for Shalpeter IMF and $153 M_{\odot} \text{ yr}$ for Chabrier IMF by correcting the dust extinction, $E_s(B - V) = 0.07(0.20)$ for A (B) components. The SFR based on the dust-corrected $H\alpha$ emission is consistent with that from the dust-corrected UV emission. If we use $E_s(B - V) = 0.20$ to correct the extinction of $H\alpha$ flux, the $H\alpha$ -derived SFR of $110 M_{\odot} \text{ yr}^{-1}$ will be significant lower than UV-derived SFR. This supports the result that the $E_g(B - V)$ is larger than $E_s(B - V)$. The average of the SFR for $z \sim 2$ star-forming galaxies is $\langle \text{SFR}_{H\alpha} \rangle = 31 M_{\odot} \text{ yr}^{-1}$ and $\langle \text{SFR}_{UV} \rangle = 29 M_{\odot} \text{ yr}^{-1}$ (Erb et al., 2006b). Despite the uncertainties in interpreting the SFR measurements, we conclude that the SFR of J0900+2234 is an order of magnitude higher than typical star-forming galaxies at $z \sim 2$.

2.5.4 Oxygen Abundance

Emission lines from H II regions can be used to measure metallicity. The oxygen abundance was calculated using the following indicators: the N2 index ($\text{N2} \equiv \log(F_{[\text{NII}]\lambda 6584}/F_{H\alpha})$) and the O3N2 index ($\text{O3N2} \equiv \log\{(F_{[\text{OIII}]\lambda 5007}/F_{H\beta})/(F_{[\text{NII}]\lambda 6584}/F_{H\alpha})\}$), which have been well calibrated using nearby extragalactic H II regions to measure O/H (Pettini & Pagel, 2004). The advantage of using the N2 and O3N2 indices as metal abundance estimators is that $H\alpha$ and the $[\text{N II}]\lambda 6584$ pair, as well as the $H\beta$ and $[\text{O III}]\lambda 5007$ pair, are close in wavelength, making these two estimators relatively insensitive to extinction.

The N2 index is sensitive to the oxygen abundance Storchi-Bergmann et al.

(1994), and was further calibrated by Raimann et al. (2000) and Denicoló et al. (2002). Here we use the best linear fit between the N2 and $(12 + \log(\text{O}/\text{H}))$ from Pettini & Pagel (2004),

$$12 + \log(\text{O}/\text{H}) = 8.90 + 0.57 \times \text{N2}, \quad (2.2)$$

where N2 is in the range from -2.5 to -0.3, and the 1σ error of the measurements of $\log(\text{O}/\text{H})$ is 0.18. We find the values of $12 + \log(\text{O}/\text{H})$ equal to 8.12 ± 0.21 and 8.23 ± 0.19 for components A and B, respectively, which are about 0.27 ± 0.13 to 0.35 ± 0.15 solar abundance (for the sun: $12 + \log(\text{O}/\text{H}_\odot) = 8.69$ (Asplund et al., 2009)).

The O3N2 index was first introduced by Alloin et al. (1979), and was well calibrated by Pettini & Pagel (2004) using 137 extragalactic H II regions. The relation between the metallicity ($12 + \log(\text{O}/\text{H})$) and the O3N2 index is:

$$12 + \log(\text{O}/\text{H}) = 8.73 - 0.32 \times \text{O3N2}, \quad (2.3)$$

where O3N2 is in the range from -1 to 1.9, and the 1σ error of the measurements of $\log(\text{O}/\text{H})$ is 0.14, which indicates a less scattering than the N2 index. We found the values of $12 + \log(\text{O}/\text{H})$ of components A and B were 8.00 ± 0.16 and 8.09 ± 0.15 , which are 0.21 ± 0.08 and 0.25 ± 0.08 solar abundance.

Both the N2 and O3N2 indices indicate that J0900+2234 has a low oxygen abundance compared with other $z \sim 2$ star-forming galaxies. Fig. 2.6 shows the stellar mass and metallicity relation in the local SDSS starburst galaxies and $z \sim 2$ star-forming galaxies (Erb et al., 2006a). The metallicity is derived from N2 index. We averaged the value $12 + \log(\text{O}/\text{H})$ of the A and B components and the stellar mass is from the broad band fitting result. Our data point is significantly lower than the mass and metallicity relation in star-forming galaxies at $z \sim 2$ (Erb et al., 2006a). Mannucci et al. (2010) proposed a more general fundamental relation

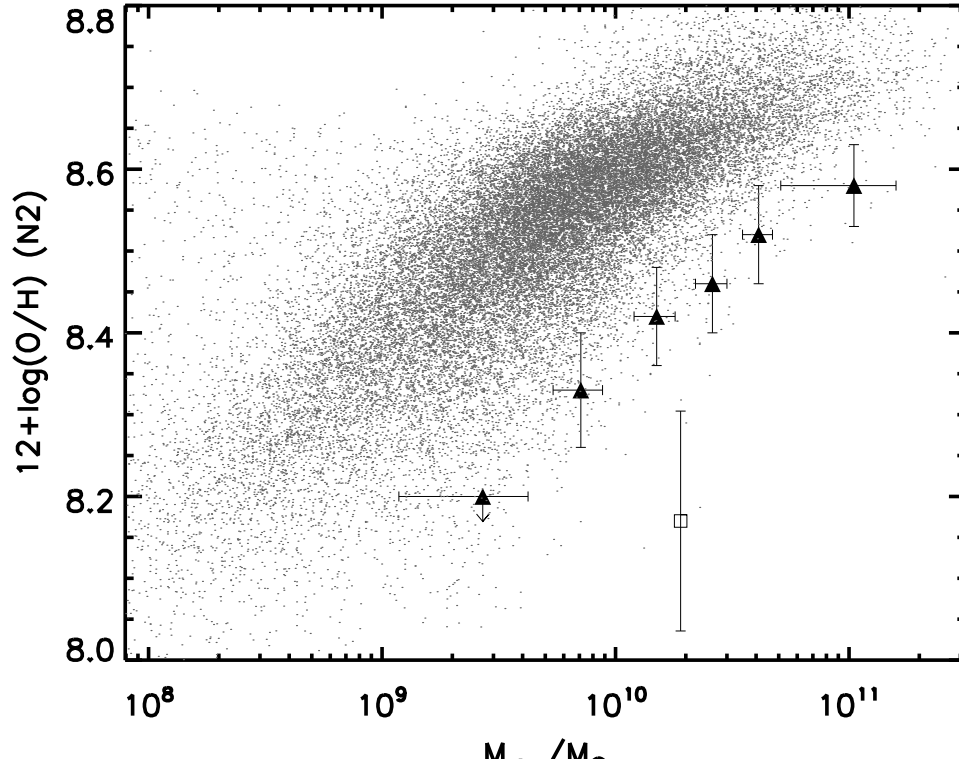


Figure 2.6: The stellar mass and metallicity relation for the SDSS galaxies (grey points) and the galaxies at $z \sim 2$ (filled triangle Erb et al., 2006a). The open rectangle represents the lensed galaxy J0900+2234, which is significant lower than the relation in the galaxies at $z \sim 2$.

between stellar mass, SFR and metallicity derived with SDSS galaxies, in which the metallicity decreases with the increase of SFR. We used the relation derived in Mannucci et al. (2010) (equation 2) to obtain the predicted metallicity from SFR and stellar mass and found the value is 8.45. Although our measured metallicity is ~ 0.27 dex lower than the predicted value, this dispersion is consistent with the results of Mannucci et al. (2010) that the distant galaxies show 0.2-0.3 dex dispersions for the fundamental metallicity relation.

2.5.5 Electron Density

The flux ratio of [S II] λ 6717 and [S II] λ 6732 was used to estimate the electron density in the H II region of J0900+2234. The IRAF task *stdas.analysis.nebular.temden* was used to compute the density. We assumed that the temperature in these regions were 10,000 K. We found the values of $F_{[\text{SII}]\lambda 6717}/F_{[\text{SII}]\lambda 6732}$ were 0.88 ± 0.24 and 0.84 ± 0.31 for the components A and B. The large error bar is due to the low S/N (< 5) of these [S II] lines in both apertures. The values of the ratio yielded a range of electron number density $1029^{+3333}_{-669} \text{ cm}^{-3}$ and $1166^{+7020}_{-855} \text{ cm}^{-3}$, respectively for these two components. Nonetheless, these densities are much higher than those typical of local H II regions $n_e \sim 100 \text{ cm}^{-3}$ (e.g., Zaritsky et al., 1994). The electron density of J0900+2234 is similar to that in the lensed galaxies, the Cosmic Horseshoe and the Clone, which is also derived from the ratio of [S II] double lines (Hainline et al., 2009). The high electron density was also found in the Cosmic Horseshoe with $5\,000\text{--}25\,000 \text{ cm}^{-3}$ derived from the ratio of C III] $\lambda\lambda$ 1906, 1908 doublet (Quider et al., 2009). The high electron density implies the compact size of the H II regions in the high- z galaxies. If these high- z H II regions follow the similar electron density-size relation found in the local galaxies (Kim & Koo, 2001), their sizes should be less than 1 pc.

2.5.6 Virial Mass and Gas Mass

The width of the emission lines can be used to probe the dynamics and the total mass of the parent galaxy. By fitting the emission lines (e.g., $\text{H}\alpha$, [O III]) as Gaussian profiles, we found that the FWHMs of $\text{H}\alpha$ of A and B knots were 19.0 Å and 21.8 Å. These observed FWHMs were corrected by subtracting the instrument resolution (~ 16 Å) in quadrature. The corrected FWHMs were converted to the 1-D velocity dispersion with $\sigma = \text{FWHM}/2.355 \times c/\lambda$. The values of σ for the A and B knots are $66 \pm 5 \text{ km s}^{-1}$ and $95 \pm 6 \text{ km s}^{-1}$ respectively. We averaged the σ

components of A and B to estimate the velocity dispersion of J0900+2234, which is $81 \pm 4 \text{ km s}^{-1}$. Our velocity dispersion is about 30% lower than that in a sample of $z \sim 2$ star-forming galaxies (Erb et al., 2003), who found a mean velocity dispersion of $\sim 110 \text{ km s}^{-1}$.

The mass of the galaxies can be estimated by assuming a simplified case of a uniform sphere (Pettini et al., 2001)

$$M_{vir} = \frac{5\sigma^2 r_{1/2}}{G} \quad (2.4)$$

$$M_{vir} = 1.2 \times 10^{10} M_{\odot} \left(\frac{\sigma}{100 \text{ km s}^{-1}} \right)^2 \frac{r_{1/2}}{\text{kpc}} \quad (2.5)$$

where G is the gravitational constant and $r_{1/2}$ is the half-light radius, which is $7.4 \pm 0.8 \text{ kpc}$ from the lens model. We find that the dynamical mass of J0900+2234 is $(5.8 \pm 0.9) \times 10^{10} M_{\odot}$, an upper limit since the line emitting gas may not be in Virial equilibrium with the gravitational potential of the galaxy.

Using the global Kennicutt-Schmidt law (Kennicutt, 1998b), we convert the surface gas density (Σ_{gas}) with the SFR derived from $H\alpha$:

$$\Sigma_{gas} = 1.6 \times 10^{-27} \left(\frac{\Sigma_{H\alpha}}{\text{erg}^{-1} \text{kpc}^{-2}} \right)^{0.71} M_{\odot} \text{pc}^{-2} \quad (2.6)$$

where $\Sigma_{H\alpha} \simeq L_{H\alpha}/r_e^2$ is the surface density of $H\alpha$ luminosity (Erb et al., 2006c; Finkelstein et al., 2009). Then the gas mass, M_{gas} , can be derived from $\Sigma_{H\alpha} \times r_e^2$, which is $5.1 \pm 1.1 \times 10^{10} M_{\odot}$. And the gas fraction, $f_{gas} = M_{gas}/(M_{gas} + M_{stellar})$, is 0.74 ± 0.19 . Erb et al. (2006a) found the gas fraction increases when the stellar mass decreases in the UV-selected star forming galaxies at $z \sim 2$. The gas fraction in J0900+2234 is higher than the mean gas fraction (0.48 ± 0.19) of Erb et al. (2006a) galaxies in the similar stellar mass bin ($1.5 \pm 0.3 \times 10^{10} M_{\odot}$), but still 1σ consistent. The total baryonic mass $M_{gas} + M_{stellar}$ is $6.9 \pm 1.1 \times 10^{10} M_{\odot}$, which is in the agreement with the dynamic mass.

2.5.7 Measurement Uncertainty

The main uncertainty of the measurement of the extinction and abundance is from the uncertainties in the measurements of the weak emission lines (e.g. $H\beta$ and S II) in the observed NIR. There are many prominent sky emission lines in the NIR, especially in the H band, which can contaminate our line measurements, especially for the weak emission lines. In the LUCIFER spectra of J0900+2234, the $H\beta$ sits near the blue cut of the H band, where there are several moderate strong sky emission lines and the instrument efficiency, which contributes large flux errors ($S/N < 5$) and underestimate/overestimate the fluxes. The higher $E_g(B - V)$ value of the A (fainter) component and systematically lower metallicities estimated from O3N2 index compared to those from N2 index may imply the flux of $H\beta$ is underestimated.

The systematic uncertainty of SFR, associated with the absolute flux of the $H\alpha$, is mainly due to the uncertainties in the absolute calibration of the NIR spectra. We calibrated the spectra with an AV star, and scaled the spectral flux to the H band magnitude to correct the light loss in the spectrograph slit. The scale factors are ~ 1.6 (~ 1.8) for the A (B) knots, which is a reasonable value for light loss. Converting the lensed $H\alpha$ luminosity to the intrinsic $H\alpha$ luminosity is another uncertainty for SFR estimation. The uncertainty of the lens model fitting is 20 – 30%. The uncertainty also affect the estimation of the stellar mass and dynamical mass, which depend on the results of the lens model. The $H\alpha$ and SFR relation (Kennicutt, 1998a) is derived from stellar synthesis models with solar metallicity. The SFR in J0900+2234 could be overestimated, given the low metallicity ($\sim 0.25 Z_\odot$) in this galaxy.

Table 2.5: Summary of the physical properties of J0900+2234.

| Knots | age | $E_s(B - V)$ | $E_g(B - V)$ | Z_{N2} | Z_{O3N2} | n_e | $\text{SFR}_{\text{H}\alpha}^{\text{a}}$ | $\text{SFR}_{\text{UV}}^{\text{a}}$ | $\log(M_{\text{stellar}})^{\text{a}}$ | $\log(M_{\text{gas}})^{\text{a}}$ | $\log(M_{\text{vir}})^{\text{a}}$ |
|-------|-----|--------------|-----------------|-----------------|-------------------|-----------------------|------------------------------------------|-------------------------------------|---------------------------------------|-----------------------------------|-----------------------------------|
| | Myr | | | Z_{\odot} | Z_{\odot} | cm^{-3} | $M_{\odot} \text{ yr}^{-1}$ | $M_{\odot} \text{ yr}^{-1}$ | M_{\odot} | M_{\odot} | M_{\odot} |
| A | 180 | 0.07 | 0.84 ± 0.31 | 0.27 ± 0.13 | 0.21 ± 0.08 | 1029^{+3333}_{-669} | 365 ± 69 | 203 ± 38 | 10.28 | 10.71 | 10.76 |
| B | 180 | 0.20 | 0.59 ± 0.08 | 0.35 ± 0.15 | 0.26 ± 0.09 | 1166^{+7020}_{-855} | - | - | - | - | - |

2.6 Conclusions

We present LBT/LUCIFER1 NIR (rest-frame optical) imaging and spectroscopy of the lensed galaxy J0900+2234 ($z = 2.03$). The lensed components A and B were placed in the slit to obtain NIR spectra covered from 1.40 to 2.20 μm . The detailed physical properties of the lensed star-forming galaxy were studied using the rest-frame optical spectra (Table 2.5). We summarize the main results as follows.

- The new imaging was used to construct a lensing model. The magnification factor for the fluxes of the lensed galaxies (A plus B) is estimated to be 4.8.
- A new lensed arc A1 was discovered by the deep NIR J , H , and Ks -band images. The colors and position imply that this arc does not have the same source galaxy as the other four components discovered before, suggesting the presence of a rare double Einstein ring. Follow-up spectroscopy shows that the C component does not have the same source galaxy as A and B.
- We fit the optical and NIR broad band photometry to theoretical stellar population spectral templates (BC03), and found the galaxy age to be 180 Myr, $E_s(B - V) = 0.07$ ($E_s(B - V) = 0.20$) for the A (B) component. The stellar mass is $1.9 \times 10^{10} M_\odot$, and the intrinsic luminosity of the galaxy is $L/L^* \approx 5 - 10$.
- Using the flux ratio of $H\alpha$ and $H\beta$, we found that the emission line gas suffers an extinction of $E_g(B - V)$ is 0.84 ± 0.31 (0.59 ± 0.08) for the A (B) component, which is much higher than $E_s(B - V)$. This result implies that there is more extinction towards the ionized gas than the stellar continuum.
- The oxygen abundance was estimated using the N2 and O3N2 indices. We found that the metallicity in this star forming galaxy is only 21 – 35% solar,

which is somewhat lower than typical star-forming galaxies at $z \sim 2$. The electron number density, n_e , was measured using the flux ratio of [S II] λ 6717 and [S II] λ 6732. The n_e is in the range of $1029^{+3333}_{-669} \text{ cm}^{-3}$ ($1166^{+7020}_{-855} \text{ cm}^{-3}$) for the A (B) component. These values are consistent with other studies of high- z galaxies (e.g., Hainline et al., 2009; Quider et al., 2009), but much larger than that in local H II regions.

- The extinction-corrected luminosity of H α emission line was used to estimate the SFR, and the intrinsic SFR of J0900+2234 is $365 \pm 69 M_{\odot} \text{ yr}^{-1}$ which is one magnitude higher than a typical $z \sim 2.0$ UV-selected star-forming galaxy. We estimate the Virial mass of J0900+2234 from the FWHM of the H α emission line and find a dynamical mass of $(5.8 \pm 0.9) \times 10^{10} M_{\odot}$. The gas mass of the galaxy is $(5.1 \pm 1.1) \times 10^{10} M_{\odot}$ estimated from the H α flux by assuming the global Kennicutt-Schmidt law.

Comparison to the local star-forming galaxies, the J0900+2234 ($z=2.03$) features as much higher electron density. The high electron density and high ionization state (e.g., Hainline et al., 2009) probably cause the offset between the H II regions in the high- z galaxies and those in the local galaxies in the BPT diagram. This star-forming galaxy also has a much higher SFR, and a relatively lower age, stellar mass, and metallicity than those in the typical high- z star-forming galaxies.

The commissioning of LUCIFER1 on the 8.4m LBT left primary mirror (SX) has allowed a detailed study of the $z = 2$ galaxy J0900+2234 in relatively short exposure times. We look forward to future NIR observations of other lensed galaxies, as well as field galaxies which are not lensed, which will give a similarly richly detailed picture of galaxies in this important stage of galaxy evolution.

CHAPTER 3

THE LBT BOÖTES FIELD SURVEY: I. THE REST-FRAME ULTRAVIOLET
AND NEAR-INFRARED LUMINOSITY FUNCTIONS AND
CLUSTERING OF BRIGHT LYMAN BREAK GALAXIES AT $z \sim 3$

We present deep LBT/LBC U_{spec} -band imaging (≈ 25.2 AB at 5σ) covering an area of 9 deg^2 in the NOAO Deep Wide-Field Survey Boötes field. A total of 14,485 photometrically-selected Lyman Break Galaxies (LBGs) at $z \sim 3$ are selected. We use this large sample to measure the rest-frame UV luminosity function (LF). The large sample size and survey area reduce the uncertainties in the LF measurements due to Poisson statistics and cosmic variance by ≥ 3 . At the bright end ($M_{1700\text{\AA}} < -23.0$), the LF shows excess power compared to the best-fit Schechter function, and the majority of the excess can be attributed to the contribution of $z \sim 3$ quasars. Using the relation between R -band and $[4.5]$ band fluxes, we compute the rest-frame near-infrared (near-IR, $1.1 \mu\text{m}$) LF and stellar mass function (SMF). We find that the density of massive $z \sim 3$ LBGs is significantly lower than that of mass-selected galaxy samples; however, the LBG population dominates the stellar mass density at the low mass end. We investigate the evolution of the UV LF and SMFs between $z \sim 7$ and $z \sim 3$ and find that the evolution trend supports the scenario that the star formation rate was smoothly rising at the early epoch of the universe. We study the spatial distributions of two bright LBG samples ($23.5 < R < 24.0$ and $24.0 < R < 24.5$) and find the clustering strength increases with the rest-frame UV luminosity. The halo occupation distribution model is applied to derive the average hosting halo mass of these two bright LBG samples. Combining with the LBG samples in previous studies, we find a tight relation between the average host galaxy halo mass and the galaxy

star formation rate. This relation can be interpreted as arising from cold flow accretion, suggesting that the star formation in LBGs is fueled by cold stream accretion. The relation also suggests that the cosmic star formation efficiency is about 5%-20% of the total cold flow mass. This cosmic star formation efficiency does not evolve with redshift (from $z \sim 5$ to $z \sim 3$), hosting dark matter halo mass ($10^{11} - 10^{13} M_{\odot}$), or galaxy luminosity (from $0.1L^*$ to $3L^*$).

3.1 Introduction

The redshifts between $1 < z < 3$ were the most active epochs of galaxy formation, when the star formation rate density and the activity of bright quasars reached their peaks (e.g., Madau et al., 1996; Fan et al., 2001). In this epoch, the Hubble sequence observed in the nearby universe was being built up and about 50% of the present-day stars formed (?). Therefore, observations in this redshift range provide crucial clues to understanding the formation and evolution of galaxies. The Lyman break technique has been well developed for surveying galaxies in this redshift range (e.g., Steidel et al., 1996a,b). Large samples of high-redshift star-forming galaxies have been established with this method (e.g., Steidel et al., 2003).

Using samples of LBGs, the rest-frame UV luminosity functions (LFs) from $z \sim 2$ to $z \sim 7 - 8$ have been well studied. (e.g., Ly et al., 2009; Reddy & Steidel, 2009; Steidel et al., 1999; Sawicki & Thompson, 2006a; Bouwens et al., 2007, 2008; Yan et al., 2011b). The rest-frame UV LF is a fundamental tracer of galaxy formation and evolution; it is used to compute the UV luminosity density after application of an extinction correction and to constrain the history of star formation (e.g., Madau et al., 1996). However, LF measurement remains uncertain for $z \sim 2 - 3$ LBGs, the measured faint end slope (α) of Schechter function ranges

from the shallowest with $\alpha = -1.05$ to the steepest with $\alpha = -1.88$ (e.g., Ly et al., 2009; Reddy et al., 2008); at the bright end, there are discrepancies between Steidel et al. (1999) and Le Fèvre et al. (2005) for the galaxies at $z \sim 3$ by factors 1.6–6.2, and $z \sim 4$ by factors 2–3.5 at the bright end. In addition, the evolution of the bright end UV LF of high-redshift LBGs is still not well constrained. Sawicki & Thompson (2006b) claimed that the number density of bright LBGs decreases with redshifts, while Bouwens et al. (2007) find that the number density remains constant. Furthermore, most of the small area surveys lacked information on the most luminous LBGs, i.e., with $M_{1700\text{\AA}} < -23$, due to the small surface density of these luminous LBGs.

Galaxy clustering can be used to test the hierarchical theory of structure formation, which predicts that the clustering of the dark matter halos strongly depends on their masses and assembly history (e.g., Mo & White, 1996). Numerical simulations can predict the dark matter distribution given underlying cosmology and initial matter power spectrum derived from the cosmological microwave background (CMB) measurements (e.g., Spergel et al., 2007). Distributions of galaxies and dark matter are connected by the halo occupation distribution (HOD, e.g., Zheng et al., 2007). The mass of dark matter halos hosting the galaxies can be determined with HOD models. Many studies show that the LBGs are strongly clustered (e.g., Adelberger et al., 1998; Giavalisco et al., 1998), and the brighter galaxies are more strongly clustered at large scales (e.g., Adelberger et al., 2005b; Ouchi et al., 2005; Lee et al., 2006; Hildebrandt et al., 2007). In addition, the correlation function of LBGs shows excess power at small scales ($\theta < 1''$), implying multiple galaxies within the same massive dark matter halo in the context of HOD (Ouchi et al., 2005; Lee et al., 2006, 2009). Combined with the UV LF, clustering results also can be used to infer the nature of star formation in

the LBGs and its dependence on their host halo mass (Lee et al., 2009).

In previous deep field surveys, survey areas were relatively small. The largest $z \sim 3$ LBG survey so far with spectroscopic redshifts only covers a total area of around 1 deg^2 in 31 individual fields with ≈ 2000 spectroscopic redshifts (Steidel et al., 2003; Reddy & Steidel, 2009). The largest coherent structures revealed in these surveys have sizes comparable to the field size: we clearly have not reached the scale of the largest structures at that time. The small sample size means that only simple statistics can be computed, and it is difficult to sub-divide the sample to probe the dependence of clustering on intrinsic properties of galaxies. Given the difficulty in obtaining even larger spectroscopic samples of faint LBGs, the only effective way to expand the sample size by a large factor is through photometrically selected samples. For example, the Garching-Bonn deep survey (Hildebrandt et al., 2007) covers $\approx 2 \text{ deg}^2$, and ≈ 8000 $z \sim 3$ photometrically-selected LBGs are selected to study the clustering properties.

The key to establishing a large $z \sim 3$ LBG sample is the availability of deep multi-wavelength imaging, especially deep U band imaging. The Large Binocular Camera (LBC, Giallongo et al., 2008) - Blue on the left arm of the $2 \times 8.4 \text{ m}$ Large Binocular Telescope (LBT) is specially designed to have high throughput and good image quality in the blue. We have carried out a large LBC survey of the NOAO Deep Wide Field Survey (NDWFS, Jannuzi & Dey, 1999) Boötes Field (9 deg^2) in U_{spec} and Y bands, building on the unique multiwavelength data set already available for the Boötes field, while filling in two critical wavelength gaps. The survey area is about five times larger than previous studies (e.g. COSMOS, Scoville et al., 2007), which allows us to build a larger LBG sample to further study the luminosity function and clustering properties, especially for the brightest LBGs at the redshift $z \sim 3$.

This is the first in a series of papers. In this paper, we will focus on the photometrically-selected LBGs and study their UV and NIR LF and the clustering properties, especially at the bright end. In following papers, we will focus on spectroscopic confirmation of the most luminous LBGs.

The paper is organized as follows: observations are discussed in section 3.2. Data reduction is described in section 3.3. Sample selection is given in section 3.4. We present our bright end rest-frame UV and near-IR LF and stellar mass function (SMF) results in section 3.5 and 3.6 and discuss the evolution of UV LF and SMF with cosmic time in section 3.7. Clustering results are presented in section 3.8. Finally, we summarize our results. Throughout this paper, we use the following cosmological parameters for the calculations: Hubble constant, $H_0 = 70 \text{ km s}^{-1} \text{ Mpc}^{-1}$; dark matter density, $\Omega_M = 0.30$; and dark energy density, $\Omega_\Lambda = 0.70$ for a flat universe (e.g., Spergel et al., 2007), and the magnitudes are expressed in AB magnitude system (Oke & Gunn, 1983).

3.2 Observations

The Boötes Field ($\alpha(J2000) = 14^h32^m$, $\delta(J2000) = +34^\circ16'$), one of the NDWFS fields, is a 9 deg^2 field covered by a deep multicolor survey in B_w -, R -, and I -optical broad bands (Jannuzi & Dey, 1999), and J and K_s near-infrared (near-IR) bands (Elston et al., 2006). A shallow z -band survey was carried out by Cool (2007). Additionally, this deep field has been observed at other wavelengths, including in the X-ray with *Chandra* (Murray et al., 2005b; Kenter et al., 2005; Brand et al., 2006), UV with *GALEX* (Hoopes et al., 2003), infrared with *Spitzer* IRAC (Ashby et al., 2009) and MIPS (Soifer & Spitzer/NOAO Team, 2004), and radio with the VLA (Becker et al., 1995; de Vries et al., 2002). A redshift survey (the AGN and Galaxy Evolution Survey; Cool, 2006) has also been conducted on

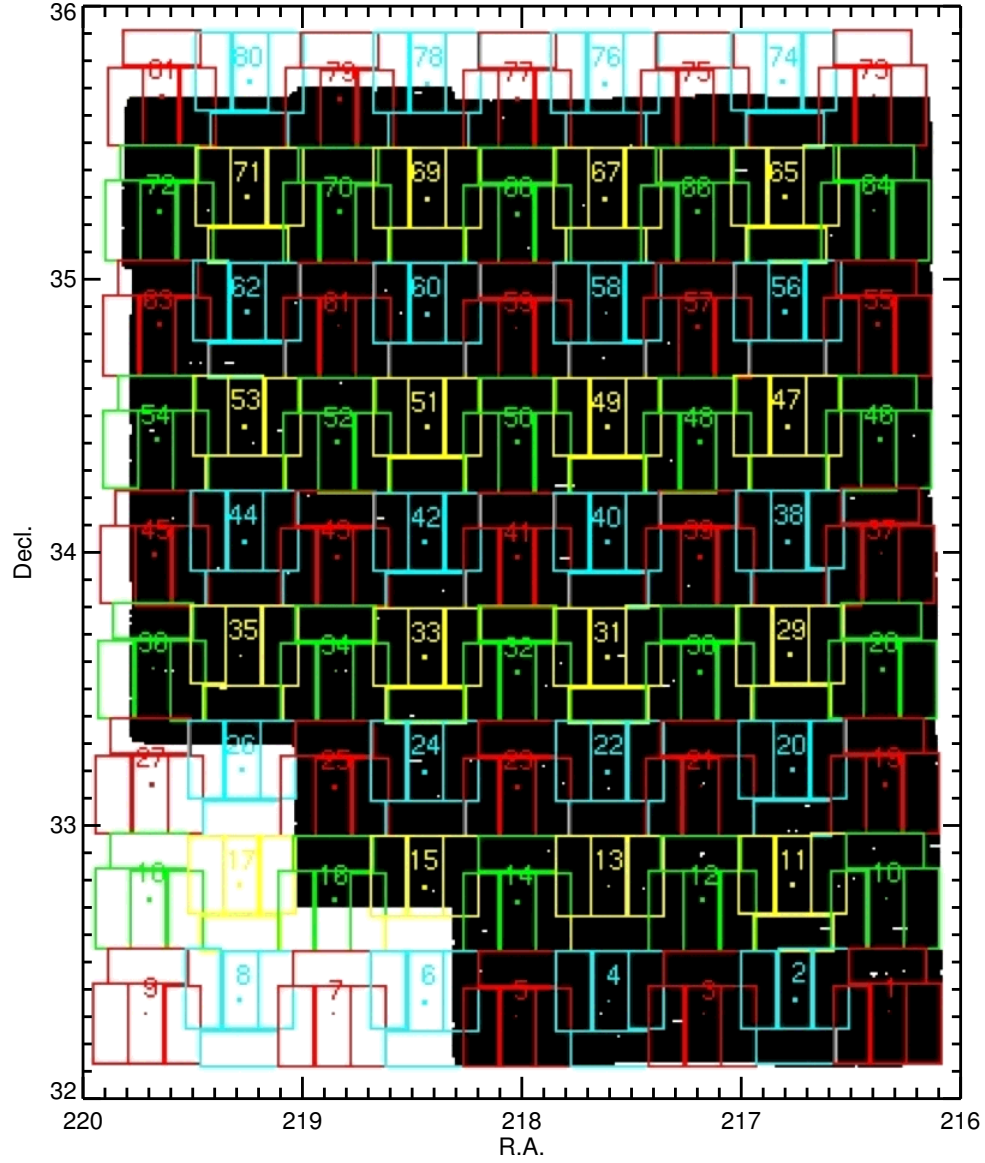


Figure 3.1: U_{spec} coverage map for the Boötes field. The black region is covered by the NDWFS B_w , R , and I bands. There are total 81 fields designed to cover the whole rectangle region. 63 of them, which has a large overlap region with the NDWFS broad band coverage, were observed.

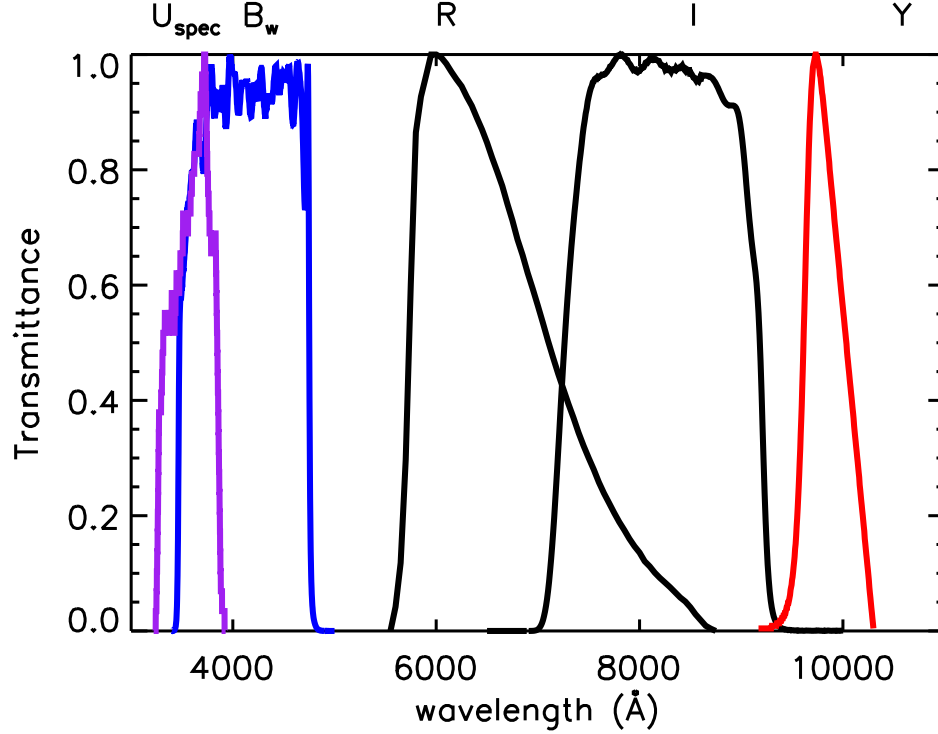


Figure 3.2: Relative transmission curves of the LBC U_{spec} -band (purple curve) and Y -band (red curve). The U_{spec} -band and Y -band filter curves have been corrected by both the CCD Q.E. curve and the atmosphere transmission. This plot also shows the transmission curves of B_w (blue curve), R and I bands in the NDWFS Boötes field. The curves are normalized by the peak transmittance.

this field, with spectra of roughly 17,000 galaxies and 3,000 AGNs down to $I \approx 20$ using the Hectospec instrument mounted on the 6.5 m Multiple Mirror Telescope (MMT).

There are two significant gaps in the optical wavelength coverage in this field: one is between B_w broad band and GALEX NUV, and the other is between I band and J band. To fill these two gaps, we have carried out the LBT Boötes field survey with the LBCs mounted on the 2×8.4 m LBT in binocular mode with U_{spec}

band ($\lambda_0 = 3590\text{\AA}$, FWHM=540 \AA) and Y band ($\lambda_0 = 9840\text{\AA}$, FWHM=420 \AA) imaging. The LBCs are comprised of two wide-field cameras, and each is mounted on one of the LBT prime foci. These two cameras can observe the same sky field simultaneously. The blue channel is optimized for the UV-B bands and the red channel is optimized for the VRIz bands. The CCD quantum efficiencies are $\approx 50\%$ and $\approx 10\%$ in U_{spec} and Y bands, respectively. The CCD pixel size is $0.225''/\text{pixel}$. Each of the camera consists of four $2k \times 4k$ chips, resulting in a $23 \times 23 \text{ arcmin}^2$ field of view (FoV). Because the layout of the CCD is not a square, the total effective FoV is about 470 arcmin^2 .

The primary goal of our survey is to use the unique Y and U_{spec} band data to search for $z \sim 7$ quasars at the epoch of cosmic reionization and $z \sim 3$ Lyman Break Galaxies (LBGs) at the epoch of the peak in star-forming and quasar activity. In this paper, we will focus on the U_{spec} band data to establish a LBG sample and publish the scientific results of the LBG sample.

A total of 81 pointings were designed to cover the entire rectangular region (Figure 3.1), and 63 of them, which have overlap with the NDWFS optical band coverage larger than 50% LBC FoV, were observed. The total survey area is about 8.8 deg^2 . For each individual field, a 1200s exposure time observing block is designed. The total 1200s exposure time is divided into five 240s exposures with $30''$ dither pattern. The dither pattern allows us to fill up the chip gaps, remove cosmic rays and bad pixels, and reduce the effects of the bright stars. The position angles of the neighboring fields in Decl. direction have a 180 degree difference and an $\approx 4' \times 7'$ overlap region, which allows us to compare the calibration with different position angles.

The observations were carried out in dark time from January 2008 to March 2009 in queue observing mode. There are a total 718 U_{spec} band science images ob-

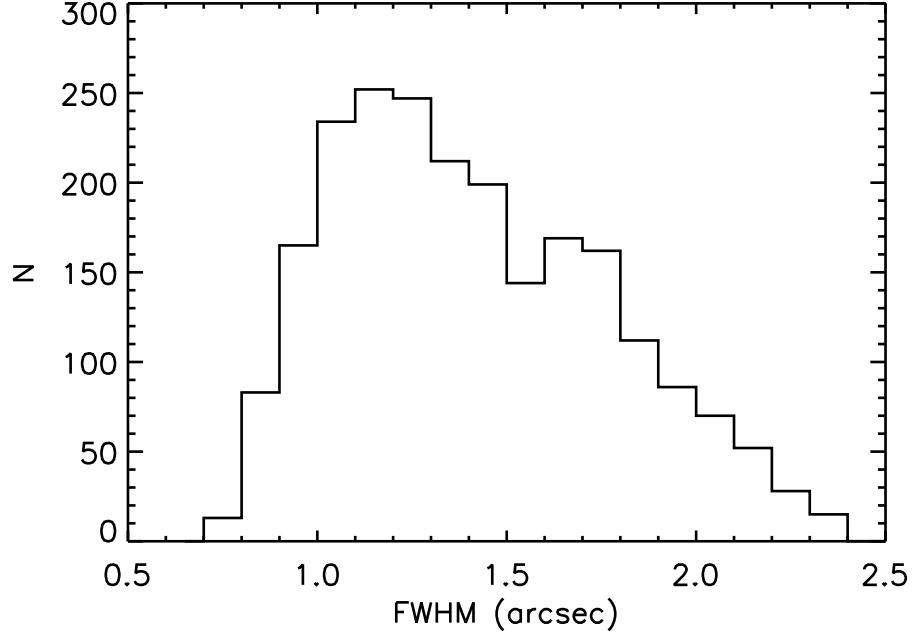


Figure 3.3: Image quality of the U_{spec} band images. The histogram shows the distribution of the FWHMs of each chip of the LBC. The median of FWHM is 1.33/1.25 before/after removing the bad image quality images (FWHM $> 1.8''$)

tained with a total open shutter time of ≈ 47.8 hours. About 30% of the data (222 images) are unusable, in which 20% (151 images) is due to motion of the telescope during the exposure and 10% (71 images) is due to poor image quality (FWHM $> 1.8''$). The median airmass is 1.11 and the median FWHM is $1.25''(1.33'')$ after (before) removing the bad quality images. The final average effective exposure time for each individual field is about 30 minutes.

3.3 Data Reduction

3.3.1 Bias and Flat Correction

All images are inspected by eye to remove elongated images due to tracking and guiding issues during observing before further processing. About 20% of images

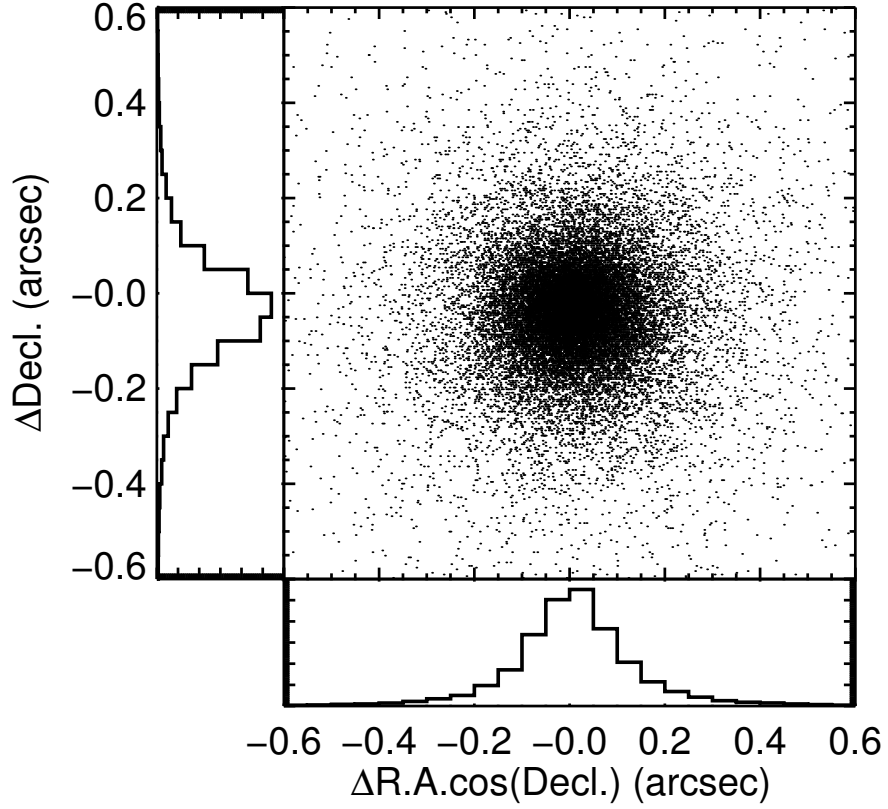


Figure 3.4: Accuracy of the astrometry. The distribution of the difference of $\text{R.A.} \times \cos(\text{Decl.})$ and Decl. between LBC U_{spec} -band images and SDSS images. The FWHMs of both R.A. and Decl. are about $0.2''$, which corresponds to a 1σ uncertainty of $0.08''$ in astrometry.

are removed in this step.

Data are reduced using custom IDL routines. The bias level measured from the overscan region is subtracted from individual bias frame images, which are then combined to construct the master bias frame. Super-sky flats are created by combining the science frames in each observation run, scaling by the mean value with 3σ clipping to remove cosmic rays and objects. Science images are overscan and bias subtracted, and then divided by the super-sky flats to correct the CCD response. Finally, cosmic rays in the images were identified rejected using an identification algorithm based on Laplacian edge detection (van Dokkum, 2001).

3.3.2 Image Quality Measurement

We estimate the FWHM of each scientific frame as follows: (1) A few stars across the field are selected, and the FWHM of the stars is measured using *imexamine* in IRAF¹ as an input for the next step. (2) A catalogue for each field is created by SExtractor (Bertin & Arnouts, 1996) with the parameter of *SEEING_FWHM* set to the value from step 1. All objects with six or more connected pixels with flux 3.0 times greater than the sky noise are detected. Well-detected bright stars ($18.5 < mag_{auto} < 20.0$ and $star_class > 0.95$) are selected from the SExtractor output catalogue. (3) Image coordinates of well-detected bright stars are used as the input information for the FWHM measure task, *psfmeasure*, in IRAF. This task fits the bright stars profile as a Moffat distribution function. The median of FWHMs of the best-fit Moffat profile in each frame is used to represent its image quality.

Figure 3.3 shows the U_{spec} band image quality. Frames with FWHM larger than $1.80''$ were not used for further analysis and co-addition. After removing

¹IRAF is distributed by the National Optical Astronomy Observatories, which are operated by the Association of Universities for Research in Astronomy, Inc., under cooperative agreement with the National Science Foundation.

the bad image quality images ($\text{FWHM} > 1.8''$), the median FWHM is $1.25''$, and the first and third quartiles are $1.07''$ and $1.50''$ respectively.

3.3.3 Astrometric Calibration

The catalogue created by SExtractor in the previous section is used as an input catalogue for SCAMP (Software for Calibrating AstroMetry and Photometry) (Bertin, 2006). To compute the astrometric solution, we use well-detected objects that meet the following criteria: (1) the object is not saturated; (2) the S/N of the object is greater than 10; and (3) the FWHM of the object in the SExtractor output catalog is between $2''$ and $10''$. These well-detected objects from the input catalogue are used to search for matches in the SDSS-DR6 catalogue within a $3''$ radius. We first use a linear model with only an x, y directional offset and without rotations to obtain a rough astrometry solution. Based on this solution, we then use third order polynomials to fit the x, y offset and the rotation to get a refined solution. Using this procedure, an accurate astrometric solution is derived for each field with the 1σ uncertainty less than $0.1''$ in both R.A. and Decl. direction (Figure 3.4).

Previous studies (e.g., Cool, 2007) have shown that there is $\approx 0.3''$ offset between the NDWFS catalog² astrometry and the SDSS astrometry. Thus, we also register the NDWFS B_w , R , and I band images to the SDSS-DR6 catalogues using the same method.

3.3.4 Image Co-addition

Before co-adding images, we subtract sky background from the science frames and generate a weight map for each frame. The background is constructed from the *-object* image created by SExtractor, in which the detected objects have been

²<http://www.noao.edu/noao/noaodeep/DR3/dr3cats.html>

subtracted from the image. First, the *-object* image is divided into ≈ 100 background mesh region with the size of $130 \text{ pixel} \times 130 \text{ pixel}$. Then the median background is computed for each region, and it is fitted by a second order polynomial and subtracted from the science images. The weight map value is computed as follows:

$$w = \frac{1}{\text{FWHM}^2 \sigma^2}, \quad (3.1)$$

where the FWHM is described in section 3.2, and σ^2 is the sky variance.

SWarp (Bertin et al., 2002) is used to co-add frames for each field. First, the input science images and weight maps are re-sampled to a common pixel grid. The interpolation function we used to re-sample images is LANCZOS3, a $\prod_d \text{sinc}(\pi x_d) \text{sinc}(\frac{\pi}{4} x_d)$ response function with $(3 < x_d \leq 3)$. The output co-added image is a weighted average of input values after 3σ clipping:

$$F = \frac{\sum_i w_i f_i}{\sum_i w_i}, \quad (3.2)$$

where w_i is the weight of the pixel from re-sampled weighted map, and f_i is flux value of the pixel from the science image. The output co-added weighted map is the sum of input weights:

$$W = \sum_i w_i. \quad (3.3)$$

Finally, we create exposure maps that the exposure time for each pixel in the co-added images.

3.3.5 Photometric Calibration

The imaging data are calibrated with SDSS data release 7 photometry. The SDSS u band transmission curve is very similar to LBC U_{spec} , with $\lambda_0 = 3540 \text{ \AA}$ and $\text{FWHM} = 570 \text{ \AA}$. Bright stars ($18.0 < u < 19.5$) in the NO. 57 field which was taken in photometric conditions are used to determine an offset between the LBC

Table 3.1: Summary of the U_{spec} , B_{W} and R -band 5σ depth

| Band | λ_0^a | Median Image Quality | Exposure time | depth ^b |
|-------------------|---------------|----------------------|---------------|--------------------|
| | Å | arcsec | second | |
| U_{spec} | 3573 | 1.25 | 1920 | 25.2 |
| B_{W} | 4133 | 1.10 | 8400 | 26.3 |
| R | 6407 | 1.10 | 6000 | 25.3 |

^aThis value is derived from average of A and B components.

^aEffective wavelength

^bDepth for 5σ detection in a $2 \times$ FWHM aperture

U_{spec} -band and SDSS u -band images, and the color term coefficient. We find the color term is very small, about $-0.01 \times (u - g)$. Bright stars ($\text{star_class} > 0.9$ and $\text{magerr}(8'') < 0.02$) in the overlap regions are used to determine the offset of the photometric zeropoint in other fields. These stars are also used to check the magnitude difference between two neighboring fields. As the position angle of the neighboring frame is offset by 180 degrees, this check will give us the upper limit of the magnitude uncertainty from the calibration. The average standard deviation of the difference is ≈ 0.05 , implying the photometric accuracy is ≈ 0.05 . Another way to check the photometric accuracy is to compare magnitudes of stars within the same field observed in different individual exposures; from this check we find the standard deviation is about 0.04. So the U_{spec} -band magnitude uncertainty in the Boötes survey is $\approx 0.04 - 0.05$. The magnitude uncertainty is mainly introduced by the flat field and the non-uniformity of the image quality across the field.

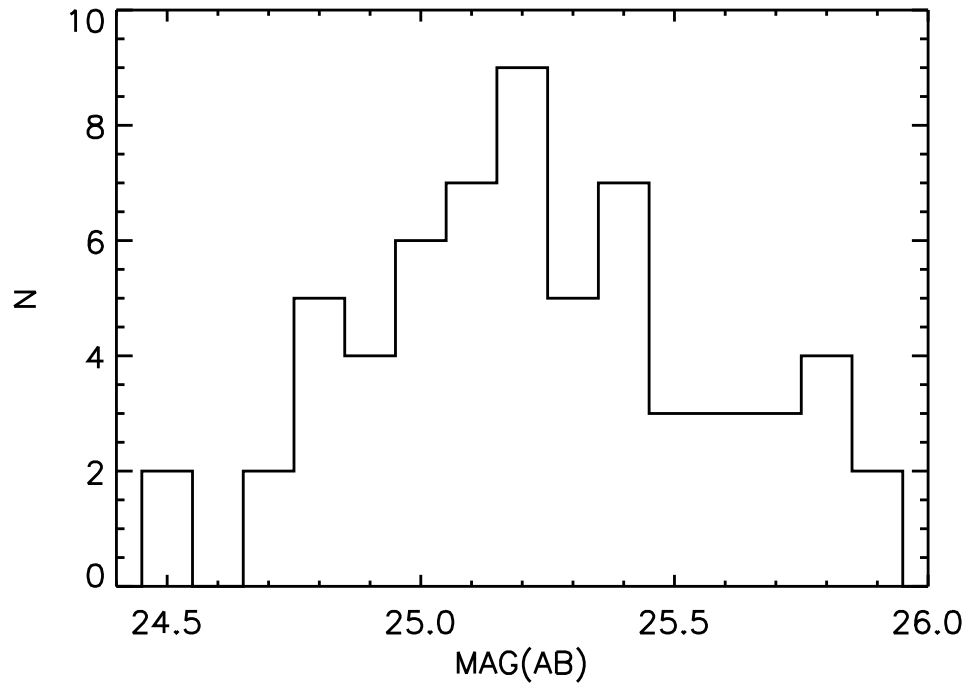


Figure 3.5: Distribution of magnitude with 5σ detection for U_{spec} band. The median depth is 25.2 mag.

3.3.6 Survey Depth

We use the following process to determine the 5σ detection depth in the U_{spec} -band for each field: (1) We generate five frames, each with 6,000 simulated stars with magnitudes between 22.0 and 28.0 added to the image. The Moffat profile with the FWHM value setting to the image quality of each individual field is used to generate the light profile of stars. (2) SExtractor is used to detect and measure the simulated objects in the same manner as for the primary catalogues. The standard deviation between the measured magnitude and input magnitude is calculated in different magnitude bins. For each field, the magnitude bin in which the standard deviation is 0.2 is considered as the magnitude limit with 5σ detection. The median depth is around 25.2 AB magnitude, and the first and third quartiles are 25.0 and 25.4 AB magnitude, respectively. The distribution of the 5σ limit magnitude is shown in Figure 3.5.

In this paper, we also use the B_W , R optical broad band images³ taken by the NOAO/KPNO Mosaic-1 (8K×8K CCD) Wide Field Imager on 4-m Mayall Telescope at Kitt Peak National Observatory (KPNO) covering the entire field. The typical exposure times in these two bands are ≈ 8400 s and ≈ 6000 s, respectively. The median depths are 26.3 and 25.3 AB magnitude for $5\text{-}\sigma$ detection in B and V bands, respectively (see Table 3.1).

3.4 LBG Sample Selection

3.4.1 Photometry

To select Lyman Break Galaxies (LBGs), the crucial step is to find the U -dropout objects. In some cases, the U -dropout objects cannot be directly detected and measured on U -band images, therefore, the NDWFS R -band images are used as

³<ftp://archive.noao.edu/ndwfs/dr3/>

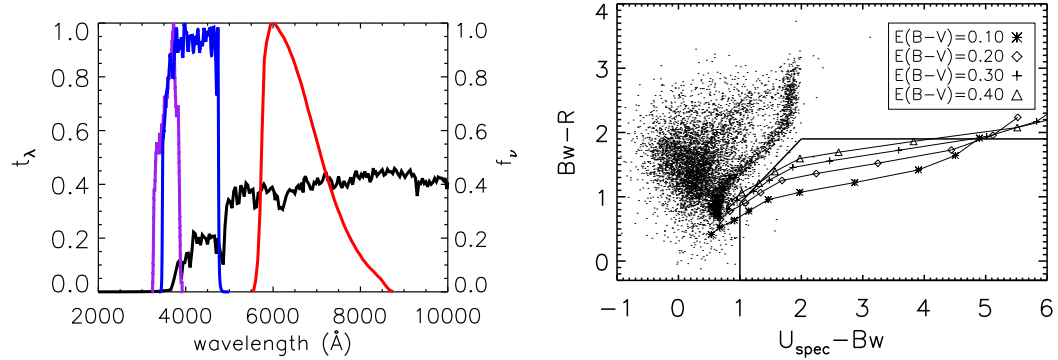


Figure 3.6: Left panel shows the U_{spec} (purple curve), B_W (blue curve), and R (red curve) broad band filters relative transmission curve and the spectrum of a model of 300 Myr old star-forming galaxy with a constant SFR at $z \sim 3$ (black curve). Right panel shows the color evolution of the model galaxy as a function of reddening and redshifts in the $B_W - R$ versus $U_{\text{spec}} - B_W$ diagram. The left-most points are for redshift $z \sim 2.5$. The point step corresponds to intervals of $\delta z = 0.1$. The region circled by the solid line indicated the selection criteria. The dots are the sources that are well detected ($\text{mag_err} < 0.05$) in all three bands, which shows a tight stellar locus.

the detection images in this study.

First, the NDWFS R -band image is mapped using SWarp to the LBT U_{spec} -band image with the same pixel size and image size. Then we run SExtractor in double-image mode with the mapped R -band images as detection images and U_{spec} -band images as measurement images. A source is considered to be detected if the number of connected pixels with flux 0.6 times greater than the sky σ exceeds four pixels after the original images convolved with a 9×9 convolution mask of a gaussian PSF with FWHM = 5.0 pixels in the R -band image. We reduce the NDWFS B_W data in the same manner. The astrometry has been registered to SDSS-DR6 catalogue as discussed in section 3.3.3.

The U_{spec} -band exposure map masks are used as the external flags to obtain the exposure time for each object. Objects with U_{spec} band exposure times less than 720s are ignored. The aperture magnitudes (mag_aper) with aperture size of $2.0 \times \text{FWHM}$ are then used for color selection. The aperture correction is estimated for each field by applying an $8''$ aperture to measure the total flux of bright stars. Then the corrections (i.e. $\Delta\text{mag} = \text{mag_aper}(8'') - \text{mag_aper}(2 \times \text{FWHM})$) – with values are around -0.2 – are used to correct the flux loss due to measurement in relative small apertures. For those U_{spec} non-detected sources, we set the magnitude upper limits as the magnitude with 1σ . Sources from the U_{spec} , B_{W} and R -band catalogues within $1''$ departure are matched together to generate the $U_{\text{spec}} - B_{\text{W}}$ versus $B_{\text{W}} - R$ color-color diagram.

3.4.2 Sample Selection Criteria

To determine the LBG sample selection, the BC03 standard stellar synthesis population model (Bruzual & Charlot, 2003) is used to build a series of spectral templates of star-forming galaxies. We adopt a spectral model with constant star formation rate (SFR), a Salpeter initial mass function (IMF) (Salpeter, 1955), one solar metallicity abundance, and 300 Myrs age to simulate the spectra of star-forming galaxies. This model will give us a typical intrinsic LBG SED (e.g. Steidel et al., 2003)

The templates are modified by the intergalactic medium (IGM) absorption model of Madau (1995) and reddened using the attenuation law of Calzetti et al. (2000) reddening of $E(B - V) = 0.0 - 0.4$. Then the wavelength of the spectra is shifted by the factor of $1 + z$ to derive the spectra in the redshift range from 2.5 to 3.6. Figure 3.6 shows one of the star-forming galaxies template spectra with $E(B - V) = 0.2$ at redshift of $z = 3$, and how the galaxies with given $E(B - V)$ evolve in the $U_{\text{spec}} - B_{\text{W}}$ and $B_{\text{W}} - R$ color-color diagram with redshifts. The

left-most point for each track represents the redshift of $z = 2.5$ and the each step corresponds to a redshift interval 0.1. The lower redshift limit is primarily determined by the $U_{\text{spec}} - B_{\text{W}}$ cut, and the upper redshift limit is mainly determined by the $B_{\text{W}} - R$ cut. We also plot the well detected stars ($> 10\sigma$) in all the three bands in the color-color diagram. It shows a stellar locus, which is well separated with the tracks of the $z \sim 3$ LBGs. To select the LBGs with $2.7 < z < 3.3$ and maintain enough separation from the stellar locus to reduce the contamination rate from stars, the following selection criteria for the $z \sim 3$ LBGs are adopted:

$$\begin{aligned}
 U_{\text{spec}} - B_{\text{W}} &> 1.0, \\
 B_{\text{W}} - R &< 1.9, \\
 B_{\text{W}} - R &< U_{\text{spec}} - B_{\text{W}} + 0.1, \\
 R &< 25.0.
 \end{aligned} \tag{3.4}$$

3.4.3 Selection Function

For a given galaxy, whose intrinsic $U_{\text{spec}} - B_{\text{W}}$ and $B - R$ colors are right in the selection region, the probability to select this galaxy as a LBG is mainly influenced by the uncertainty of the magnitude scattering the intrinsic color-color photometric scatter removing objects from the selection criterion boundary and detection limits. In this paper, the completeness is derived from the selection function, which describes the detection probability ($P(m, z, SED)$) of a LBG spectral template with a given redshift, magnitude and spectral energy distribution (SED) falling within the selection criteria.

The procedures to calculate the LBG selection function are as follows: The spectral templates generated in section 3.4.2 are used to derive the intrinsic color distribution. For galaxies with a constant star formation rate, Salpeter IMF, solar metallicity, and 300 Myr age, as is typical for an LBG SED (e.g., Steidel et al., 2003)

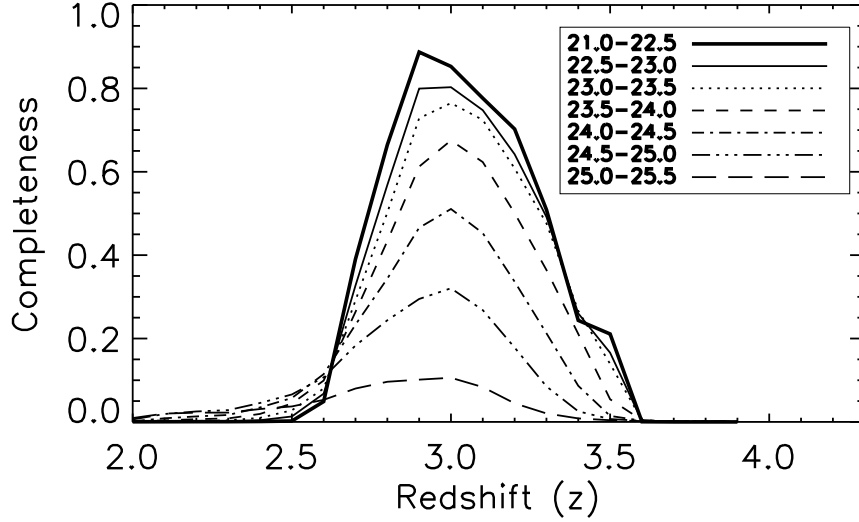


Figure 3.7: Selection completeness as a function of redshift in different R -band magnitude bins.

the SEDs of the galaxies are only influenced by reddening $E(B - V)$. Therefore, in this case, $P(m, z, SED)$ is equivalent to $P(m, z, E(B - V))$. The detection probability is then a function of magnitude, redshift and dust extinction. The $E(B - V)$ distribution of our sample is taken from the results of Reddy et al. (2008) Table 5, which is from -0.1 to 0.4. A series of SEDs are generated with $2.0 < z < 4.0$ ($\Delta z = 0.1$) and $E(B - V)$ from -0.1 to 0.4 ($\Delta E(B - V) = 0.1$). The broad band colors are fixed for a given magnitude, dust extinction and redshift combination. The expected colors of $U_{\text{spec}} - B_W$ and $B_W - R$ for a given redshift and $E(B - V)$ are derived by convolving the spectral template with the filter curves. Ten thousand simulated objects, following expected $U_{\text{spec}} - B_W$ and $B_W - R$ colors, are put on the U_{spec} , B_W , and R images for each R magnitude ($\Delta \text{mag} = 0.5$), redshift ($\Delta z = 0.1$), and $E(B - V)$ ($\Delta E(B - V) = 0.1$) bin, based on their expected noise characteristics on the real images. The size of faint LBGs is compact with $r_e < 0.5''$ (e.g.,

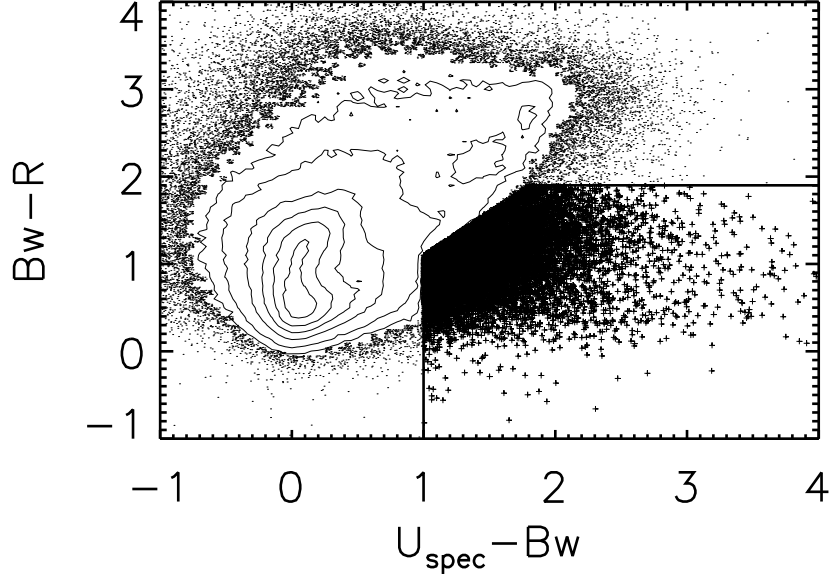


Figure 3.8: $B_W - R$ versus $U_{\text{spec}} - B_W$ color-color diagram. The photometrically-selected LBGs at $z \sim 3$ are selected in the region bounded by the solid line. Total 14,485 photometrically-selected LBGs are selected as U-dropouts. The crosses represent the selected LBG. The reason for the sharp edge at $B_W - R = 1.9$ and $U_{\text{spec}} - B_W = 1.0$ is that we do not plot the U_{spec} band undetected sources without falling in the selection criterion region.

Ferguson et al., 2004), which cannot be resolved in our ground-based images, therefore, we use the Moffat profile to simulate the light distribution of the LBGs. The method of detection and measurement of these simulated objects is the same as that used for our real objects. Then the $P(m, z, E(B - V))$ is derived from the fraction of the simulated objects meeting the selection criteria. By weighting $P(m, z, E(B - V))$ with the distribution of the $E(B - V)$ (Reddy et al., 2008), the selection function, i.e., the LBG detection probability, as a function of redshift for a given magnitude bin is finally determined.

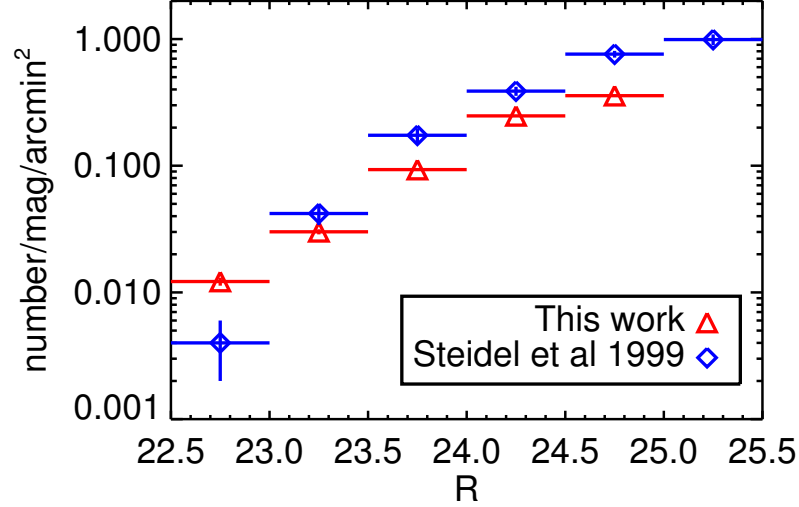


Figure 3.9: Surface density of $z \sim 3$ LBGs as function of R -band magnitude in this work (red triangles) and in Steidel et al. (1999) (blue diamonds).

Figure 3.7 shows the selection function as a function of redshift in different R -band magnitude bins from 21.0 to 25.0. The redshift range is $2.7 < z < 3.3$ with a peak at $z = 2.9$.

3.4.4 A Photometrically-Selected Sample of $z \sim 3$ LBGs

Figure 3.8 shows the distribution of objects from the Boötes field in the $U_{\text{spec}} - B_W$ and $B_W - R$ color-color diagram. The figure shows the distribution of both stars and low redshift galaxies. Since we do not require the object to be well detected (10σ detection) in all three bands as we did in Figure 3.6, the stellar locus and galaxy distribution have greater scattering than those in Figure 3.6, which contributes to the contamination of the LBG sample. Using the above criteria 3.4, a total of 14,485 photometrically-selected LBGs (cross symbol in Figure 3.8) are selected in the 8.8 deg^2 area, leading to a LBG surface density $\Sigma = 0.47 \pm 0.03$ galaxies arcmin^{-2} . This value is smaller than the result, $\Sigma \sim 1.8$ galaxies arcmin^{-2} , in

Steidel et al. (2003), which is 0.5 magnitude deeper than our survey. Figure 3.9 shows that the surface number density of the $z \sim 3$ LBGs in this work is systematically lower than that in Steidel et al. (1999). The low number density is mainly due to the narrower redshift selection function in our sample compared to that in Steidel et al. (1999). Our shallower survey also increases the photometric errors for a given magnitude, which reduces the completeness.

3.5 UV Luminosity Function

In this section, we will measure the rest-frame UV luminosity function of LBGs based on their R -band magnitudes.

3.5.1 Results

The R -band filter ($\lambda_{\text{eff}} = 6407\text{\AA}$) traces the rest-frame UV ($\sim 1700\text{\AA}$) for this LBG sample with a mean redshift of $z \sim 2.9$. The following formula is used to convert apparent R -band AB magnitude (m_R) to the absolute magnitude at rest-frame 1700\AA ($M_{1700\text{\AA}}$)

$$M_{1700\text{\AA}} = m_R - 5 \log_{10}(d_L/10\text{pc}) + 2.5 \log_{10}(1+z) + (m_{1700} - m_{\lambda_{\text{obs}}}/(1+z)), \quad (3.5)$$

where d_L is the luminosity distance in pc and z is the redshift. The second and third terms of the right side are the distance modulus, and the fourth term is the K-correction between rest-frame 1700\AA and the R -band, which is ≈ 0 (Sawicki & Thompson, 2006a). From the simulation in section 3.4.3, the mean redshift of the LBG sample is 2.9, which corresponds to the distance modulus of 45.46.

The luminosity function at rest-frame 1700\AA ($\Phi(M_{1700\text{\AA}})$) and the statistical uncertainty for a given magnitude bin can be computed from:

$$\Phi(M_{1700\text{\AA}}) = \frac{1}{\Delta m} \frac{N(1-f)}{V_{\text{eff}}}, \quad (3.6)$$

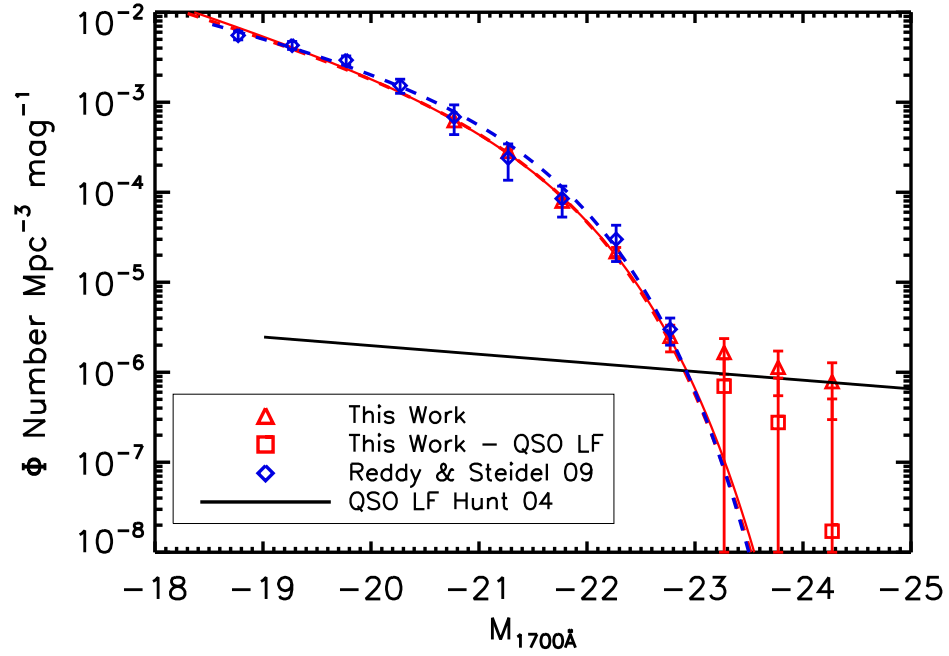


Figure 3.10: Rest-frame UV (1700Å) luminosity function of the $z \sim 3$ LBGs in Boötes field (red triangles) and the best-fit Schechter function (red solid lines). For comparison, the LF of the $z \sim 3$ LBGs in Reddy & Steidel (2009) and best-fit Schechter function are also plotted (blue diamonds and the dashed line) which explores the faint end of the LBGs. The bright end of the LF in this work shows excess compared with the Schechter function. The excess can be explained by the $z \sim$ quasar LF (black solid line) (Hunt et al., 2004). The red squares represent the residue value that quasar LF is subtracted from the LBG LF measurements.

and

$$\Delta\Phi(M_{1700\text{\AA}}) = \frac{1}{\Delta m} \frac{\sqrt{N(1-f)}}{V_{\text{eff}}}, \quad (3.7)$$

where Δm is the magnitude bin size, which is 0.5 in this paper, N is the number of U-dropout LBG candidates falling into the magnitude bin, f is the fraction of the contamination for the magnitude bin. In this paper we do not have any spectral observations of these candidates. Therefore, we adopt the contamination fraction, f , from Table 3 Reddy et al. (2008). The value of f is about 0.7 at the bright end and less than 0.01 at the faint end. We will discuss how this affects our LF measurements later. V_{eff} is the effective comoving volume in units of Mpc^3 .

In a flat universe, the comoving volume per solid angle per redshift can be calculated as

$$\frac{dV}{d\Omega dz} = \frac{cr(z)^2}{H(z)}, \quad (3.8)$$

where $r(z) = \int \frac{cdz}{H(z)}$. The effective comoving volume (V_{eff}) can be converted from the comoving volume,

$$V_{\text{eff}} = \int_{\Delta z} \int_{\Delta m} dz dm P(m, z) \frac{V(z)}{dz dm} \quad (3.9)$$

where $P(m, z)$ is the completeness of the sample as a function of redshift (z) and R -band magnitude (m), which has been determined in section 3.4.3. The effective volume for a given magnitude is computed by integrating from equation 3.9 using the results of the selection function $P(m, z)$. Then the luminosity function is calculated for each magnitude bin.

The red triangles in Figure 5.2 represent the UV LF measurement result of our LBG sample. The UV LF is fitted by the Schechter function:

$$\begin{aligned} \Phi(M_{1700\text{\AA}})dM(1700\text{\AA}) = \\ \frac{2}{5} \Phi^* \ln(10) [10^{\frac{2}{5}(M^*-M)}]^{\alpha+1} \exp[-10^{\frac{2}{5}(M^*-M)}] dM, \end{aligned} \quad (3.10)$$

and the best fit parameters for the Schechter function are $\Phi^* = (1.06 \pm 0.02) \times 10^{-3} \text{ Mpc}^{-3}$, $M^* = -21.11 \pm 0.08$, and $\alpha = -1.94 \pm 0.10$. For the LF fitting, we do not use the LF in the magnitude bin brighter than $M_{1700\text{\AA}} = -23$, as they are significantly overestimated due to contamination by quasars. The survey depth of Boötes field is only about 0.5 magnitude fainter than M^* , thus this data cannot be used to constrain the faint end slope of LF very well. Therefore, we combined our data with data at $M(1700\text{\AA}) > -20.5$ from Reddy & Steidel (2009) to fit the Schechter function (3.10). We find that the best fit parameters are $\Phi^* = (1.12 \pm 0.01) \times 10^{-3} \text{ Mpc}^{-3}$, $M^* = -21.08 \pm 0.05$, and $\alpha = -1.90 \pm 0.05$. Combining the LF measurements from different datasets could bring significant systematic errors on the LF fitting due to the quite different filter sets and selection criteria. We compared the LF measurements in this work and those in Reddy & Steidel (2009) at the overlapping absolute magnitude range of $-23 < M(1700\text{\AA}) < -20.5$. They are consistent with each other within 1σ .

3.5.2 UV Luminosity Density

The UV luminosity density from integrating the Schechter function for a faint luminosity limit is given by:

$$\rho_{L_{\text{UV}}} = [\Gamma(\alpha + 2) - \gamma(\alpha + 2, L_{\text{lim}}/L^*)]\Phi^*L^*, \quad (3.11)$$

where $\Gamma(x) = \int_0^{+\infty} e^{-t} t^{x-1} dt$, and $\gamma(x, l) = \int_0^l e^{-t} t^{x-1} dt$. To compare with previous results (e.g., Sawicki & Thompson, 2006b, and references therein), the faint luminosity limit is set as $0.1L^*$. The luminosity density at 1700\AA can be computed from

$$L_{1700\text{\AA}} = \frac{4\pi d_L^2}{1+z} 10^{-\frac{2}{5}(48.6+m_R)}. \quad (3.12)$$

The characteristic luminosity density, $L_{1700\text{\AA}}^* = 1.2 \times 10^{29} \text{ erg s}^{-1} \text{ Hz}^{-1}$ based on our best Schechter fit. Both the LF measured by this work and LF measured by

Table 3.2: Schechter Parameters of UV LFs and Luminosity Densities

| redshift | α | $M^*(1700\text{\AA})$ | $\Phi^* (\times 10^{-3})$ Mpc $^{-3}$ | $\rho_{L_{\text{UV}}} (\times 10^{26})$ erg s $^{-1}$ Hz $^{-1}$ Mpc $^{-3}$ | ref |
|-----------------|-------------------------|--------------------------|------------------------------------------|---------------------------------------------------------------------------------|------------------------------------|
| $2.7 < z < 3.3$ | -1.94 ± 0.10 | -21.11 ± 0.08 | 1.06 ± 0.06 | 2.19 ± 0.08 | this work |
| $2.7 < z < 3.3$ | -1.90 ± 0.05 | -21.08 ± 0.05 | 1.12 ± 0.01 | 2.18 ± 0.05 | this work + Reddy & Steidel (2009) |
| $2.7 < z < 3.4$ | -1.73 ± 0.13 | -20.97 ± 0.14 | 1.71 ± 0.53 | 2.55 ± 0.25 | Reddy & Steidel (2009) |
| $3.0 < z < 3.4$ | -0.83 | -20.69 | 1.54 | 1.15 | Shim et al. 2007 |
| $2.7 < z < 3.3$ | $-1.43^{+0.17}_{-0.09}$ | $-20.90^{+0.22}_{-0.14}$ | $1.70^{+0.59}_{-0.25}$ | 1.81 ± 0.04 | Sawicki & Thompson 2006a,b |

combining this work and the faint-end data points from Reddy & Steidel (2009) are used to compute the UV luminosity densities. The total UV luminosity densities derived from these two measurements are consistent with each other, which are $2.19 \pm 0.08 \times 10^{26} \text{ erg s}^{-1} \text{ Hz}^{-1} \text{ Mpc}^{-3}$ and $2.18 \pm 0.05 \times 10^{26} \text{ erg s}^{-1} \text{ Hz}^{-1} \text{ Mpc}^{-3}$, respectively. In Table 2, we summarize the results of LF measurements and the total UV luminosity densities from this work, Reddy & Steidel (2009), Shim et al. (2007), Sawicki & Thompson (2006a,b). We find that our UV luminosity density results agree with that from Reddy & Steidel (2009) within the 1σ uncertainty, but are significantly larger than that from Sawicki & Thompson (2006a,b) (by about 6σ) and from Shim et al. (2007). This discrepancy is mainly due to the different faint-end slopes estimated. Compared to the results from Sawicki & Thompson (2006a,b) and Shim et al. (2007), this work and Reddy & Steidel (2009) shows a much steeper faint-end slope of UV LF (table 2), and the faint LBGs make a significant contribution to the UV luminosity density.

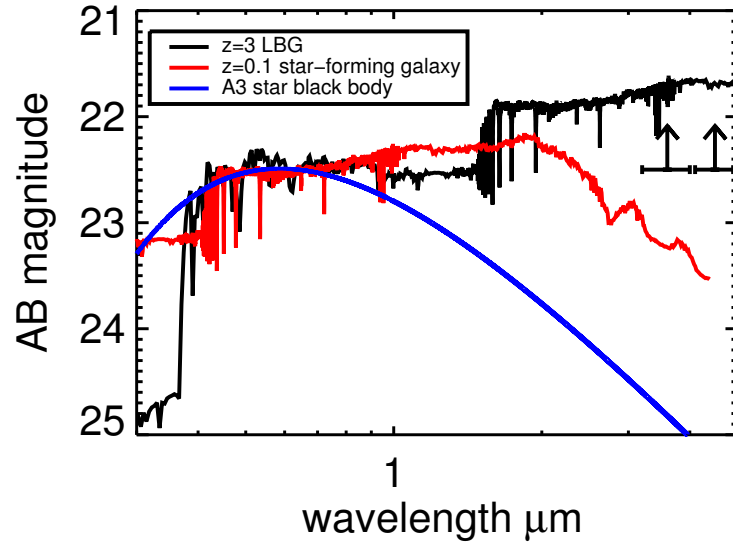
3.5.3 Systematic uncertainties of LF measurement

The following effects are considered for their impact on the LF measurements, especially in term of the possibility of introducing systematic errors:

- Contamination fraction: For the LF measurement, we use the fraction of the low redshift interlopers from Reddy et al. (2008), in which the spectroscopically confirmed sample is used to constrain the contamination rate in each magnitude bin. At the faint end, the fraction approaches to zero, while it is about 70% at the bright end. The reason why the contamination rate is low at the faint end is that (1) Galactic type A stars are not as faint as $R = 25$; and (2) the LF of low redshift galaxies ($z \sim 0.1$) becomes flat at the faint end and the survey volume at $z \sim 3$ is about two orders of magnitude higher than that at $z \sim 0.1$.

We use *Spitzer* IRAC photometry to estimate the bright-end contamination rate of the low redshift interlopers. The majority of the interlopers are A type stars and star-forming galaxies at $z \sim 1$. Figure 3.11 shows the observed-frame model SED of $z \sim 3$ LBGs and those two types of interlopers at the wavelength range between 3000\AA to $5\mu\text{m}$, which suggests that the interlopers, both A type stars and high redshift galaxies, are expected to have bluer $R - [3.6]$ and $[3.6] - [4.5]$ colors than $z \sim 3$ LBGs. We use the $R - [3.6]$ and $[3.6] - [4.5]$ colors to estimate the contamination rate of galaxy candidates in the R -band magnitude range between 22.0 and 22.5. The magnitude limit in $[3.6]$ band is about 22.5 AB (5σ). As shown in Figure 3.11, the bright $z \sim 3$ LBGs should have firm detections in both $[3.6]$ and $[4.5]$ bands (e.g., Bian et al., 2012), while either A type stars or low redshift galaxies cannot be detected in $[3.6]$ and $[4.5]$ bands. There are about 360 LBG candidates in the R -band magnitude range between 22.0 and 22.5; among them, about 110 candidates have both $[3.6]$ and $[4.5]$ detections and with $[3.6] - [4.5] > 0.0$. The latter color cut will exclude most of the galaxies/AGNs lower than $z \sim 1.5$ (e.g., Donley et al., 2008). Our follow-up spectroscopic observations have shown this color cut is very robust in rejecting contamination from low redshift interlopers (Bian et al. 2012 in preparation). This result indicates that the contamination rate of low redshift interlopers in the bright LBG candidates is indeed about 70%. We cannot distinguish AGNs/quasars from LBGs at $z \sim 3$ using $[5.8] - [8.0]$ color (Lacy et al., 2004; Stern et al., 2005; Donley et al., 2008) due to the shallow $[5.8]$ and $[8.0]$ imaging data.

- Redshift distribution: When we calculate the luminosity of LBGs, all LBGs are assumed at the same redshift ($z = 2.9$) rather than with a redshift dis-



[h]

Figure 3.11: Model spectra of $z \sim 3$ LBGs and low redshift interlopers: $z = 1.1$ star-forming galaxy and an A type star. All the spectra are scaled to the $R = 22.5$. The two upward arrows represent the 5σ flux limits of the [3.6] and [4.5] band in Boötes field.

tribution. The FWHM of the redshift distribution (Figure 3.7) is about 0.6 ($2.7 < z < 3.3$), which scatters the LBGs from a given absolute magnitude bin into neighboring magnitude bins. There are more LBGs in the fainter magnitude bin, introducing a bias, especially at the bright end. To estimate the influence of this effect, we conduct a Monte Carlo (MC) simulation. We focus on the 22.0-22.5, 22.5-23.0 and 23.0-23.5 magnitude bins. Each magnitude bin is divided into 10 sub magnitude bins. The number of the galaxies is generated for each sub-bin following the Schechter function (equation 3.10), and the magnitude scattering is mainly due to the redshift distribution in Figure 3.7. The final number of galaxies in the 22.5-23.0 magnitude bin is compared the initial number of galaxies falling into this magnitude bin, and we find that the LF for 22.5-23.0 magnitude bin can be overestimated by $\sim 18\%$ due to this effect. For comparison, the statistical error of this magnitude bin is 7%.

- Galaxy spectral template model: The effective comoving volume calculation depends on the galaxy spectral template. The spectral template used in our simulation is a spectrum of an idealized galaxy with a 300 Myrs old stellar population and a constant star formation rate, solar metallicity and Salpeter IMF, and the $E(B-V)$ distribution is from the Reddy et al. (2008). All these parameters can affect the value of V_{eff} . We perform a MC simulation to estimate the effective comoving volume with different ages (from 100 Myr to 1 Gyr) and find that the effective comoving volumes change less than 5% due to the ages, which is consistent with the results in Sawicki & Thompson (2006a). Another factor that introduces uncertainty is the distribution of $E(B-V)$. We allow the fraction of the LBGs in each $E(B-V)$ to vary by 20% and perform a MC simulation and find that the uncertainty of LF

caused by the $E(B - V)$ uncertainty is less than 10%. The spectral template does not include the Lyman α emission/absorption, which could also influence our results. In the redshift range that the selection criteria are sensitive to, the Ly α line falls into the B_W -band filter. For a LBG with observed-frame Ly α equivalent width of 50 Å, the real intrinsic $U_{\text{spec}} - B_W / B_W - R$ color will be 0.05 magnitude redder/bluer than that in our simulation, which will make galaxies at lower redshift fall into the selection criterion, but the difference is much smaller than a typical uncertainty of U_{spec} -band magnitude (≈ 0.5) and B_W -band magnitude (≈ 0.1). This effect will influence the effective volume estimation by less than 3%. Therefore, either the galaxy age of the template spectra or the Ly α emission/absorption line does not make a large effect on selection function.

- Cosmic variance: Cosmic variance is another possible source of systematic uncertainty for the LF measurement due to the limited survey volume and the fluctuations of the dark matter density on large scales. Using the cosmic variance calculator⁴ (Trenti & Stiavelli, 2008), we find that the cosmic variance for Boötes field is about 4% for the minimum halo mass of $8 \times 10^{11} M_\odot h^{-1}$. For a comparison, the cosmic variance in one deg² area is 9% for the minimum halo mass of $8 \times 10^{11} M_\odot h^{-1}$. Cosmic variance dominates the uncertainty of the LF at the bright end compared to Poisson errors.

We conclude that the greatest degree of uncertainty in the LF measurement comes from the contamination fraction; all other factors combined will contribute $\leq 30\%$ uncertainty to the LF measurement.

⁴<http://casa.colorado.edu/~trenti/CosmicVariance.html>

3.5.4 Discussion

The large survey field also allows us to select a sizable sample of luminous LBGs with $-23 > M_{1700\text{\AA}} > -25$ ($L > 6L^*$); probing the UV LF in this range for the first time. Our measurement (the brightest three points) shows an excess power compared to the Schechter function fit. This excess power can be partially explained by the LF of $z \sim 3$ quasars (Hunt et al., 2004). We subtract the quasar LF value from these three points to statistically remove the quasar contribution. The three red squares present the residual values, which are still higher than the best-fit Schechter function. It is worth noting that the degree of the uncertainty of the quasar LF measurements from Hunt et al. (2004) due to the small size of the faint quasar sample, therefore, the excess power of the LBG LF can be within the uncertainty of the quasar LF measurements. If the excess is real, it can be caused by the lens effect which boosts the fainter LBGs to the bright end (e.g., Jain & Lima, 2011). It is also possible that the LF of LBGs actually shows excess power at the very luminous end. The similar excess power at the bright end ($L > 2L^*$) of UV LF has been found in $z \sim 7 - 8$ LBGs sample (e.g., Yan et al., 2011a,b). The bright end cutoff of UV LF is regulated by feedback process and dust obscuration (e.g., Lacey et al., 2011). If the excess power is real, that would suggest that those physical mechanisms are probably not efficient in these most UV luminous LBGs. To have an accurate measurements of the bright end LF, follow-up spectroscopic observations for the bright end of the LBGs are required (Bian et al. 2012, in preparation).

3.6 Near-IR Luminosity Function

The *Spitzer* Deep-Field Survey (Ashby et al., 2009) covers the whole 9 deg^2 ND-WFS Boötes field with IRAC four bands at the wavelength of $3.6 \mu\text{m}$, $4.5 \mu\text{m}$,

5.8 μm , and 8.0 μm , respectively. There are to 4 epochs in the survey with a total exposure time of 12×30 s. In this paper, we use the IRAC2 (4.5 μm , [4.5]) band to probe the rest-frame near-IR emission of LBGs at $z \sim 3$. The advantages of the [4.5] band are: (1) this band is less influenced by the AGN power-law component than [5.8] and [8.0] bands; (2) the rest-frame wavelength of [4.5] at $z \sim 3$ is at 1.1 μm (J -band at $z \sim 0$), which probes the evolved stellar population and is not affected by strong emission lines that bias the rest-frame near-IR continuum measurements. The rest-frame near-IR LF is derived based on the UV LF and the relation between the R -band magnitude and the $R - [4.5]$ color in the LBGs at $z \sim 3$. We follow the method developed by Shapley et al. (2001), who estimated the K -band (rest-frame V-band) LF of LBGs at $z \sim 3$ based on their UV LF and UV-optical colors.

3.6.1 The Rest-frame UV/Near-IR Color Relation of LBGs

We carry out photometry on the [4.5] band images with SExtractor using the parameters from the table 2 in Ashby et al. (2009), except that a lower detection threshold ($DETECT_THRESH = 1.0$) is used to detect fainter sources. We use the 4'' aperture magnitude as the output magnitude. We first apply the aperture correction on the magnitude and then covert Vega magnitude to AB magnitude. The limit magnitude is 23.4 AB in 2.5σ . Finally, the positions of sources are matched with the LBG positions.

The distribution of R -band magnitude versus $R - [4.5]$ color is shown in Figure 3.12. The solid line represents the magnitude limit of the [4.5] band. As there are only upper limits of $R - [4.5]$ color in a large fraction of LBGs, survival analysis methods in *stsdas.analysis.statistics* package of IRAF are used to study the correlation between R and $R - [4.5]$ color. We find that the slope, $\Delta(R - [4.5])/\Delta R$, is 0.22. The probability of correlation between R and $R - [4.5]$ color is greater than

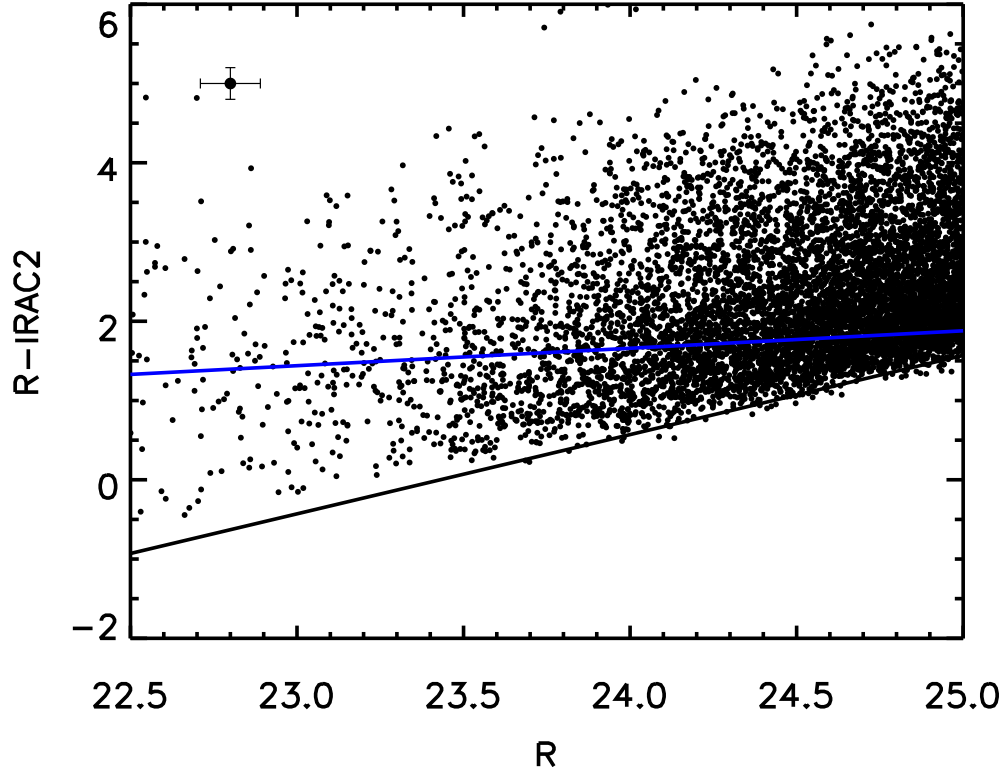


Figure 3.12: Relation between R magnitude and $R - [4.5]$ color. The black solid line shows the typical magnitude limits of the $[4.5]$ band, and the blue solid line represents the best-fitted linear regression line with survival analysis method. The error bar represents typical errors for R -band magnitude and $R - [4.5]$ color.

99.98%.

3.6.2 Results

We estimate the near-IR LF using simulated galaxy colors based on the UV LF measurements and the rest-frame UV/near-IR color relation, following Shapley et al. (2001) : (1) we generate 100,000 galaxies with R -band magnitude range from 22.5 to 27.0. The distribution of the R -band magnitudes follows the distribution of UV LF in section 3.5.1. (2) We derive the distribution of $R - [4.5]$ in the

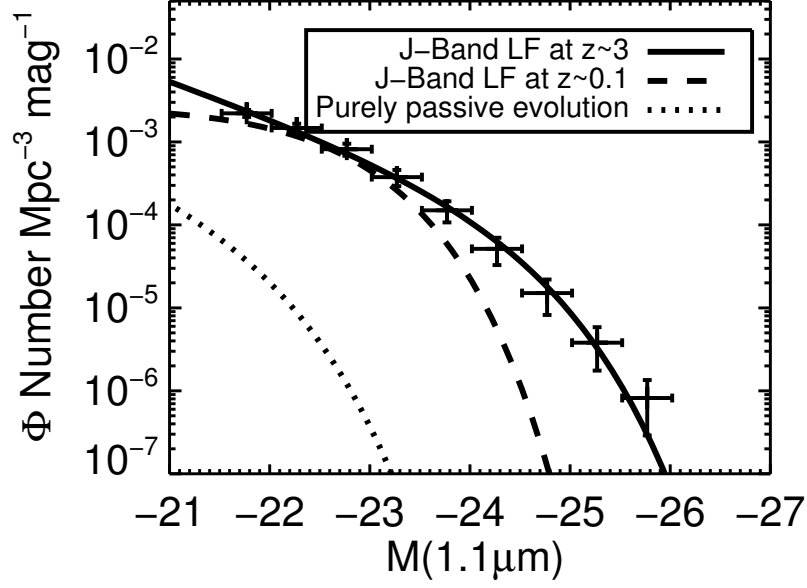


Figure 3.13: $z \sim 3$ LBG LF of [4.5] band (rest-frame J -band) The solid line represents the best-fit Schechter function for the [4.5] band (rest-frame $1.1\mu\text{m}$) LF, and the dashed line represents the J -band LF for the galaxy in the local universe. The dotted line is the predicted J -band LF at $z \sim 0.1$ if we assume a purely passive evolution in these galaxies from $z \sim 3$.

$23.4 < R < 23.5$ magnitude bin. In this magnitude bin, the [4.5] band detection rate is about 75%, and quasar/AGN contamination rate is low. We assume the $R - [4.5]$ distribution follows a Gaussian distribution. At $R \approx 23.5$, the $R - [4.5]$ color distribution is truncated at $R - [4.5] \approx 0$ due to the detection limit of [4.5] band. Therefore, we only use galaxies with $R - [4.5]$ color values in the range between 0 and 4 to fit the Gaussian function. (3) We generate 100,000 $R - [4.5]$ colors that follows the Gaussian distribution function derived in step(2). For each $R - [4.5]$ value, an offset ($\Delta(R - [4.5])$) is applied based on its R -band magnitude, $\Delta(R - [4.5]) = 0.22(R - 23.45)$, to get the final relation between R -band magnitude

and [4.5] magnitude for each galaxy. Using this method, the [4.5] magnitudes for a sample of 100,000 galaxies are generated based on their R -band magnitude and the relation between R magnitude and $R - [4.5]$ color, and the [4.5] band luminosity function are derived. (4) We use the MC simulation to estimate the uncertainty of the near-IR LF. 10,000 simulated UV LFs are generated based on the uncertainty of UV LF measurements in section 3.5.1. The same procedure as above is used to transfer the R -band magnitude to the [4.5] magnitude in $z \sim 3$ LBGs. When we use the R -band magnitudes to calculate the [4.5] magnitudes, the uncertainties, including the R -band and [4.5] band photometric error, the uncertainty slope between R and $R - [4.5]$ color, and the uncertainty of Gaussian distribution of the $R - [4.5]$ color for the given R magnitude range, are also considered. Finally, total 100,000 simulated near-IR LFs are derived. The standard deviations of the 10,000 near-IR LFs in each magnitude bin are considered as the uncertainties of the near-IR LF. (5) We fit the [4.5] band (rest-frame $1.1\mu\text{m}$) LF with a Schechter function (Figure 3.13) and find that the best-fit Schechter function parameters for the rest-frame $1.1\mu\text{m}$ LF of $z \sim 3$ LBGs are $\phi_J^* = (3.1 \pm 1.9) \times 10^{-4} \text{ Mpc}^{-3}$, $M_J^* = -24.00 \pm 0.30$, and $\alpha_J = -2.00 \pm 0.17$.

3.6.3 Discussion

To compare the rest-frame $1.1\mu\text{m}$ LF of $z \sim 3$ LBGs to the J -band LF of nearby galaxies, the J -band LF of nearby galaxies at $z \sim 0.1$ is shown in Figure 3.13 (Cole et al., 2001). The best-fit Schechter function parameters for nearby galaxies are $\phi_J^* = (3.57 \pm 0.36) \times 10^{-3} \text{ Mpc}^{-3}$, $M_J^* = -23.13 \pm 0.02$, and $\alpha_J = -0.93 \pm 0.04$. The rest-frame J -band LFs show significant evolution from $z = 3$ to $z \sim 0.1$. Compared to the local LF, the rest-frame J -band LF at $z \sim 3$ has smaller ϕ_J^* by an order of magnitude, a steeper faint-end slope (α), and brighter characteristic luminosity (M_J^*) by ≈ 1.0 magnitude.

These trends are also found in the rest-frame optical (V -band) LF between $z \sim 3$ and $z \sim 0$ (Shapley et al., 2001). The steep faint-end slope of rest-frame near-IR LF is mainly due to the steep faint-end slope of the rest-frame UV LF and the positive correlation between R magnitude and $R - [4.5]$ color. A similarly steep faint-end slope ($\alpha = -1.85 \pm 0.15$) is also found in optical (V -band) LF of LBG at $z \sim 3$ (Shapley et al., 2001), which is consistent within the errors of our near-IR faint-end slope, and the optical LF in Shapley et al. (2001) is derived based on a UV faint-end slope of $\alpha \sim -1.57$. If the authors adopt a much steeper UV faint-end slope, such as that in Reddy & Steidel (2009) and this work, the faint-end slope of optical LF will get even steeper. One of the caveats of the rest-frame near-IR LF derived in this work is that the IRAC depth of LBG sample is shallow. We obtain the $R - [4.5]$ color distribution based on a bright magnitude bin and assume that this distribution does not change in the fainter magnitude bins, therefore, it is unclear whether the $R - [4.5]$ color distribution and the positive slope between R magnitude and $R - [4.5]$ color will still be held at the faint end of the LBGs.

To derive the rest-frame J -band luminosity density of LBG at $z \sim 3$, we integrate the Schechter function to a faint luminosity limit, $0.1 L^*$, which is about the magnitude limit of the $[4.5]$ band images and find $\log_{10} \rho_J$ ($\text{erg s}^{-1} \text{Hz}^{-1}$) $= 27.04^{+0.09}_{-0.11}$.

We consider a simple purely passive-evolving model for the evolution of the near-IR LF. Using BC03 model, we generate SEDs of galaxies with a constant star formation history of 300 Myr, which is about typical age of LBGs at $z \sim 3$ (Shapley et al., 2001), then we shut down the star formation in the galaxies and make these galaxies passively evolve in the following 11.0 Gyr, from $z \sim 3$ and $z \sim 0.1$. We find that the absolute J -band magnitude (after reddening with $E(B - V) = 0.15$)

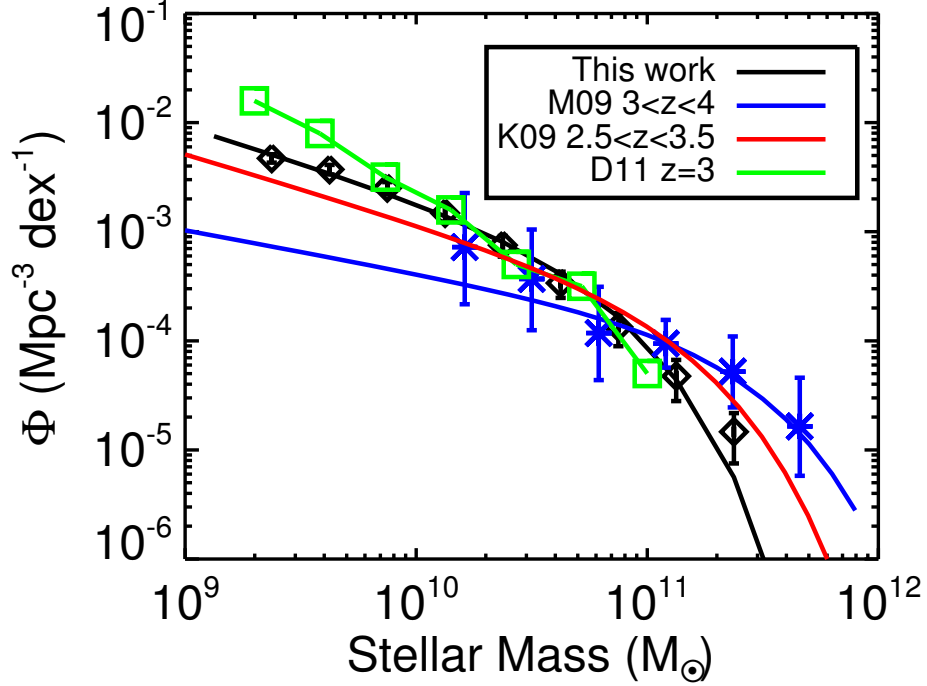


Figure 3.14: Stellar mass functions of $z \sim 3$ LBGs from this work (black solid line), and K-selected galaxies (Kajisawa et al., 2009; Marchesini et al., 2009, K09, red curve, M09, blue curve). The green curve represents the $z \sim 3$ stellar mass function derived from cosmological simulations with momentum-conserved wind feedback model (Davé et al., 2011, D11).

at $z \sim 3$ right after shutting down star formation is about 2.7 magnitudes brighter than that at $z \sim 0$. In Figure 3.13, the dotted curve represents the predicted local near-IR LF based on this purely passive evolution model.

3.6.4 Stellar mass function

Since the near-IR is a good tracer of the old and evolved stellar population, the rest-frame Near-IR LF can be used to derive the stellar mass function (SMF) of LBGs at $z \sim 3$. We adopt the relation between the rest-frame $1.1\mu\text{m}$ absolute

magnitude and the stellar mass in Reddy et al. (2012):

$$\log(M_{\text{stellar}}/M_{\odot}) = -(0.56 \pm 0.09)M_{1.1} - (2.42 \pm 1.94), \quad (3.13)$$

in which the mass-to-light ratio decreases with increasing $1.1\mu\text{m}$ magnitude.

Using this relation, the faint-end slope of stellar mass function will be flatter compared to that of the rest-frame J -band LF. In Figure 3.14, we show the stellar mass function and best-fit Schechter function of LBGs at $z \sim 3$. The best-fit parameters are $\phi^* = (2.8 \pm 1.1) \times 10^{-4} \text{ Mpc}^{-3}$, $\log_{10} M_{\text{stellar}}^*(M_{\odot}) = 10.78 \pm 0.11$, and $\alpha = -1.65 \pm 0.09$. The large survey area allows us to reduce cosmic variance, which contributes significant uncertainty on the previous SMF measurements (e.g. Marchesini et al., 2009). In Figure 3.14, we also show the SMFs derived from $z \sim 3$ K -selected (mass-selected) galaxy sample in deep field surveys (Marchesini et al., 2009; Kajisawa et al., 2009) and the galaxy SMF at $z \sim 3$ predicted by cosmological hydrodynamic simulations (Davé et al., 2011). For comparison, we scale the galaxy stellar mass derived based on different IMFs to the mass based on a Kroupa IMF (Kroupa, 2001). The K -selected galaxy sample in Marchesini et al. (2009) is selected from about 400 arcmin^2 , which is about 4 times larger than that in Kajisawa et al. (2009); on the other hand, the survey depth in Kajisawa et al. (2009) is about 1-2 magnitudes deeper than that in Marchesini et al. (2009). Therefore, Marchesini et al. (2009) put stronger constraints on SMF at the massive end, while Kajisawa et al. (2009) measure the low mass end of SMF more accurately.

At the high mass end, the M_{stellar}^* in LBG sample is smaller than those in the K -selected galaxy samples (Marchesini et al., 2009; Kajisawa et al., 2009) at a 2σ significant level, indicating a lower characteristic mass in the LBGs. For galaxies with stellar mass greater than $10^{11} M_{\odot}$, the density of LBGs is significantly smaller than that of mass selected galaxies, especially for the sample from Marchesini

et al. (2009). We find that the ratio of stellar mass density between this work and Marchesini et al. (2009)/Kajisawa et al. (2009) is $0.26^{+0.20}_{-0.15}/0.38^{+0.62}_{-0.26}$ at the stellar mass range of 10^{11} – $10^{12} M_{\odot}$, which suggests that LBGs are not the dominant galaxy population at the high mass end of galaxy SMF at $z \sim 3$. LBGs are selected based on the rest-frame UV colors, therefore, this method cannot select the highly obscured galaxies or passively evolving early type galaxies. van Dokkum et al. (2006) study a sample of massive mass-selected galaxies ($M_{\text{stellar}} > 10^{11} M_{\odot}$) and find that the LBGs only makes up 20% of the sample, and the rest of the sample are distant red galaxies (Franx et al., 2003).

At the low mass end, the SMF shows somewhat steeper low mass end slope, although this difference is statistically insignificant. The value of the slope agrees with that in Marchesini et al. (2009) ($\alpha = -1.39^{+0.63}_{-0.55}$) and Kajisawa et al. (2009) ($\alpha = -1.63^{+0.14}_{-0.15}$) within 1σ error. This suggests that the LBG population dominates the low mass end of the galaxy SMF at $z \sim 3$. This steep slope also suggests that the UV-selected star-forming galaxies make significant contributions to the total stellar mass density (e.g., Kajisawa et al., 2009; Reddy & Steidel, 2009). By integrating the LBG SMF, we find the stellar mass density of $z \sim 3$ LBGs with stellar mass between 10^8 – $10^{10} M_{\odot}$ to be $51 \pm 4\%$ of the total $z \sim 3$ LBG stellar mass density, which agrees with the result in Reddy & Steidel (2009).

At the mass range between $10^{9.5}$ and $10^{11} M_{\odot}$, the SMF of LBGs is consistent with that derived from cosmological hydrodynamic simulations (Davé et al., 2011). In this type of simulation, stellar mass is regulated by momentum-driven winds (Murray et al., 2005a) and recycled wind mode accretions (Oppenheimer et al., 2010). At the low mass end, the model overproduces the number of the galaxies, showing a steeper low mass end slope with $\alpha = -2.0$. On the other hand, the SMF at the massive end predicted by the model is consistent with that

of LBGs, but is smaller than that in mass selected galaxies; this may reflect the finite simulation volume that under-predicts the massive galaxy population.

3.7 The Evolution of UV LF and SMF

We compare our $z \sim 3$ UV LF and SMF results with those from other high redshift LBG ($z > 4$) studies (Bouwens et al., 2007; Lee et al., 2012) to study the evolution of UV LF and SMF with cosmic time. Figures 3.15 shows how the best-fit Schechter function parameters, including dust corrected $M_{\text{UV}}^*/M_{\text{stellar}}^*$ evolve with redshift, ϕ^* , and α , in UV LF and SMF. For the UV LF evolution, the black open triangle at $z \sim 3$ is from this work. The LF measurements in LBG at $z \sim 4$, $z \sim 5$, and $z \sim 6$ are from Bouwens et al. (2007), and the data point at $z \sim 7$ is from Bouwens et al. (2011b). In the plot, we use the dust corrected M_{UV}^* ($M_{\text{UV},\text{cor}}^*$) rather than observed M_{UV}^* , as the dust corrected M_{UV}^* can be used to represent the SFRs in the galaxies. Bouwens et al. (2009, 2012) measure the UV-continuum slope, which is a direct indicator of the dust extinction in LBGs from $z \sim 3$ to $z \sim 7$. We adopt their UV slope measurements and the relation between the UV-continuum slope (β) and the UV dust extinction (A_{UV}) (Meurer et al., 1999) to correct the M_{UV}^* at different redshifts. For the evolution plot of SMF, the black triangle is from this work and the two red diamonds at $z \sim 4$ and $z \sim 5$ are from Lee et al. (2012). In both UV LF and SMF, the parameters, α and ϕ^* , are roughly constant with redshift. On the other hand, the characteristic luminosity and mass, $M_{\text{UV},\text{cor}}^*$ in UV LF and M_{stellar}^* in SMF, increase with cosmic time. The evolutionary trend provide crucial information on how the galaxies built up their mass in the early universe. Here we will use two simple toy models to interpret the evolution of UV LF.

In the first model, we assume that the increasing $M_{\text{UV},\text{cor}}^*/M_{\text{stellar}}^*$ is mainly

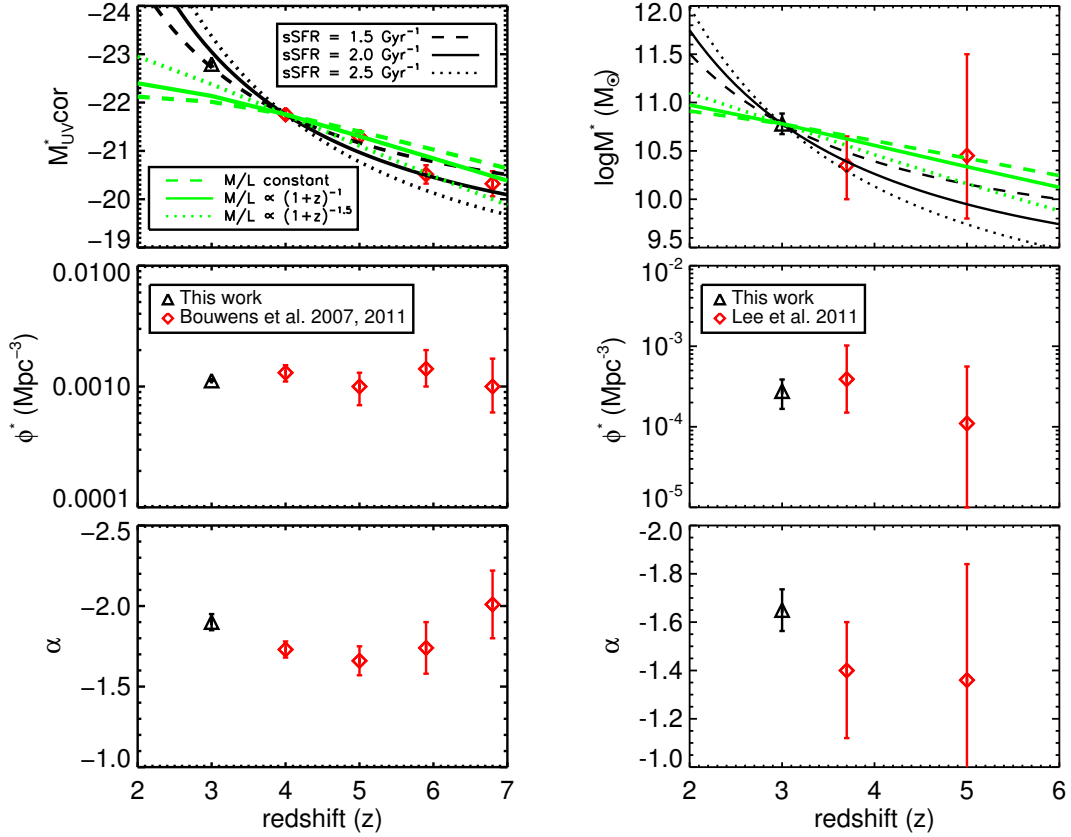


Figure 3.15: Evolution of best-fit parameters of Schechter functions of UV LF (left panel) and SMF (right panel) with redshifts. Left panel: For characteristic absolute magnitude, we use the dust-corrected value ($M_{UV,cor}^*$). The black triangle is from this work, and the red diamonds are from Bouwens et al. (2007, 2011b). Right panel: The black triangle is from this work, and the red diamonds are from Lee et al. (2011). The prediction of two different galaxy evolution models are plotted in both panels. The green curves represent the hierarchical star formation model with different assumptions on evolution of the halo mass to dust corrected UV luminosity or stellar mass ratio. The green dashed, solid and dotted curves represent models with the ratio constant with cosmic time, $\propto (1+z)^{-1}$, and $\propto (1+z)^{-1.5}$, respectively. The black solid curves represent the smoothly rising star formation model. The dashed, solid and dotted black curves represent models with sSFR of 1.5 Gyr^{-1} , 2.0 Gyr^{-1} , and 2.5 Gyr^{-1} , respectively.

due to the hierarchical galaxy formation process (e.g. Mo et al., 1998). In this model, small dark matter halos merge into larger systems and the SFR history in the high- z galaxies is episodic with a duty cycle of $\sim 25\%$. The increasing $M_{\text{UV}}^*/M_{\text{stellar}}^*$ mainly reflects the increasing mass of hosting dark halo with cosmic time. Bouwens et al. (2007, 2008) use this model to interpret the evolution of M_{UV}^* in UV LF from $z \sim 6$ to $z \sim 4$. We follow the method in Bouwens et al. (2007) to determine how the halo mass near the knee of UV LF and SMF increases with time based on the halo mass function of Sheth & Tormen (1999). We assume three different halo mass to UV luminosity/stellar mass ratio relations: (1) the halo mass to light/stellar mass ratio is constant with cosmic time (green dashed curve Bouwens et al., 2007); (2) the halo mass to light/stellar mass ratio varies as $(1+z)^{-1}$ (green solid curve Bouwens et al., 2008); and (3) the halo mass to light/stellar mass ratio varies as $(1+z)^{-1.5}$ (Stark et al., 2007, green dotted curve). The curves are scaled by the $M_{\text{UV},\text{cor}}^*$ data point at $z \sim 3$ in UV LF and by the M_{stellar}^* data points at $z \sim 4$ in SMF. The $M_{\text{UV},\text{cor}}^*/M_{\text{stellar}}^*$ in relation (1) increases with time faster than that in relation (2).

In the second model, we assume (1) L^*/M_{stellar}^* galaxies are on the main sequence for star-forming galaxies (Daddi et al., 2007), and the specific star formation rate (sSFR=SFR/stellar mass) in the LBGs from $z \sim 7$ to $z \sim 3$ is a constant and about $1.5 - 2.5 \text{ Gyr}^{-1}$ (e.g. Stark et al., 2009; González et al., 2010; Rodighiero et al., 2011); (2) the LBGs are in a continuous growth stage in this epoch. This model suggests a smoothly rising star formation history in the LBGs (e.g. Finlator et al., 2011; Papovich et al., 2011; Lee et al., 2011). The long lasting star formation could be the consequence of the cold mode accretion Dekel et al. (2009). In this scenario, the LBGs duty cycle is high (≈ 1), and ϕ^* does not change with redshift. Therefore, the higher redshift $L_{\text{UV}}^*/M_{\text{stellar}}^*$ galaxies are the pro-

genitors of the $L_{\text{UV}}^*/M_{\text{stellar}}^*$ galaxies at lower redshift. As the mass is being built up, M_{stellar}^* will increase with the cosmic time following the relation: $M_{\text{stellar}}^*(z_2) = M_{\text{stellar}}^*(z_1) \times \exp(\text{sSFR} \times (t(z_2) - t(z_1)))$. The L_{UV}^* will increase with the same relation. In Figure 3.15, the black curves are the predicted evolution of $M_{\text{UV}}^*/M_{\text{stellar}}^*$ based on the smoothly rising star formation history model. The dotted, solid, and dashed curves represent different values of sSFR, which are 1.5 Gyr^{-1} , 2.0 Gyr^{-1} , and 2.5 Gyr^{-1} , respectively. The growth rate of $M_{\text{UV}}^*/M_{\text{stellar}}^*$ increases with the increasing sSFR. In both models, both ϕ^* and α are expected to be a constant.

In Figure 3.15, we compare these two models with our observations. For the evolution of dust corrected M_{UV}^* , the hierarchical galaxy formation model (green curves) is consistent with the data points between $z \sim 4$ and $z \sim 7$ (Bouwens et al., 2008), while the predicted $M_{\text{UV},\text{cor}}^*$ is significantly smaller than the observed $M_{\text{UV},\text{cor}}^*$ at $z \sim 3$. On the other hand, the smoothly rising star formation history model (the black curves) can fit the evolution of $M_{\text{UV},\text{cor}}^*$ from $z \sim 3$ to $z \sim 7$ very well. For the evolution of SMF, the predicted M_{stellar}^* in hierarchical galaxy formation model evolves slower than that in the smoothly rising star formation history model. Due to the large uncertainties of SMF measurements for high-redshift galaxies, especially for galaxies at $z \sim 5$, comparison with models is not conclusive. Larger surveys with smaller statistical errors and cosmic variance are needed to differentiate different models.

Generally speaking, the ratio of UV luminosity to stellar mass, $M_{\text{UV},\text{cor}}^*/M_{\text{stellar}}^*$, evolves much more rapidly in the smoothly rising star formation model than in the hierarchical galaxy formation model. This is due to the fact that the dark matter halo mass growth rate decreases with cosmic time in the hierarchical galaxy formation model, while the SFR in galaxies increases with cosmic time from $z \sim 7$ to $z \sim 3$. The smoothly rising star formation history model fits the data points

better than the hierarchical galaxy formation model, especially for the data point at $z \sim 3$. The halo merger rate is about 1 Gyr^{-1} at $z \sim 5$ for the halo mass with $10^{10} M_{\odot}$ and become 0.3 Gyr^{-1} at $z \sim 3$, while the measured sSFR is about $1.5\text{--}2.5 \text{ Gyr}^{-1}$, which is about a factor of 2 to 10 larger than the merger rate from $z \sim 5$ to $z \sim 3$. This suggests that the mass build-up in high redshift galaxies cannot only be from halo merger processes. Other processes, i.e., the cold flow accretion, must make a significant contribution to the mass build-up process, especially at the redshift range from $z \sim 5$ to $z \sim 3$. Beyond $z \sim 6$, the merger rate becomes comparable to the sSFR. So at very early epoch ($z > 6$), the hierarchical galaxy assembly could be the dominate process to build up stellar mass of galaxies.

It is still controversial whether high redshift LBGs have continuous star formation activity from $z \sim 7$ to $z \sim 3$ (Finlator et al., 2011), or the star formation history in LBGs is much shorter with a typical scale of $\sim 300 \text{ Myr}$ (Stark et al., 2009; Lee et al., 2011). The relatively young stellar population (Stark et al., 2009) and short star formation duty cycles from the clustering measurements (Lee et al., 2009) in high- z LBGs support the latter scenario, in which the star formation history is episodic. On the other hand, Finlator et al. (2011) argue that the short duty cycle from the LBG clustering measurements is due to the outflow feedback suppression of star formation in the low-mass halos, therefore, there are only a small fraction of dark matter halos (0.2-0.4) hosting galaxies. In this scenario, the actual star formation duty cycle is about unity and the star formation history in LBGs is smoothly rising. Our results on the evolution of UV LF and SMF favor the continuous star formation history model.

3.8 Clustering Properties of LBGs

In this section, we measure clustering of the bright LBGs ($L > L^*$) at $z \sim 3$. The bright LBG sample is divided into two sub-samples with $24.0 < R < 24.5$ and $23.0 < R < 24.0$ to study the relation between clustering and LBG luminosity. The clustering properties also allow us to estimate the mass of dark matter halos hosting the LBGs. The real-space 3D correlation function can be transferred from 2D angular correlation function (ACF) with the redshift distribution information with Limber function (Peebles, 1980). We do not have the redshift of individual galaxy, therefore, we measure the ACF and fit it as $\omega = A_\omega \theta^{-\beta}$. Combining the redshift distribution information obtained from our simulation (in section 5.1), we can obtain the clustering properties, i.e., the comoving correlation lengths for these two sub-samples from the ACF.

3.8.1 Result

The following estimator is used, first introduced by Landy & Szalay (1993), to measure the ACF:

$$\omega(\theta) = \frac{DD - 2DR + RR}{RR}, \quad (3.14)$$

where DD, RR, and DR are the numbers of galaxy pairs with a separation between θ and $\theta + \delta\theta$ in the observed galaxy catalogue, random catalogue with the same field geometry, and between the observed galaxy and random catalogue, respectively. The number of objects in the random catalogue (n_R) is ~ 100 times larger than the number of the observed galaxies (n_G). The DD, DR, and RR are multiplied by $n_R \times (n_R - 1)$, $(n_R - 1) \times (n_G - 1)$, and $n_G \times (n_G - 1)$, respectively. The Poissonian errors for the ACF are estimated as:

$$\Delta\omega = \sqrt{\frac{1 + \omega(\theta)}{DD}}. \quad (3.15)$$

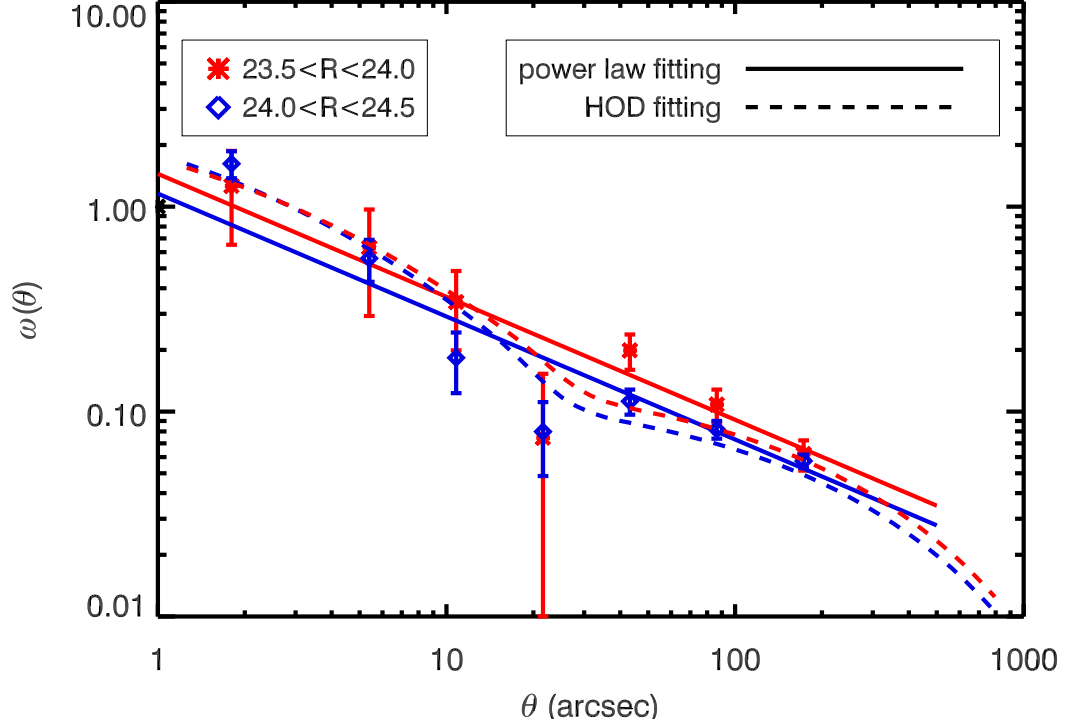


Figure 3.16: Angular correlation functions for two subsamples at $23.5 < R < 24.0$ (red asterisks) and at $24.0 < R < 24.5$ (blue diamonds). The red and blue solid lines present the best-fit power law of the bright and faint subsamples, respectively. The red and blue dashed curves are the best-fit HOD models of the bright and faint, respectively.

The $\omega(\theta)$ is calculated in each individual LBC pointing field. The final result is the average of the individual $\omega(\theta)$.

The finite survey area makes the clustering results artificially weak. The difference between the true correlation function, $\omega_{\text{true}}(\theta)$, and the measured correlation function, $\omega_{\text{measure}}(\theta)$ is a constant, which is also known as integral constraint, IC (Adelberger et al., 2005b):

$$\omega_{\text{true}}(\theta) = \omega_{\text{measure}}(\theta) + \text{IC}, \quad (3.16)$$

and the integral constant equals to the matter variance in the size of the survey volume. There are two approaches to estimate the integral constraint. One of the methods is to integrate the $\omega_{\text{true}}(\theta)$ over the field of view (see details in Roche & Eales, 1999):

$$IC = \frac{\sum_i RR\omega(\theta_i)}{\sum_i RR}, \quad (3.17)$$

and the other method is to use the linear theory to estimate the galaxy variance in the survey volume. In this paper, we apply theoretical estimate method to estimate the value of IC (Adelberger et al., 2005b) (see details in Appendix A). We find the value of $IC \approx 0.02$ for both samples and the IC value is added to the measured clustering results, $\omega_{\text{measure}}(\theta)$, to compute the values of $\omega_{\text{true}}(\theta)$

The ACF is fitted with a power-law form with fixed power-law index $\beta = 0.6$, which is consistent with the results in Adelberger et al. (2005b); Lee et al. (2006),

$$\omega(\theta) = A_\omega \theta^{-\beta}. \quad (3.18)$$

The best-fit parameters for $23.0 < R < 24.0$ sample are $\{A_\omega, \beta\} = \{1.44 \pm 0.14, 0.60\}$ and for $24.0 < R < 24.5$ sample $\{A_\omega, \beta\} = \{1.13 \pm 0.06, 0.60\}$ (Figure 3.16).

Then, the 2D ACF is transformed to the 3D real space correlation function

$$\xi = \left(\frac{r}{r_0}\right)^{-\gamma}. \quad (3.19)$$

The parameters r_0 and γ can be computed from the following relations:

$$A = r_0^\gamma B[1/2, (\gamma - 1)/2] \int_0^\infty dz N^2 r(z)^{1-\gamma} g(z) \left[\int_0^\infty dz N(z) \right]^{-2}, \quad (3.20)$$

(see, e.g., Adelberger et al., 2005b; Lee et al., 2006)

$$\begin{aligned}\gamma &\equiv \beta + 1 \\ B[1/2, (\gamma - 1)/2] &\equiv \frac{\sqrt{\pi}\Gamma[(\gamma - 1)/2]}{\Gamma(\gamma/2)} \\ g(z) &\equiv \frac{H(z)}{c} \\ r(z) &= \int_0^z \frac{cdz}{H(z)} \\ H(z) &= H_0\sqrt{\Omega_\Lambda + \Omega_M(1+z)^3}.\end{aligned}$$

From above equations, we find that the power-law index $\gamma = 1.6$ and the comoving correlation lengths r_0 for $23.0 < R < 24.0$ and $24.0 < R < 24.5$ LBG samples are $5.77 \pm 0.36 h^{-1}$ Mpc and $5.14 \pm 0.16 h^{-1}$ Mpc, respectively. The comoving correlation lengths of the brighter LBG sample is larger than that of the fainter LBG sample at 1σ significant level.

The LBGs in this study is about 1-2 magnitudes brighter those in previous studies. But the survey area and the sample size of the bright LBGs ($R < 24.5$) is an order of magnitude larger, which gives better constraints on the clustering of bright LBGs. In our two bright LBGs subsamples, we find the similar trend that the clustering increases with galaxy UV luminosity, as noted in previous studies (Giavalisco et al., 1998; Adelberger et al., 2005b; Lee et al., 2006; Hildebrandt et al., 2007). In this bright LBG sample, we do not find significant excess power at the small scale of the ACF ($\theta < 10''$) compared to pure power-law fitting, which is found in the faint $z \sim 3$ LBG sample with R magnitude down to 25.5 (e.g., Lee et al., 2006), as well as in the faint $z \sim 4$ LBG sample Ouchi et al. (e.g., 2005). The excess power is due to the excess number of nearby galaxy pairs in the same dark matter halos, e.g., 1-halo term, and contribution of the 1-halo term decreases with increasing UV luminosity. This suggests that satellite galaxies in a dark matter halos are more likely to be faint LBGs than bright LBGs.

Table 3.3: ACF and the Comoving Correlation Lengths for $z \sim 3$ LBGs

| brightness | A_ω | β | r_0 | ref |
|-------------------|------------------------|---------|---------------------|-------------------|
| $23.5 < R < 24.0$ | 1.44 ± 0.14 | 0.6 | 5.77 ± 0.36 | this work |
| $24.0 < R < 24.5$ | 1.13 ± 0.06 | 0.6 | 5.14 ± 0.16 | this work |
| $R < 24.0$ | $1.56^{+0.14}_{-0.17}$ | 0.6 | $7.8^{+0.4}_{-0.5}$ | Lee et al. (2006) |
| $R < 24.5$ | $1.16^{+0.06}_{-0.08}$ | 0.6 | $6.5^{+0.2}_{-0.3}$ | Lee et al. (2006) |

The correlation lengths in our two subsample of bright LBGs are significantly larger than that in a fainter LBG sample from Adelberger et al. (2005b), in which $r_0 = 4.0 \pm 0.6 h^{-1}$ Mpc. A similar trend was also found by Lee et al. (2006), who extend the clustering measurements to bright $z \sim 3$ LBGs, and the ACF best-fit parameters they find are similar to those in this study in the same UV luminosity range. However, our correlation lengths are relatively smaller than those in Lee et al. (2006) (see table 3.3). The main reason for this discrepancy is the redshift distribution. The redshift distribution in Lee et al. (2006) spans from $z \sim 2$ to $z \sim 3$ (see Figure 1 in Lee et al., 2006), which is much wider than that in this study. This will cause a larger correlation length. The redshift distributions from both works are based on simulations, therefore, further spectroscopic observations on these galaxies are required to determine the redshift distributions of the LBG sample.

To obtain the mass of the dark matter halo hosting the bright LBGs, we adopt the halo occupation distribution (HOD) from Hamana et al. (2004); Lee et al. (2006) and fit the HOD results with our ACF measurements (see details in appendix B). The best-fit 2D angular correlation function is shown in Figure 3.16. From the fitting, the best-fit parameters are $\{M_{\min}, \alpha, M_1\} = \{8.1^{+1.4}_{-1.1} \times 10^{11} h^{-1} M_\odot, 0.5, 4.8 \pm 1.0 \times 10^{13} h^{-1} M_\odot\}$ and $\{(1.2 \pm 0.3) \times 10^{12} h^{-1} M_\odot, 0.5, 7.5^{+3.0}_{-2.5} \times 10^{13} h^{-1} M_\odot\}$

for the sample of LBGs with $24.0 < R < 24.5$ and $23.5 < R < 24.0$, respectively.

The mean mass of the hosting halo can be estimated from:

$$\langle M_{\text{host}} \rangle = \frac{\int_{M_{\text{min}}}^{\infty} dM M N_g(M) n_{\text{halo}}(M)}{\int_{M_{\text{min}}}^{\infty} dM N_g(M) n_{\text{halo}}(M)}, \quad (3.21)$$

where n_{halo} is the dark matter halo mass function. The mean masses of the hosting halo for $24.0 < R < 24.5$ and $23.5 < R < 24.0$ samples are $2.5 \pm 0.3 \times 10^{12} h^{-1} M_{\odot}$ and $3.3_{-0.4}^{+0.6} \times 10^{12} h^{-1} M_{\odot}$, respectively. This result confirms that the more massive dark matter halos host more luminous LBGs, and the relation between the UV luminosity and the dark matter halo mass is $L_{\text{UV}} \propto M_{\text{halo}}^{1.5}$. This relation is the similar to those in the LBGs at $z \sim 4$ and $z \sim 5$ (Ouchi et al., 2005; Lee et al., 2006).

3.8.2 Discussion

The trend between clustering strength and UV luminosity shows that LBGs with larger UV luminosities have larger clustering strengths and live in more massive dark matter halos. R -band magnitude, which corresponds to the rest-frame UV brightness at redshift of $z \sim 3$, is a good tracer for the SFRs. Therefore, this trend also suggests that galaxies with higher SFRs are in more massive dark matter halos. This correlation can be understood in the context of the cold flow mode of galaxy formation: gas is accreted into dark matter halos from the IGM and finally falls into galaxies within the dark matter halos. This process provides the material to form stars in galaxies. Dekel et al. (2009) find that the cold mode accretion rate (\dot{M}) is a function of halo mass (M_{halo}) and redshift (z):

$$\dot{M} = 6.6 \left(\frac{M_{\text{halo}}}{10^{12} M_{\odot}} \right)^{1.15} (1+z)^{2.25} \frac{f_b}{0.165} M_{\odot} \text{ yr}^{-1}, \quad (3.22)$$

where f_b is the baryonic fraction in the halos. This relation shows that the cold mode accretion rate increases with the increasing redshift and halo mass, suggesting cold flow accretion is an important process to feed the star formation in

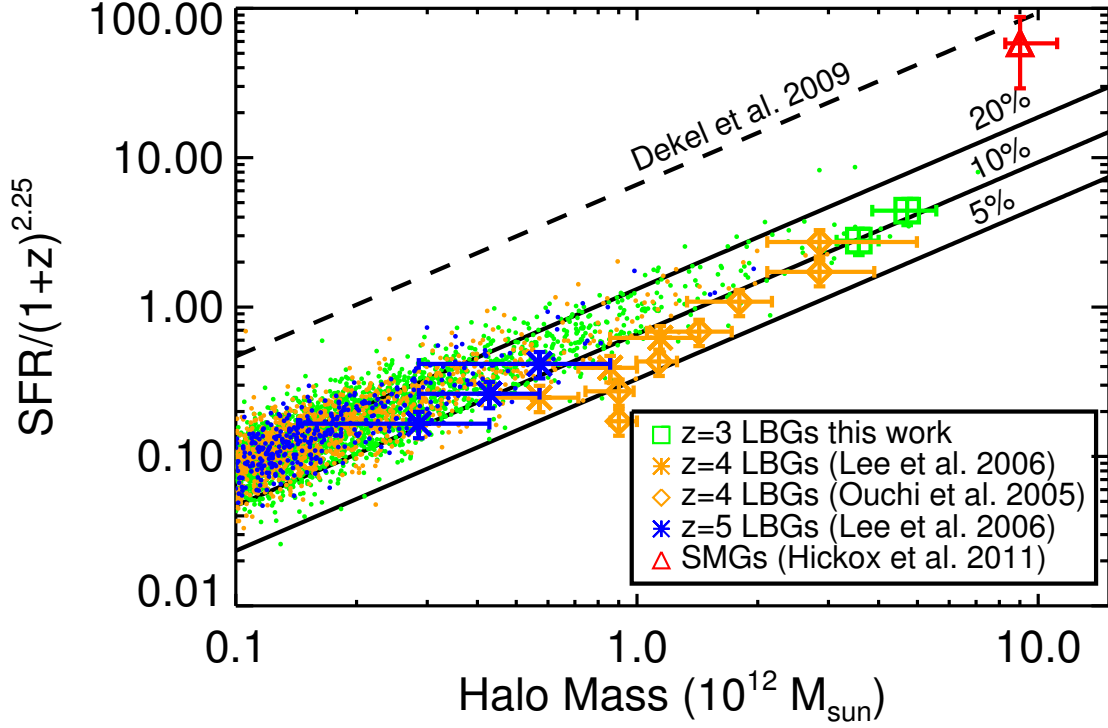


Figure 3.17: Scaled star formation rate (SFR) versus hosting halo mass. The dashed line represents the relation in Eq. 3.22 derived from the cold flow model (Dekel et al., 2009), and the solid lines represent that the star formation efficiencies are 20%, 10% and 5% of the total cold flow accretion mass. The LBGs at $z \sim 3$ (green open squares (this work)), $z \sim 4$ (orange asterisks (Lee et al., 2006) and diamonds ((Ouchi et al., 2005))), and $z \sim 5$ (blue asterisks (Lee et al., 2006)) follow the 10% cosmic star formation efficiency line very well, while the SMGs (red triangle) at $z \sim 2$ is about 0.85 dex higher. The filled circles are the predictions of the cosmic star formation efficiency from the cosmological simulations with momentum-driven gas outflows recipe (Oppenheimer & Davé, 2008). The points are color coded by redshift (green $z=3$, orange $z=4$, and blue $z=5$).

high- z star-forming galaxies (Dekel et al., 2009). The cold flow accretion model describes how gas is accreted into dark matter halos at large scales, but does not include any physical processes down to the galaxy scale to convert the accreted gas into the stars and regulate star formation. Our measurements of SFRs in the galaxies and their hosting dark matter masses will allow us to connect the large scale cold accretion process and the small scale star formation process together.

Figure 3.17 shows the redshift-scaled SFR ($\text{SFR}/(1+z)^{2.25}$) as a function of the hosting halo mass. The SFRs are estimated from dust corrected UV luminosities. They are derived from the R -band magnitude for $z \sim 3$ LBGs in this work, z -band magnitude for $z \sim 4$ and 5 LBGs in Lee et al. (2006) and i -band magnitude for $z \sim 4$ LBGs in Ouchi et al. (2005), by assuming a typical dust extinction $E(B - V) = 0.15$ for LBG samples at $z \sim 3$ and $z \sim 4$ and $E(B - V) = 0.10$ for LBG sample at $z \sim 5$ (e.g., Bouwens et al., 2009). In Figure 3.17, the dashed line represents that the relation of the equation 3.22, and the three solid lines from top to bottom represent 20%, 10%, and 5% cold flow gas converted into star formation.

From Figure 3.17, we find that the observed redshift-scaled SFR as a function of mass from this work and other works (Ouchi et al., 2005; Lee et al., 2006) follows the trend predicted by the cold flow accretion model very well over about two orders of magnitude of dark matter halo mass. This relation suggests that the star formation in LBGs is fueled by cold flows and the cosmic star formation efficiency ($\text{sSFE} = \text{SFR}/\dot{M}$), which is defined as the efficiency of the conversion of cold flow accretion gas into star formation, is between 5% and 20%. The cosmic star formation efficiency does not change with the redshift ($3 < z < 5$), dark halo mass ($10^{11} - 10^{13} M_{\odot}$), or LBG luminosity ($0.1L^* - 3L^*$) significantly. The low efficiency is consistent with cosmological simulations (e.g., Oppenheimer & Davé, 2008) in which the cosmic star formation efficiency is about 20% (Figure 3.17).

The low cosmic star formation efficiency is set by a combination of momentum-driven outflows at low masses, which can eject up to 80% of the total inflow at the smallest halo masses shown, and retardation of accretion by a hot gaseous halo that emerges at larger halo masses (Kereš et al., 2005). These effects conspire to set the efficiency to about 20% over this mass range.

This predicted cosmic star formation efficiency is about a factor of two higher than the measurements. Therefore, there is probably more strong feedback due to outflows in these galaxies, or other feedback effects need to be introduced, to regulate the star formation process. We also note that the systematic uncertainty of the SFR measurements, e.g., different IMFs and dust extinction, can also offset the measured cosmic star formation efficiency by a factor of 2 or even larger (e.g., Narayanan & Davé, 2012a). It is worth noting that although the cosmic star formation efficiency does not change significantly with halo mass, the relation between of UV luminosity and the halo mass ($L \propto M^{1.5}$) in the LBGs at $z \sim 3$, $z \sim 4$, and $z \sim 5$ implies that the cosmic star formation efficiency weakly increases with halo mass.

In Figure 3.17, we also show the redshift-scaled SFR and the hosting dark matter halo mass in submillimeter galaxies (SMGs) (Hickox et al., 2011). The redshift-scaled SFR in SMGs is about 0.85 dex higher than that in LBGs. There are two different star formation laws found, which are long-lasting modes in disk galaxies (e.g., BzK galaxies) fueled by cold flows, and starburst modes in merging galaxies (e.g., SMGs) triggered by major mergers (e.g. Daddi et al., 2010a). The plot shows that the cosmic star formation efficiency in SMGs is about 10 times greater than that in LBGs, which is consistent with the result that the SFRs in starbursts are 4-10 times larger than those in disk galaxies at fixed molecular gas mass (e.g. Daddi et al., 2010a; Genzel et al., 2010). Therefore, the plot demonstrates that LBGs with

$L < 2.5L^*$ follows a long-lasting mode in disk galaxies, which are similar to local spirals and BzK galaxies.

3.9 SUMMARY

We carry out a LBC imaging survey in the NDWFS Boötes field, covering 9 deg^2 fields with U_{spec} and Y -band, to fill the two main optical wavelength gaps in the NDWFS. The depth of U_{spec} is 25.5 with 5σ detection. The wide field allows us to select a statistical sample of luminous LBGs. Using this sample, we studied the bright end LF and clustering properties of LBGs. The main scientific results are summarized as following:

1. Using the LBT U_{spec} band images and the NDWFS B_w , R images, 14,485 LBGs at the redshift of ~ 3 are selected in the 9 deg^2 NDWFS Boötes field, which is the largest color-selected LBG sample at $z \sim 3$ to date.
2. Combined with the faint-end LF measurements from Reddy & Steidel (2009), the rest-frame UV LF of $z \sim 3$ LBGs is measured. Our large field survey puts a strong constraint on the bright end of the LBGs. The Schechter function is fit to the UV LF, and the best-fit parameters are $\Phi = (1.06 \pm 0.01) \times 10^{-3} \text{ Mpc}^{-3}$, $M^* = -20.11 \pm 0.08$, and $\alpha = -1.94 \pm 0.10$ by fitting our bright end data alone, and $\Phi = (1.12 \pm 0.01) \times 10^{-3} \text{ Mpc}^{-3}$, $M^* = -20.08 \pm 0.05$, and $\alpha = -1.90 \pm 0.05$ by combining our bright end data and the faint end data points from Reddy & Steidel (2009). Both results support a steep faint-end slope of the LBG UV luminosity function rather than a relatively shallower faint-end slope as suggested by Shim et al. (2007) and Sawicki & Thompson (2006a,b). This implies that the faint LBGs make a significant contribution to the UV luminosity function and dominate the SFR density at $z \sim 3$. With the large survey area and sample of LBGs, this work gives accurate mea-

surements of the bright-end UV LF of $z \sim 3$ LBGs, and allows us to probe the LBG luminosity range $-23.0 < M_{\text{UV}} < -25.0$. At the brightest end, the AGN/Quasar population dominates the LF. After subtracting the quasar LF from our measured LF, we still find a excess comparing with the Schechter function. Further spectroscopic observations on the galaxy candidates will allow us to reveal the bright LBG LF and study whether the LF follows the Schechter function at the bright end.

3. The rest-frame near-IR LF of the $z \sim 3$ LBGs is estimated. The best-fit Schechter function parameters are $\phi_J^* = (3.1 \pm 1.9) \times 10^{-4} \text{ Mpc}^{-3}$, $M_J^* = -24.00 \pm 0.30$, and $\alpha_J = -2.00 \pm 0.17$, which shows significant evolution compared to the rest-frame near-IR of local galaxies. The SMF of the $z \sim 3$ LBGs is derived based on the near-IR LF. The density of LBGs is lower than that of K -selected galaxies at $z \sim 3$ at the massive end ($M > 10^{11} M_{\odot}$), suggesting that UV-selected star-forming galaxies do not make a dominant contribution to the SMF of $z \sim 3$ galaxies at the massive end. The LBG SMF shows a steep slope ($\alpha = -1.65 \pm 0.09$) and dominates the galaxy stellar mass density at the low mass end. By comparing our measured SMF of LBG with cosmological hydrodynamical simulations with a momentum-driven wind model, we find that the SMF derived from the simulation is consistent with the measured SMF of LBGs at the massive and intermediate mass range, but the simulation overproduces galaxies at the low mass end and does not produce enough massive dead and red galaxies.
4. The evolution of the LBG UV LF and SMF with cosmic time is studied. We compare the evolution with the hierarchical galaxy formation model and the smoothy rising star formation model, and find that the evolutionary

trend supports the model with a steady rising star formation history. In this scenario, the galaxies keep forming star in the redshift range between $z \sim 7$ and $z \sim 3$ and the SFR increases with increasing stellar mass to make the sSFR constant. This stellar mass increasing mode makes the M_{stellar}^* and dust corrected L^{UV} increase exponentially with cosmic time and the parameters α and ϕ^* remain constant.

5. The clustering of two samples ($23.5 < R < 24$ and $24 < R < 24.5$) of the bright LBGs are studied. The comoving correlation lengths, r_0 , for these two samples are calculated which shows $5.77 \pm 0.36 h^{-1}$ Mpc and $5.14 \pm 0.16 h^{-1}$ Mpc, respectively. This result shows that the galaxies with higher UV luminosity have stronger spatial clustering, implying that the galaxies with higher UV luminosity are in more massive dark matter halos. HOD model is applied to measure the mean hosting dark matter halo mass for these two LBG samples, which are $2.5 \pm 0.3 \times 10^{12} h^{-1} M_{\odot}$ and $3.3_{-0.4}^{+0.6} \times 10^{12} h^{-1} M_{\odot}$, respectively. Combining with other clustering measurements of LBG samples at different redshifts, we find that the relationship of the redshift-scaled SFR and the hosting halo mass can be interpreted by the cold flow gas accreted by the host dark matter halos, and the cosmic star formation efficiency in LBGs is about 5%-20% of the total cold flow gas.

CHAPTER 4

AN ULTRAVIOLET ULTRA-LUMINOUS LYMAN BREAK GALAXY AT $Z = 2.78$ IN
NDWFS BOÖTES FIELD

We present one of the most ultraviolet (UV) luminous Lyman Break Galaxies (LBGs) (J1432+3358) at $z = 2.78$, discovered in the NOAO Deep Wide-Field Survey (NDWFS) Boötes field. The R -band magnitude of J1432+3358 is 22.29 AB, more than two magnitudes brighter than typical L^* LBGs at this redshift. The deep z -band image reveals two components of J1432+3358 separated by $1.''0$ with flux ratio of 3:1. The high signal-to-noise ratio (S/N) rest-frame UV spectrum shows $\text{Ly}\alpha$ emission line and interstellar medium absorption lines. The absence of N V and C IV emission lines, the non-detection in X-ray and radio wavelengths and mid-infrared (MIR) colors indicate no or weak active galactic nuclei (AGN) ($< 10\%$) in this galaxy. The galaxy shows broader line profile with the full width half maximum (FWHM) of about 1000 km s^{-1} and larger outflow velocity ($\approx 500 \text{ km s}^{-1}$) than those of typical $z \sim 3$ LBGs. The physical properties are derived by fitting the spectral energy distribution (SED) with stellar synthesis models. The dust extinction, $E(B - V) = 0.12$, is similar to that in normal LBGs. The star formation rates (SFRs) derived from the SED fitting and the dust-corrected UV flux are consistent with each other, $\sim 300 \text{ M}_\odot \text{ yr}^{-1}$, and the stellar mass is $(1.3 \pm 0.3) \times 10^{11} \text{ M}_\odot$. The SFR and stellar mass in J1432+3358 are about an order of magnitude higher than those in normal LBGs. The SED-fitting results support that J1432+3358 has a continuous star formation history with the star formation episode of $6.3 \times 10^8 \text{ yr}$. The morphology of J1432+3358 and its physical properties suggest that J1432+3358 is in an early phase of 3:1 merger process. The unique properties and the low space number density ($\sim 10^{-7} \text{ Mpc}^{-3}$) are consistent with

the interpretation that such galaxies are either found in a short unobscured phase of the star formation or that small fraction of intensive star-forming galaxies are unobscured.

4.1 Introduction

Over the last decade, the dropout method (the Lyman break technique), which uses the fact that little flux is emitted bluewards of the Lyman limit (912 Å), has been fundamental in searching for high-redshift star-forming galaxies (e.g., Steidel et al., 1996b,b). Spectroscopic follow-up observations show that the efficiency of this method is high (e.g., Steidel et al., 2003). Large samples of Lyman Break Galaxies (LBGs) from $z \sim 2$ up to $z \sim 10$ have been established (e.g., Bouwens et al., 2008, 2011a). These samples of LBGs provide crucial information on determining the cosmic star formation history (e.g., Madau et al., 1996; Lilly et al., 1996; Cowie et al., 1996), mapping the growth of large scale structures (e.g., Adelberger et al., 1998; Giavalisco et al., 1998; Adelberger et al., 2005a; Lee et al., 2006, 2009), and studying the properties of dark matter halos hosting the LBGs.

Optical and near-infrared (NIR) photometric and spectroscopic observations of these galaxies reveal the properties of the UV-selected galaxies at $z \sim 2 - 3$. The median stellar mass of the $z \sim 3$ LBGs is about $2.4 \times 10^{10} M_{\odot}$ (e.g., Shapley et al., 2001), and the mean star formation rate (SFR) derived from the $H\alpha$ and UV luminosity is about $30 M_{\odot} \text{ yr}^{-1}$ (e.g., Erb et al., 2006b). The median dust extinction ($E(B - V)$) is around 0.15 (e.g., Shapley et al., 2001). The $z \sim 2 - 3$ LBGs show compact morphologies (half-light radii, $r_e < 0.''5$) in Hubble space telescope (HST) images.

However, most of optical/NIR surveys for high-redshift galaxies are deep field surveys with survey area less than 1 deg^2 . So far, the largest $z \sim 2 - 3$

LBGs survey with spectroscopic redshifts only covers a total area of around one deg^2 with > 2000 spectroscopic redshifts (e.g., Steidel et al., 2003; Reddy & Steidel, 2009). Due to the small survey volume, combined with the rapid decline of galaxy luminosity function at the bright end, these surveys are not suited to reveal the most luminous and most massive systems; previous studies have been focusing on the LBGs with luminosity of L^* or sub- L^* ($r > 24.5$). A sample of bright LBGs was discovered in Sloan Digital Sky Survey (SDSS), however, HST follow-up observations show that these galaxies are unresolved point sources indicating that these objects are quasars rather than galaxies (Bentz et al., 2008). To date only one unlensed LBG at $z \sim 3$ with R -band magnitude brighter than 22.5 has been found (Cooke et al., 2008).

Finding UV ultra-luminous $z \sim 2 - 3$ galaxies requires wide-field surveys with deep, multi-color broad band images. In this paper, we report a UV ultra-luminous LBG, J1432+3358, with $R_{\text{AB}} = 22.29$ at $z = 2.78$ discovered in the NOAO Deep Wide Field Survey (NDWFS) Boötes field. Through this paper, we adopt $\Omega_m = 0.3$, $\Omega_\Lambda = 0.7$, and $H = 70 \text{ km s}^{-1} \text{ Mpc}^{-1}$ (Spergel et al., 2007). All the magnitudes are AB magnitudes.

4.2 Observations

In 2008 and 2009, we carried out deep U - and Y -band imaging of the 9 deg^2 NOAO Deep Wide-Field Survey (NDWFS) Boötes Field (Jannuzi & Dey, 1999). Our survey used the $2 \times 8.4 \text{ m}$ Large Binocular Telescope (LBT) (Hill et al., 2008) equipped with two prime focus Large Binocular Cameras (LBC, Giallongo et al., 2008). This new LBT survey builds on the available unique multi-wavelength data of the Boötes and fills in two critical wavelength gaps at 3500 \AA and $1 \mu\text{m}$ with the U and Y bands. The deep U -band images (25.2 AB magnitude with

5σ detection), together with the existing B_W - and R -band images taken with the Mosaic CCD camera on Kitt Peak 4 m Mayall telescope, allow us to search for the star-forming galaxies at $z \sim 3$ using the U-dropout technique, and total 15,000 LBG candidates are selected based on the $U - B_W$ and $B_W - R$ color-color diagram, with the selection criterion being

$$\begin{aligned}
 U - B_W &> 1.0, \\
 B_W - R &< 1.9, \\
 B_W - R &< U - B_W - 0.1, \\
 R &< 25.0.
 \end{aligned} \tag{4.1}$$

The typical image quality in the R -band is $1''$ and thus can not resolve typical LBGs. Nevertheless, the large survey area allows us to select and study the most UV luminous LBGs at $z \sim 3$ with $R < 22.5$ ($L > 7L^*$ at $z \sim 3$).

Spectroscopic follow-up observations of 12 of bright LBG candidates were obtained using the blue channel spectrograph on 6.5 m Multiple Mirror Telescope (MMT) on 2010 April 15. Typically 20-40 minutes exposures were taken for each candidate. The wavelength coverage is 4000-7500 Å. One out of 12 candidates was confirmed as a UV ultra-luminous LBG (J1432+3358) at $z = 2.78$, and the coordinates of this galaxy are R.A.=14^h32^m21^s.84 and Decl.=33°58'18".2, J2000. The remaining eleven candidates are all quasars in the redshift range of $2 < z < 3$. All these quasars show broad Ly α , N V, and C IV emission lines and they are all point sources.

A high signal-to-noise ratio (S/N) spectrum of J1432+3358 was obtained with the 8.2 m Gemini-N telescope and GMOS instrument on 2011 March 9 and 10 (Program ID: GN-2011-C-5). The sky was clear and the resulting image quality was $0.''6 - 0.''7$. The total exposure time was 4 hr and was divided into eight 30-

min individual exposures. The slit width was $1''$. The B600-G5307 grating was used, and two central wavelengths of 5200 \AA and 5300 \AA were used to fill the gaps between different CCD chips. The wavelength coverage was from 4000 \AA to 6500 \AA , and the spectral resolution ($R = \lambda/\delta\lambda$) is 850. The airmass of the object during the observing was about 1.05, thus we did not use the parallactic angle. The slit oriented in P.A.=-60 degrees (300 degrees), which was roughly along the galaxy extended direction (Figure 1). The spectrophotometric standard G191-B2B was observed for flux calibration, and a CuAr arc lamp was used for wavelength calibration. The spectra were reduced and calibrated using standard Gemini IRAF package. The final spectrum has been smoothed by 4 \AA . The S/N per spectral element ($\sim 4 \text{ \AA}$) is 8-10.

MIR photometry of J1432+3358 was obtained by the Spitzer Deep Wide-Field Survey (Ashby et al., 2009). In addition, H -band image with one hour exposure was obtained using the SWIRC on 6.5 m MMT on 2012 January 5. We also got deep z -band image from the Subaru Boötes field survey (BoötesZ Survey) (Y. Lin et al. 2012, in preparation). The image quality of the z -band image is $0.''5$. The total magnitudes of J1432+3358 are measured with SExtractor (Bertin & Arnouts, 1996), and are listed in table 4.1.

4.3 Results

4.3.1 Lensed or Unlensed?

In the last decade, a sample of bright lensed high-redshift galaxies has been established through systematic searches towards galaxy clusters (e.g. Mehlert et al., 2001; Sand et al., 2005) and red galaxies in the SDSS images (e.g. Smail et al., 2007; Allam et al., 2007; Diehl et al., 2009; Lin et al., 2009). It is crucial to determine whether J1432+3358 is lensed or not. Studies suggest that the total fraction of

Table 4.1: Magnitude and morphological properties of J1432+3358.

| Filter | Magnitude ^a | r_e ^b | n ^c | b/a ^d | θ ^e | χ^2/ν ^f |
|----------------------|------------------------|--------------------|------------------|--------------------|-----------------------|---------------------------|
| <i>U</i> | 24.35 ± 0.13 | - | - | - | - | - |
| <i>B_W</i> | 23.26 ± 0.02 | 0.73 ± 0.20 | 3.10 ± 0.77 | 0.49 ± 0.05 | -73.17 ± 3.75 | 1.310 |
| <i>R</i> | 22.29 ± 0.03 | 0.89 ± 0.04 | 1.23 ± 0.27 | 0.45 ± 0.04 | -63.81 ± 2.84 | 1.078 |
| <i>I</i> | 22.20 ± 0.03 | 0.82 ± 0.05 | 1.37 ± 0.37 | 0.38 ± 0.05 | -55.04 ± 3.05 | 1.104 |
| <i>z</i> | 22.13 ± 0.03 | | | | | |
| $z(a)^g$ | 22.62 ± 0.04^i | 0.26 ± 0.03 | 4 | 0.69 ± 0.08 | 14.04 ± 13.21 | 1.168 |
| $z(b)^h$ | 23.71 ± 0.07^i | 0.21 ± 0.03 | 1 | 0.67 ± 0.14 | 82.43 ± 19.12 | 1.168 |
| <i>Y</i> | 22.19 ± 0.09 | - | - | - | - | - |
| <i>H</i> | 21.54 ± 0.36 | - | - | - | - | - |
| IRAC1 | 20.88 ± 0.06 | - | - | - | - | - |
| IRAC2 | 20.66 ± 0.07 | - | - | - | - | - |
| IRAC3 | 20.69 ± 0.37 | - | - | - | - | - |
| IRAC4 | 20.42 ± 0.33 | - | - | - | - | - |

^aTotal AB magnitude from SExtractor.

^bEffective radius (") from the GALFIT fitting.

^cSérsic index from the GALFIT fitting.

^dThe ratio of minor axis (b) and major axis (a) from the GALFIT fitting.

^eThe position angle from the GALFIT fitting.

^fThe reduced chi-square from the GALFIT fitting.

^gThe GALFIT fitting results of the brighter components in *z*-band image.

^hThe GALFIT fitting results of the fainter components in *z*-band image.

ⁱThe magnitude is from the GALFIT fitting.

high-redshift galaxies and quasars that are lensed is small (e.g., Turner et al., 1984; Jain & Lima, 2011), but the lensing contribution becomes larger with increasing brightness. Jain & Lima (2011) find that the lensing contribution becomes significant when $L > 10L^*$, and about 1/3-1/2 of the LBGs with $L = 7L^*$ are lensed galaxies (van der Burg et al., 2010).

The structure of J1432+3358 is well resolved by the ground-based imaging observations. The broad band U -, B_W -, R -, I -, z - and Y -band images (Figure 4.1) of J1432+3358 show extended morphology. The deep multi-band images show that there is no foreground lensing galaxy and the morphology of the galaxy is also consistent with being unlensed. Especially, in the deep Subaru z -band image with image quality of $0.''5$, J1432+3356 is resolved into two components, and separation of these two parts is by $1.''0$ (7.8 kpc). These two components do not show stretched arc structures at the resolution of the image. Furthermore, the central wavelengths of $\text{Ly}\alpha$ emission from these two components have a small offset ($237 \pm 23 \text{ km s}^{-1}$) and the $\text{Ly}\alpha$ flux ratio of these two components is not consistent with the continuum flux ratio of these two components (see detail in section 3.3). Meanwhile, the spectrum of J1432+3358 does not show any other redshift systems that could be from the lensing galaxy. Therefore, we conclude that J1432+3358 is not a lensed galaxy.

4.3.2 Morphology

The deep z -band image reveals two components in J1432+3358. We use GALFIT (Peng et al., 2002) to fit the light distribution of these two components with either exponential disk or DeVaucouleurs profiles. We find that the DeVaucouleurs profile is better to fit the brighter component and the exponential disk is better to fit the fainter component. The effective radius are $0.''26 \pm 0.''03$ and $0.''21 \pm 0.''03$, respectively, which correspond to about 2.0 kpc in physical size. This size is com-

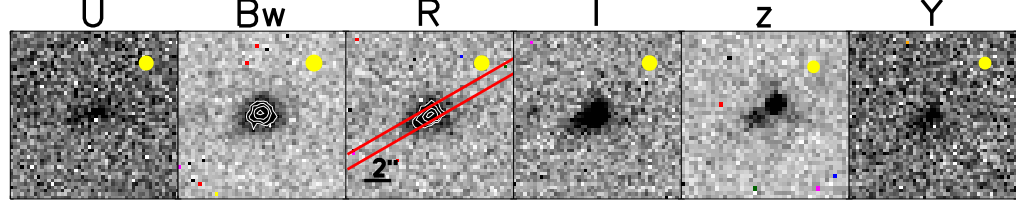


Figure 4.1: The U -, B_W -, R -, I -, z -, and Y -band images of J1432+3358. A contour plot is also shown in B_W - and R -band images. The yellow filled circles represent the size of point spread functions (PSF) in each image. The typical image qualities for U -, B_W -, R -, I -, z -, and Y -band images are $1''.0$, $1''.3$, $1''.2$, $1''.2$, $0''.5$ and $0''.6$, respectively. The slit position and orientation are also shown in R -band image.

parable to the typical size of LBGs at $z \sim 3$ (e.g. Ferguson et al., 2004). The distance between these two components is about $1''.0$, which is about 7.8 kpc. The brightness ratio between these two components in J1432+3358 is 3 to 1. Assuming a simple relation between luminosity and stellar mass, the mass ratio of the two components is also 3 to 1 implying that it is a 3:1 merger. These two components are barely resolved by the z -band image. Further high resolution HST follow-up imaging observations will help us to fit the systems more accurately and to reveal more detailed structure of this galaxy.

The morphology of J1432+3358 in B_W -band image and that in R - and I -band images look different (figure 1). To characterize the morphology in these bands, we use GALFIT to model the galaxy light distribution in the B_W -, R -, and I -band images of J1432+3358. The Sérsic profile (Sérsic, 1963) is used to fit the light profile of J1432+3358. The GALFIT fitting results are listed in table 4.1. The R - and I -band morphologies of J1432+3358 can be well fit by a disk-like profile with Sérsic index $n \approx 1.3$, while the Sérsic index is about 3.10 for the morphology in B_W -band image, which is much larger than that in R - and I -band images (Table

1). Furthermore, the galaxy light distribution in B_W -band image can not be well fitted by a single Sérsic profile component, with reduced chi-square of 1.310. The B_W -band morphology is round rather than elongated. The strong $\text{Ly}\alpha$ emission line lies within the B_W filter at the redshift of 2.78. We therefore interpret the diffuse B_W morphology as being likely due to a diffuse $\text{Ly}\alpha$ halo around J1432+3358 (c.f., Steidel et al., 2011). The $\text{Ly}\alpha$ photons from the central galaxy are scattered by the neutral hydrogen gas in the galaxy's circum-galactic medium (CGM) and form the diffuse $\text{Ly}\alpha$ halo. We do not carry out the fitting on U - and Y - band images, because their S/N is too low.

4.3.3 Spectroscopy

Figure 5.1 shows the high S/N rest-frame UV spectrum of J1432+3358 taken using Gemini GMOS-N. The spectrum covers the rest-frame wavelength from 1100-1700 Å, and shows the strong $\text{Ly}\alpha$ emission line and a few absorption features from the interstellar medium (ISM) (e.g., Si II, O I, Si IV, and C IV). In the spectrum, there is no prominent N V 1240 emission line detected at the level of equivalent width of 2 Å (1σ level) corresponding to rest-frame equivalent width (EW_0) of 0.5 Å, which is much smaller than the EW_0 of 18 ± 10 Å measured in a sample of bright quasars (Forster et al., 2001). Similarly, the C IV 1548, 1551 doublet line shows an absorption rather than emission feature.

J1432+3358 is not detected at the X-ray energies (0.5-7.0 keV) with 30 ks *Chandra* observation (P.I. Murray Obs ID 13134) (also see, Murray et al., 2005b). The flux limit of the X-ray data is about 4×10^{-16} erg cm $^{-2}$ s $^{-1}$. By assuming the X-ray spectrum as a common AGN power-law spectrum with photon index $\Gamma = 1.7$ (e.g., Kenter et al., 2005), the Galactic neutral hydrogen column density $N_{\text{H}} = 1 \times 10^{20}$ cm $^{-2}$ (e.g., Dickey & Lockman, 1990), and the X-ray-to-optical power-law slope $\alpha_{\text{ox}} = -1.45$ (e.g., Just et al., 2007), we find that less than 10% of the optical

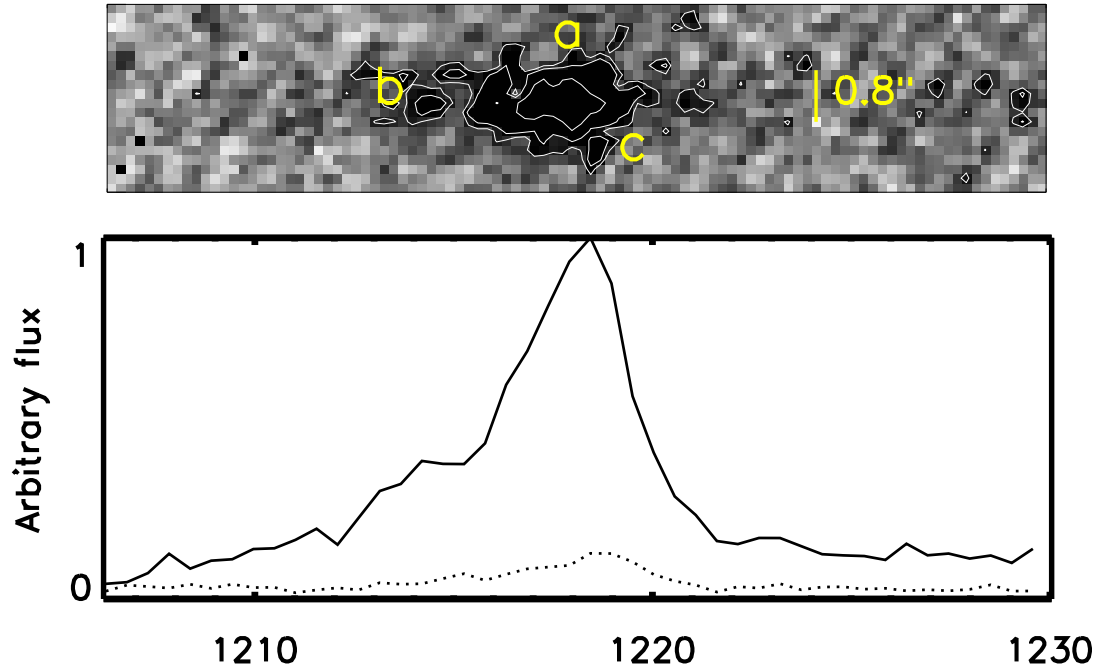


Figure 4.2: The 2D spectrum (top panel) and the 1D spectrum (top panel) of the $\text{Ly}\alpha$ emission line. There are 3 significant components resolved in 2D spectrum image. The components of 'a' and 'b' correspond to the redshifted stronger peak and the blueshifted weaker peak, respectively. The component of 'c' corresponds to the $\text{Ly}\alpha$ emission from the fainter component which was resolved in z -band image. The central wavelength difference between components 'a' and 'c' is about 3.6 \AA .

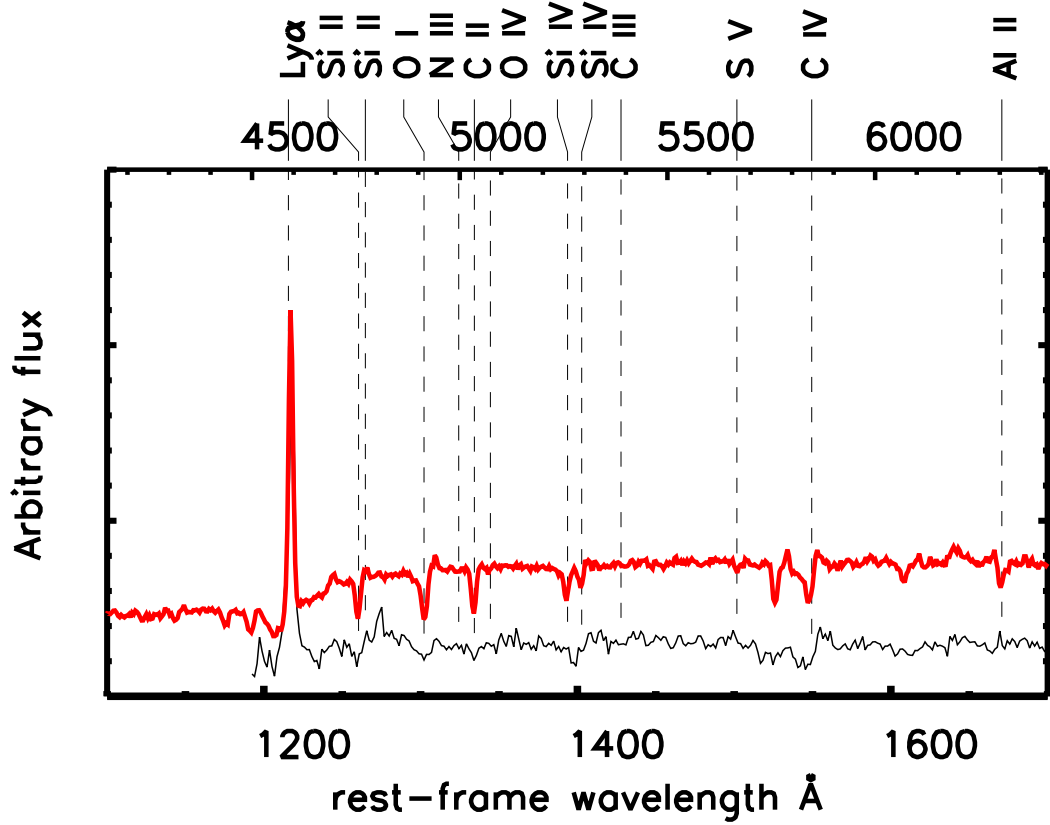


Figure 4.3: The rest-frame UV spectrum of J1432+3358 in the wavelength range 1100-1700 Å (the thin black solid curve). For comparison, the composite spectrum of a sample of $z \sim 3$ LBGs is also shown with a red thick solid curve (Shapley et al., 2003). The top x-axis represents the observed-frame wavelength. Both spectra are scaled by the peak value of the Ly α emission line, and the composite spectrum is shifted by +0.1 in flux density direction for clarity.

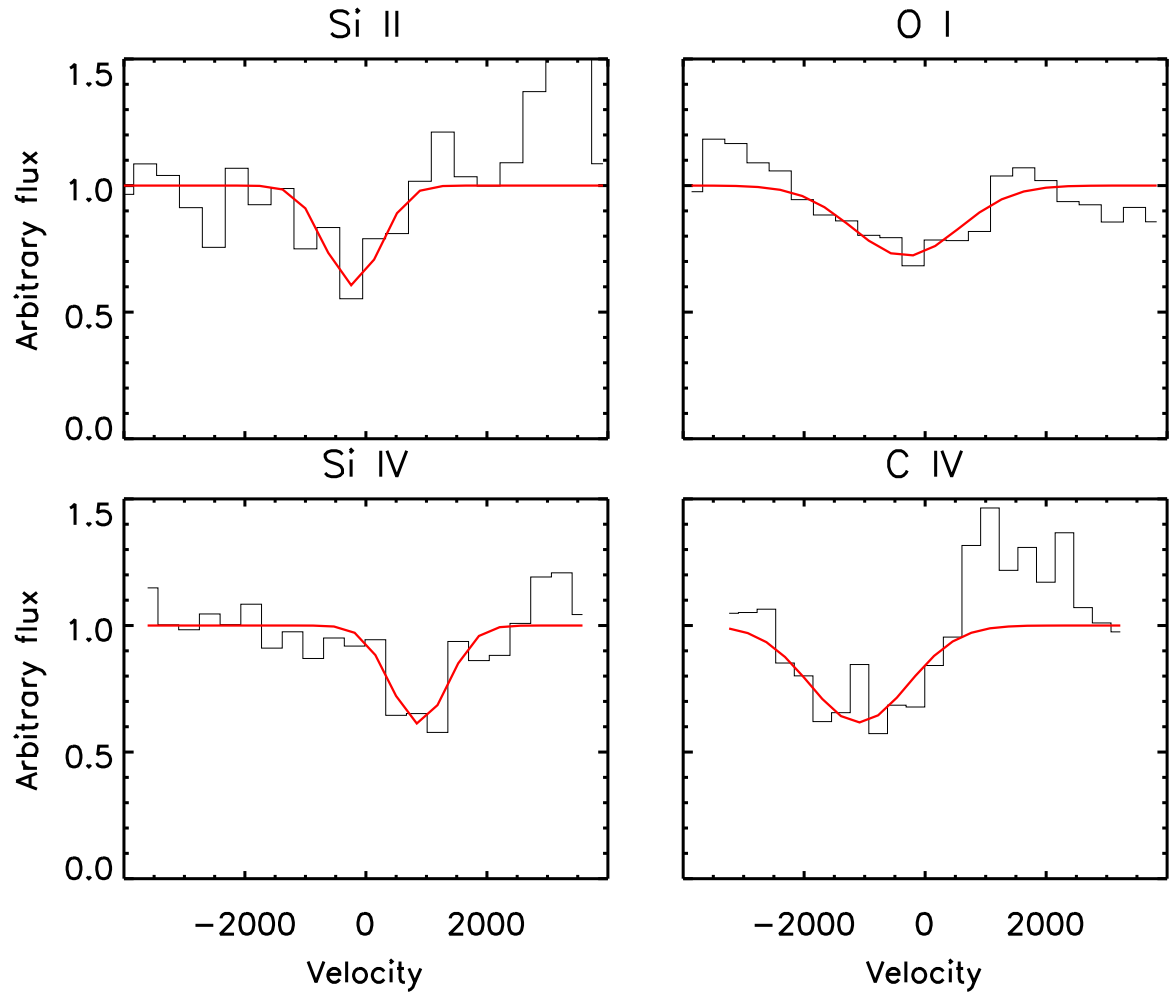


Figure 4.4: The spectra around the absorption lines (the back curves in histogram mode) and best-fit Gaussian models (the red curves). The flux is scaled by the continuum flux.

Table 4.2: Ly α emission and strong interstellar absorption lines.

| line | $\lambda_{\text{rest}}^{\text{a}}$ Å | λ_{obs} Å | EW Å | FWHM km s $^{-1}$ | redshift | Δv^{b} km s $^{-1}$ |
|---------------------------|-----------------------------------------|-----------------------------|------------------|----------------------|-------------------|---------------------------------------|
| Ly α^{c} | 1215.08 | 4592.99 ± 0.59 | 34.97 ± 2.74 | 1431 ± 81 | 2.780 ± 0.000 | 392 ± 38 |
| Ly $\alpha(a)^{\text{d}}$ | 1215.08 | 4597.41^{g} | 27.46 ± 2.59 | 852 ± 56 | 2.784 | 680 |
| Ly $\alpha(b)^{\text{e}}$ | 1215.08 | 4582.52^{g} | 9.86 ± 1.38 | 1073 ± 151 | 2.771 | −291 |
| Ly $\alpha(c)^{\text{f}}$ | 1215.08 | 4601.05 ± 0.36 | 4.5 ± 1.5 | 200 ± 25 | 2.787 | 923 ± 25 |
| Si II | 1259.83 | 4752.42 ± 1.83 | -1.89 ± 0.52 | 1004 ± 288 | 2.772 ± 0.001 | -222 ± 115 |
| O I | 1302.69 | 4912.05 ± 4.33 | -2.65 ± 0.89 | 2031 ± 643 | 2.771 ± 0.003 | -346 ± 264 |
| Si IV | 1393.18 | 5274.68 ± 2.00 | -2.11 ± 0.50 | 1041 ± 259 | 2.786 ± 0.001 | 872 ± 113 |
| C IV | 1548.91 | 5825.82 ± 2.41 | -4.04 ± 0.83 | 1901 ± 384 | 2.761 ± 0.002 | -1101 ± 123 |

^aAir wavelengths.

^bThe line velocity relative to the systemic redshift. The negative (positive) values correspond to blueshift (redshift).

^cThe whole Ly α emission.

^dThe primary peak of the Ly α emission corresponding to the ‘a’ component in Figure 2.

^eThe secondary peak of the Ly α emission corresponding to the ‘b’ component in Figure 2.

^fThe Ly α emission from the faint component corresponding to the ‘c’ component in Figure 2. The information of this component is derived from Extractor measurement and Gaussian fitting in the 2D spectra image.

^gTo deblend the two peaks of the Ly α emission line, the central wavelength values are set to the peak values of these two lines and fixed during the fitting.

radiation could be from the AGN. J1432+3358 is not detected at 20cm in radio wavelength (de Vries et al., 2002), with 1σ sensitivity limit of $28\mu\text{Jy}$ corresponding to a specific luminosity of $4.7 \times 10^{30} \text{ erg s}^{-1} \text{ Hz}^{-1}$. This radio limit can not put a good constraint on the AGN activity in J1432+3358 by adopting the relation between optical and radio luminosity derived from the SDSS quasar sample (White et al., 2007). The rest-frame NIR excess does not show in the *Spitzer* bands, which suggests absence of hot dust and obscured AGN. The IRAC [3.6]-[4.5] and [5.8]-[8.0] colors are located out of the AGN selection area in MIR color-color space (e.g, Lacy et al., 2004; Stern et al., 2005). The rest-frame UV spectrum, the non-detection in X-ray and radio bands and MIR colors imply that there is no or only weak AGN ($< 10\%$) in J1432+3358, therefore, we suggest that the UV emission is dominated by the emission from massive stars rather than a central AGN.

The properties of the well detected ($S/N > 3$) lines in the rest-frame UV spectrum are listed in table 5.2. Because the observed wavelength of $\text{Ly}\alpha$ emission and ISM absorption lines are affected by galactic-scale outflows, the redshifts from these lines do not represent the systemic redshift (e.g., Adelberger et al., 2005a). Typically, the systemic redshift can be derived from absorption lines that are clearly associated with photospheric features (e.g., S V 1502, C III 1176, O VI 1343, etc) (e.g., Dey et al., 1997; Shapley et al., 2003), but we can not identify these lines from the spectrum at current S/N level. Therefore, we follow Adelberger et al. (2005a), in which they calibrate the redshifts of the $\text{Ly}\alpha$ and ISM absorption lines with the $\text{H}\alpha$ nebular line in a sample of $z \sim 2 - 3$ LBGs (see details in Adelberger et al., 2005a). The scattering of this relation is less than 0.0015. Here the systemic redshift of J1432+3358 is estimated from the $\text{Ly}\alpha$ and absorption lines using the equations 1 and 2 in Steidel et al. (2010), which are 2.7745 and 2.7755, respectively. This result is also consistent with the systemic redshift

calculated using the equation 3 in Adelberger et al. (2005a). The systemic redshift of 2.775 ± 0.001 is adopted for further analysis in this paper.

The composite spectrum of LBGs at $z = 2 - 3$ is also shown in Figure 5.1 for comparison (Shapley et al., 2003). The continuum shape of the spectrum is similar to that of LBG composite spectrum, indicating that the dust extinction in J1432+3358 is similar to the dust extinction in the typical LBGs. This property is also supported by the SED fitting results (see details in section 4.3.4).

The prominent $\text{Ly}\alpha$ emission line is shown in Figures 4.2 and 5.1 with EW_0 of 35 Å. In Figures 4.2, the $\text{Ly}\alpha$ emission shows two peaks separated by 970 km s^{-1} and the full width at half maximum (FWHM) of the $\text{Ly}\alpha$ emission line is $\sim 1500 \text{ km s}^{-1}$, which is much larger than the $\text{FWHM}(\text{Ly}\alpha) = 450 \pm 150 \text{ km s}^{-1}$ typically found in $z \sim 3$ LBGs (Shapley et al., 2003). The secondary peak is real rather than noise, because the double-hump profile is exhibited in the individual spectra of the eight individual 30-min exposures. Two Gaussian profiles are used to deblend the $\text{Ly}\alpha$ emission lines. The FWHMs of the two $\text{Ly}\alpha$ components are $\sim 1000 \text{ km s}^{-1}$. Like most of the LBGs with multiply-peaked $\text{Ly}\alpha$ emission (Kulas et al., 2012), J1432+3358 shows stronger redshifted $\text{Ly}\alpha$ emission than blueshifted. The separation of the two $\text{Ly}\alpha$ peaks is $\sim 1000 \text{ km s}^{-1}$, which is comparable to the separation in other multiple-peaked LBGs (Kulas et al., 2012). Such a $\text{Ly}\alpha$ line profile is observed in the expansion shell model (Verhamme et al., 2006), which predicts that a primary $\text{Ly}\alpha$ peak is redshifted by approximately two times the expansion velocity and another blueshifted $\text{Ly}\alpha$ emission is located around the expansion velocity.

In the 2-dimensional (2D) spectral image of the $\text{Ly}\alpha$ emission (Figure 4.2), there are three significant components of $\text{Ly}\alpha$ emission detected. The ‘a’ and ‘b’ components which are resolved in the wavelength direction correspond to

the double-peak feature in the 1-dimensional (1D) spectrum. The ‘c’ component resolved in the slit (spatial) direction is the $\text{Ly}\alpha$ emission from the fainter component detected in the z -band image. To determine the wavelength of ‘c’ component, SExtractor and GALFIT are used to obtain the centroid and GAUSSIAN fitting central positions of ‘a’ and ‘c’ components. The offsets of the central wavelength between ‘a’ and ‘c’ components are 3.90 \AA and 3.25 \AA from the measurements with above two methods, respectively. We adopt the 3.64 ± 0.36 as the offset of the central wavelength between ‘a’ and ‘c’ components, which corresponds to a velocity difference of $237 \pm 23 \text{ km s}^{-1}$. The $\text{Ly}\alpha$ flux ratio between the components ‘a’ and ‘c’ is about 7:1 from the SExtractor measurement, which is higher than the continuum flux ratio between these two components. The velocity offset and the difference in flux ratio of $\text{Ly}\alpha$ and continuum in components of ‘a’ and ‘c’ also support that J1432+3358 is not a lensed system.

The spectrum also shows weak absorption lines originated from the interstellar medium (ISM), which are Si II, O I, Si IV, and C IV lines (Figure 4.4). The EW_0 of these absorption features are a few \AA , comparable to those in typical LBGs. However, the FWHMs of these lines are 1000 km s^{-1} or even larger (Table 5.2), about two times larger than those in typical LBGs. The absorption lines show blueshifts with velocities of $200\text{-}1000 \text{ km s}^{-1}$, which can be interpreted by a galactic scale outflow model (Heckman et al., 2000; Steidel et al., 2010). The average outflows velocity estimated from Si II, O I and C IV absorption lines is $-556 \pm 103 \text{ km s}^{-1}$. We do not use the Si IV 1392 absorption line for the analysis, because the measurements of this line is contaminated by the S IV 1402. Steidel et al. (2010) find that average outflow velocity of LBGs derived from the ISM absorption lines is $164 \pm 16 \text{ km s}^{-1}$ with a wide range distribution from 0 to 500 km s^{-1} , and we find the outflow velocities in J1432+3358 are larger than the outflow velocities in most

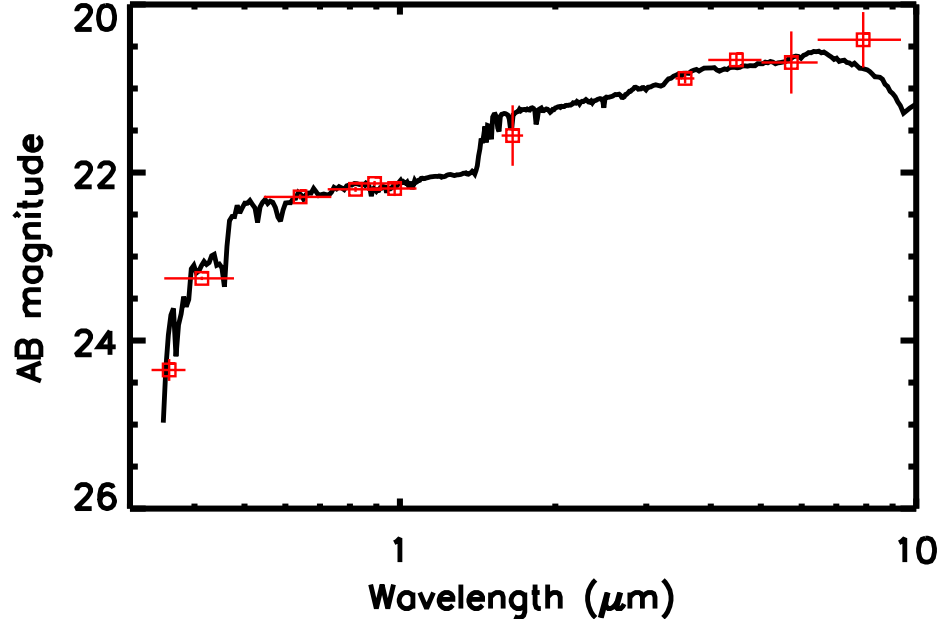


Figure 4.5: The best-fit stellar synthesis model (solid curve) and photometric data points from U -band to IRAC4-band (red squares).

(> 98%) of LBGs. .

4.3.4 Physical Properties

An IDL-based code FAST (Fitting and Assessment of Synthetic Templates) (Kriek et al., 2009) is used to fit the broad band (U , B_W , R , I , Y , H , IRAC1, IRAC2, IRAC3, and IRAC4) photometry with stellar population synthesis models (Bruzual & Charlot, 2003, BC03) and to derive the physical properties of J1432+3358. First, we use an exponential star formation rate ($\text{SFR} \propto \exp(-t_{sf}/\tau)$) with a Salpeter initial mass function (IMF) (Salpeter, 1955) and solar metallicity. We adopt the dust extinction law proposed by Calzetti et al. (2000) and the intergalactic medium (IGM) absorption model in Madau (1995). From the SED fitting, we place constraints on the exponential star formation time scale, $\log(\tau(\text{yr})) = 10.00^{+1.00}_{-1.66}$. The large τ value indicates that the SFR declines slowly, suggesting that J1432+3358

has continuous constant star formation history. Therefore, we adopt a constant star formation history model for further analysis. In Figure 5.7, we show the best-fit spectral energy distribution overlaid on the optical (U , B_W , R , and I , Y), NIR (H), and MIR (IRAC1 ($3.6\mu\text{m}$), 2 ($4.5\mu\text{m}$), 3 ($5.8\mu\text{m}$), 4 ($8.0\mu\text{m}$)) photometry. From the fitting, we find that the galaxy age, $\log(t_{sf}(\text{yr})) = 8.8^{+0.2}_{-0.2}$, the SFR is $280^{+70}_{-60} \text{ M}_{\odot} \text{ yr}^{-1}$, the dust extinction is $E(B - V) = 0.12 \pm 0.02$, and the stellar mass is $(1.3 \pm 0.3) \times 10^{11} \text{ M}_{\odot}$. The SFR derived from the dust-corrected UV luminosity is $310 \text{ M}_{\odot} \text{ yr}^{-1}$ (Kennicutt, 1998a), which is consistent with that derived from the SED fitting. The SFR in J1432+3358 thus is one order of magnitude higher than that in typical $z \sim 3$ LBGs (Shapley et al., 2001). The SED fitting suggests that the star formation age (t_{sf}) is about two times longer than the median star formation time in typical $z \sim 3$ LBG sample (Shapley et al., 2001). This age is also longer than the typical time scale of the starburst in submillimeter galaxies (SMGs), which is about 200 Myr (e.g., Narayanan et al., 2010). The star formation history and high stellar mass (about ten times higher than the median stellar mass in typical $z \sim 3$ LBG sample (Shapley et al., 2001)) in J1432+3358 indicate that it is a massive system with a long-term intensive star formation process rather than a low massive system which harbors a star formation burst. However, the physical properties derived from SED fitting are not reliable due to the weak constraints on the star formation time scale (τ). The star formation ages t_{sf} have significant degeneracies with the τ values (see details in Shapley et al., 2001, 2005), which could affect our above conclusion. On the other hand, the stellar mass estimation is much more reliable, because the rest-frame NIR M/L is reasonably constraint by the SED fitting and nearly independent on the τ values.

The gas mass can be estimated using the global Kennicutt-Schmidt law (Ken-

nicutt, 1998b):

$$\Sigma_{\text{gas}} = 361 \times \left(\frac{\Sigma_{\text{SFR}}}{1 \text{ } M_{\odot} \text{ yr}^{-1} \text{ kpc}^{-2}} \right)^{0.71} M_{\odot} \text{ kpc}^{-2}, \quad (4.2)$$

where $\Sigma_{\text{SFR}} = \text{SFR}/r_e^2$ and the gas mass, M_{gas} , can be derived from $\Sigma_{\text{gas}} \times r_e^2$, which is $3.7 \times 10^{10} M_{\odot}$. The fraction of gas in J1432+3358, $M_{\text{gas}}/(M_{\text{gas}} + M_{\text{stellar}})$, is 0.2. The low gas fraction is consistent with the gas fraction in the UV-selected galaxies at the most massive end (Erb et al., 2006a) and comparable to that in sub-millimeter galaxies (Tacconi et al., 2008).

4.4 Discussion

J1432+3358 shows unique properties compared to normal LBGs characterized by: (1) a high SFR (about $300 M_{\odot} \text{ yr}^{-1}$), (2) a 3:1 merger-like morphology with a $1.0''$ separation of the two components, (3) a high stellar mass ($1.3 \times 10^{11} M_{\odot}$), and (4) a long continuous star formation history (630 Myr), which is twice longer than median star formation history of LBGs.

One of the key questions is regarding the nature of UV ultra-luminous LBGs. By integrating the UV luminosity function (e.g., Reddy & Steidel, 2009), we find that the space number density of the UV ultra-luminous LBGs with $L > 7L^*$ is a few 10^{-7} Mpc^{-3} in the redshift range from 2.7 to 3.3, which corresponds to a spatial number density of $\sim 0.3 \text{ deg}^{-2}$. This is consistent with the result that there is only one UV ultra-luminous LBG found in the 9 deg^2 Boötes within uncertainties. The space number density of UV ultra-luminous LBGs is about 2-3 orders of magnitude smaller than that of typical star-forming galaxies (e.g., LBGs, BzK galaxies) at $z \sim 2 - 3$, which is about $10^{-4} - 10^{-5} \text{ Mpc}^{-3}$ (e.g., Reddy et al., 2005). On the other hand, the space density of galaxy with its stellar mass greater than $10^{11} M_{\odot}$ is about 10^{-4} Mpc^{-3} based on the stellar mass function (e.g., Drory et al., 2005). The low space density of UV ultra-luminous LBGs

can be interpreted by the following two different scenarios: the first one is that UV ultra-luminous LBGs can only be found in a short evolutionary phase for the most intensive star-forming galaxies. Though the SED-fitting result shows that the star formation time (t_{sf}) in J1432+3358 is 630 Myr, this galaxy may only be selected by UV-selection method during a short time period, i.e., most of the time the galaxy is highly obscured by dust. The other interpretation is that most of the galaxies that form stars at high intensity are dusty and highly obscured, e.g., SMGs (Chapman et al., 2005) or DOGs (dust-obscured galaxies) (Dey et al., 2008; Fiore et al., 2008), and only small fraction of galaxies that show high SFR is unobscured by dust.

Another crucial question is whether the extremely high SFR in J1432+3358 is triggered by galaxy major mergers or fueled by rapid accretion of cold gas from the intergalactic medium (IGM). Hopkins et al. (2008) investigate the role of mergers in the evolution of starburst and quasars and suggest an evolution track from a ‘typical’ galaxy to a gas-rich major merger (see a schematic outline in Figure 1 in Hopkins et al., 2008). In this scenario, at the early stage of merger, i.e. their phase (c), the two interacting galaxies are within one halo but still well separated and can be identified as a merger pair (e.g., Lotz et al., 2004). In this stage, the SFR starts to increase to about $100 M_{\odot} \text{ yr}^{-1}$ due to the tidal torques, but the enhanced effect of the SFR is relatively weak compared to the latter coalescence phase. The timescale of this phase is about several million years. The AGN activity in this phase is relatively low. These features are consistent with the properties of J1432+3358.

A tight correlation between the stellar mass (M_{stellar}) and SFR (main sequence) in normal star forming galaxies has been found in both local and high-redshift universe (e.g., Daddi et al., 2005). The mean value of the specific SFR ($\text{sSFR} = \text{SFR} / M_{\text{stellar}}$)

is about $1.8 \times 10^{-9} \text{ yr}^{-1}$ in star-forming galaxies at $z \sim 2$ at the high stellar mass end ($10^{11.0} M_{\odot} < M_{\text{stellar}} < 10^{11.5} M_{\odot}$). The galaxies with sSFR greater than $\sim 5.6 \times 10^{-9} \text{ yr}^{-1}$ are considered to be off the main sequence and suggested to be merger-driven starburst galaxies (e.g., Rodighiero et al., 2011). The sSFR of J1432+3358 is $1.9 \times 10^{-9} \text{ yr}^{-1}$, which would locate our galaxy right on the galaxy main sequence at $z \sim 2$. This result implies that the SFR in J1432+3359 is not enhanced by the merger process, which is also consistent that this system is in the early phase of the merger process. However, above conclusion is based on the SED fitting results which are subject to large systematic uncertainty as discussed in Section 3.3. Therefore, further high resolution space-based imaging and ground-based IFU observations will be requested to provide more firm evidence to distinguish whether J1432+3358 is a major merger or a clumpy disk galaxy.

The outflow properties of J1432+3358 can be studied and compared to the typical LBGs. Steidel et al. (2010) does not find a correlation between the SFR and the velocity of the wind in the UV-selected galaxies at $z \sim 2$, which is found in other high-redshift galaxies (Weiner et al., 2009). One interpretation is that the SFR dynamic range in Steidel et al. (2010) sample is too small to reveal the relation. With the SFR an order of magnitude higher than typical $z \sim 2$ UV-selected galaxies, J1432+3358 will provides enough dynamic range to check whether there exists correlation between the SFR and outflow velocity. Comparing J1432+3358 to the typical $z \sim 2$ UV-selected galaxies (Steidel et al., 2010), we do find that the outflow velocity increases with SFR, and roughly follows the relation found in Weiner et al. (2009), $v_{\text{out}} \propto \text{SFR}^{0.3}$.

CHAPTER 5

THE LBT BOÖTES FIELD SURVEY: II. A POPULATION OF UV
ULTRA-LUMINOUS LBGs AT $Z \sim 3$

We present a population of ultra-luminous Lyman break galaxies (ULBGs) discovered in the NOAO Boötes field. These galaxies have $R \lesssim 22.8$ and $L \gtrsim 5L^*$, and their number density is $\sim 3 \times 10^{-7} \text{ Mpc}^{-3}$. They are some of the rarest and most intensely star-forming galaxies at the early Universe. The blueshifted interstellar medium absorption lines in the composite spectrum suggest that the outflow velocity is about 280 km s^{-1} in ULBGs, which is about 2 times larger than that in typical LBGs. The prominent of C IV P-Cygni profile implies a top-heavy initial mass function in the ULBGs. The physical properties derived from the SED fitting show that the ULBGs have larger stellar mass and SFR, but smaller dust extinction compared to typical L^* LBGs. The majority of the ULBGs locate between the SFR-stellar main sequence relation and 4 times SFR-stellar main sequence relation. Therefore, the SFR activity of the ULBGs is relatively higher than normal star-forming galaxies, but lower than starbursts. This result, together with their large galaxy size and/or multiple core morphologies, suggests that the ULBGs are probably in the early phase of the major merger process.

5.1 Introduction

The redshift range between $1 < z < 4$ was a very unique epoch of the Universe. At this epoch, the cosmic star-formation rate (SFR) density is an order of magnitude higher than local cosmic SFR density (e.g., Madau et al., 1996), which corresponds to a period when a large fraction of present-day galaxy stellar mass is built up. Observing galaxies at this redshift range provides crucial information

on how galaxies, especially massive galaxies, build up their stellar mass in the early Universe.

The deep field surveys have significantly improved our knowledge of the high redshift galaxies over the last decade (e.g., Steidel et al., 1996). The resulting sample of high-redshift star-forming galaxies, has provided important information on the large scale distribution (e.g., Adelberger et al., 1998), the underlying dark matter distribution (e.g., Adelberger et al., 2005, Ouchi et al. 2005), the cosmic star formation history (Madau et al., 1998) and the basic properties (e.g. star formation rate (SFR), ages, stellar masses, metallicities and dust reddening) of the high- z star-forming galaxies (e.g., Pettini et al., 2001, Shapley et al., 2001).

However, the solid angles of the previous deep field surveys are still relatively small. For example, the largest $z \sim 3$ LBG survey with spectroscopic redshifts only covers a total of area of 3261 arcmin² in 31 individual fields with ~ 2000 spectroscopic redshifts (Steidel et al., 2003, Reddy & Steidel, 2009). The number density of the UV/optical selected galaxies falls very quickly at the bright end, meaning that deep field surveys are not suited to reveal the most luminous UV/optical selected galaxies

The dust obscuration in some luminous galaxies is much more severe than that in faint galaxies. Therefore, most of the previous studies have focused on the highly dust obscured sub-millimeter galaxies (SMGs) and dust-obscured galaxies (DOGs). These galaxies correspond to a crucial phase during which galaxy mass builds up quickly and massive galaxies form at the early Universe. In this study, we will focus on the luminous UV-selected star-forming galaxies. With the NOAO deep and wide field survey (NDWFS) Boötes field, we could build up a sample of luminous $z \sim 3$ LBGs with $L > 5L_*$ for the first time. We will reveal the properties of these luminous galaxies, and determine whether they are in a

crucial transition phase to build up massive galaxies or they are more like faint LBGs but in a starburst phase.

In the first paper (see Chapter 3), we presented a large sample of photometrically-selected LBGs in the LBT Boötes field survey and study the luminosity function and clustering of bright LBGs. We found that more luminous LBGs are in more massive dark matter halos and this could be interpreted by the fact that the baryonic material inflow rates increases with in the halo mass. In this paper, we will focus on the spectroscopically-confirmed ultra-luminous LBGs (ULBGs) with the blue channel spectrograph (BCS) mounted on the multiple-mirror telescope (MMT). This paper is organized as follows: in section 5.2, we will discuss how we select the ultra-luminous ULBGs, using the U-dropout method and IRAC colors, and describe the MMT blue channel spectroscopic follow-up observations and data reduction; in section 5.3, we will analyze the MMT spectra of the ULBGs, measure the bright end UV luminosity function, compare the ULBGs rest-frame UV composite spectrum with that of typical LBGs, and study the physical properties of ULBGs; in section 5.4, we discuss the evolutionary stages, outflows velocity, and initial mass function in the ULBGs; and in section 5.5, we will summarize the main results.

5.2 Observations

5.2.1 Imaging Observations and Target Selection

In 2008 and 2009, the LBT Boötes field survey was conducted. This survey builds on the unique multi-wavelength datasets of the NOAO Boötes field and fills in two critical wavelength gaps at 3500\AA and $1\mu\text{m}$ with *U*- and *Y*-bands. This survey covers the whole 9 deg^2 NOAO deep wide field survey (NDWFS) Boötes field with the two Large Binocular Cameras (LBCs) mounted on the primary foci

of the 2×8.4 m Large Binocular Telescope (LBT) in U - and Y -bands (see details in Bian et al., 2012 submitted). The deep U -band images (25.2 AB magnitude with 5σ detection), together with the existing B_W - and R -band images taken by NOAO Mosaic CCD camera on 4 m Mayall telescope, allow us to search for star-forming galaxies at $z \sim 3$ with U-dropout technique. The large solid angle of the survey enables us to explore the LBGs at the bright end of the luminosity function (LF) (Bian et al., 2012 submitted).

We select the luminous LBG candidates at $z \sim 2 - 3$ with $R < 22.8$ ($L > 5L^*$) based on the following selection criteria:

$$\begin{aligned}
 U - B_W &> 1.0, \\
 B_W - R &< 1.9, \\
 B_W - R &< U - B_W + 0.1, \\
 R &< 22.8.
 \end{aligned} \tag{5.1}$$

The images of the selected targets are inspected by eye to get rid of the targets near bright objects or blended with other objects. At the bright end, the contamination rate from low redshift interlopers is high, and can even reach 70% (e.g., Reddy & Steidel, 2009, Bian et al. 2012 submitted). As discussed in Bian et al. 2012, the $R - [3.6]$ and $[3.6] - [4.8]$ colors of interlopers are expected to be bluer than those in $z \sim 3$ LBGs. To eliminate low-redshift interlopers, we also apply the following constraints using the IRAC observations:

$$\begin{aligned}
 R - [3.6] &> 0.0, \\
 [3.6] - [4.5] &> 0.1.
 \end{aligned} \tag{5.2}$$

The resulting sample is also contaminated by quasars at the similar redshifts. The optical colors of these quasars are similar to those of the LBGs (e.g., Fan,

1999). In principle, the $[5.8] - [8.0]$ color could be used to distinguish high-redshift star-forming galaxies and quasars. Quasars have relatively red colors, as these two IRAC bands sample the power-law spectra energy distribution (SED) in active galactic nuclei (AGNs) (e.g., Lacy et al., 2004; Stern et al., 2005). In practice, it is hard to use the $[5.8] - [8.0]$ color to separate galaxies and quasars using the existing data due to the large uncertainties (≈ 0.5) of $[5.8] - [8.0]$ color, so our selection does not rely on the $[5.8] - [8.0]$ color. Instead, we reduce the quasar contaminations by using the fact that that quasars should be point sources, while UV luminous LBGs are spatially extended. Though previous studies have shown that the high-redshift galaxies are compact (e.g., Ferguson et al., 2004), We (Bian et al., 2012) have found that bright LBGs are more extended than typical LBGs and can be spatially resolved in ground-based images with image quality of $\sim 1''$. Therefore, in this study, the morphology information is used to get rid of quasars/AGNs, especially for the data from 2011 and 2012. Based on what we have learned in the survey of 2010, we require that the good galaxy candidates not only satisfy above color selection criteria but also show extended morphology (*star_class* < 0.8 of SExtractor parameter; Bertin & Arnouts, 1996) in at least two different band images. Finally, the priority of each galaxy candidate is assigned based on the location in $U - B_W$ and $B_W - R$ color-color diagram, the IRAC colors and its morphology.

5.2.2 MMT Spectroscopic observations and Data Reduction

Spectroscopic follow-up observations on the bright LBG candidates were obtained with the blue channel spectrograph (BCS) instrument on the 6.5 m multiple mirror telescope (MMT) on 2010 April 15 and 16, 2011 April 29, 30 and May 1, and 2012 April 18. The observing conditions are varied (Table 5.1), with resulting image quality of 0.8-1.0. The 300 lines/mm grating is used. We set the central

Table 5.1: Observing log.

| date | condition |
|---------------|-----------------------------------------|
| April 15 2010 | clear, image quality $0''.6 - 0''.8$ |
| April 16 2010 | partially cloudy, image quality $1''.0$ |
| April 29 2011 | clear, image quality $1''.0$ |
| April 30 2011 | clear, image quality $1''.0$ |
| May 1 2011 | clear, image quality $2''.0$ |
| April 18 2012 | clear, image quality $0''.8$ |

wavelength of the grating at 5000\AA to cover $3600\text{-}7500\text{\AA}$, which corresponds to rest-frame $900\text{-}1800\text{\AA}$ UV spectra of LBGs at $z = 3$. This wavelength range will cover the $\text{Ly}\alpha$ emission/absorption line and most interstellar medium (ISM) absorption lines (e.g., Si II, O I, C II, Si IV etc.). These line features are crucial for identifying whether or not the galaxy candidates are real LBGs. Slit widths of $1''.0$ to $1''.5$ were used based on the seeing conditions. The wavelength resolution is $6.5\text{-}10\text{\AA}$ depends on the slit widths and imaging quality. Parallactic angle was used when performing the observations to minimize the spectral slit losses due to differential atmospheric refraction (Filippenko, 1982). Typically 30-40 minutes exposure is taken for each target based on the observing condition and the brightness of the target. Typically, a HeAr/Ne lamp was taken immediately following each science exposure for wavelength calibration. The flexure of the MMT/BCS is small. The wavelength varies about 0.9 pixel ($\approx 1.7\text{\AA}$) from the most eastern position to the most western position of the telescope pointing. The Spectrophotometric standard stars of Feige34 and G138-31 were taken at different airmasses for flux calibration.

We followed the standard procedure to reduce the spectra with IRAF¹. The two-dimensional (2-D) spectral images were first subtracted by the bias frame and divided by the normalized bright continuum flat. Then the cosmic rays were identified and removed from the 2-D spectral images with the Laplacian Cosmic Ray Identification (L.A.Cosmic) method developed by van Dokkum (2001)². After that the one-dimensional (1-D) spectra were extracted from the 2-D spectral images. Finally, the 1-D spectra are wavelength and flux calibrated. The signal-to-noise ratio (S/N) per resolution element of the spectra is only a few, but in most of the cases it is good enough to identify LBGs even for those without significant Ly α emission line.

5.3 Results

5.3.1 Spectral Identification

We observed a total 57 galaxy candidates in the three-year observing campaign. We use the XCSAO task in RVSAO package (Kurtz & Mink, 1998) in IRAF for classification and redshift determination. The XCSAO cross-correlates a observed spectrum against template spectra to determine the best-fit template spectrum and redshift of the observed spectrum. We used two categories of the template spectra, quasars and LBGs, to cross-correlate the observed spectra of LBG candidate. There are four quasar spectra used, which includes two quasar normal spectra and two broad absorption line (BAL) quasar spectra. These spectral templates are adopted from spectral cross-correlation templates of sloan digital sky survey (SDSS) data release 7 (DR7)³. For the LBG templates, we used six LBGs

¹IRAF is distributed by the National Optical Astronomy Observatories, which are operated by the Association of Universities for Research in Astronomy, Inc., under cooperative agreement with the National Science Foundation.

²<http://www.astro.yale.edu/dokkum/lacosmic/>

³<http://www.sdss.org/dr7/algorithms/spectemplates/>

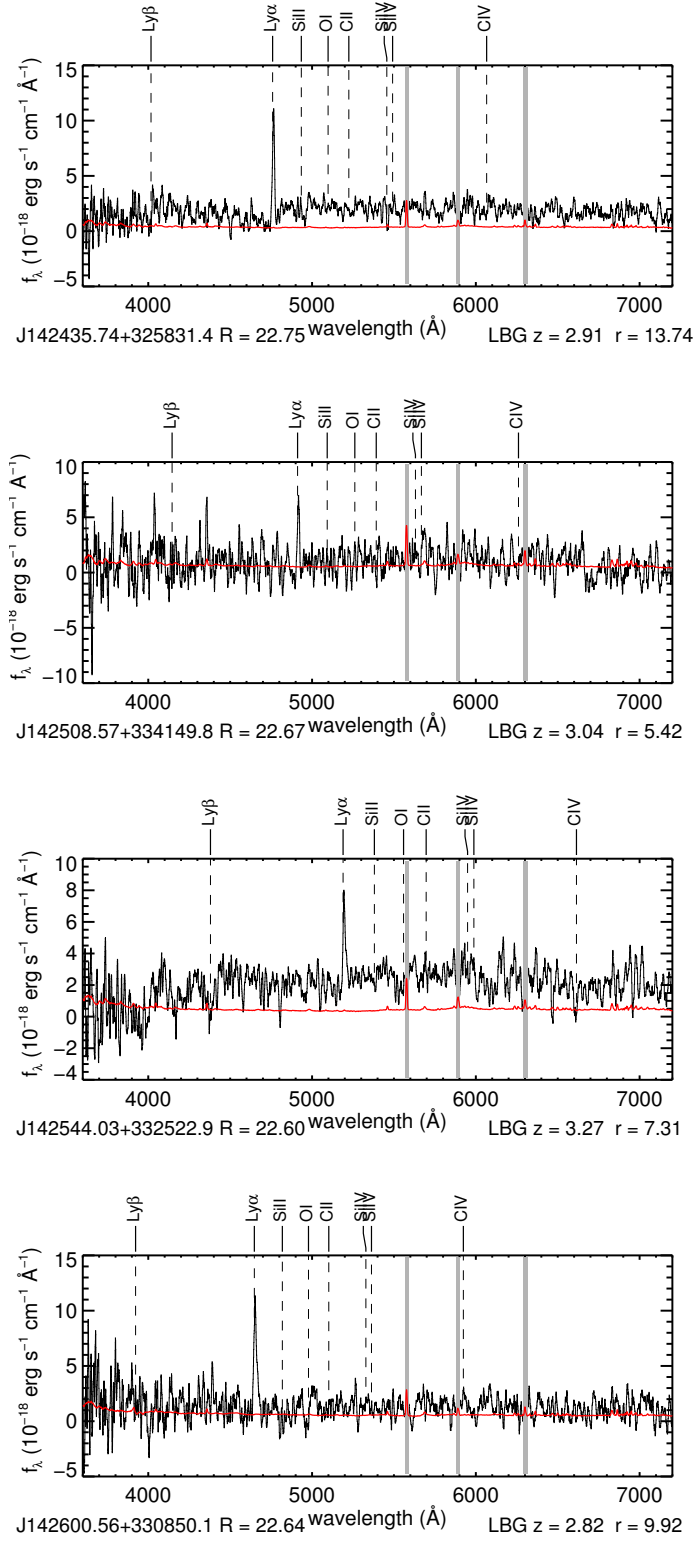


Figure 5.1: The MMT BCS spectra of confirmed ULBGs.

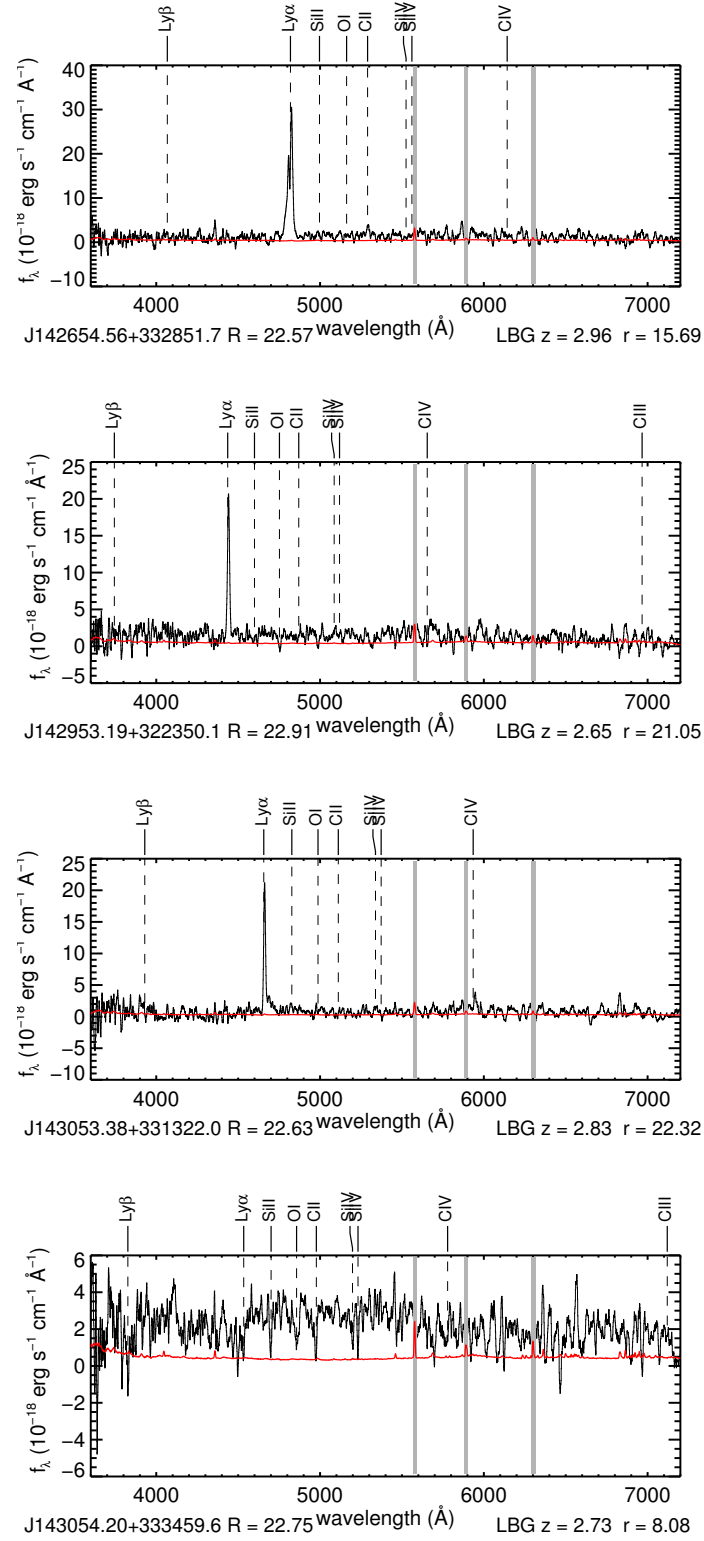


Figure 5.1: Continued figure.

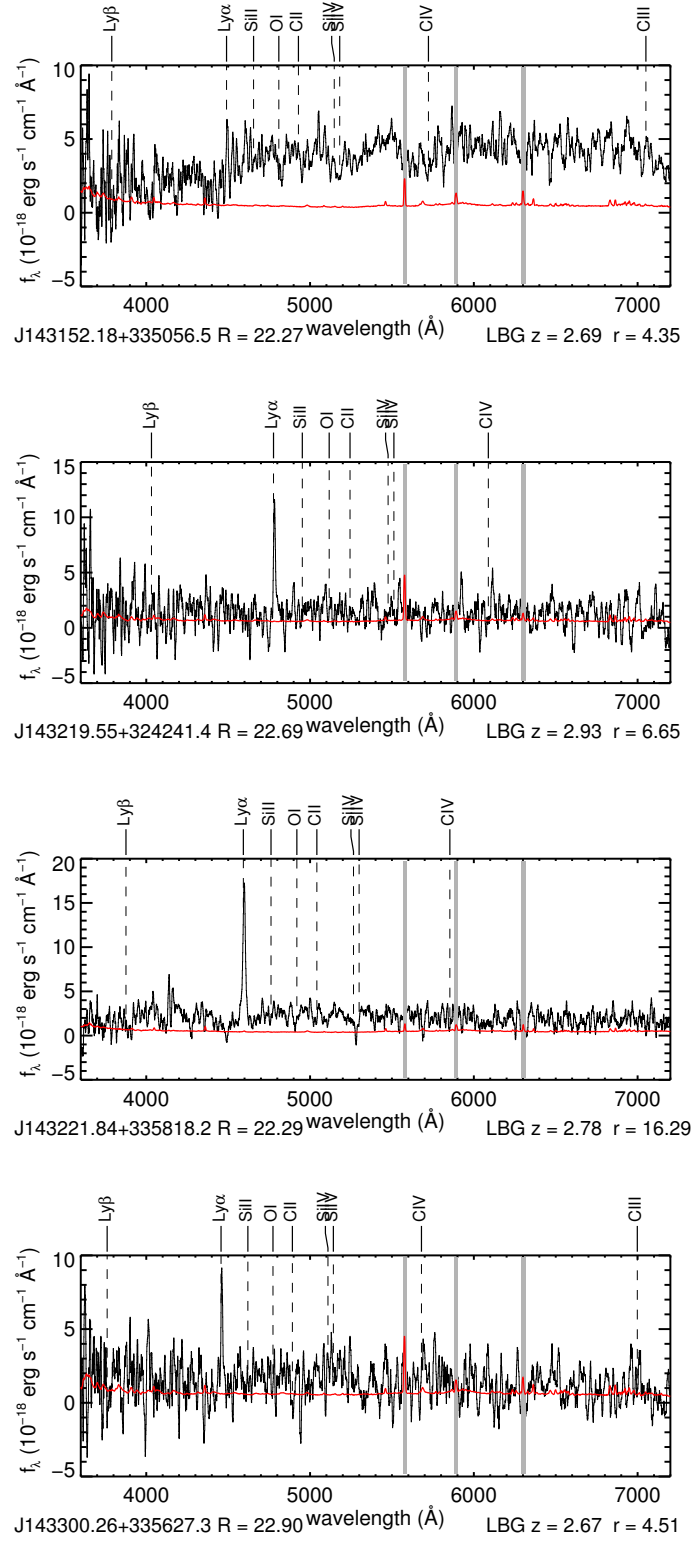


Figure 5.1: Continued figure.

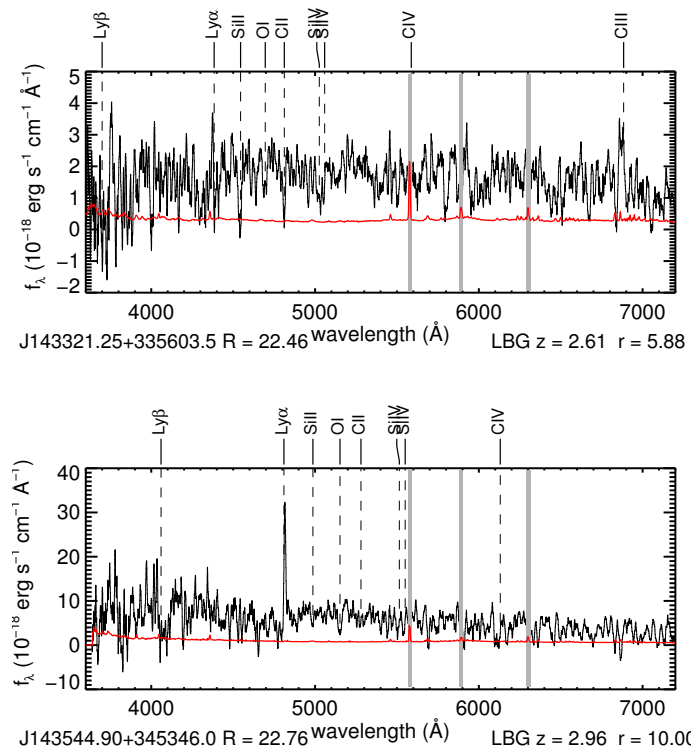


Figure 5.1: Continued figure.

rest-frame UV spectra. One is MS 1512-cB58 (Pettini et al., 2000), which is one of the best observed lensed LBGs at $z \sim 3$, and one is the composite spectrum of the all the LBGs spectra of Shapley et al. (2003). The remaining four spectra are the composite spectra in each of 4 quartile bins in $\text{Ly}\alpha$ emission strength (Steidel et al., 2003).

At first, we inspected the 1-D and 2-D spectra to make a roughly classification. If the spectrum showed one or more significant broad emission lines, which is the signature of quasar/AGN, we cross-correlated it with quasar spectral templates. If the spectrum showed a single narrow emission line and/or a few absorption features, we cross-correlated it with the LBG spectral templates. The narrow emission and absorption lines can also come from low redshift galaxies, especially, we can not resolve the $[\text{O II}]\lambda\lambda 3726, 2729$ doublet lines due to the low spectral resolution. So the emission line could also be the $[\text{O II}]$ doublet from late-type galaxies at $z \sim 0.2$. Similarly, the absorption feature could also be from low redshift early-type galaxies (e.g., the Ca II H+K, G band, Mg and Na D absorptions). Therefore, we also cross-correlated these observed spectra with the early-type and late-type galaxy spectral templates from SDSS DR7. We used the r parameter in XSCAO to evaluate the reliability of the redshift determination. Kurtz & Mink (1998) found that successful rate to determine the redshift of galaxies is about 90% at $r = 2.5 - 3.0$. This result is further supported by Ly et al. (2009), who used the XCSAO to determine the redshifts of a sample of LBGs at $z \approx 1.8 - 2.8$. The threshold of $r = 4.0$ is adopted in this study to obtain more reliable redshifts determination. We also visually inspected each cross-correlation result to make sure that the redshift results make sense. Finally, we discovered 14 LBGs among the 57 LBG candidates.

The 1-D MMT spectra of the confirmed LBGs are shown in Figure 5.1. The

results of the XCSAO in the bottom of each 1-D spectra, including object types, redshifts and r parameter.

5.3.2 Notes on Individual LBGs

J142435.74+325831.4 ($z = 2.91$). It has a strong $\text{Ly}\alpha$ emission. The rest-frame EW is about 40\AA and the FWHM is about 800 km s^{-1} .

J142508.57+334149.8 ($z = 3.04$). The $\text{Ly}\alpha$ emission is weak. The rest-frame EW of $\text{Ly}\alpha$ is about 25\AA and FWHM is about 800 km s^{-1} .

142544.03+332522.9 ($z = 3.27$). The galaxy was discovered in the survey of 2012. The rest-frame EW of $\text{Ly}\alpha$ is about 20\AA and the FWHM is about 700 km s^{-1} .

J142600.56+330850.1 ($z = 2.82$). The rest-frame EW of $\text{Ly}\alpha$ is about 50\AA and the FWHM is about 1000 km s^{-1} .

J142654.56+332851.7 ($z = 2.96$). This galaxy has the strongest $\text{Ly}\alpha$ emission in the galaxy sample. The $\text{Ly}\alpha$ emission shows double peak profile, and those double peaks are spatially resolved along the slit. The velocity of these two components is offset by $\sim 1000\text{ km s}^{-1}$. The FWHMs of those two components are 400 km s^{-1} (blue peak) and 600 km s^{-1} (red peak), and the fluxes are $2.2 \times 10^{-16}\text{ ergs s}^{-1}\text{ cm}^{-2}$ (blue peak) and $4.3 \times 10^{-16}\text{ ergs s}^{-1}\text{ cm}^{-2}$ (red peak), corresponding to the luminosity of $1.7 \times 10^{43}\text{ ergs s}^{-1}$ and $3.3 \times 10^{43}\text{ ergs s}^{-1}$.

J142953.19+322350.1 ($z = 2.65$). The rest-frame EW of $\text{Ly}\alpha$ is about 40\AA and FWHM is about 600 km s^{-1} . This galaxy is selected with $z \sim 2$ selection criterion. We will not use this galaxy in the LF measurement.

J143053.38+331322.0 ($z = 2.83$). The rest-frame EW of $\text{Ly}\alpha$ is about 60\AA and FWHM is about 400 km s^{-1} .

J143054.20+333459.6 ($z = 2.73$). The spectra does not show $\text{Ly}\alpha$ emission, and it is identified by the ISM absorption features. The value of r parameter is 8.08 for this galaxy.

J143152.18+335056.5 ($z = 2.69$). It is the brightest galaxy discovered in our survey ($R = 22.27$). The spectrum does not show Ly α emission, and it is identified by the ISM absorption features. The value of r parameter is 4.35 for this galaxy.

J143219.55+324241.4 ($z = 2.93$). The rest-frame EW of Ly α is about 20 Å and the Ly α line is not barely resolved, and the FWHM is about 400 km s⁻¹.

J143221.84+335818.2 ($z = 2.78$). A deep Gemini-N/GMOS-N spectroscopic follow-up observation was conducted on this object. It has a strong Ly α emission line with rest-frame EW of 35 Å and broad Ly α and ISM absorption lines with FWHM of 1000 km s⁻¹ (Bian et al., 2012).

J143300.26+335627.3 ($z = 2.67$). This galaxy was discovered in the survey of 2011. The rest-frame EW of Ly α is about 20 Å and the Ly α line is not resolved, and the FWHM is less than 500 km s⁻¹.

J143321.25+335603.5 ($z = 2.61$). This galaxy was discovered in the survey of 2011. The spectrum does not show Ly α emission, and it is identified by the ISM absorption features. The value of r parameter is 5.88 for this galaxy.

J143544.90+345346.0 ($z = 2.96$). The rest-frame EW of Ly α is about 15 Å and the Ly α line is not barely resolved, and the FWHM is about 300 km s⁻¹.

5.3.3 The Bright End UV Luminosity Function

The LF of LBGs has been well studied in the early Universe (e.g., Sawicki & Thompson, 2006a; Bouwens et al., 2007; Reddy & Steidel, 2009; Ly et al., 2009). Especially in Reddy & Steidel (2009), about 2000 spectroscopically-confirmed LBGs and 31000 LBGs in a total area of 3261 arcmin² are used to give the most robust measurements of LF and to probe the faint end LF down to $L = 0.1L^*$ at $z \sim 2-3$. As it is discussed in the introduction, the small survey area makes it difficult to establish a sample of the LBGs to explore the bright end ($M_{UV} < -22.5$) of the LF at $z \sim 3$. In this section, we will constrain the bright end of the UV LF

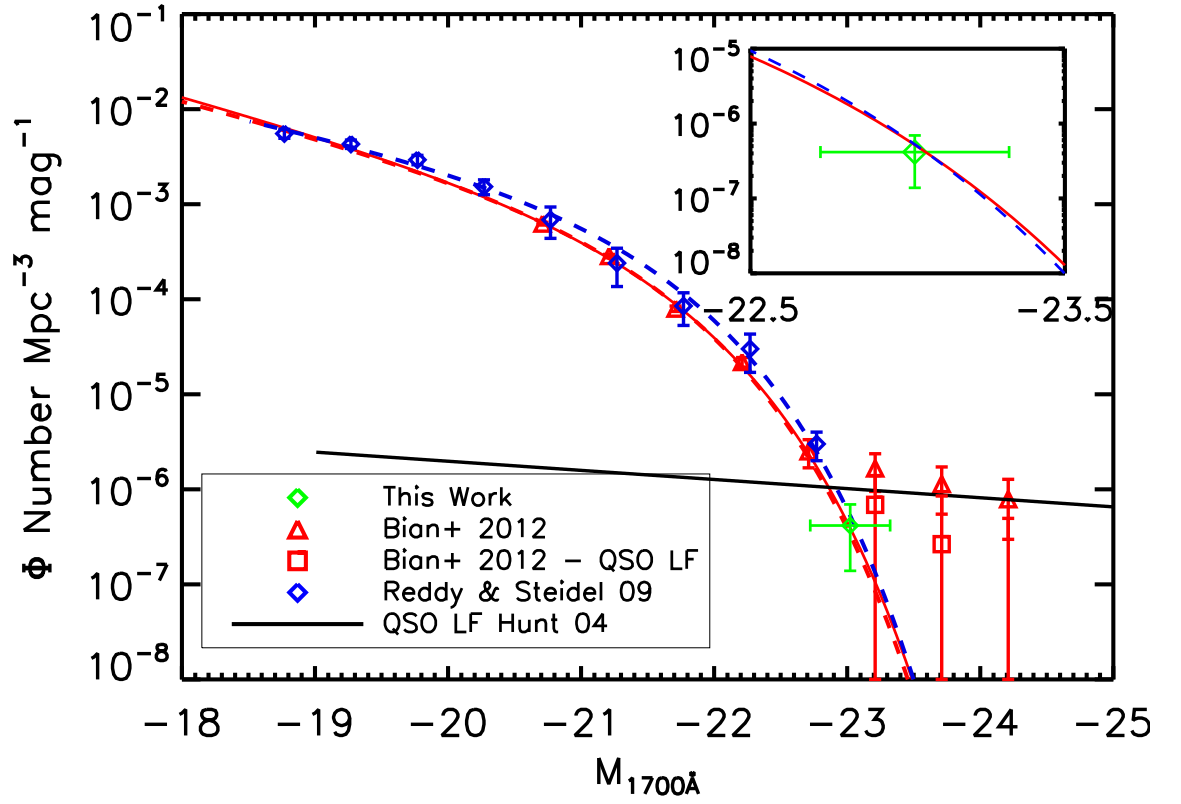


Figure 5.2: Rest-frame UV LF of ULBGs. The red data points and curve are the LF measurements and best-fitted Schechter function from Bian et al. (2012), and the blue data points and curve are the LF measurements and best-fitted Schechter function from Reddy & Steidel (2009). The green data point is the LF measurement of the ULBG sample, which probes the luminosity regime that has never been studied before.

with $M_{\text{UV}} < -22.5$ with the first spectroscopically-confirmed LBG sample in this luminosity regime.

We used the same method in Bian et al. (2012) to measure the UV LF. (1) A library of LBG spectral energy distribution (SED) templates was generated using BC03 stellar synthesis model (Bruzual & Charlot, 2003); (2) the SED templates are modified by the IGM attenuation (Madau, 1995) and dust extinction (Calzetti et al., 2000); (3) the magnitudes of U , B_w , R , [3.6] and [4.5] bands were derived by convolving the SED templates through the filter throughput; (4) fake objects with the broad-band magnitudes derived from SED templates were put on the real images and the same procedures that we used in the real data were applied to detect the objects and measure the magnitudes; and (5) the same selection criteria are used to obtain the selection completeness as a function of redshifts (see more details in Bian et al. 2012). As the ULBGs are selected with the resolved extended morphology, this could result in a bias towards selecting large size of the LBGs. Law et al. (2012) systematically studied the rest-frame UV/optical morphology of UV-selected galaxies with HST/WFC3 and classified the galaxies into three types: Type I: Single nucleated sources; Type II: Two or more distinct nucleated sources; Type III: Highly irregular objects with extended features. We use a sample of representative Galfit models of the LBGs provided by D. Law (private communication). We adjust the brightness of the Galfit models to 22.5 magnitude, convolve the profile with $1''$ gaussian profile, and put them on the real R -band image. SExtractor is used to detect galaxy models and analyze the light distribution. Finally, we found that about 70% of the modeled galaxies could be resolved. Therefore, we correct the LF measurements by multiplying a factor of 1.5.

Figure 5.2 shows the results of the rest-frame UV LF of LBGs at $z \sim 3$ in this

work and previous studies. Bian et al. (2012) used a sample of photometrically-selected LBGs in Boötes field to measure the bright end of the UV luminosity function (red triangles in Figure 5.2, and found an excess of LF at the bright end compared to best-fitted Schechter function. This excess is mainly due to the contribution of the QSO LF. The systematic error of the bright LF derived from the photometrically-selected LBG sample is large and the faint end of the QSO LF is not well constrained (e.g., Siana et al., 2008). These two factors make it difficult to compare the best-fitted Schechter function with the residual values (red squares in Figure 5.2) derived from the difference between the LBG LF and the QSO LF. In Figure 5.2, we show the LF measurement with the ULBG sample in this work with green diamond. This is the first UV LF measurement at this luminosity regime with a sample of spectroscopically-confirmed LBGs. The result is consistent with the best-fitted Schechter functions derived from the LBGs with the absolute magnitude of $M_{UV} > -22.5$ in Bian et al. (2012) (red solid line) and Reddy & Steidel (2009) (the blue dashed line).

5.3.4 Rest-frame UV Spectrum of Ultra-luminous LBGs

The S/N of each individual spectrum is low, therefore, we combine the spectra of the spectroscopically-confirmed LBGs to obtain a relatively high S/N rest-frame UV composite spectrum. Figure 5.3 shows the composite rest-frame UV spectrum (blue curve) of the most luminous LBGs ($L > 5L^*$). For comparison, we also plot the rest-frame UV composite spectrum of typical LBGs from Shapley et al. (2003), in which about 800 LBG spectra are used, and luminosities of most of the LBGs in Shapley et al. (2003) are between $0.4L^*$ and $1L^*$, which is 5-10 times fainter than the ULBGs. Both spectra are normalized with the continuum flux density between 1300Å and 1400Å. For the first glance, these two spectra are quite similar to each other. Both spectra show prominent Ly α emission, and

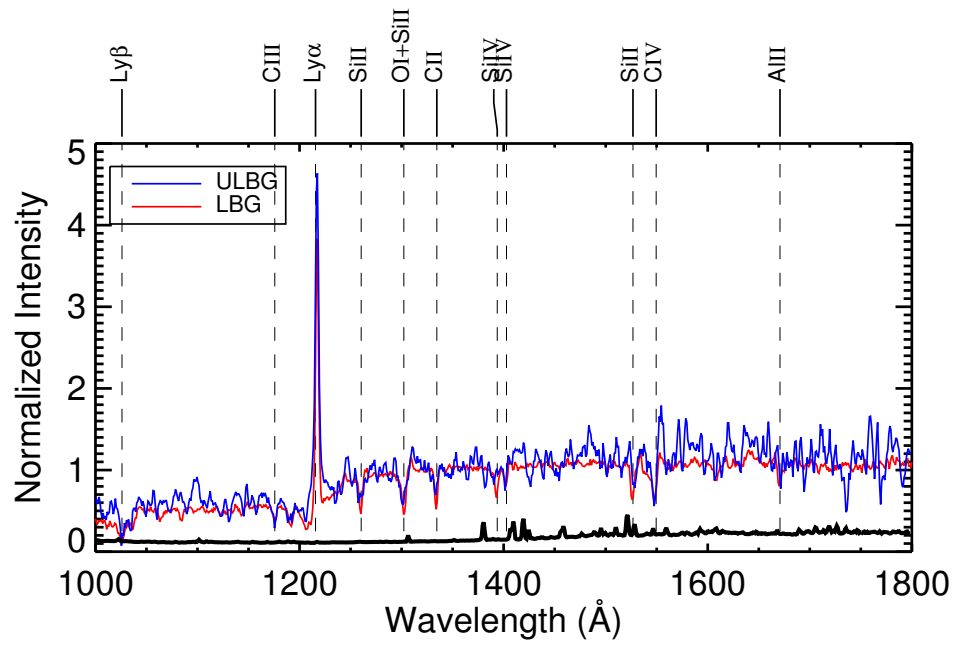


Figure 5.3: Rest-frame UV composite spectrum of ULBGs (blue curve). For comparison, the composite spectrum of typical LBGs is also plotted (red curve)

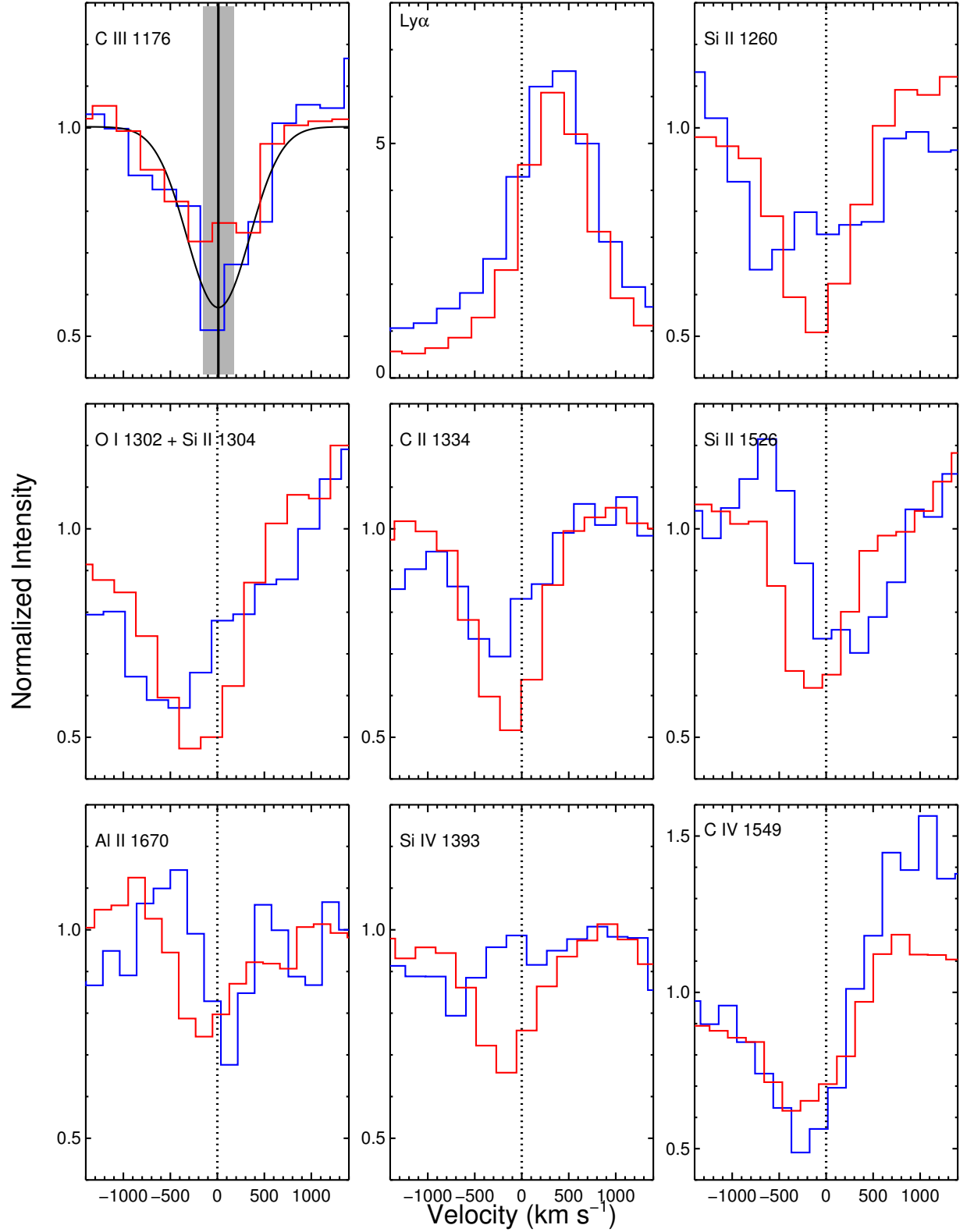


Figure 5.4: Zoom-in spectra of C II stellar photospheric absorption line, Ly α emission line, low ionized ISM absorption lines, and high ionized ISM absorption

absorption features of $\text{Ly}\beta$, C III, Si II, O I+Si II, C II, Si II, and C IV. The ISM absorption line features in typical LBGs are deeper than those in ULGs, implies a smaller covering fraction in ULGs. We applied Gaussian functions to fit the line profile of the $\text{Ly}\alpha$ emission line and the well-detected ISM absorption lines in the composite spectrum of the ULGs, and listed the fitting results in table 5.2. These lines in ULGs have similar rest-frame EW, broader line profile, and bluer central wavelength compared to those in typical LBGs (Shapley et al., 2003).

5.3.4.1 Systemic Redshift

The systemic redshift of the individual galaxy is important to construct the ULBG composite spectrum. The uncertainty of the systemic redshift of the individual galaxy could make the line shallower and the line width broader, and the systematic uncertainty of the systemic redshift would shift the center of the lines in the composite spectrum. The $\text{Ly}\alpha$ emission lines and the ISM absorption lines can not be used to measure the systemic redshift, because the wavelengths of these lines are affected by the outflows. Ideally, the stellar photospheric absorption lines (e.g. C III $\lambda 1176$, O IV $\lambda 1343$, and S V $\lambda 1501$) could be used to measure the systemic redshift through rest-frame UV spectra (Dey et al., 1997), but it is difficult to detect these weak absorption lines in the individual low S/N spectrum. Another method is to use the nebular emission lines (e.g. [O II], $\text{H}\alpha$) associated with H II regions to measure the systemic redshift (Steidel et al., 2010). A secondary method was also developed based on the systemic redshift measured with the nebular emission lines. With this method, the redshifts derived from $\text{Ly}\alpha$ and/or ISM absorption lines can be corrected to the systemic redshifts (Adelberger et al., 2003; Steidel et al., 2010). In this work, we cross-correlate the individual ULBG spectrum to the LBG templates to derive the redshift of the LBGs. As the redshifts of the LBG templates are well-calibrated with this secondary method (Shapley

et al., 2003), the measured redshifts should be close to the systemic redshifts. In the composite ULBG spectrum, the C III $\lambda 1176$ stellar photospheric line is well detected in 10σ . In Figure 5.4, we show the C III $\lambda 1176$ lines in this work and in (Shapley et al., 2003). A Gaussian function was used to fit the C III line profile, and we found a velocity offset of $\Delta v = 10 \pm 163 \text{ km s}^{-1}$. This demonstrates that the systematic shift of the rest-frame UV spectrum is small. The statistical uncertainty of the redshift from this cross-correlation method is about 100 km s^{-1} , which has been removed when we calculate the FWHM of the lines.

5.3.4.2 Galactic-scale Outflows

In the section 5.3.4.1, we have demonstrated that the wavelength of the ULBG composite spectrum is quite close to the rest-frame wavelength based on the well centered C III absorption line. Therefore, the offset velocity of the ISM absorption lines in the rest-frame UV spectrum respective to the line rest-frame wavelength could be used to study the outflow kinematic properties in these luminous LBGs. In Figure 5.4, we show the velocity profile of $\text{Ly}\alpha$ emission line, low ionization ISM absorption lines of Si II, O I+Si II, C II, and Si II, and high ionization ISM absorption lines of Si IV and C IV in the luminous LBGs (blue curves) and typical LBGs (red curves). The well detected ($S/N \gtrsim 3$) low ionized absorption lines, including Si II $\lambda 1226$, O I $\lambda 1302$ +Si II $\lambda 1304$, and C II $\lambda 1334$, in the luminous LBGs show broader line profile and more blueshifted component than those in typical LBGs, which suggests a larger outflow velocity in the ultra-luminous LBGs. We use the Si II $\lambda 1260$ and C II $\lambda 1334$ to derive the outflow velocity, as the S/N s of Si II $\lambda 1526$ and Al II $\lambda 1671$ lines are low, and the O I $\lambda 1302$ and Si II $\lambda 1304$ lines are blended, thus the central wavelength could be affected by the relative flux of these two lines. We found that the average outflow velocity derived from these two ISM absorption lines is $\Delta v = 280 \pm 110 \text{ km s}^{-1}$ in the ULBGs. We averaged the

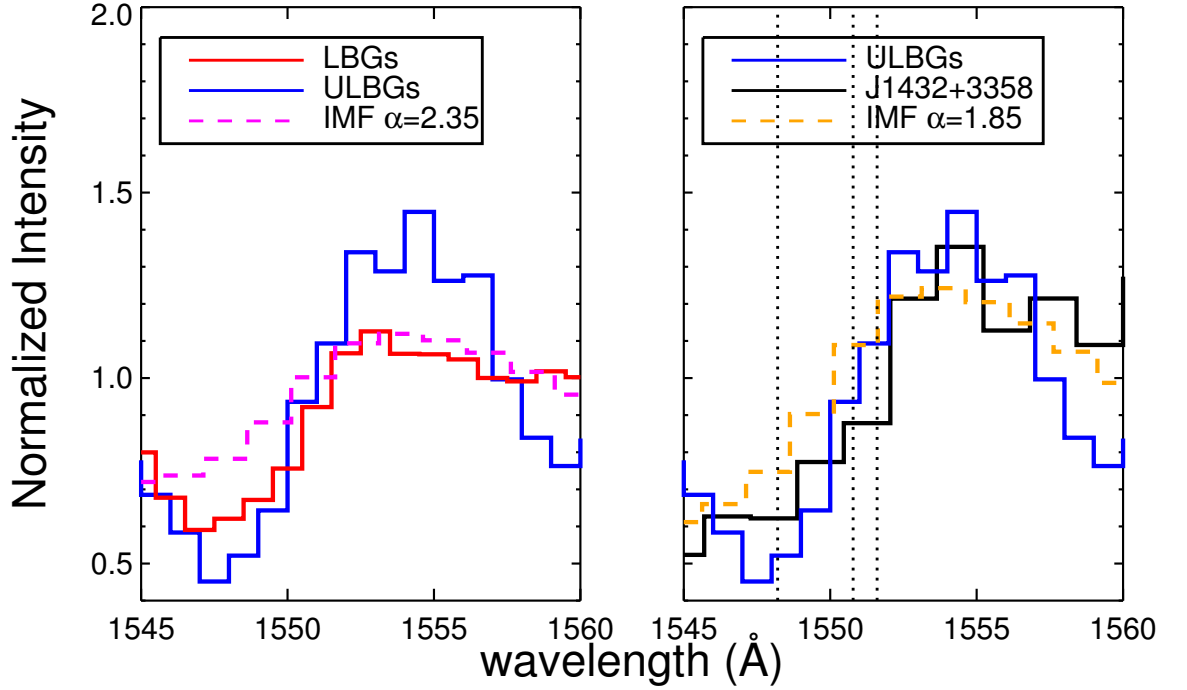


Figure 5.5: The P-Cygni profile of the C IV and model spectra with different IMF.

outflow velocities of the S II $\lambda 1260$ and C II $\lambda 1334$ lines in the Table 1 in Shapley et al. (2003), and found $\Delta v = -130 \text{ km s}^{-1}$. This result is comparable to the outflow velocity of $164 \pm 16 \text{ km s}^{-1}$ in Steidel et al. (2010). Thus, the outflow velocity in ULBGs is twice that of typical LBGs.

5.3.4.3 Initial Mass Function

In Figure 5.4, the C IV line shows a prominent P-Cygni profile. This feature mainly forms in the stellar winds of the most massive OB stars. The strength of the C IV P-Cygni feature relative to the UV continuum is sensitive to the shape of the initial mass function (IMF) (e.g., Steidel et al., 2004). The relative strength increases with the increasing population of star at high mass end of IMF (e.g., shallower power-law slope, α , a higher mass cutoff at the high mass end, M_{up}).

We used the STARBURST99 model spectra with different IMF slopes to fit the P-Cygni profile in the composite spectrum of the ULBGs. To generate the theoretical UV spectrum, we use the 400 Myrs of continuous star formation history, with one solar metallicity. Actually, the far-UV spectrum is not sensitive to the age beyond the ages > 100 Myr for a continuous star formation history. Two types of IMF are used, $\alpha = 2.35$ (Salpeter IMF) and $\alpha = 1.85$ (top-heavy IMF), with the $M_{up} = 100 M_{\odot}$. All the theoretical and observed spectra are normalized by the UV continuum at the wavelength range between 1570\AA and 1650\AA , and the theoretical spectra are smoothed by a Gaussian filter to the same resolution of the observed spectrum. Figure 5.5 shows the observed spectrum and two theoretical spectra with Salpeter IMF and top-heavy IMF, which suggests that the Salpeter IMF could fit the C IV P-Cygni profile in the typical LBGs very well, but underproduces the C IV P-Cygni profile in the ULBGs and the top-heavy IMF can fit the P-Cygni profile of the ULBGs much better. This result is not consistent with previous studies, which found that the IMFs in a few well-studied L^* galaxies at redshift of $z \sim 1 - 3$ agree with a universal Salpeter IMF (e.g., Pettini et al., 2000; Steidel et al., 2004; Quider et al., 2010).

5.3.5 IRAC Colors

As is mentioned in section 5.2.1, the IRAC colors are useful to eliminate the low redshift interlopers and to separate LBGs from QSOs/AGNs. In Figure 5.6, we show the IRAC colors of LBGs (the black triangles) and QSOs (the red diamonds) in $[3.6] - [4.5]$ versus $[5.8] - [8.0]$ IRAC color-color diagram. The solid lines circle a empirical selection region of QSOs/AGNs from Stern et al. (2005). The typical errors of the IRAC colors of LBGs and QSOs are shown at the right bottom of the plot. The large uncertainty of $[5.8] - [8.0]$ makes it hard to judge whether or not an individual object is in the QSOs/AGNs selection region. But with a sample of

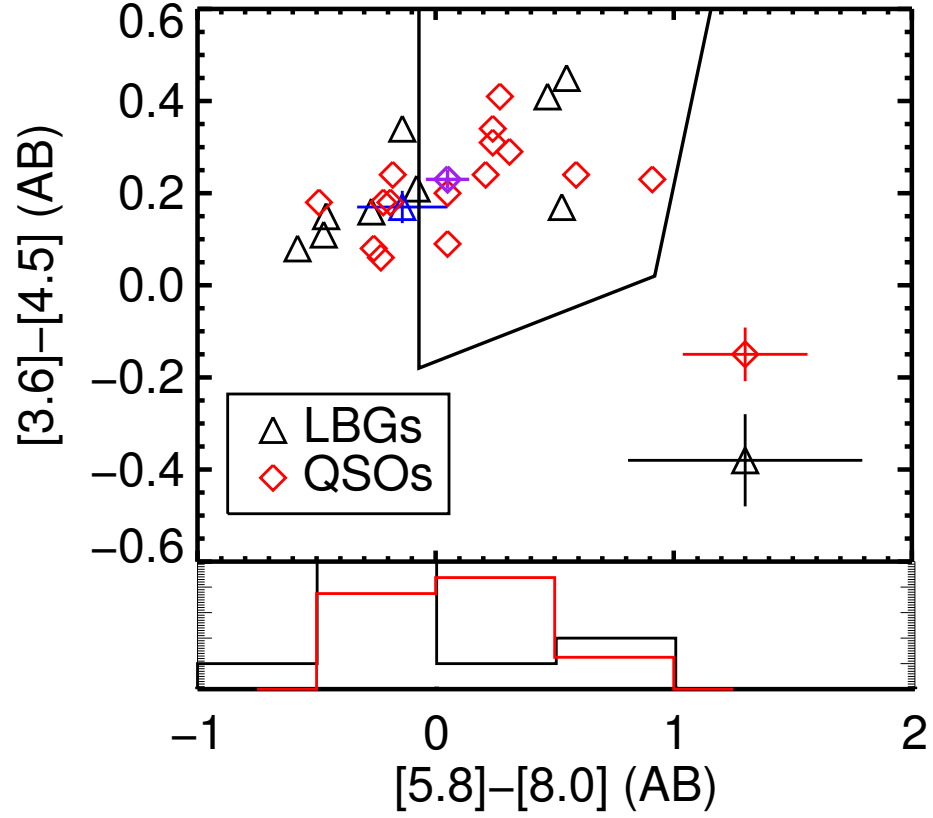


Figure 5.6: Distribution of LBGs and QSOs in the $[3.6] - [4.5]$ versus $[5.8] - [8.0]$ color-color diagram. The region enclosed by the black solid line is the AGN/QSOs selection region. The blue triangle represents the average color of the LBG sample and the pink diamond represents the average color of the QSO sample.

LBGs, we can check the trend that whether or not the IRAC colors of LBGs prefer to locating in the QSO/AGN selection region.

The distribution histogram of $[5.8] - [8.0]$ color of LBGs and QSOs/AGNs is shown at the bottom of the Figure 5.6. The distribution of $[5.8] - [8.0]$ color in LBGs peaks between -0.5 and 0.0, which is out of the QSOs/AGNs selection region. This indicates that a large fraction of LBGs (67%) are out of the QSOs/AGN selection region. On the other hand, the distribution of $[5.8] - [8.0]$ color in QSOs/AGNs is redder, which spreads from -0.5 to 0.5. The average $[3.6] - [4.5]$ and $[5.8] - [8.0]$ colors of the LBG (blue triangle) and QSO/AGN (purple diamond) sample are also shown in Figure 5.6. The average IRAC colors of the LBG sample is at the edge of the QSO/AGN selection region, and the average $[5.8] - [8.0]$ color in the LBG sample is bluer than that in the QSO/AGN sample, but they are consistent with each other within the uncertainty. From both the distribution of $[5.8] - [8.0]$ color and the average of $[5.8] - [8.0]$ color, we find a trend that the LBGs sample has bluer $[5.8] - [8.0]$ color than the QSO/AGN sample. This trend is consistent with the fact that the galaxy SED turnovers between $5.8 \mu\text{m}$ and $8.0 \mu\text{m}$ at $z \sim 3$, while the AGN/QSO SED keeps increasing from $5.8 \mu\text{m}$ to $8.0 \mu\text{m}$. This color trend suggests that stellar population features dominate the emissions between $5.8 \mu\text{m}$ and $8.0 \mu\text{m}$ and AGN activity level is weak in these LBGs.

It is worth noting that about half of the QSOs/AGNs are out of the QSO/AGN selection wedge, and the morphology of the QSOs shows extended structures. This could imply that the emissions from the QSO host galaxy are comparable to those from QSO itself. The QSOs in this work are about 1-2 magnitude fainter than those in previous QSO surveys (e.g., SDSS), which allows us to probe the luminosity regime where the brightness of QSO host galaxies is similar to that of QSO. This QSO sample could be the best QSO samples to study the relation

between AGNs and their host galaxies at high redshift.

5.3.6 Physical Properties

We applied an IDL-based code FAST (Fitting and Assessment of Synthetic Templates, Kriek et al., 2009) to fit the broad band (U , B_W , R , I , Y , IRAC1, IRAC2, IRAC3, and IRAC4) photometry to derive the physical properties of the luminous LBGs. The stellar population synthesis models from Bruzual & Charlot (2003) with Salpeter IMF (Salpeter, 1955) and solar metallicity were used to construct the theoretical spectral energy distributions (SEDs) of the galaxy. We adopted a continuous star formation history with constant SFR (e.g., Erb et al., 2006a). The SEDs are modified by the dust extinction law proposed by Calzetti et al. (2000) and the intergalactic medium (IGM) absorption model from Madau (1995). In the fitting process, we constrain the ages of the galaxies between 20 Myr and 2 Gyr. The lower limit is the dynamical timescale of the LBGs (e.g., Shapley et al., 2001), and the upper limit is the age of the universe at $z \sim 3$. The best-fitted SED model and the photometric data points are shown in Figure 5.7. The physical properties of these galaxies on the stellar mass (M_{stellar}), the SFR, the dust extinction ($E(B-V)$), and the galaxy age (t_{sf}) are derived from the fitting and listed in Figure 5.7.

Figure 5.8 shows the distribution of the stellar mass (M_{stellar}), SFR, $E(B-V)$, and galaxy age (t_{sf}) of the ultra-luminous LBGs (black histogram). These physical properties have been well studied in typical LBGs at $z = 2 - 3$. Shapley et al. (2001) used the Ks -band imaging observations from Keck/NIRC of a sample of $z \sim 3$ LBGs with the luminosity of $\approx L^*$, and Shapley et al. (2005) extended the study using the Spitzer/IRAC mid-infrared observations of a sample of $z \sim 2$ L^* LBGs. For comparison, we also show the distribution of these physical properties in Shapley et al. (2001) (red histogram) and Shapley et al. (2005) (blue histogram) in Figure 5.8. There is a trend that the ULBGs have larger stellar mass and higher

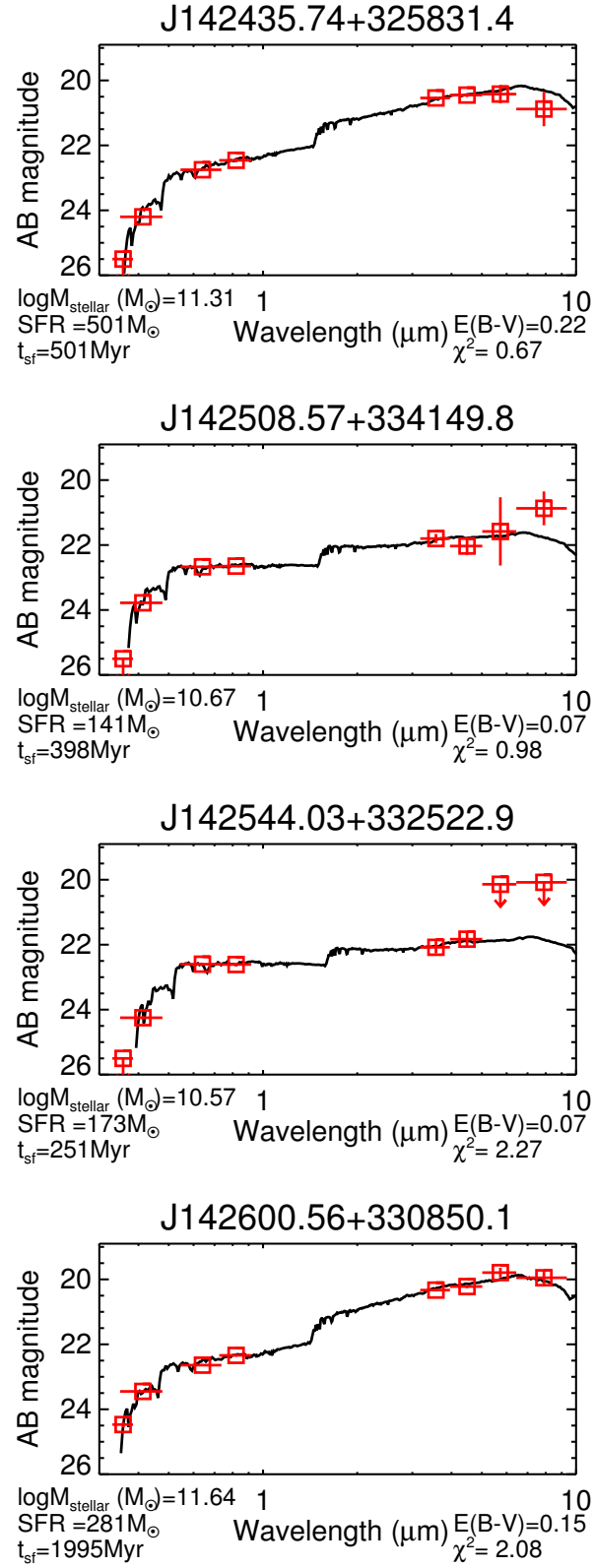


Figure 5.7: Broad band photometry SED fitting results.

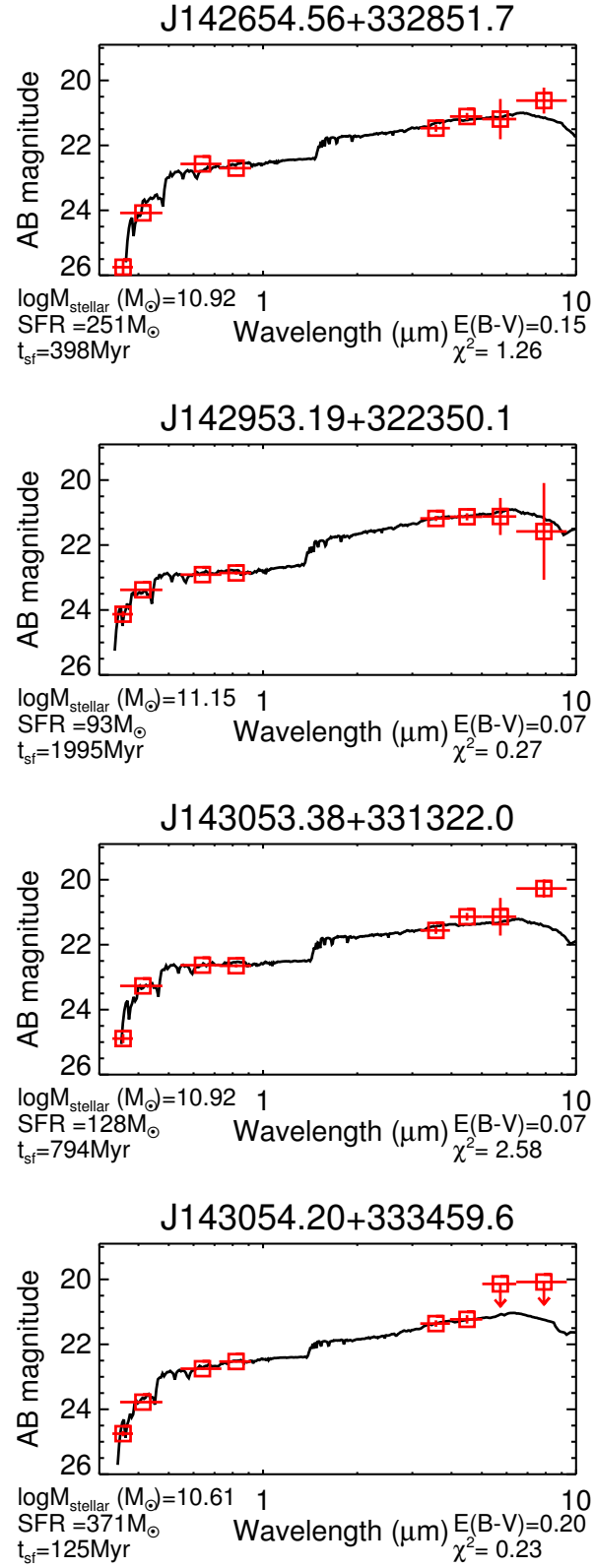


Figure 5.7: Continued figure.

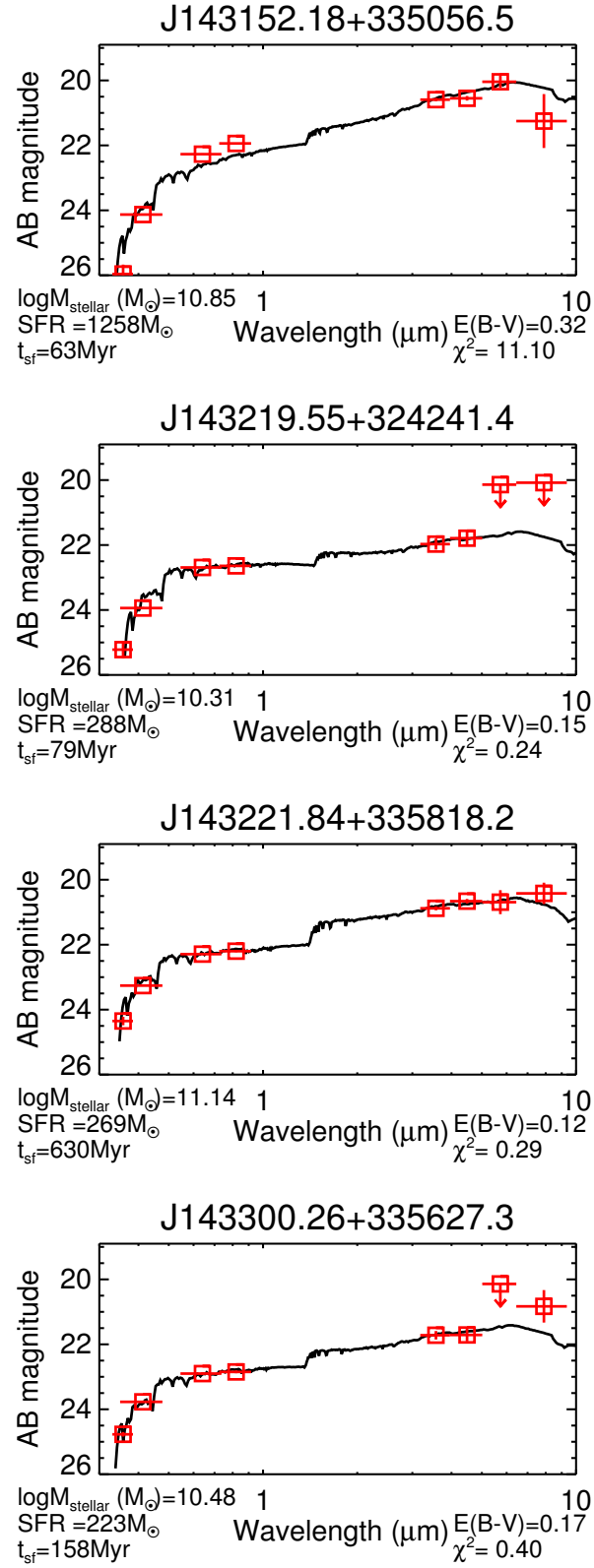


Figure 5.7: Continued figure.

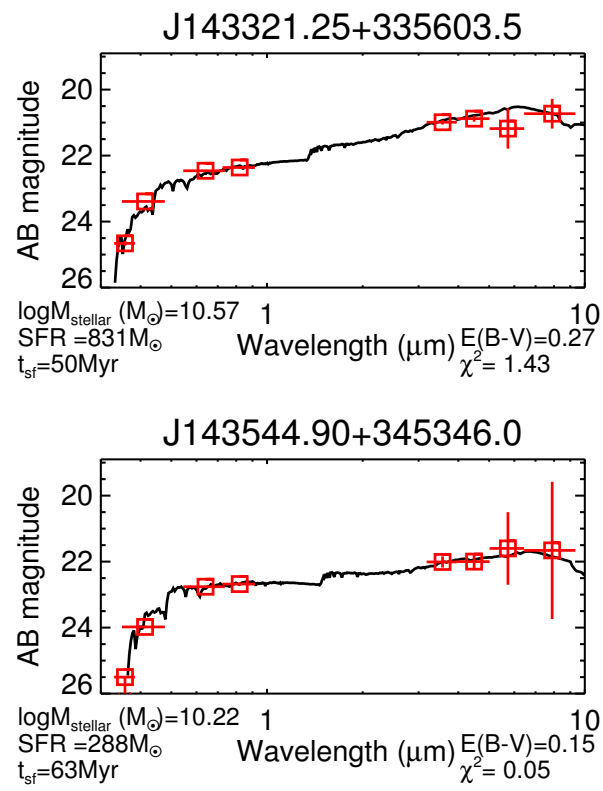


Figure 5.7: Continued figure.

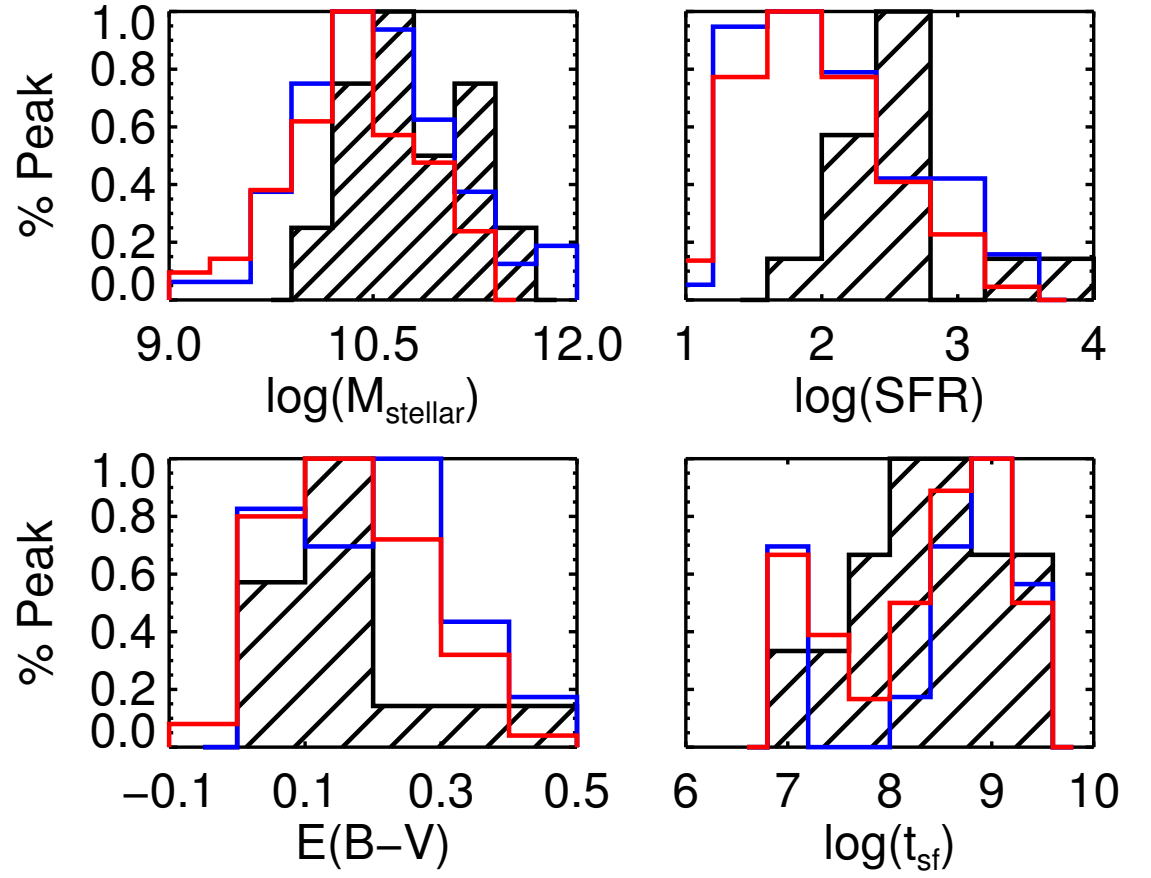


Figure 5.8: Distribution of stellar mass, SFR, $E(B - V)$ and age of ULBGs (Black), $z \sim 3$ LBGs (red) and $z \sim 2$ UV-selected galaxies (blue).

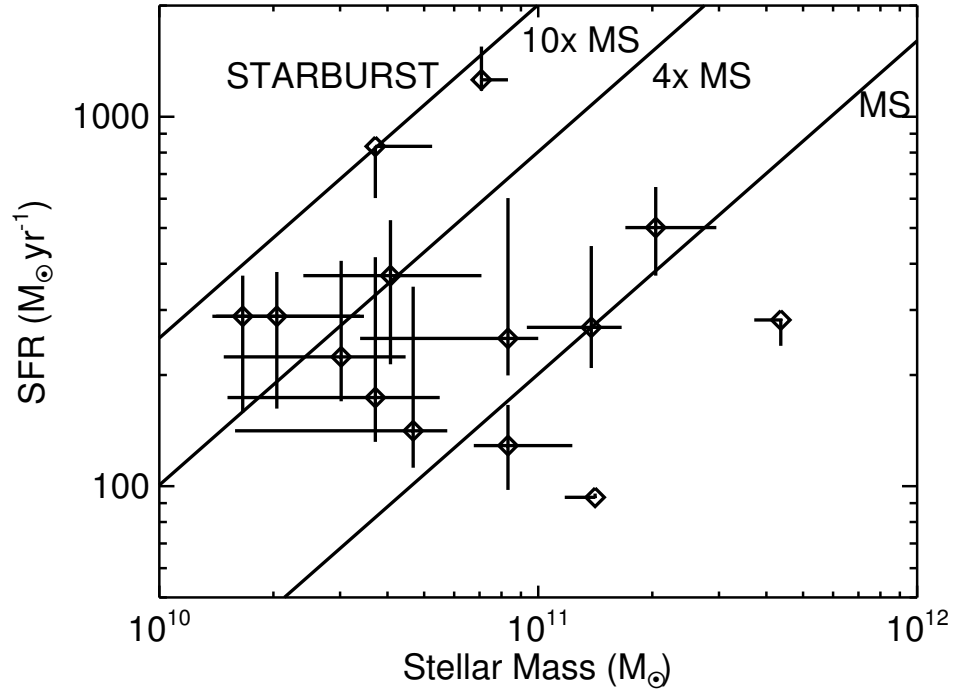


Figure 5.9: SFR and stellar mass relation of ULBs. The SFR and stellar mass are derived from the broad band SED fitting. The solid lines represent the relation of main sequence (Daddi et al., 2007), and the SFRs are four times ($4 \times \text{MS}$) and ten times ($10 \times \text{MS}$) higher than those in main sequence galaxies for a given stellar mass.

SFR, but smaller dust extinction (Table 5.3). The physical properties of these two subsample of LBGs are shown in Table 5.3.

5.4 Discussion

5.4.1 Evolutionary Stage of ULBGs

In Figure 5.9, we show the SFR and stellar mass relation of the ULBGs. Both SFR and stellar mass are derived from the SED fitting. The SFRs from the SED fitting and those derived from the dust corrected UV luminosity are consistent with each other. A tight correlation (main sequence, MS) between SFR and stellar mass has been found in star-forming galaxies both in the local Universe and at high redshifts (e.g. Peng et al., 2010b; Daddi et al., 2007). The galaxies on the main sequence play an important role on the stellar mass build-up process in the early Universe (e.g., Rodighiero et al., 2011). The outliers of the MS have high specific SFRs ($s\text{SFR} = \text{SFR} / M_{\text{stellar}}$), such as ultra-luminous infrared galaxies (ULIRGs) and submillimeter galaxies (SMGs). The high specific SFR could probably be driven by major mergers. Here we adopt the main sequence (MS) relation found in $z \sim 2$ star-forming galaxies (Daddi et al., 2007) and we consider a galaxy in an off MS stage if the $s\text{SFR}$ of the galaxy is 4 times larger than that in the typical MS galaxy. The $4\times\text{MS}/10\times\text{MS}$ line in Figure 5.9 presents that the $s\text{SFR}$ s are 4 times/10 times higher than those in MS relation. We find that majority of the ULBGs (11/14) locates above the MS relation, but only 5 out of 14 galaxies locate above the $4\times\text{MS}$ line, and none of the galaxies locates above the $10\times\text{MS}$ line. Therefore, the star formation in ULBGs is more active than that in typical MS star-forming galaxies, but less active than that in SMGs. This suggests that these ULBGs are probably in a transition phase between the starburst phase and the main sequence galaxies. The low number density ($\sim 10^{-7} \text{ Mpc}^{-3}$) of the ULBGs implies that this transition

phase is short. In the following paragraphs, we will discuss two evolutionary scenarios for these ULBGs: the post-starburst and pre-starburst scenarios.

5.4.1.1 Post-starburst Scenario

Shapley et al. (2001) propose an evolutionary track between the young L^* LBGs and old L^* LBGs. The young L^* LBGs with the age younger than 35 Myr have higher SFRs ($\sim 420 M_{\odot} \text{ yr}^{-1}$), higher dust extinction ($E(B - V) = 0.26$), and lower stellar mass ($5.8 \times 10^9 M_{\odot}$) than old LBGs with the age of ~ 1000 Myr (Table 5.3). The young LBGs are in a dusty starburst stage. After this stage, the SFRs decrease and the dust extinction becomes lower, because dust is destroyed and/or blown out. Finally, the galaxies evolve into the old L^* LBG stage, with moderate SFR ($\sim 50 M_{\odot} \text{ yr}^{-1}$) and dust extinction ($E(B - V) = 0.10$), and high stellar mass ($8.0 \times 10^{10} M_{\odot}$). As shown in Table 5.3, the SFRs, dust extinction and the stellar mass in ULBGs are right between those in young LBGs and old LBGs. Therefore, the ULBGs are probably in a quick transition phase between the ‘young’ and ‘old’ LBGs. In this scenario, the timescale of the dust destruction is shorter than the timescale of the SFR decay. In the ULBG stage, the SFRs are still high, but the dust extinction in the LBGs has been significantly reduced. Thus these galaxies show extremely high UV luminosity ($L > 5L^*$). The number density of ULBGs is 3 orders of magnitude lower than that of L^* galaxies, considering that the whole evolution timescale from the ‘young’ LBGs to the ‘old’ LBGs is about 1000 Myr, thus the timescale of the ULBG phase is about 1 Myr.

The caveats of this scenario are: (1) The ‘young’ LBG population is more likely to follow the SMC-like extinction law rather than Calzetti et al. (2000) law. This will affect the estimation of the physical properties significantly, which may change the evolution picture from the ‘young’ LBGs to the ‘old’ LBGs; (2) Bian et al. 2012 show that the star formation in L^* LBG is driven by the cold flow process

rather than the starburst mode; and (3) the galaxy size of the ULBGs should be right between the ‘young’ and ‘old’ galaxies, but the large galaxy size may rule out that the ULGs are in the post-starburst phase.

5.4.1.2 Pre-starburst Scenario

The large size and/or multiple nuclei morphology of the LBGs indicate that the ULBGs are in the pre-starburst phase. Hopkins et al. (2008) propose an evolutionary track from a normal star-forming galaxy to a gas-rich major merger (see a schematic outline in Figure 1 in Hopkins et al., 2008). The ULBGs could fit into this scenario. The morphology of ULBGs implies that the ULBGs are at the early stage of major merger, i.e. the phase (c) in Figure 1 in Hopkins et al. (2008). In this phase, the two interacting galaxies are within the same dark matter halo but still well separated and can be identified as a merger pair (e.g., Lotz et al., 2004). In this situation, the SFR in the galaxies begins to increase to $\sim 100 M_{\odot} \text{ yr}^{-1}$ due to the tidal torques, but the enhanced effect of the SFR is relatively weak compared to the latter coalescence phase, and the AGN activity in this phase is relatively low. The timescale of this phase is about several million years.

The properties of the ULGs, especially the morphologies, prefer the pre-starburst scenario, but it is difficult to make a solid conclusion from the limited information of the ULBGs. The major merger is not the only process that can boost the SFR, the minor merger and/or smooth cold flow stream could also enhance the SFR to a few hundred solar mass per year (Davé et al., 2010). The follow-up observations, especially the high resolution HST WFC3 imaging and the ground-based integral field unit spectroscopic observations, are necessary to distinguish the different evolutionary phases and test whether the high SFRs are triggered by the major merger or cold flow accretion.

5.4.2 Outflows Velocity in LBGs

The galactic-scale outflows play a crucial role in regulating the efficiency to convert the baryon materials into stars and the chemical abundances in galaxies (e.g., Finlator & Davé, 2008). The outflow winds have been found in both nearby starburst galaxies (e.g., Heckman et al., 2000) and high-redshift galaxies (e.g., Pettini et al., 2000; Shapley et al., 2001; Weiner et al., 2009; Steidel et al., 2010) based on the blueshifted ISM absorption lines.

Two major models, energy-driven winds (e.g., Larson, 1974) and momentum-driven winds (e.g., Murray et al., 2005a), are proposed to interpret the outflows in star-forming galaxies. In previous studies, it has been found that the outflow velocity increases with the SFRs, with the relation of $V \sim \text{SFR}^{0.30-0.35}$, in both local ULIRGs (Martin, 2005) and $z \sim 1.4$ star-forming galaxies (Weiner et al., 2009). This relation supports the momentum-driven wind model, in which the galactic-scale outflows are driven through the radiation pressure (e.g., Murray et al., 2005a). However, there is no strong correlation between SFR and outflow velocity found in LBGs (Steidel et al., 2010). This result could be due to the small dynamic range of the SFR in their LBG sample (Steidel et al., 2010). Our ULBG sample, together with the faint LBG sample, provides a larger SFR dynamic range allowing us to revisit this problem. The median R magnitude of the LBGs for creating the composite spectrum in Shapley et al. (2001) is 25.0, which is about 10 times fainter than the ULBGs. If we assume the dust extinction is similar in these two LBG samples, the SFRs of ULGs are about 10 times higher than those of the LBGs in Shapley et al. (2001), and the average outflow velocity of ULBGs is about 2 times higher than that of LBGs in Shapley et al. (2001). We find that the relation between outflow velocity and SFR is $V \sim \text{SFR}^{0.3}$. This suggests that the $z \sim 3$ LBGs follow the same SFR and outflow velocity relation as is found in local

ULIRGs and $z \sim 1.4$ star-forming galaxies, and the outflows in LBGs are driven by the radiation pressure from massive stars.

We should admit that the outflow results are based on the relatively low S/N composite spectrum of fourteen ULBGs, especially for the measurements of the absorption lines. In this composite spectrum, the low ionized Si II $\lambda 1526$ and Al II $\lambda 1671$ even shows redshifted velocity rather than blueshifted velocity. The strength of these two lines is relatively weak, and even worse the observed-frame wavelength of those two lines is around 6000-6500Å, where the MMT/BCS sensitivity becomes quite low. The S/Ns of those two lines are $\lesssim 2.0$. Further high S/N spectroscopic observations will help us draw a firm conclusion on the outflow velocities of these ULBGs.

5.4.3 Initial Mass Function

Compared to typical LBGs, a more prominent P-Cygni profile of C IV was found in the ULBGs. In § 5.3.4.3, this profile is interpreted as it is due to a top heavy IMF in the ULBGs. Other effects could also produce the strong C IV P-Cygni profile.

First, metallicities could affect the strength of C IV emission, and the higher metallicity could produce stronger C IV emissions. In this work, we use the solar metallicity to generate the starburst99 model spectrum. If the metallicity in these ULBs is much higher than solar metallicity, even standard Salpeter IMF could produce such strong C IV P-Cygni profile in the ULBGs. The major rest-frame optical lines of most of the ULBGs in our sample do not fall in the atmosphere transmission window in near-IR, thus we could not directly measure the metallicities in the ULBGs with these optical diagnostic lines (e.g., Hainline et al., 2009; Bian et al., 2010). We use the mass-metallicity relation in $z \gtrsim$ UV-selected galaxies to estimate the metallicities in these ULBGs (Erb et al., 2006a). We found that the metallicities ($12+\log (\text{O}/\text{H})$) in these galaxies are about 8.52, ~ 0.17 dex smaller

than solar metallicity (Asplund et al., 2009). Therefore, these ULBGs are unlikely to have super solar metallicity to produce the prominent C IV profile.

Secondly, a population of young star with age of less than 100 Myr could also produce stronger C IV emission. We use the starburst99 to generate the model spectra with different ages of the galaxies. The C IV P-Cygni profile in model spectra were compared with that in the observed composite spectrum. To produce such strong C IV P-Cygni profile in the ULBGs, it requires that the age of the star population as young as 5-10 Myr. This age is much smaller than the dynamical time scale of the LBGs of ~ 50 Myr and the median age of the ULBGs of ~ 400 Myr, therefore, it is difficult to produce the strong C IV P-Cygni profile in the ULBGs by a population of young stars.

Although super-solar metallicities and a extremely young stellar population could also produce the strong C IV P-Cygni profile in the ULBGs, the physical properties of ULBGs suggests that the ULBGs are unlikely to have either high metallicities or a extremely young stellar population, thus the shape of the IMF is the dominant factor to affect the strength of C IV profile in this case. The more top-heavy/bottom light IMF corresponds to higher SFRs in the LBGs. Narayanan & Davé (2012b) found the similar trend in their cosmological simulations, in which the Kroupa IMF broken power-law turnover mass increases with SFRs (Kroupa, 2001). This indicates more top-heavy/bottom light IMF in higher SFR galaxies.

5.5 Summary and Conclusions

We have presented a population of ultra-luminous LBGs. Total 14 luminous $z \sim 3$ LBGs with $R \lesssim 22.8$ ($L > 5L^*$) are discovered in the Boötes field. The large survey area of Boötes field (9 deg^2) allows us to reveal these luminous galaxies at $z \sim 3$.

We summarize the conclusions as follows:

1. With the new spectroscopically-confirmed ULBG sample, the rest-frame UV LF at $M_{1700\text{\AA}}^{\circ} = -23.0$ is measured for the first time. After correcting the incompleteness due to the morphology pre-selection method, the LF is consistent with the best-fitted Schechter function extrapolating from the UV LF measurements at $M_{1700\text{\AA}}^{\circ} > -22.5$ very well.
2. The composite spectrum of the ULBGs is quite similar to that of typical LBGs. However, the ULBGs show larger outflow velocity and broad $\text{Ly}\alpha$ emission and ISM absorption line profiles. The much more prominent C IV P-Cygni profile may imply a top-heavy IMF in these ULBGs.
3. The distribution of these ULGs in the IRAC $[3.6] - [4.5]$ versus $[5.8] - [8.0]$ color-color diagram suggests that stellar population features dominate the emissions between $5.8\mu\text{m}$ and $8.0\mu\text{m}$ and AGN activity level is weak in these LBGs.
4. From the SED fitting, we obtain the SFRs, dust extinctions, stellar masses and ages of these ULBGs, and find that the ULBGs have larger stellar mass and SFR, but smaller dust extinction than the typical L^* LBGs at $z \sim 2 - 3$.
5. Two evolutionary scenarios, pre-burst and post-burst, are considered and the properties of the ULGs, especially the morphologies, prefer the pre-starburst scenario. Further high spatial resolution HST imaging and IFU spectroscopic observations will allow us distinguish these two scenarios.

Table 5.2: Ly α emission and strong interstellar absorption lines.

| line | $\lambda_{\text{rest}}^{\text{a}}$ | λ_{obs} | EW | FWHM | Δv^{b} |
|-------------|------------------------------------|------------------------|------------------|----------------|-----------------------|
| | Å | Å | Å | km s $^{-1}$ | km s $^{-1}$ |
| Ly α | 1215.67 | 1217.16 ± 0.04 | 21.07 ± 0.77 | 874 ± 23 | 366 ± 10 |
| Si II | 1260.42 | 1259.73 ± 0.71 | -2.43 ± 0.61 | 1718 ± 437 | -165 ± 167 |
| O I+Si II | 1303.27 | 1301.01 ± 0.46 | -2.88 ± 0.53 | 1368 ± 276 | -521 ± 104 |
| C II | 1334.53 | 1332.79 ± 0.65 | -1.14 ± 0.42 | 817 ± 365 | -392 ± 147 |
| Si II | 1526.71 | 1527.59 ± 0.82 | -1.19 ± 0.63 | 571 ± 374 | 173 ± 160 |
| C IV | 1549.48 | 1547.02 ± 0.52 | -2.44 ± 0.65 | 811 ± 251 | -477 ± 100 |
| Al II | 1670.79 | 1671.40 ± 0.48 | -0.84 ± 0.41 | 149 ± 202 | 109 ± 85 |

Table 5.3: Physical Properties of ULBGs and typical LBGs.

| | M_{stellar} | SFR | $E(B - V)$ | age | reference |
|----------------------|----------------------|-----------------------------|------------|--------|-----------------------|
| | M_{\odot} | $M_{\odot} \text{ yr}^{-1}$ | | Myr | |
| ULBG | 6.0×10^{10} | 280 | 0.15 | 398 | this work |
| $z \sim 3 L^*$ LBG | 2.4×10^{10} | 90 | 0.16 | 320 | Shapley et al. (2001) |
| $z \sim 3$ young LBG | 5.8×10^9 | 420 | 0.26 | < 35 | Shapley et al. (2001) |
| $z \sim 3$ old LBG | 8.0×10^{10} | 50 | 0.10 | 1000 | Shapley et al. (2001) |
| $z \sim 2 L^*$ LBG | 3.6×10^{10} | 93 | 0.21 | 640 | Shapley et al. (2005) |

CHAPTER 6

CONCLUSION AND FUTURE STUDIES

6.1 Conclusion

In this thesis, I focus on the luminous high-redshift star-forming galaxies at $z \sim 2 - 3$, the peak of the cosmic star formation activity.

First, we studied the detailed physical properties of a lensed high-redshift star-forming galaxy (J0900+2234) at $z = 2.03$ with the LBT/LUCIFER high S/N near-IR spectroscopic observations. The near-IR H+K spectrum covers the rest-frame optical nebular diagnostic lines, including $H\beta$, [O III] doublets, $H\alpha$, [N II], and [S II] doublets. With this well measured emission line and broad band SED fitting, we studied wide range of physical properties of this galaxy. The larger $E(B-V)$ derived from the Balmer decrement than that derived from the UV slope suggests that there is more extinction towards the ionized gas than the stellar continuum. We found that the metallicity in this star forming galaxy is only 21 – 35% solar metallicity, which is somewhat lower than typical star-forming galaxies at $z \sim 2$. The electron number density, n_e , is much larger than that in local H II regions. The SFR is measured from the extinction-corrected luminosity of $H\alpha$ emission line, which is $365 \pm 69 M_\odot \text{ yr}^{-1}$. The Virial mass of J0900+2234 is derived from the FWHM of the $H\alpha$ emission line and we found a dynamical mass of $(5.8 \pm 0.9) \times 10^{10} M_\odot$. The gas mass of the galaxy is $(5.1 \pm 1.1) \times 10^{10} M_\odot$ estimated from the $H\alpha$ flux by assuming the global Kennicutt-Schmidt law.

Secondly, we use the LBT Boötes field survey to identify a large sample of LBGs at $z \sim 3$. With this large sample of LBGs, we probe the bright end luminosity function, stellar mass function and clustering properties of LBGs ($1L^* < L < 2.5L^*$). The large sample of LBGs reduces the statistical error and cosmic variance

by a factor of 3, compared to previous studies. We found an excess power of the LF at the brightest end. This excess is dominated by the AGN/Quasar population. The stellar mass function suggests that the faint $z \sim 3$ LBGs dominate the low mass end stellar mass density, but only contribute a small fraction of stellar mass density at the high galaxy mass end. Together with other LF and SMF measurements at other redshifts, the evolution of LF and SMF can be well described by continuously rising star formation history model. The clustering and hosting halo mass of two subsample of LBGs ($24.5 < R < 24.0$ and $24.0 < R < 23.0$) are measured. Together with the similar measurements, a tight relation between the average host galaxy halo mass and the galaxy star formation rate is found, which can be interpreted as arising from cold flow accretion. The relation also suggests that the cosmic star formation efficiency is about 5%-20% of the total cold flow mass. This cosmic star formation efficiency does not evolve with redshift (from $z \sim 5$ to $z \sim 3$), hosting dark matter halo mass ($10^{11} - 10^{13} M_{\odot}$), or galaxy luminosity (from $0.1L^*$ to $3L^*$).

Thirdly, we conducted spectroscopic follow-up observations in the Boötes field to search for ultra-luminous LBGs (ULBGs, $L > 5L^*$). The first ULBG, J1432+3358, was discovered in the Boötes field in 2010. This galaxy shows very unique properties compared to typical L^* LBGs. With the deep Gemini/GMOS spectrum, we found that the ULBG has larger outflow velocity, broader $\text{Ly}\alpha$ emission and ISM absorption features. From the SED fitting, we found that J1432+3358 is very massive with stellar mass of $10^{11} M_{\odot}$, and SFRs derived from SED fitting and UV luminosity are consistent with each other, which are $300 M_{\odot} \text{ yr}^{-1}$. The deep Subaru z -band image shows a double core morphology of this galaxy, implying this galaxy is probably in the early phase of the major merger.

Finally, motivated by the discovery of this unique galaxy, we carried out a

spectroscopic survey of ULBGs in Boötes field and SDSS stripe 82 field. A sample of ULBGs has been established in this survey. With the new spectroscopically-confirmed ULBG sample, the rest-frame UV LF at $M_{1700\text{\AA}}^{\circ} = -23.0$ was measured for the first time, and it is consistent with the Schechter function extrapolating from the UV LF measurements at $M_{1700\text{\AA}}^{\circ} > -22.5$ very well. We compared the composite spectrum of the ULBGs with typical LBGs, and found that the ULBGs have larger outflow velocity, broader Ly α emission and ISM absorption line profiles, and more prominent C IV P-Cygni profile. This profile may imply a top-heavy IMF in these ULBGs. The distribution of these ULGs in the IRAC [3.6]–[4.5] versus [5.8]–8.0 color-color diagram suggests that stellar population features dominate the emissions between 5.8 μm and 8.0 μm and AGN activity is weak in these LBGs. From the SED fitting, the SFRs, dust extinctions, stellar masses and ages of these ULBGs were derived. The ULBGs have larger stellar mass and SFR, but smaller dust extinction than the typical L^* LBGs at $z \sim 2 - 3$. We proposed two evolutionary scenarios, pre-starburst and post-starburst. The properties of the ULBGs, especially their morphologies, prefer the pre-starburst scenario. Further high spatial resolution HST imaging and IFU spectroscopic observations will allow us to distinguish these two scenarios.

6.2 Further Studies

In my future works, I plan to continue studying the properties of the $z \sim 3$ ULBGs and reveal the nature of these high-redshift luminous galaxies, and I will also extend the study to ULBGs at higher redshift ($4 < z < 6$) in the existing deep wide field survey, such as CFHT surveys, and upcoming deep wide surveys, including Dark Energy Survey and Hyper Supreme-Cam Survey.

6.2.1 The Nature of the ULBGs

I will study these luminous LBGs with the high spatial resolution imaging taken by HST/WFC3. In addition to the HST imaging, I plan to conduct a survey on these galaxies with a near-IR integral field spectrograph. These surveys will explore the stellar structure and gas kinematics in the galaxies down to sub-kpc scale. I will look for signatures of major mergers, measure the relative contribution of the nuclear point source to the total luminosity, and make quantitative kinematical and morphological measurements. These analyses will help us to understand the triggering mechanisms of the intense star formation in these galaxies, constrain their star formation and assembly histories, and reveal their evolutionary stage in the overall sequence of galaxy formation. With this survey, I will establish a comprehensive view of the formation of these galaxies. Furthermore, with the future full array of ALMA, I plan to carry out high spatial resolution CO spectroscopy and dust continuum imaging to map the gas dynamics and study the dust properties of these ultra-luminous LBGs.

6.2.2 Galaxy Evolution in the Early Universe with the Deep and Wide Surveys

The upcoming deep and wide field surveys, especially the Hyper Suprime-Cam Survey (HSC survey) and the Dark Energy Survey (DES) will cover a few thousand square degrees with multi-band (*grizy* broad-band plus narrow-band filters) imaging reaching the depth down to $r \simeq 25.0 - 26.0$. This deep and wide survey provides unique capabilities to explore galaxy formation and evolution in the early Universe. Using these surveys, I plan to extend my current research on LBGs to both the higher redshifts and the fainter end.

In this survey, I plan to search for the ULBGs in the redshift interval, $4 < z < 6$. I will study the spatial clustering of these ULBGs at high redshifts. This new measurement in the deep and wide field surveys will not only fill in the high lumi-

nosity ($10L^*$) and massive dark matter halo ends at $z \sim 4-5$, but it will also extend the LBG clustering measurements to $z \sim 6$. Furthermore, I plan to use the gravitational lensing in these deep and wide fields to probe the faint end of the high-redshift galaxies ($0.4L^*$). These intrinsically faint LBGs ($0.4L^*$), together with my ultra-luminous LBGs ($5L^*$) sample and the intermediate luminosity LBGs sample (L^*) in the GOODS field, will provide the most comprehensive sample of LBGs in the early Universe.

APPENDIX A

INTEGRAL CONSTRAINT

Following the procedures in Adelberger et al. (2005b), we calculate the total IC from:

$$IC = \frac{1}{\sum_1^n RR_i} \sum_1^n \sigma_i^2 DD_i, \quad (\text{A.1})$$

where the RR_i is the random pair number in the i th field in the chosen angular bin, i.e., the sum sign means to sum over all the individual field. The σ_i for each field can be calculated from,

$$b = \frac{\sigma}{\sigma_{CDM}} = \frac{\sigma_{8,g}}{\sigma_8(z)}, \quad (\text{A.2})$$

where $\sigma_8(z)$ is the linear matter fluctuation in spheres of comoving $8 h^{-1}$ Mpc. We can get it from $\sigma_8(z) = \sigma_8(0) * D(z)$, where $\sigma_8(0) = 0.9$, and $D(z)$ is linear growth factor. $\sigma_{8,g}$ is the galaxies variance at the same scale, and it is calculated from

$$\sigma_{8,g}^2 = \frac{72(r_0/8h^{-1}\text{Mpc})^\gamma}{(3-\gamma)(4-\gamma)(6-\gamma)2^\gamma}, \quad (\text{A.3})$$

where r_0 and γ are the comoving correlation length and the power-law index in the 3-D correlation function. σ_{CDM} , the relative variance of the dark matter from one field to another, can be calculated from

$$\sigma_{CDM} = \frac{1}{(2\pi)^{3/2}} \left(\int d^3k P_L(|k|) |W_k(k)| \right)^{1/2}, \quad (\text{A.4})$$

where $P_L(k)$ is the linear cold dark matter (CDM) power spectrum, and W_k is the Fourier transform of a survey volume, which can be computed as

$$W_k = \exp \left(\frac{k_z^2 l_z^2}{2} \right) \frac{\sin(k_x I_x/2)}{k_x I_x/2} \frac{\sin(k_y I_y/2)}{k_y I_y/2}, \quad (\text{A.5})$$

where I_x and I_y are the comoving dimensions of the field of view for each field, and I_z is comoving dimensions of the radial direction, which can be convert from

the redshift distribution. As the field of view and selection function are almost the same for each field, we adopt the same σ for all the fields.

APPENDIX B

HALO OCCUPATION DISTRIBUTION

The halo occupation distribution (HOD) is applied to our LBG clustering results to interpret hosting dark matter halo properties for these two bright LBG subsample. Following the procedure of Hamana et al. (2004), the dark matter halo mass function from Sheth & Tormen (1999) is used. The number distribution for a given galaxy population as a function of the hosting dark matter halo is adopted as:

$$N_g(M) = \begin{cases} (M/M_1)^\alpha & \text{for } M \geq M_{\min} \\ 0 & \text{for } M < M_{\min}, \end{cases} \quad (\text{B.1})$$

where M_{\min} is the minimum mass of halo hosting the galaxy population, M_1 is the typical mass of halo hosting one galaxy and α is the power-law index. For close galaxy pairs in the same dark matter halo, the following number distribution of the galaxy pairs as function of halo mass is applied (Bullock et al., 2002):

$$\langle N_g(N_g - 1) \rangle(M) = \begin{cases} N_g^2(M) & \text{for } N_g(M) \geq 1 \\ N_g^2(M) \log(4N_g(M)) / \log(4) & \text{for } 1 > N_g(M) \geq 0.25 \\ 0 & \text{for } N_g(M) < 0.25. \end{cases} \quad (\text{B.2})$$

From the halo mass distribution described above and the galaxy population distribution as a function of the halo mass, we can further derive the number density of the galaxy populations and the galaxy power spectrum, which is comprised of two components, one is from the galaxy pairs in the same dark matter halo, the 1-halo term, and the other is from the galaxies in two different dark matter halos, the 2-halo term. Then the galaxy spectrum is converted to the 2D ACF.

We fit both 2D ACF and number density of the galaxy population results with our measurements.

APPENDIX C

ULTRA-LUMINOUS LBGs IN SDSS STRIPE 82 FIELD

SDSS Deep Stripe provide an ideal field to search these luminous LBGs. Over the last decade, SDSS (York et al. 2000) has performed multiple scans of Fall Equatorial Stripe covering $\sim 300 \text{ deg}^2$. Over 80 epoch images have been taken, reaching u and $r \sim 24.5$, which is the widest multi-epoch deep optical imaging data to date. The $z \sim 3$ LBG candidates are selected by the U-dropout method (i.e. Lyman Break method). By using the BC03 stellar synthesis model, we simulated the distribution of the $z \sim 3$ star-forming galaxies in $u - g$ versus $g - r$ diagram to determine the selection criterion of $z \sim 3$ LBGs as follows: (A) $\sigma_r < 0.1$ and $\sigma_g < 0.3$; (B) $u - g > 1.9 \times g - r + 0.6$; (C) $0 < g - r < 1.2$; (D) $r < 22.5$.

In the last three years survey with the MMT BCS, 14 ULBGs are discovered figure C.1. They have r -band magnitude of 21 – 22.3, 2 – 3 magnitudes brighter than that of LBGs in previous samples. Their morphology and the lack of obvious lensing galaxy or multiple components suggest that these galaxies are intrinsically luminous and not significantly boosted by lensing. These galaxies are characterized by: (1) extremely high star formation rate (SFR). The SFR derived from UV luminosity is several hundreds to more than one thousand solar masses per year, an order of magnitude higher than typical LBGs; (2) large galaxy size. $z \sim 2 - 3$ LBGs are known to have compact morphology (half-light radii $< 0.5''$, Giavalisco et al. 1996). However, all our objects could be resolved under ground-based seeing conditions. Most show substructure, often with bright nuclei and extended nebosity at 1 – 3'' scale; (3) a wide range in the level of AGN activity. Spectra of most of the galaxies show narrow $\text{Ly}\alpha$ emission or absorption lines but no other prominent emission lines (e.g. NV and CIV), indicating that there

is no/weak unobscured AGN activities in these galaxies, while there are a few galaxies show CIV emission or wide $\text{Ly}\alpha$ emission lines, implying strong AGN activities, coeval with intense star formation.

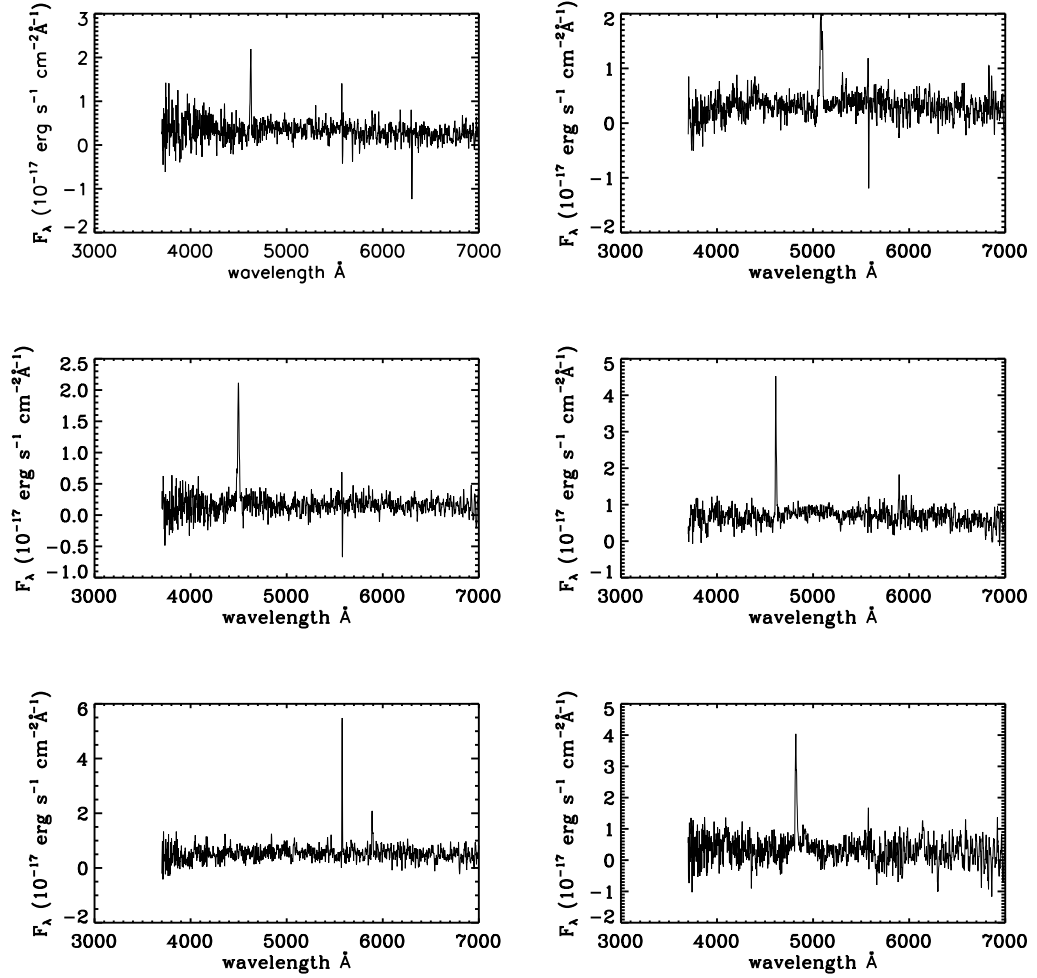


Figure C.1: The MMT BCS spectra of confirmed ULBGs in SDSS Deep Stripe Field.

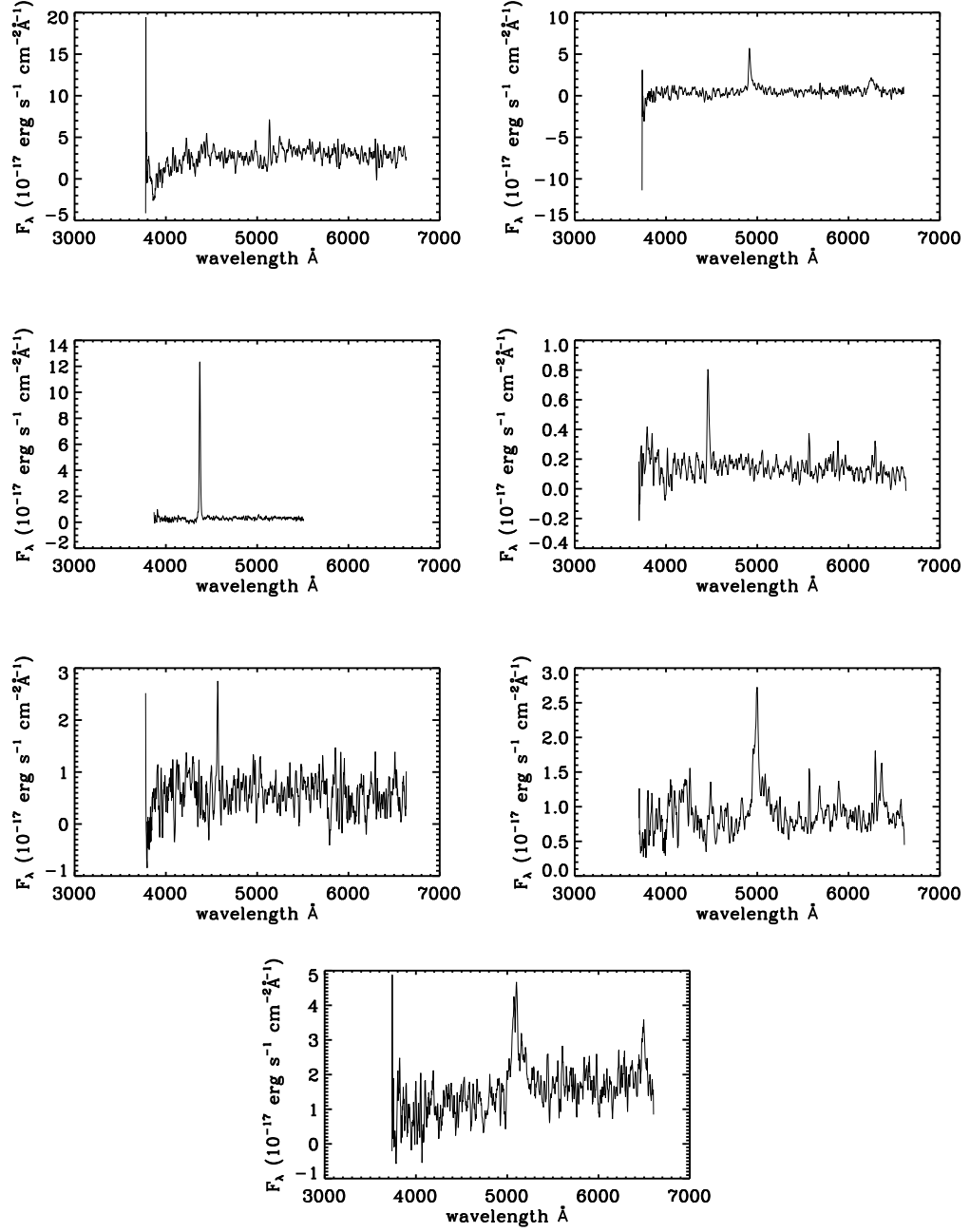


Figure C.1: Continued figure

REFERENCES

- Adelberger, K. L., Shapley, A. E., Steidel, C. C., Pettini, M., Erb, D. K., & Reddy, N. A. 2005a, *ApJ*, 629, 636
- Adelberger, K. L., Steidel, C. C., Giavalisco, M., Dickinson, M., Pettini, M., & Kellogg, M. 1998, *ApJ*, 505, 18
- Adelberger, K. L., Steidel, C. C., Pettini, M., Shapley, A. E., Reddy, N. A., & Erb, D. K. 2005b, *ApJ*, 619, 697
- Adelberger, K. L., Steidel, C. C., Shapley, A. E., & Pettini, M. 2003, *ApJ*, 584, 45
- Ageorges, N., et al. 2010, in Society of Photo-Optical Instrumentation Engineers (SPIE) Conference Series, Vol. 7735, Society of Photo-Optical Instrumentation Engineers (SPIE) Conference Series
- Allam, S. S., Tucker, D. L., Lin, H., Diehl, H. T., Annis, J., Buckley-Geer, E. J., & Frieman, J. A. 2007, *ApJL*, 662, L51
- Alloin, D., Collin-Souffrin, S., Joly, M., & Vigroux, L. 1979, *A&A*, 78, 200
- Ashby, M. L. N., et al. 2009, *ApJ*, 701, 428
- Asplund, M., Grevesse, N., Sauval, A. J., & Scott, P. 2009, *ARA&A*, 47, 481
- Baker, A. J., Lutz, D., Genzel, R., Tacconi, L. J., & Lehnert, M. D. 2001, *A&A*, 372, L37
- Baldwin, J. A., Phillips, M. M., & Terlevich, R. 1981, *PASP*, 93, 5
- Bechtold, J., Yee, H. K. C., Elston, R., & Ellingson, E. 1997, *ApJL*, 477, L29

- Becker, G. D., Rauch, M., & Sargent, W. L. W. 2009, *ApJ*, 698, 1010
- Becker, R. H., White, R. L., & Helfand, D. J. 1995, *ApJ*, 450, 559
- Belokurov, V., Evans, N. W., Hewett, P. C., Moiseev, A., McMahon, R. G., Sanchez, S. F., & King, L. J. 2009, *MNRAS*, 392, 104
- Bentz, M. C., Pogge, R. W., & Osmer, P. S. 2008, *AJ*, 136, 498
- Bertin, E. 2006, in *Astronomical Society of the Pacific Conference Series*, Vol. 351, *Astronomical Data Analysis Software and Systems XV*, ed. C. Gabriel, C. Arviset, D. Ponz, & S. Enrique, 112
- Bertin, E., & Arnouts, S. 1996, *A&AS*, 117, 393
- Bertin, E., Mellier, Y., Radovich, M., Missonnier, G., Didelon, P., & Morin, B. 2002, in *Astronomical Society of the Pacific Conference Series*, Vol. 281, *Astronomical Data Analysis Software and Systems XI*, ed. D. A. Bohlender, D. Durand, & T. H. Handley, 228
- Bian, F., et al. 2010, *ApJ*, 725, 1877
- . 2012, *ApJ*, 757, 139
- Bouwens, R. J., Illingworth, G. D., Franx, M., & Ford, H. 2007, *ApJ*, 670, 928
- . 2008, *ApJ*, 686, 230
- Bouwens, R. J., et al. 2009, *ApJ*, 705, 936
- . 2011a, *Nature*, 469, 504
- . 2011b, *ApJ*, 737, 90
- . 2012, *ApJ*, 754, 83

- Brand, K., et al. 2006, *ApJ*, 641, 140
- Brinchmann, J., Charlot, S., White, S. D. M., Tremonti, C., Kauffmann, G., Heckman, T., & Brinkmann, J. 2004, *MNRAS*, 351, 1151
- Bruzual, G., & Charlot, S. 2003, *MNRAS*, 344, 1000
- Bullock, J. S., Wechsler, R. H., & Somerville, R. S. 2002, *MNRAS*, 329, 246
- Calzetti, D., Armus, L., Bohlin, R. C., Kinney, A. L., Koornneef, J., & Storchi-Bergmann, T. 2000, *ApJ*, 533, 682
- Chabrier, G. 2003, *PASP*, 115, 763
- Chapman, S. C., Blain, A. W., Smail, I., & Ivison, R. J. 2005, *ApJ*, 622, 772
- Chapman, S. C., & Casey, C. M. 2009, *MNRAS*, 398, 1615
- Chapman, S. C., et al. 2000, *MNRAS*, 319, 318
- Cole, S., et al. 2001, *MNRAS*, 326, 255
- Cooke, J., Barton, E. J., Bullock, J. S., Stewart, K. R., & Wolfe, A. M. 2008, *ApJL*, 681, L57
- Cool, R. J. 2006, in *Bulletin of the American Astronomical Society*, Vol. 38, American Astronomical Society Meeting Abstracts, 1170
- Cool, R. J. 2007, *ApJS*, 169, 21
- Cowie, L. L., & Hu, E. M. 1998, *AJ*, 115, 1319
- Cowie, L. L., Songaila, A., Hu, E. M., & Cohen, J. G. 1996, *AJ*, 112, 839

- Daddi, E., Cimatti, A., Renzini, A., Fontana, A., Mignoli, M., Pozzetti, L., Tozzi, P., & Zamorani, G. 2004, *ApJ*, 617, 746
- Daddi, E., et al. 2005, *ApJL*, 631, L13
- . 2007, *ApJ*, 670, 156
- . 2010a, *ApJL*, 714, L118
- . 2010b, *ApJ*, 713, 686
- Davé, R., Finlator, K., Oppenheimer, B. D., Fardal, M., Katz, N., Kereš, D., & Weinberg, D. H. 2010, *MNRAS*, 404, 1355
- Davé, R., Oppenheimer, B. D., & Finlator, K. 2011, *MNRAS*, 415, 11
- de Vries, W. H., Morganti, R., Röttgering, H. J. A., Vermeulen, R., van Breugel, W., Rengelink, R., & Jarvis, M. J. 2002, *AJ*, 123, 1784
- Dekel, A., et al. 2009, *Nature*, 457, 451
- Denicoló, G., Terlevich, R., & Terlevich, E. 2002, *MNRAS*, 330, 69
- Dey, A., van Breugel, W., Vacca, W. D., & Antonucci, R. 1997, *ApJ*, 490, 698
- Dey, A., et al. 2008, *ApJ*, 677, 943
- Dickey, J. M., & Lockman, F. J. 1990, *ARA&A*, 28, 215
- Dickinson, M., Papovich, C., Ferguson, H. C., & Budavári, T. 2003, *ApJ*, 587, 25
- Diehl, H. T., et al. 2009, *ApJ*, 707, 686
- Donley, J. L., Rieke, G. H., Pérez-González, P. G., & Barro, G. 2008, *ApJ*, 687, 111

- Drory, N., Salvato, M., Gabasch, A., Bender, R., Hopp, U., Feulner, G., & Pannella, M. 2005, *ApJL*, 619, L131
- Elbaz, D., et al. 2007, *A&A*, 468, 33
- Elston, R. J., et al. 2006, *ApJ*, 639, 816
- Erb, D. K., Shapley, A. E., Pettini, M., Steidel, C. C., Reddy, N. A., & Adelberger, K. L. 2006a, *ApJ*, 644, 813
- Erb, D. K., Shapley, A. E., Steidel, C. C., Pettini, M., Adelberger, K. L., Hunt, M. P., Moorwood, A. F. M., & Cuby, J.-G. 2003, *ApJ*, 591, 101
- Erb, D. K., Steidel, C. C., Shapley, A. E., Pettini, M., Reddy, N. A., & Adelberger, K. L. 2006b, *ApJ*, 647, 128
- . 2006c, *ApJ*, 646, 107
- Fan, X. 1999, *AJ*, 117, 2528
- Fan, X., et al. 2001, *AJ*, 121, 54
- Ferguson, H. C., et al. 2004, *ApJL*, 600, L107
- Filippenko, A. V. 1982, *PASP*, 94, 715
- Finkelstein, S. L., Papovich, C., Rudnick, G., Egami, E., Le Floch, E., Rieke, M. J., Rigby, J. R., & Willmer, C. N. A. 2009, *ApJ*, 700, 376
- Finlator, K., & Davé, R. 2008, *MNRAS*, 385, 2181
- Finlator, K., Oppenheimer, B. D., & Davé, R. 2011, *MNRAS*, 410, 1703
- Fiore, F., et al. 2008, *ApJ*, 672, 94

- Forster, K., Green, P. J., Aldcroft, T. L., Vestergaard, M., Foltz, C. B., & Hewett, P. C. 2001, *ApJS*, 134, 35
- Förster Schreiber, N. M., et al. 2009, *ApJ*, 706, 1364
- Francis, P. J., et al. 1996, *ApJ*, 457, 490
- Franx, M., et al. 2003, *ApJL*, 587, L79
- Genzel, R., et al. 2010, *MNRAS*, 407, 2091
- Giallongo, E., et al. 2008, *A&A*, 482, 349
- Giavalisco, M., & Dickinson, M. 2001, *ApJ*, 550, 177
- Giavalisco, M., Steidel, C. C., Adelberger, K. L., Dickinson, M. E., Pettini, M., & Kellogg, M. 1998, *ApJ*, 503, 543
- González, V., Labbé, I., Bouwens, R. J., Illingworth, G., Franx, M., Kriek, M., & Brammer, G. B. 2010, *ApJ*, 713, 115
- Hainline, K. N., Shapley, A. E., Kornei, K. A., Pettini, M., Buckley-Geer, E., Allam, S. S., & Tucker, D. L. 2009, *ApJ*, 701, 52
- Hamana, T., Ouchi, M., Shimasaku, K., Kayo, I., & Suto, Y. 2004, *MNRAS*, 347, 813
- Heckman, T. M., Lehnert, M. D., Strickland, D. K., & Armus, L. 2000, *ApJS*, 129, 493
- Hickox, R. C., et al. 2011, *ArXiv e-prints*
- Hildebrandt, H., Pielorz, J., Erben, T., Schneider, P., Eifler, T., Simon, P., & Dietrich, J. P. 2007, *A&A*, 462, 865

- Hill, J. M., et al. 2008, in Society of Photo-Optical Instrumentation Engineers (SPIE) Conference Series, Vol. 7012, Society of Photo-Optical Instrumentation Engineers (SPIE) Conference Series
- Hoopes, C. G., Heckman, T. M., Jannuzi, B. T., Dey, A., Brown, M. J. I., Ford, A., & GALEX Science Team. 2003, in Bulletin of the American Astronomical Society, Vol. 35, American Astronomical Society Meeting Abstracts, 1371
- Hopkins, P. F., Hernquist, L., Cox, T. J., & Kereš, D. 2008, *ApJS*, 175, 356
- Hu, E. M., & McMahon, R. G. 1996, *Nature*, 382, 231
- Hunt, M. P., Steidel, C. C., Adelberger, K. L., & Shapley, A. E. 2004, *ApJ*, 605, 625
- Jain, B., & Lima, M. 2011, *MNRAS*, 411, 2113
- Jannuzi, B. T., & Dey, A. 1999, in Astronomical Society of the Pacific Conference Series, Vol. 191, Photometric Redshifts and the Detection of High Redshift Galaxies, ed. R. Weymann, L. Storrie-Lombardi, M. Sawicki, & R. Brunner, 111
- Jones, T., Stark, D. P., & Ellis, R. S. 2012, *ApJ*, 751, 51
- Just, D. W., Brandt, W. N., Shemmer, O., Steffen, A. T., Schneider, D. P., Chartas, G., & Garmire, G. P. 2007, *ApJ*, 665, 1004
- Kajisawa, M., et al. 2009, *ApJ*, 702, 1393
- Kartaltepe, J. S., et al. 2011, ArXiv e-prints
- Kauffmann, G., et al. 2003, *MNRAS*, 346, 1055
- Kennicutt, Jr., R. C. 1998a, *ARA&A*, 36, 189
- . 1998b, *ApJ*, 498, 541

- Kenter, A., et al. 2005, *ApJS*, 161, 9
- Kereš, D., Katz, N., Weinberg, D. H., & Davé, R. 2005, *MNRAS*, 363, 2
- Kewley, L. J., Dopita, M. A., Sutherland, R. S., Heisler, C. A., & Trevena, J. 2001, *ApJ*, 556, 121
- Kim, K.-T., & Koo, B.-C. 2001, *ApJ*, 549, 979
- Koester, B. P., Gladders, M. D., Hennawi, J. F., Sharon, K., Wuyts, E., Rigby, J. R., Bayliss, M. B., & Dahle, H. 2010, *ApJL*, 723, L73
- Kriek, M., van Dokkum, P. G., Labbé, I., Franx, M., Illingworth, G. D., Marchesini, D., & Quadri, R. F. 2009, *ApJ*, 700, 221
- Kroupa, P. 2001, *MNRAS*, 322, 231
- Kubo, J. M., Allam, S. S., Annis, J., Buckley-Geer, E. J., Diehl, H. T., Kubik, D., Lin, H., & Tucker, D. 2009, *ApJL*, 696, L61
- Kulas, K. R., Shapley, A. E., Kollmeier, J. A., Zheng, Z., Steidel, C. C., & Hainline, K. N. 2012, *ApJ*, 745, 33
- Kurtz, M. J., & Mink, D. J. 1998, *PASP*, 110, 934
- Lacey, C. G., Baugh, C. M., Frenk, C. S., & Benson, A. J. 2011, *MNRAS*, 412, 1828
- Lacy, M., et al. 2004, *ApJS*, 154, 166
- Landy, S. D., & Szalay, A. S. 1993, *ApJ*, 412, 64
- Larson, R. B. 1974, *MNRAS*, 169, 229
- Law, D. R., Steidel, C. C., Shapley, A. E., Nagy, S. R., Reddy, N. A., & Erb, D. K. 2012, *ApJ*, 745, 85

- Le Fèvre, O., et al. 2005, *Nature*, 437, 519
- Lee, K.-S., Giavalisco, M., Conroy, C., Wechsler, R. H., Ferguson, H. C., Somerville, R. S., Dickinson, M. E., & Urry, C. M. 2009, *ApJ*, 695, 368
- Lee, K.-S., Giavalisco, M., Gnedin, O. Y., Somerville, R. S., Ferguson, H. C., Dickinson, M., & Ouchi, M. 2006, *ApJ*, 642, 63
- Lee, K.-S., et al. 2011, *ApJ*, 733, 99
- . 2012, *ApJ*, 752, 66
- Lilly, S. J., Le Fevre, O., Hammer, F., & Crampton, D. 1996, *ApJL*, 460, L1+
- Lin, H., et al. 2009, *ApJ*, 699, 1242
- Liu, X., Shapley, A. E., Coil, A. L., Brinchmann, J., & Ma, C.-P. 2008, *ApJ*, 678, 758
- Lotz, J. M., Primack, J., & Madau, P. 2004, *AJ*, 128, 163
- Ly, C., et al. 2009, *ApJ*, 697, 1410
- Madau, P. 1995, *ApJ*, 441, 18
- Madau, P., Ferguson, H. C., Dickinson, M. E., Giavalisco, M., Steidel, C. C., & Fruchter, A. 1996, *MNRAS*, 283, 1388
- Maiolino, R., et al. 2008, *A&A*, 488, 463
- Mannucci, F., Cresci, G., Maiolino, R., Marconi, A., & Gnerucci, A. 2010, *MNRAS*, 408, 2115
- Marchesini, D., van Dokkum, P. G., Förster Schreiber, N. M., Franx, M., Labbé, I., & Wuyts, S. 2009, *ApJ*, 701, 1765

- Martin, C. L. 2005, *ApJ*, 621, 227
- Mehlert, D., et al. 2001, *A&A*, 379, 96
- Meurer, G. R., Heckman, T. M., & Calzetti, D. 1999, *ApJ*, 521, 64
- Mo, H. J., Mao, S., & White, S. D. M. 1998, *MNRAS*, 295, 319
- Mo, H. J., & White, S. D. M. 1996, *MNRAS*, 282, 347
- Murray, N., Quataert, E., & Thompson, T. A. 2005a, *ApJ*, 618, 569
- Murray, S. S., et al. 2005b, *ApJS*, 161, 1
- Narayanan, D., & Davé, R. 2012a, *MNRAS*, 423, 3601
- . 2012b, ArXiv e-prints
- Narayanan, D., Hayward, C. C., Cox, T. J., Hernquist, L., Jonsson, P., Younger, J. D., & Groves, B. 2010, *MNRAS*, 401, 1613
- Noeske, K. G., et al. 2007, *ApJL*, 660, L43
- Oesch, P. A., et al. 2010, *ApJL*, 725, L150
- Oke, J. B., & Gunn, J. E. 1983, *ApJ*, 266, 713
- Oppenheimer, B. D., & Davé, R. 2008, *MNRAS*, 387, 577
- Oppenheimer, B. D., Davé, R., Kereš, D., Fardal, M., Katz, N., Kollmeier, J. A., & Weinberg, D. H. 2010, *MNRAS*, 406, 2325
- Osterbrock, D. E., & Ferland, G. J. 2006, *Astrophysics of gaseous nebulae and active galactic nuclei*
- Ouchi, M., et al. 2005, *ApJL*, 635, L117

- Papovich, C., Dickinson, M., & Ferguson, H. C. 2001, *ApJ*, 559, 620
- Papovich, C., Finkelstein, S. L., Ferguson, H. C., Lotz, J. M., & Giavalisco, M. 2011, *MNRAS*, 412, 1123
- Peebles, P. J. E. 1980, *The large-scale structure of the universe*, (Princeton: Princeton Univ. Press)
- Peng, C. Y., Ho, L. C., Impey, C. D., & Rix, H.-W. 2002, *AJ*, 124, 266
- . 2010a, *AJ*, 139, 2097
- Peng, C. Y., Impey, C. D., Rix, H.-W., Kochanek, C. S., Keeton, C. R., Falco, E. E., Lehár, J., & McLeod, B. A. 2006, *ApJ*, 649, 616
- Peng, Y.-j., et al. 2010b, *ApJ*, 721, 193
- Pettini, M., & Pagel, B. E. J. 2004, *MNRAS*, 348, L59
- Pettini, M., Rix, S. A., Steidel, C. C., Adelberger, K. L., Hunt, M. P., & Shapley, A. E. 2002, *ApJ*, 569, 742
- Pettini, M., Shapley, A. E., Steidel, C. C., Cuby, J.-G., Dickinson, M., Moorwood, A. F. M., Adelberger, K. L., & Giavalisco, M. 2001, *ApJ*, 554, 981
- Pettini, M., Steidel, C. C., Adelberger, K. L., Dickinson, M., & Giavalisco, M. 2000, *ApJ*, 528, 96
- Pettini, M., et al. 2010, *MNRAS*, 402, 2335
- Prescott, M. K. M., Dey, A., & Jannuzi, B. T. 2012, *ApJ*, 748, 125
- Press, W. H., Teukolsky, S. A., Vetterling, W. T., & Flannery, B. P. 1992, *Numerical recipes in FORTRAN. The art of scientific computing*

- Quider, A. M., Pettini, M., Shapley, A. E., & Steidel, C. C. 2009, MNRAS, 398, 1263
- Quider, A. M., Shapley, A. E., Pettini, M., Steidel, C. C., & Stark, D. P. 2010, MNRAS, 402, 1467
- Raimann, D., Storch-Bergmann, T., Bica, E., Melnick, J., & Schmitt, H. 2000, MNRAS, 316, 559
- Reddy, N., et al. 2011, ArXiv e-prints
- Reddy, N. A., Erb, D. K., Pettini, M., Steidel, C. C., & Shapley, A. E. 2010, ApJ, 712, 1070
- Reddy, N. A., Erb, D. K., Steidel, C. C., Shapley, A. E., Adelberger, K. L., & Pettini, M. 2005, ApJ, 633, 748
- Reddy, N. A., Pettini, M., Steidel, C. C., Shapley, A. E., Erb, D. K., & Law, D. R. 2012, ArXiv e-prints
- Reddy, N. A., & Steidel, C. C. 2009, ApJ, 692, 778
- Reddy, N. A., Steidel, C. C., Pettini, M., Adelberger, K. L., Shapley, A. E., Erb, D. K., & Dickinson, M. 2008, ApJS, 175, 48
- Richard, J., Stark, D. P., Ellis, R. S., George, M. R., Egami, E., Kneib, J.-P., & Smith, G. P. 2008, ApJ, 685, 705
- Riechers, D. A., Carilli, C. L., Walter, F., & Momjian, E. 2010, ApJL, 724, L153
- Roche, N., & Eales, S. A. 1999, MNRAS, 307, 703
- Rodighiero, G., et al. 2011, ApJL, 739, L40

- Salpeter, E. E. 1955, *ApJ*, 121, 161
- Sand, D. J., Treu, T., Ellis, R. S., & Smith, G. P. 2005, *ApJ*, 627, 32
- Sawicki, M., & Thompson, D. 2006a, *ApJ*, 642, 653
- . 2006b, *ApJ*, 648, 299
- Scoville, N., et al. 2007, *ApJS*, 172, 1
- Sérsic, J. L. 1963, *Boletin de la Asociacion Argentina de Astronomia La Plata Argentina*, 6, 41
- Shapley, A. E., Steidel, C. C., Adelberger, K. L., Dickinson, M., Giavalisco, M., & Pettini, M. 2001, *ApJ*, 562, 95
- Shapley, A. E., Steidel, C. C., Erb, D. K., Reddy, N. A., Adelberger, K. L., Pettini, M., Barmby, P., & Huang, J. 2005, *ApJ*, 626, 698
- Shapley, A. E., Steidel, C. C., Pettini, M., & Adelberger, K. L. 2003, *ApJ*, 588, 65
- Sheth, R. K., & Tormen, G. 1999, *MNRAS*, 308, 119
- Shim, H., Im, M., Choi, P., Yan, L., & Storrie-Lombardi, L. 2007, *ApJ*, 669, 749
- Siana, B., et al. 2008, *ApJ*, 675, 49
- . 2009, *ApJ*, 698, 1273
- Smail, I., Ivison, R. J., & Blain, A. W. 1997, *ApJL*, 490, L5
- Smail, I., et al. 2007, *ApJL*, 654, L33
- Soifer, B. T., & Spitzer/NOAO Team. 2004, in *Bulletin of the American Astronomical Society*, Vol. 36, American Astronomical Society Meeting Abstracts #204, 746

- Spergel, D. N., et al. 2007, *ApJS*, 170, 377
- Stark, D. P., Ellis, R. S., Bunker, A., Bundy, K., Targett, T., Benson, A., & Lacy, M. 2009, *ApJ*, 697, 1493
- Stark, D. P., Ellis, R. S., Chiu, K., Ouchi, M., & Bunker, A. 2010, *MNRAS*, 408, 1628
- Stark, D. P., Loeb, A., & Ellis, R. S. 2007, *ApJ*, 668, 627
- Stark, D. P., Schenker, M. A., Ellis, R. S., Robertson, B., McLure, R., & Dunlop, J. 2012, *ArXiv e-prints*
- Steidel, C. C., Adelberger, K. L., Giavalisco, M., Dickinson, M., & Pettini, M. 1999, *ApJ*, 519, 1
- Steidel, C. C., Adelberger, K. L., Shapley, A. E., Pettini, M., Dickinson, M., & Giavalisco, M. 2003, *ApJ*, 592, 728
- Steidel, C. C., Bogosavljević, M., Shapley, A. E., Kollmeier, J. A., Reddy, N. A., Erb, D. K., & Pettini, M. 2011, *ApJ*, 736, 160
- Steidel, C. C., Erb, D. K., Shapley, A. E., Pettini, M., Reddy, N., Bogosavljević, M., Rudie, G. C., & Rakic, O. 2010, *ApJ*, 717, 289
- Steidel, C. C., Giavalisco, M., Dickinson, M., & Adelberger, K. L. 1996a, *AJ*, 112, 352
- Steidel, C. C., Giavalisco, M., Pettini, M., Dickinson, M., & Adelberger, K. L. 1996b, *ApJL*, 462, L17+
- Steidel, C. C., Shapley, A. E., Pettini, M., Adelberger, K. L., Erb, D. K., Reddy, N. A., & Hunt, M. P. 2004, *ApJ*, 604, 534

- Stern, D., et al. 2005, *ApJ*, 631, 163
- Storchi-Bergmann, T., Calzetti, D., & Kinney, A. L. 1994, *ApJ*, 429, 572
- Tacconi, L. J., et al. 2008, *ApJ*, 680, 246
- . 2010, *Nature*, 463, 781
- Teplitz, H. I., et al. 2000, *ApJL*, 533, L65
- Trenti, M., & Stiavelli, M. 2008, *ApJ*, 676, 767
- Turner, E. L., Ostriker, J. P., & Gott, III, J. R. 1984, *ApJ*, 284, 1
- van der Burg, R. F. J., Hildebrandt, H., & Erben, T. 2010, *A&A*, 523, A74
- van Dokkum, P. G. 2001, *PASP*, 113, 1420
- van Dokkum, P. G., et al. 2006, *ApJL*, 638, L59
- Verhamme, A., Schaerer, D., & Maselli, A. 2006, *A&A*, 460, 397
- Weiner, B. J., et al. 2009, *ApJ*, 692, 187
- White, R. L., Helfand, D. J., Becker, R. H., Glikman, E., & de Vries, W. 2007, *ApJ*, 654, 99
- Wuyts, E., Rigby, J. R., Sharon, K., & Gladders, M. D. 2012, *ApJ*, 755, 73
- Wuyts, S., et al. 2011, *ApJ*, 742, 96
- Yan, H., et al. 2011a, *ArXiv e-prints*
- . 2011b, *ApJL*, 728, L22
- Yee, H. K. C., Ellingson, E., Bechtold, J., Carlberg, R. G., & Cuillandre, J.-C. 1996, *AJ*, 111, 1783

York, D. G., et al. 2000, *AJ*, 120, 1579

Zaritsky, D., Kennicutt, Jr., R. C., & Huchra, J. P. 1994, *ApJ*, 420, 87

Zheng, Z., Coil, A. L., & Zehavi, I. 2007, *ApJ*, 667, 760